Dissertation

submitted to the

Combined Faculties of Mathematics, Engineering and Natural Sciences

of Heidelberg University, Germany

for the degree of

Doctor of Natural Sciences

Put forward by

Deepthy Maria Mootheril Thomas

born in: Fortkochin, Kerala, India

Oral examination: 26.06.2023

Electron impact ionization studies from atoms to complex molecules and clusters

Referees: Priv.-Doz. Alexander Dorn
Priv.-Doz. Wolfgang Quint

Abstract

In this work, a series of electron impact ionization studies on targets ranging from simple atoms to complex systems like clusters are summarized. The momenta of the ionization fragments are measured using a recoil-ion and electron momentum spectrometer called 'Reaction Microscope' (ReMi). The objectives of the thesis are two-fold. Firstly, two new target beam sources were constructed in order to enable, for the first time, kinematically complete (e,2e) experiments with the ReMi on substances which are solid at room temperature. As a result (e,2e) experiments were conducted on fundamental lithium and on a complex molecule, 1-Methyl,5-Nitroimidazole, which is among the potential radio-sensitizers under study for radiation therapy. The second part of the work is the study of intermolecular Coulombic decay (ICD) in the biologically relevant systems, thiophene dimers and pyridine$\cdots D_2O$ dimers. ICD initiated after ionization of the inner valence orbital $7a_1$ is identified in thiophene dimers. A comparison of the obtained kinetic energy release (KER) distribution with *ab initio* molecular dynamics simulations indicates that a majority of the ionized dimers have a T-shaped conformational structure. In the hydrated pyridine dimer, it was found that ICD is initiated by the inner valence ionization of O $2s^{-1}$ orbital of D_2O. ICD initiated from the C $2s^{-1}$ and N $2s^{-1}$ orbitals of pyridine is assumed to be quenched by the open Auger and electron transfer mediated decay (ETMD) channels.

Zusammenfassung

In dieser Arbeit wird eine Reihe von Studien zur Elektronenstoß-Ionisierung an Targets, die von einfachen Atomen bis zu komplexen Systemen wie Clustern reichen, zusammengefasst. Die Impulse der Ionisationsfragmente werden mit einem Rückstoß-Ionen- und Elektronenimpulsspektrometer, dem "Reaktionsmikroskop" (ReMi) gemessen. Diese Arbeit hat zwei Ziele. Erstens wurden zwei neue Targetstrahlquellen konstruiert, um erstmals kinematisch vollständige (e,2e)-Experimente mit dem ReMi an Substanzen zu ermöglichen, die bei Raumtemperatur fest sind. Als Ergebnis wurden (e,2e)-Experimente an grundlegendem Lithium und an einem komplexen Molekül, 1-Methyl,5-Nitroimidazol, durchgeführt, das zu den potenziellen Radiosensibilisatoren gehört, die in der Strahlentherapie Verwendung finden könnten. Der zweite Teil der Arbeit befasst sich mit der Untersuchung des intermolekularen Coulomb-Zerfalls (ICD) in biologisch relevanten Systemen, Thiophen-Dimeren und Pyridin$\cdots D_2O$-Dimeren. In Thiophen-Dimeren wird ICD nach der Ionisierung des inneren Valenzorbitals $7a_1$ initiiert. Ein Vergleich der, in der Coulombexplosion erhaltenen kinetischen Energieverteilung der Ionen (KER) mit Molekulardynamiksimulationen zeigt, dass die Mehrzahl der ionisierten Dimere eine T-förmige Konformation aufweist. Im hydratisierten Pyridindimer wurde festgestellt, dass die ICD durch die innere Valenzionisierung des O $2s^{-1}$-Orbitals von D_2O initiiert wird. Es wird angenommen, dass ICD, der von den C $2s^{-1}$- und N $2s^{-1}$-Orbitalen des Pyridins ausgeht, durch offene Auger- und Elektronentransfer vermittelten Zerfallskanäle (ETMD) unterdrückt wird.

Contents

Chapter 1

Introduction

The fields of atomic and nuclear physics were born together with the discovery of the nucleus and the structure of atom with Rutherford scattering experiment in 1911 [1]. Pioneering experiments with free electrons were first conducted even before that by Philip Lennard, which was called cathode rays at that time [2]. Studies on cross-sections of electron scattering by atoms began with Ramsauer measurements in 1921, where he studied total cross-sections and observed minima and maxima as a function of electron energy, more importantly a very low minimum at low electron energies [3]. This was also observed by Townsend and Bailey in 1922 as a transparency to the electrons in rare gases at very low energy [4]. Such a threshold effect termed as Ramsauer-Townsend effect provided a powerful stimulus to the development of quantum mechanics. Early electron collision experiments also gave insights to the discrete structure of the bound energy levels, such as the one performed by Frank and Hertz on mercury vapour [5].

Electron impact ionization experiments, therefore, served mainly two goals: firstly understanding the structure of the target (atom, molecule, surface etc) using coincident detection techniques of more than one particles. Secondly, to understand the collision dynamics by measuring the differential cross-sections which can act as a benchmark for the stringent test of theoretical models. Early (e,2e) spectroscopy, which deals with coincident detection of two outgoing electrons from an ionization event, were mostly focussed on determination of the momentum density function of the target electron. First such measurements were conducted on Carbon films with high impact energies from 0.1 to 10 keV range by Amaldi et al. in 1969 [6]. Parallelly, the studies on the dynamics of the collisions started by the measurements of Ehrhardt et al. on helium atoms where he studied the ionization by low energy electrons of 100 eV [7]. They presented the first ever triple differential cross-sections measurement and discussed the formation of the binary and recoil lobes. The experimental setups for the early measurements were based on two movable energy sensitive detectors which could be rotated with respect to the incoming beam direction. They allowed the coincidence detection and momentum determination of the two outgoing electrons thereby constituting kinematically complete experiments.

Since then, there have been tremendous improvements on the experimental side, especially with the introduction of the 'Reaction microscope' (ReMi) [8] by Ullrich et al. (2003). The ReMi is an improved version of the recoil-ion momentum spectrometer, which was originally developed for ion collision experiments [9] and facilitates the coincidence detection of ions and electrons in 4π solid angle. Usage of cold targets like supersonic gas jets and laser-cooled atomic traps improved the resolution tremendously [10]. Recent developments of the ReMi targets include the incorporation of an optical dipole

trap, which is envisaged for the imaging of molecular Bose-Einstein condensates [11] and a trapped ion source [12]. (e,2e) studies found an enormous level of advancement in measurements using ReMi due to the high momentum resolution and improved solid angle acceptance. Unlike conventional electron spectrometers, where the detection was restricted to the coplanar plane in most cases, the ReMi uses stationary detectors and, electric and magnetic fields to project the particles onto the detectors enabling 4π solid angle acceptance. Employment of ReMi in the (e,2e) studies provided the measurement of three dimensional fully differential cross-sections [13] and even, concidence detection of two or more electrons which enabled the study of Coulomb four-body break up dynamics [14, 15].

Concerning the theoretical description of the (e,2e) processes the major difficulty arises because the Schrödinger equation is analytically unsolvable beyond two particles interacting with each other. At high impact energies, the problem can be reduced effectively to a two-body system, whereas for intermediate and low energies long-range Coulomb interaction comes to play, which makes the problem unsolvable analytically and computationally expensive. Over the years several perturbative and non-perturbative models were developed. Perturbative models are based on Born approximations and the non-perturbative ones solve the Schrödinger equation exactly. Therefore, simple systems like helium, hydrogen, etc are treated using non-perturbative models, whereas complex systems like molecules and clusters are normally treated perturbatively. Simple three-body systems that have been solved with exact numerical calculation so far are electron impact ionization of hydrogen [16] and helium [17]. Some of the successful numerical models are exterior complex scaling [18], convergent close coupling [19], time-dependent close coupling [20] etc. For heavier atoms and for molecules several perturbative approaches based on Born approximations were developed. Distorted-wave Born approximation (DWBA) [21] and R-matrix method [22] are some of the most important among them. Challenges have to be dealt with when it comes to modelling collisions with molecular targets larger than H_2, because the theory has to take care of the multi-centre nature and the complex electronic structure of the target. Another problem is that the non-spherical molecular potential, which is randomly oriented in space due to the random orientation of molecules, necessitates averaging a large number of spatial orientations of the molecules, for a precise description of the collision process. One of the important models that take care of these types of collisions is the molecular three-body distorted wave (M3DW) [23] which makes use of orientation-averaged molecular orbitals (OAMO) [24]. Recent developments by Zhang and co-workers [25] takes care of this problem using a multi-center potential for the target.

On the experimental side, several measurements were performed in the past, from light atoms to rare gases and complex molecules, and comparisons were done with the available theoretical models. An overall agreement with the theory has been achieved for rare gases with complex energy level structures, like argon and neon [26, 27], whereas disagreements exist for molecular systems [28, 29]. Most of the targets previously used were gases and liquids using the supersonic gas jet. Modification of the existing reaction microscope to incorporate gas targets for solid substances would facilitate studies of a plethora of new targets, from simple three-electron systems like lithium to much more complex targets, that cannot be prepared via a supersonic gas jet. The motivation to perform measurements on lithium is mainly because alkali metals are hydrogen-like systems and, therefore, very fundamental targets where theoretical models should be able to obtain accurate results. Apart from that complete kinematics of all interactions like ionization-

excitation [30], inner shell ionization, etc can be studied. Another important motivation is the study of threshold double ionization of lithium and to look at the angular correlation of the outgoing electrons [31]. A second beam source for targets that do not require intensive heating is also implemented, and measurements are done using a complex molecular target, 1-Methyl,5-Nitroimidazole. This enables the validity check of the most advanced theoretical models like, multi-centre three distorted wave model (MCTDW) [28, 32] for much more complex molecules compared to those that have already been studied.

Reaction microscopes proved to be highly versatile, such that nowadays it is used in a variety of experiments including ion impact, positron impact, strong field ionization, multi-photon ionization, etc. studying a multitude of phenomena. Some of them include the relaxation mechanisms after the inner valence ionization in atomic or molecular clusters like Auger decay, interatomic/intermolecular Coulombic decay (ICD), etc. ICD is the process that takes place in atomic/molecular clusters, in which the internal energy after the inner valence ionization is transferred to the neighbouring atom/molecule and is ionized too. It was initially proposed by Cederbaum and co-workers [33]. Although the first experimental study was not done with reaction microscope [34], it provided a great leap in the study of ICD in different systems, from the studies on IC-decaying states to ICD lifetimes using pump-probe techniques [35, 36, 37]. ICD in argon dimers was studied using the (e,2e) reaction microscope by detecting all the outgoing five particles in coincidence [38]. A large number of experiments in a variety of loosely bound systems suggested that ICD is a general phenomenon occurring in these systems. Discussions started on the implications of ICD, particularly in biological matter, which may lead to DNA strand breaks when the low energy ICD electron gets attached to it [39].

Ionization induced by electrons comes into this picture, since the interaction of low energy electrons (LEE) with energies below 100 eV, produced by most of the ionizing radiations, is of great importance to the understanding of radiation damage to biological matter. Electron impact ionization measurements were performed on biologically relevant systems like tetrahydrofuran (THF), which is considered a surrogate of deoxyribose and has shown that the presence of water as an environment can catalyze the ring-breaking mechanism in such systems [40]. ICD studies were performed on THF$\cdots$water dimer and the results have shown that ICD is initiated from the O $2s^{-1}$ inner valence orbital of water. An additional channel to the dimer Coulomb explosion, involving hydrogen loss shows that an α-cleavage is initiated by the ICD process [41]. Furthermore, ICD studies on pure carbon-based systems like Benzene, bound by the aromatic $\pi\cdots\pi$ and CH$\cdots\pi$ interactions, were performed and found that ICD is initiated from the C $2s^{-1}$ inner valence vacancy [42]. The studies presented in this thesis are an extension of this research to the aromatic systems containing heteroatoms like S and N since they introduce additional inner valence orbitals from which ICD can take place. Studies on pure molecular dimers also facilitate the identification of their conformational geometries [42]. Recently, it has been theoretically predicted that the ICD and Auger process can be affected by the position of water attached to the biomolecule, whether it acts as an electron density donor (oxygen with excess negative charge is oriented towards the neighbouring molecule) or acceptor (a proton with excess positive charge is oriented towards the neighbouring molecule). A series of complexes are studied theoretically [43]. ICD studies on this research have started, with Pyridine$\cdots D_2O$, in which the D_2O molecule acts as an electron density acceptor attached to the nitrogen atom.

The research detailed in this thesis is presented in the following chapters. The subsequent chapter 2 goes through the theoretical aspects, starting by introducing the basics

of (e,2e) experiments and measured differential cross-sections. An overview of selected theoretical models describing the triple differential cross-sections is given. A description of the theory behind the cluster formation, the interactions among them, and inner valence relaxations mechanisms are described. In chapter 3 the experimental setup is described, particularly, the modifications on the existing reaction microscope, ie, three different target sources and the data acquisition system are explained. The next chapter (chapter 4) is dedicated to the data analysis tools, focusing on the reconstruction of momenta using *Go4* and the 'GENERiC' analysis code. Methods of data calibration and, determination of resolution and acceptance for the fragments are given. Chapter 5 presents the experimental results. This chapter focuses on two parts, (e,2e) and ICD studies. TDCS for single ionization of lithium and 1-Me,5-NIZ are discussed in the first part. The second part deals with ICD studies in thiophene dimers and pyridine-D_2O dimers. The final chapter summarizes the results and an outlook is given.

Chapter 2

Theoretical concepts

This chapter describes the theoretical concepts of reactions studied in this thesis. It starts by introducing the classification of different collisions and explains how charged particle-impact ionization is different from photon-impact ionization. An overview of different models to describe the dynamics of the outgoing electrons after the collision is given next. A particular focus is given on the multi-center three distorted wave (MCTDW) model which is used to compare the experimental triple differential cross-sections (TDCS) for the single ionization of outer valence orbitals of 1-Methyl,5-Nitroimidazole (1-Me,5-NIZ). In the second part, a brief introduction to cluster formation and different interactions in clusters is given, which is relevant to the second objective of this work. Different relaxation processes after inner valence ionization are introduced next with a detailed description of Interatomic or Intermolecular Coulombic decay (ICD), which is the topic of interest in the second part.

2.1 Fundamentals of electron impact ionization

Collisions can be classified broadly into two, elastic and inelastic collisions. The collision of interest for the work presented in this thesis contains an electron as a projectile having a particular energy E_0 colliding with a target species. For ionization the reaction products are one or more bound electrons ejected into the continuum, the scattered projectile and the ionized target. Here the collision is termed inelastic since a fraction of the kinetic energy of the colliding projectile is converted into internal energy of the target species. Therefore, the kinetic energy is not conserved for these reactions, whereas the momentum is conserved. A few examples of inelastic collisions are as follows.

$$\left.\begin{aligned} e^- + A &\rightarrow A^+ + 2e^- \\ e^- + A &\rightarrow A^{*+} + 2e^- \\ e^- + A &\rightarrow A^{2+} + 3e^- \end{aligned}\right\} \text{Inelastic collisions} \tag{2.1}$$

For elastic collisions the projectile electron scatters off the target, thereby conserving both kinetic energy and momentum.

$$e^- + A \rightarrow A + e^- \qquad \text{Elastic collision} \tag{2.2}$$

Such reactions can be abbreviated as (e,ne), where n is the number of outgoing electrons. The main difference between charged particle-impact ionization and photoionization is in the angular distribution of the ejected electrons. It shows the probability that the bound electron to get ejected at a particular solid angle. The symmetric double lobe structure for

the photoionization angular distribution called the dipole emission pattern changes to an asymmetric emission pattern as shown in the figure 2.1 for charged particle-impact ionization. The dipole emission pattern for photoionization is due to the transfer of a single quantum of angular momentum during the ionization process. An analogous scenario in charged particle-impact ionization is a collision with high energetic projectile accompanied by negligibly small momentum transfer. Here the projectile interacts in a very small time duration with the bound electron and knocks it off. Such a scenario of collision with the fast electron can be described as an exchange of a single virtual photon. However, a wide range of angular momentum transfer $\vec{q}$ is possible at a single energy transfer. Thus a transfer of several quanta of angular momenta can induce non-dipole transitions which then lead to a non-dipolar asymmetric emission pattern. This difference vanishes as $\vec{q}$ approaches $h\nu/c$ and it is called optical limit where the angular distributions and cross-sections are the same for charged particle-impact ionization and photoionization. The large lobe in the direction of momentum transfer $\vec{q}$ is called the binary lobe and the small lobe in the direction $-\vec{q}$ is called the recoil lobe. A direct electron-electron scattering gives rise to the binary lobe and the electron-electron collision followed by the scattering of the target electron from the ion core produces the recoil lobe.

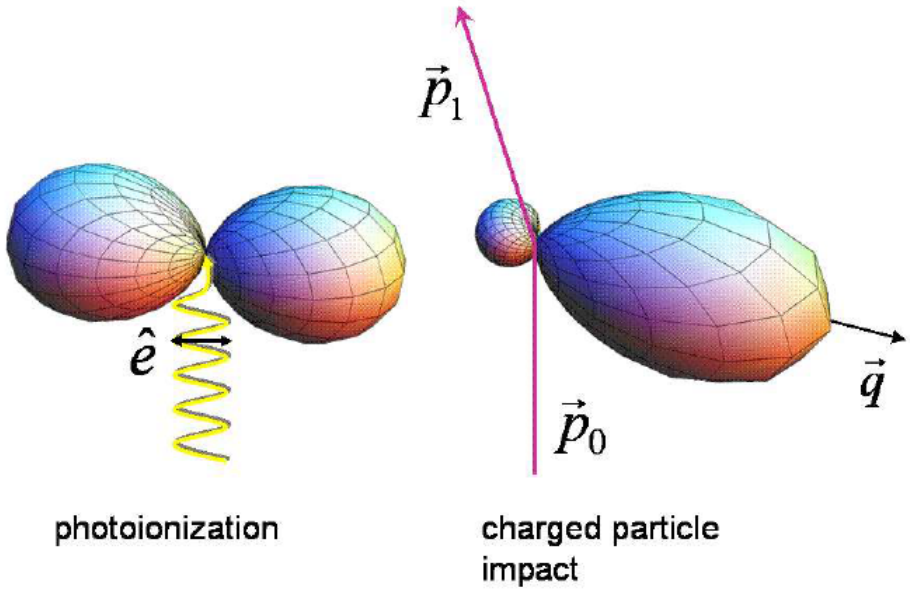

Figure 2.1: Non-dipole asymmetric emission pattern characteristic to the particle impact ionization processes. Image adapted from [44].

Depending on the projectile energy, the collisions can be divided into three main regimes. The high energy regime, where the projectile energy is typically greater than 20 times the ionization potential. Here the interaction time between the projectile and the target is so small that the initial and final state projectile wavefunctions can be considered non-distorted plane waves. Such kind of interactions can be described as an exchange of a single virtual photon. In this regime, the system is described theoretically using the First Born Approximation (FBA). Ejected electron emission is excepted predominantly in the scattering plane where the incoming projectile and the momentum transfer lie. Out of the scattering plane usually shows the momentum distribution of the electron within the bound state of the target ([45], [46]). The second regime is the intermediate energy regime which is typically in the range 5 IP $\leq E_0 \leq$ 20 IP. Here the projectile energy is

slower and higher-order interactions between the projectile and the target come into play. As a result, the binary and recoil lobe shift away from the symmetry axis (momentum transfer direction) and there will be additional emissions in the plane perpendicular to the scattering plane. When it comes to an energy range close to the threshold, ie. 1.5 IP $\leq E_\circ \leq$ 5 IP, exchange processes play an important role and the outgoing scattered projectile and the ejected electron becomes indistinguishable. In this regime, the system is strongly correlated and the initial and the final state are described by a strongly interacting asymptotic wavefunction.

The most important observable from the (e,ne) measurements are the cross-sections, which is the probability of electron emission in this case. For simplicity, let us consider an (e,2e) process where we have three freely-moving particles, one incoming projectile and two outgoing electrons with energy and momentum E_i, $\vec{p}_i$ ($i = 0, 1, 2$), provided that the motion of the nucleus is neglected. Here we can define four different cross-sections: total cross-section ($\sigma(E_0)$) and single ($\frac{d\sigma}{dE}$), double ($\frac{d^2\sigma}{d\Omega dE}$) and triple ($\frac{d^3\sigma}{d\Omega_1 d\Omega_2 dE_2}$) differential cross-sections.

The total cross-section is the measure of the ionization probability as a function of impact energy and it usually has a value around 10^{-16} cm^2 at the maximum. Typically, such a maximum is found at impact energy around the range of 3 to 5 times the ionization potential. Below that energy, one can define a threshold region where the cross-section linearly goes down. Variation of cross-section as a function of excess energy (E_0- IP) is described by Wannier in the famous Wannier threshold law as $\sigma \propto (E_0 - \text{IP})^{1.127}$ ([47]). Such a variation, which is contradictory to the case of photoionization where the cross-section increases steeply after the threshold ([48]) is because the system at the threshold is a three-body problem with a strongly correlated pair of electrons attached to the ion. Beyond the maximum, the cross-section decreases as a function of impact energy. At high energies, it becomes similar to the photoionization cross-section.

2.1.1 Differential cross-sections

Single differential cross-section

The single differential cross-section, $d\sigma/dE$, shows the energy distribution of the outgoing electrons at a particular projectile energy (E_0). It describes how the excess energy is distributed between the two outgoing electrons. An example of such a curve is shown in figure 2.2. The curve changes for different regimes of impact energy. In high-energy regime, the scattered projectile and the ejected electron can be distinguished separately from each other as 'fast' and 'slow' electrons. In the energy distribution, it appears as two groups at the high and low energy end respectively, with a minimum at ($\frac{E_0-IP}{2}$). For lower impact energies, the two distributions start to merge, owing to the increasing exchange interactions. At the threshold, the distribution becomes uniform, making the two electrons indistinguishable from each other.

Double differential cross-section

Double differential cross-sections (DDCS), $d^2\sigma/d\Omega dE$, show the angular and energy distributions of either the scattered projectile or the ejected electron. An example of such distributions is shown in figure 2.3. It shows the DDCS of both the scattered projectile and the ejected electron for an impact energy of 200 eV on helium. Figure 2.3a shows the angular distribution of scattered projectiles with energy, $E_1 = 165.4$ eV, therefore differential in both energy and angle. For high and intermediate impact energies the scat-

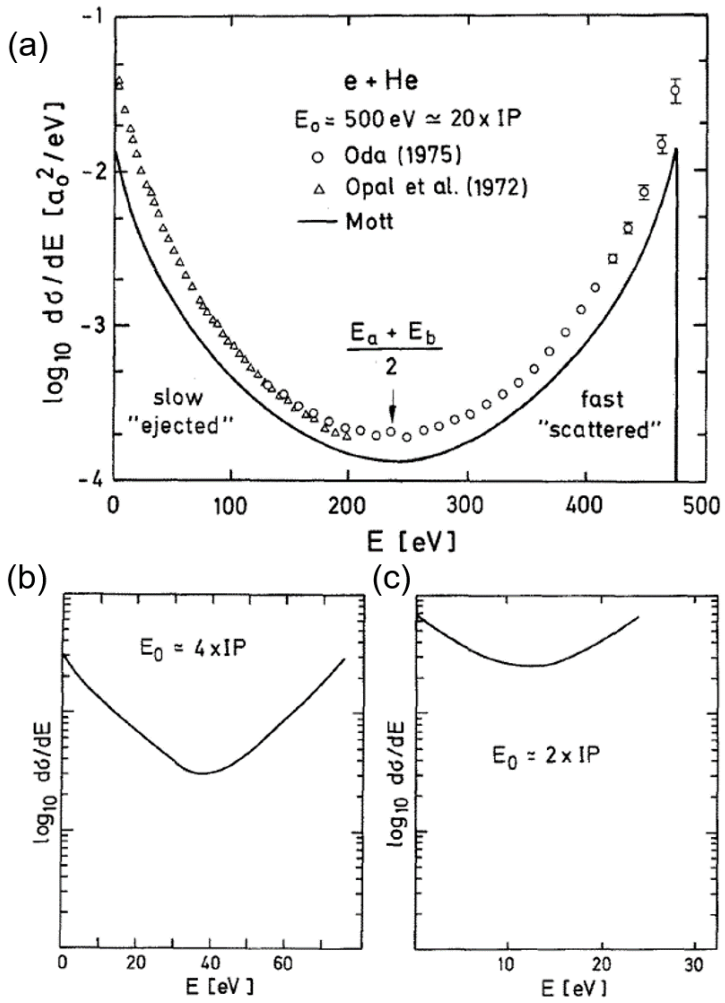

Figure 2.2: Single differential cross-section for different impact energies, E_0. (a) $E_0 = 20\times$ IP on helium. Comparison of experimental data ([49],[50]) with calculation ([49]). (b) $E_0 = 4\times$ IP on helium, derived from eq (5) of [51]. (c) $E_0 = 2\times$ IP on molecular hydrogen. Derived from the double differential cross-sections from [52]. Image is slightly adapted from [53].

tered projectile is preferably emitted in the forward direction. Therefore, the distribution peaks at 0°. Since collisions at high energies are similar to that of the photoionization, the fast-oscillating projectile's electric field induces ionization and therefore, only less momentum is transferred causing the projectile to lose only a little energy and deflected to a small angle. Slow electrons on the other hand are uniformly distributed in all directions with a small maximum typically around 60° wrt the forward direction, for high and intermediate impact energies indicating the binary peak.

Triple differential cross-section

Triple differential cross-section (TDCS), $d^3\sigma/d\Omega_1 dE_1 dE_2$ is a function of all collision parameters like the energies and emission angles of the outgoing electrons and therefore, provides a stringent test of theories. It is usually represented as the angular distributions of the ejected electron at a specific momentum transfer and for a specific energy of the ejected electrons. The first such experiment was reported by Ehrhardt et al [7]. Figure 2.4 shows such distributions at low- and high-impact energies and for different momentum transfers. In the photoionization limit ($|\vec{q}|_{min} \sim 0.2$ a.u.) and in the

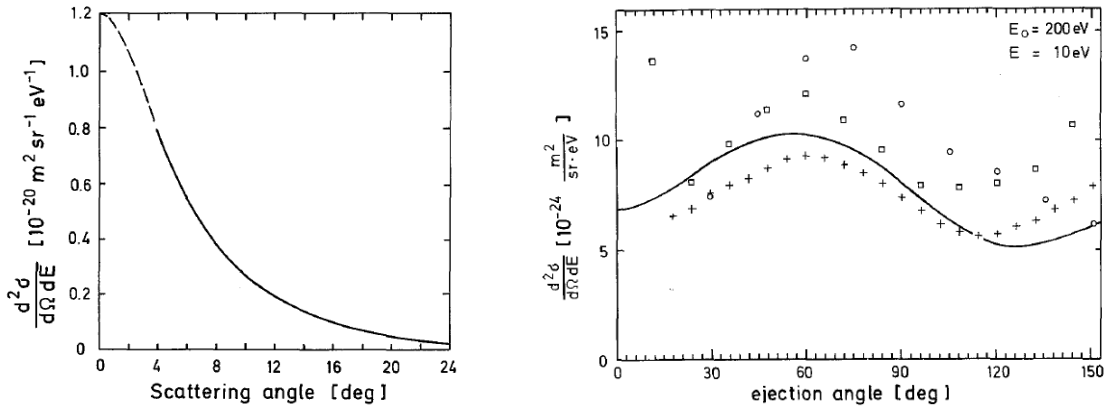

(a) (b)

Figure 2.3: (a) Double differential cross-sections of helium for scattered projectile with $E_1 = 165.4$ eV and impact energy $E_0 = 200$ eV. — Experimental data([51]) - - Extrapolated curve ([51]). (b) Double differential cross-sections of helium for ejected electrons with $E_2 = 10$ eV and impact energy $E_0 = 200$ eV. — Calculation([54]), Experimental data + [51], □ [55], ○ [50]. Images are adapted from [53].

binary limit($|\vec{q}|_{max} >> 1$ a.u.), emission pattern aligns with the symmetrical axis, which is the direction of $\vec{q}$. At maximum $|\vec{q}|$, which appears for the symmetric geometry case ($E_1 = E_2$, $\theta_1 = \theta_2$), recoil peak disappears, meaning the complete momentum transfer goes to the electron in the binary collision. To understand such a variation one has to include contributions from the higher partial waves in the transition, therefore, effectively taking non-dipole transitions into account. Most of the collisions happen between $|\vec{q}|_{min}$ and $|\vec{q}|_{max}$ where one can see the shift of binary and recoil lobe from the momentum transfer direction. Such a tilt starts to appear in the intermediate energy regime and is mainly attributed to the post-collision interactions (PCI), where both final state electrons interact by Coulomb forces allowing the exchange of energy and angular momenta.

For low-impact energies, the interference of the three scattering amplitudes f (direct scattering), g (momentum exchange) and h (particle exchange) and multiple partial waves play a role and therefore, the shape of TDCS completely changes. The influence of the PCI is strong enough to invert the intensity relations between the binary and recoil peak and the particle and momentum exchange amplitude becomes even comparable to that of the direct scattering amplitude.

2.2 Theoretical description of cross-sections

Few-body dynamics, which is generally described using the time-dependent Schrödinger equation is one of the most challenging problems in physics. The difficulties arise because when the interaction between more than two interacting particles is studied, the Schrödinger equation becomes complicated and impossible to solve analytically. This is the case, especially, when ionizing collisions are studied because one has to deal with the long-range Coulomb forces. Such an issue is generally mitigated by introducing approximations or by solving numerically. The existing theories which describe electron impact ionization can be broadly classified into perturbative and non-perturbative approaches. Perturbative models typically describe the ionization as a small time scale perturbation to the target state and by introducing approximations to the Schrödinger equation. Most such models are based on the Born approximations which treat the scattering process

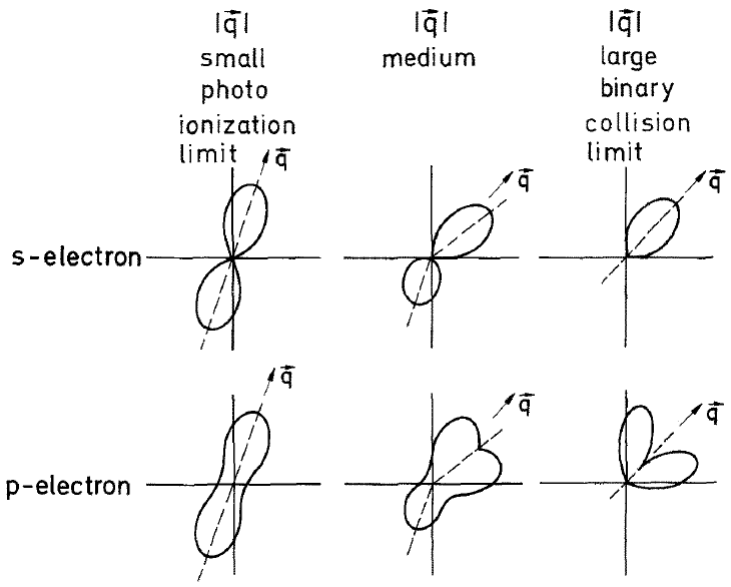

(a)

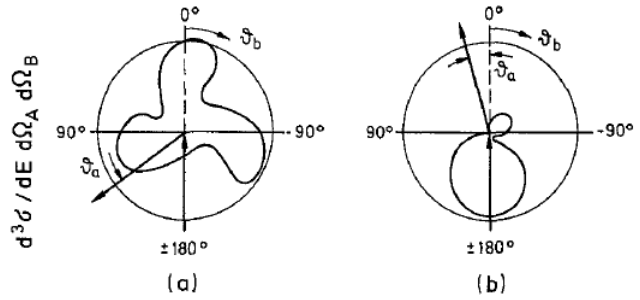

(b)

Figure 2.4: (a) Triple differential cross-section for the ejection of s and p electrons with varying momentum transfer at high impact energies. (b) Triple differential cross-section at low energy regime for large and small momentum transfers (ϑ_a, the scattering angle is an indication of momentum transfer). Images are adapted from [53].

of the particles as discrete orders of interaction. Whereas, the non-perturbative methods like exterior complex scaling (ECS) [18], convergent close-coupling (CCC) [19], time-dependent close-coupling (TDCC) [20], and B-spline R-matrix (BSR) theories [56] treat the problems exactly and solve the complete Schrödinger equation numerically. Although, simple atoms such as hydrogen [18, 19, 20] and helium [56, 17, 57] are well described by these models, more complex atoms like neon, argon etc and molecules which have multi-centre nature are still challenging for them. These non-perturbative models will not be described in detail in this work as they are out-of-scope of this thesis. In this section, beginning with the general formalism of the time-dependent Schrödinger equation for the scattering process, an overview of different models (perturbative) that describe the (e,2e) processes relevant for this work are presented.

In perturbative methods, the incoming projectile is treated as a free particle plane wave at t$\rightarrow$-∞ before it interacts with the target state and induces a transition to the final state. The outgoing products are also considered to be free particle plane waves at the asymptote (t$\rightarrow\infty$). The detailed theoretical formalism of the problem can be found elsewhere [58, 59]. A summary of the perturbative formalism is given in the next section.

2.2.1 Lippmann-Schwinger equation

Quantum mechanically the system is described by the total Hamiltonian given by,

$$H = H_0 + V \tag{2.3}$$

where H_0 represent the Hamiltonian corresponding to the non-interacting system and V, the interaction potential. H_0 can be further separated into two, corresponding to the Hamiltonian of the target and the projectile $H_0 = H^0_{traget} + H^0_{projectile}$. The initial state and final state of the system can be treated as plane waves at time t$\rightarrow\pm\infty$ with asymptotic eigenstates defined by,

$$H_0|\Phi_{i,f}\rangle = E_{i,f}|\Phi_{i,f}\rangle \tag{2.4}$$

where $E_{i,f}$ are the energy eigenvalues of the asymptotic states (indices i and f denote the initial and final states). Since the energy is conserved for the reactions under consideration, $E_i = E_f$. The dynamics of the complete quantum mechanical system is described by the time-dependent Schrödinger equation given by,

$$i\hbar\frac{\partial}{\partial t}|\Psi(t)\rangle = H|\Psi(t)\rangle \tag{2.5}$$

$|\Psi(t)\rangle$ represents the scattering state of the system developed from the asymptotic initial and final states $\Phi_{i,f}$ using the time evolution operator $U(t,t_0) = \exp(iH_0t)\exp(-H(t-t_0))\exp(-iH_0t_0)$ in the interaction picture. They can be described as,

$$\begin{aligned} |\Psi(t)_+\rangle &= \lim_{t\to-\infty} U(t_0,t)|\Phi_i\rangle \\ |\Psi(t)_-\rangle &= \lim_{t\to\infty} U(t_0,t)|\Phi_f\rangle \end{aligned} \tag{2.6}$$

Ψ_+ is the 'outgoing wave' evolved from the state Φ_i from the remote past and similarly, Ψ_- is the 'incoming wave' developed from the state Φ_f from the far future.

In order to find a solution for $|\Psi_\pm\rangle$, one has to solve the time-independent Schrödinger equation

$$\begin{aligned} (H-E)|\Psi_\pm\rangle &= 0 \\ (H_0-E)|\Psi_\pm\rangle &= V|\Psi_\pm\rangle \end{aligned} \tag{2.7}$$

The solution for $\Psi_\pm$ can be formulated using the Green's operator, G as follows,

$$|\Psi_\pm\rangle = |\Phi\rangle + G_\pm V|\Psi_\pm\rangle \tag{2.8}$$

where G is defined as,

$$G_\pm = \lim_{\epsilon\to0}\frac{1}{E-H_0\pm i\epsilon} \tag{2.9}$$

This equation is called the Lippmann-Schwinger equation. The transition from the state $|\Psi_+\rangle$ to $|\Psi_-\rangle$ is defined using the scattering matrix, S, as follows,

$$\langle\Phi_f|S|\Phi_i\rangle = \langle\Psi_-|\Psi_+\rangle \tag{2.10}$$

A detailed derivation of the S matrix can be found in [58]. The scattering matrix is directly proportional to the transition matrix from $i \rightarrow f$ or T-matrix defined in two equivalent forms as 'prior form' and 'post form'.

$$T^{fi} = \langle\Psi_+|V|\Phi^i\rangle \qquad \text{Prior form} \tag{2.11}$$

$$T^{fi} = \langle \Phi^f | V | \Psi_- \rangle \qquad \text{Post form} \tag{2.12}$$

One can relate the fully differential cross-section (FDCS) to the transition matrix as follows,

$$\text{FDCS} = i\frac{(2\pi)^4}{v_p}\delta(E_i - E_f)\delta(\vec{P}_i - \vec{P}_f)\left|T^{fi}\right|^2 \tag{2.13}$$

where v_p is the velocity of the incoming projectile and $\vec{P}_{i,f}$ are the centre of mass momenta in the initial and final state. For the full derivation of equation (2.13) refer to [58].

2.2.2 Born approximations

Lippmann-Schwinger (2.8) can be expanded iteratively by substituting into itself to obtain the full expression of the scattering states.

$$|\Psi_\pm\rangle = |\Phi_{i,f}\rangle + G_\pm V|\Phi_{i,f}\rangle + G_\pm V G_\pm V|\Phi_{i,f}\rangle ... \tag{2.14}$$

Similarly, the transition matrix can now be expanded by substituting for $\Psi_\pm$ in the prior (2.11) or post (2.12) form which gives an equivalent result.

$$T^{fi} = \langle \Phi_f | V + VGV + VGVGV + ... | \Phi_i \rangle \tag{2.15}$$

This is called the Born series, which is the expansion of the scattering states and T-matrix in the powers of the 'perturbation', V. For ionization reaction, the perturbation V is the Coulomb interaction between the projectile and the target constituents which can be represented as,

$$V = \frac{Z_p Z_N}{r_p} + \sum_{i=1}^{n} \frac{Z_p}{r_p - r_i} \tag{2.16}$$

The first term represents the interaction of the projectile with the ionic core and the second term represents the interaction between the ejected electrons and the projectile. Calculating the cross-sections using the Born approximation involves substituting the equation (2.16) to the Born series (2.15). For the fast projectiles, the first term of the Born series dominates in the assumption that the interaction is small and weak, whereas for the low-energy projectile, all the terms in the Born series contribute to the cross-section and therefore, it is practically impossible to solve using such a perturbative method. We can visualize the transition amplitudes in equation (2.15) as multiple scattering series in which the projectile interacts repeatedly with the target and propagates freely between those two interactions as shown in the figure 2.5.

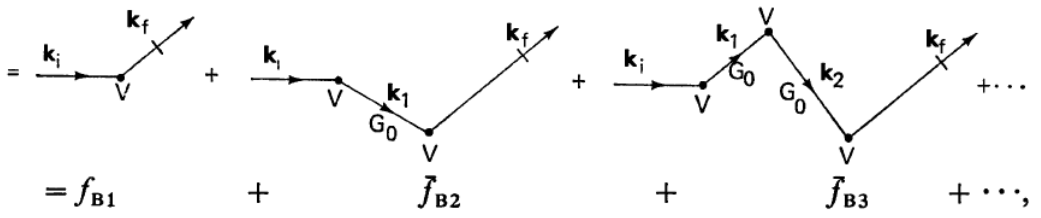

Figure 2.5: Each diagram in the figure represents each transition amplitude in the equation (2.15), where $k_{i,f}$ shows the incoming and outgoing projectile and $k_{1,2..}$ shows the intermediate momenta. The Greens operator, G_0 acts as a propagator during the interaction. Image is adapted from [58].

First-Born approximation

The first term in the Born series (2.15) gives the first Born amplitude. Here the assumption is that the initial state comprises a plane wave with momentum $\vec{k_0}$ describing the projectile and the eigenstate of the target ($|\Phi_i\rangle = |\vec{k_0}\rangle|\phi_i\rangle$) which interacts with the target with a perturbation, V, to produce the final state which consists of another plane wave with momentum $\vec{k_1}$ and the eigenstate of the target consisting the continuum electrons and the residual ion ($|\Phi_f\rangle = |\vec{k_1}\rangle|\phi_f\rangle$). It is assumed that the projectile does not interact with the rest of the system and the ejected electron is described as a Coulomb wave moving in the field of the residual ion. Therefore, in first-born approximation, the three-body system is now reduced to a two-body problem.

The first term from the equation (2.16) vanishes as there is no interaction between the target and the projectile. The second term gives rise to a transition amplitude,

$$T_{i,f}^{B1} \propto \langle\phi_f| \exp(i\vec{q}.\vec{r})|\phi_i\rangle \tag{2.17}$$

Therefore, the process can now be seen as an exchange of a virtual photon with momentum $\vec{q} = \vec{k_0} - \vec{k_1}$. From equation (2.13) and using the full form of equation (2.17), one can get the expression for the FDCS.

$$\text{FDCS} = \left(\frac{Z_p}{v_p}\right)^2 \frac{1}{q^4} \langle\phi_f| \exp(i\vec{q}.\vec{r})|\phi_i\rangle \tag{2.18}$$

Hence, one can see that the cross-sections depend strongly on the strength of the electric field of the projectile from Z_p and the momentum transfer amplitude q. For small momentum transfer towards the optical limit, the term $\exp(i\vec{q}.\vec{r}) = 1 + i\vec{q}.\vec{r} + ...$, can be approximated by neglecting the higher powers of $\vec{q}$, thereby resembling the dipole approximation or the optical limit.

Second-Born approximation

The second-Born approximation includes the second term of the Born series in the calculation of the cross-section along with the first Born amplitude.

$$\begin{aligned} T_{i,f}^{B2} &= \langle\Phi_f|VGV|\Phi_f\rangle \\ &= \lim_{\epsilon\to 0} \sum_n \int d^3k_{p'} \frac{\langle\phi_f|\langle\vec{k_1}|V|\vec{k_{p'}}\rangle|\phi'_n\rangle\langle\phi'_n|\langle\vec{k_{p'}}|V|\vec{k_0}\rangle|\phi_f\rangle}{E - E_n - E_{p'} + i\epsilon} \end{aligned} \tag{2.19}$$

The expression for the second Born amplitude (2.19) can be understood as the projectile undergoing two separate interactions or virtual photon exchanges with the target with the interaction potential V. First step is that the target gets excited to an intermediate state $|\phi'_n\rangle$ with energy eigenvalue E_n (bound or continuum) in collision with the incoming projectile transferring a momentum $(\vec{k_0} - \vec{k_{p'}})$. In a second step, the target in the intermediate state gets ionized to the continuum upon a second interaction with the projectile with intermediate momentum $\vec{k_{p'}}$, transferring another fraction of momenta $(\vec{k_{p'}} - \vec{k_1})$. Since an infinite number of intermediate states for the target and momenta of the projectile is possible the transition amplitude should integrate over all momentum $\vec{k'_p}$ and sum over all intermediate states ϕ'_n. The second Born amplitude uses several approximations, one important among them is the 'closure approximation' where the energy E_n of the intermediate states is replaced by an averaged energy $\overline{E}$ [60]. Due to the double scattering nature in the SBA, the symmetry with respect to the total momentum transfer direction $\vec{q} = \vec{k_0} - \vec{k_1}$ is broken. Since the second Born amplitude calculation is already challenging with multiple approximations, calculating higher-order Born amplitudes is practically impossible.

Distorted-wave Born approximation

In the distorted-wave Born approximation the outgoing and the incoming electrons eigenstates are transformed to 'distorted waves' χ_0 and $\chi_{1,2}$ using a distorting potential (U), which describes the effect of the target-projectile interaction on the initial and final state. The total Hamiltonian of the scattering system now looks like this,

$$\begin{aligned} H^{DW} &= H_0^{DW} + (V - U) \\ &= K + H_T + U + (V - U) \end{aligned} \tag{2.20}$$

where K is the kinetic energy operator for the projectile/ejected electron and the last term in the bracket represents the residual interaction. Here the initial and final distorted-wave channel states are represented by $\chi_\pm$, which are the products of the distorted waves for the incoming projectile/(scattered projectile + ejected electron) and the unperturbed target states.

$$\begin{aligned} |\chi_+\rangle &= |\chi_0\rangle|\phi_i\rangle \\ |\chi_-\rangle &= |\chi_1\rangle|\chi_2\rangle|\phi_f\rangle \end{aligned} \tag{2.21}$$

Distorted waves must be chosen such that it satisfies the eigenvalue equation given by, $(\epsilon_i - K - U)|\chi_i\rangle = 0$. Now the distorted-wave channel state and scattering state should satisfy the eigenvalue equations.

$$\begin{aligned} (E - H_0^{DW})|\chi_\pm\rangle &= 0 \\ (E - H^{DW})|\Psi_\pm\rangle &= 0 \end{aligned} \tag{2.22}$$

Using the Lippmann Schwinger equation (2.8) equation (2.22) can be solved as,

$$\begin{aligned} |\chi_\pm\rangle &= |\Phi_{i,f}\rangle + \frac{1}{E - K - H_T} U|\chi_\pm\rangle \\ |\Psi_\pm\rangle &= |\chi_\pm\rangle + \frac{1}{E - H_0^{DW}}(V - U)|\Psi_\pm\rangle \end{aligned} \tag{2.23}$$

It can be shown that the 'post form' of the transition matrix in the distorted wave approximation now takes the form [59],

$$\langle\Phi_f|\tilde{T}|\Phi_i\rangle = \langle\Phi_f|U|\chi_+\rangle + \langle\chi_-|(V - U)|\Psi_+\rangle \tag{2.24}$$

The first term represents the elastic scattering of the plane wave projectile by the potential U. The second term is the distorted wave T-matrix element.

The first calculation of (e,2e) cross-sections using distorted-wave Born approximation (DWBA) were done by Madison et al. on helium at an impact energy of 256.6 eV [21]. Although calculations were in good agreement with the theory at higher energy, at low energies DWBA failed since the distorted waves do not include the post-collision interactions (PCI) which effectively tilts the binary and recoil peaks away from the momentum transfer direction.

Another theory using plane-wave born approximation was introduced, which included the electron-electron interaction in the final state in the so-called 3C wave function [61]. Similar modification is introduced later to DWBA by multiplying the electron-electron Coulomb interaction term in the final state distorted waves in the so-called 3DW method [62]. Numerous other models explaining the (e,2e) cross-sections for single atoms to complex molecules were introduced, whose detailed description is out of the scope of this thesis. Review articles by Madison et al. [63] and [64] provide a detailed overview.

3D cross-sections

An example of the 3D cross-section for electron emissions in first-order Born approximation and the changes in it due to the introduction of higher-order effects is shown in figure 2.6. Figure 2.6a shows a typical 3D cross-section for single ionization of helium in the high-impact energy regime which can be described by first-order Born approximation. The emission pattern shows a axially symmetric distribution with respect to the momentum transfer direction $\vec{q}$. It has a double lobe structure with unequal intensities. In the plane perpendicular to the projectile scattering plane and along the projectile direction ($\vec{k}_0$), called the perpendicular plane (for details about collision planes refer section 4.4), the emission is minimal. A deviation from this pattern can be seen for collisions in intermediate and threshold impact energy regimes as more and more higher-order effects come into play. An example is given in figure 2.6b which shows the 3D cross-section for single ionization of helium with 70.6 eV electrons calculated using convergent close coupling (CCC) [19]. Here the symmetry with respect to the momentum transfer direction $\vec{q}$ is completely lost and the lobes start to tilt way from $\vec{q}$. This is due to post-collision interactions (PCI) between the outgoing electrons and the residual ion. A flattening of the lobes leading to emission out of the plane containing $\vec{q}$ and $\vec{k}_0$ (scattering plane) is also observed. Another important feature as a manifestation of higher-order interaction between the projectile and the residual ion is the considerable emission in the perpendicular plane which appears as a merging of binary and recoil lobes. A descriptive reason for this feature is that the momentum transfer $\vec{q}$, which is determined as $\vec{k}_0 - \vec{k}_1$ will be different from the emission direction of the ejected electron if the scattered projectile undergoes further collisions with the residual ion which essentially deviates its direction from the collision with the bound electron. Therefore, it appears in the 3D distribution as if the electron is emitted away from the momentum transfer direction filling the gap between the binary and recoil lobes.

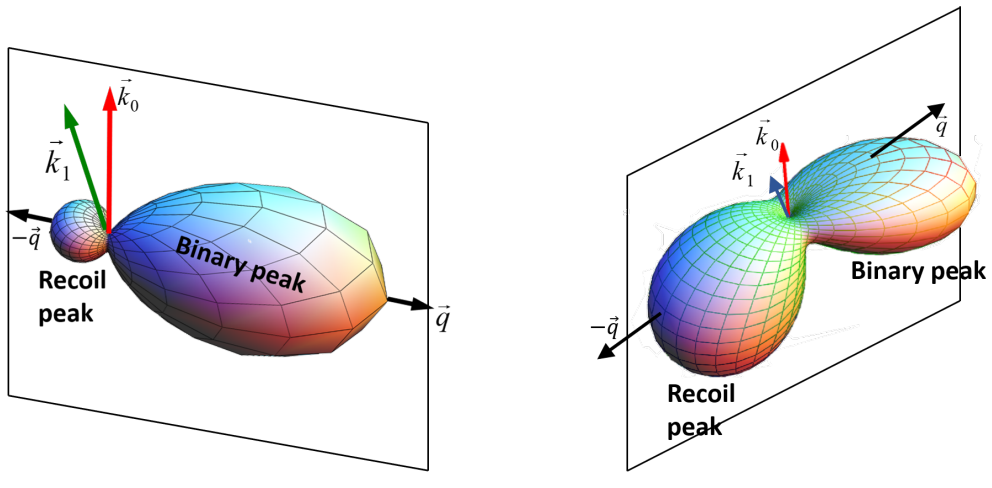

(a) (b)

Figure 2.6: (a) A typical first Born like 3D cross-section. Image is adapted from [44]. (b) The theoretical 3D cross-section for single ionization of helium with 70.6 eV electrons, for ejected electron energy $E_2 = 5$ eV and scattering angle $\theta_1 = -20^\circ$ calculated using convergent close-coupling (CCC) model. Image is adapted from [17].

2.2.3 Multi-center three distorted wave (MCTDW)

Electron impact single ionization of molecules was studied for 2-3 decades. Many of the studies were concentrated on 'electron momentum spectroscopy'(EMS) using high impact energies, at which the FDCS is related to the square of momentum space wavefunctions for the active orbital averaged over all orientations (Dyson orbital). For low and intermediate-impact energy collisions with molecular targets, the challenge was to use multi-centre wavefunctions, unlike in atoms which have one scattering centre with spherically symmetric wavefunctions. Another challenge was that the traditional (e,2e) measurements provide FDCS averaged over all molecular orientations. Fundamental FDCS depends on the orientation of the molecule since the charge distribution and the molecular orbitals depend on the orientation. Therefore calculating a proper average over all orientations is computationally expensive. One of the important models which took care of this problem is the molecular 3-body distorted wave approach (M3DW) [24, 65]. Here the static potentials of the molecular electrons were obtained by averaging over all possible orientations and that of the nucleus is also averaged by placing the charge on a sphere of radius R which is the distance of the nucleus from the centre of mass. The sum of both nuclear and molecular electronic parts is used to solve the Schrödinger equation. Here the orbitals and charge distributions are not spherical harmonics like in atoms but rather expressed in terms of a numerical 3D grid. The computational challenge of averaging over orientations is overcome by using the orientation averaged molecular orbital(OAMO) [24] in which a single average molecular orbital is used to approximate over all orientations.

In this thesis, we use a new model called multi-centre three distorted wave (MCTDW) [28, 26] for comparing the fully differential cross-sections for the single ionization of valence orbitals from 1-Me,5-NIZ molecule, which has much more complex structure compared to the previously studied molecules ([28, 26]). Here the continuum wavefunctions of the incoming projectile and the two outgoing electrons are considered distorted waves under a true anisotropic multi-centre potential of the neutral molecule and molecular ion respectively. This model is an extension of a previously presented multi-centre distorted-wave method (MCDW), where the multi-centre nature of the molecule is considered by describing only the slow ejected electron with the multi-centre distorted wave [25]. It uses the frozen core Hartree-Fock approximation [59] with which the n-electron problem is reduced to a one-active electron problem. The multi-centre nature is introduced using the anisotropic multi-centre potentials for each distorted wave (ejected, scattered and incoming electrons) given by,

$$V^{m}_{e,s,i} = V^{st}_{e,s,i} + V^{cp}_{e,s,i} + V^{model-exc}_{e,s,i} \tag{2.25}$$

where V^{st}, V^{cp} and $V^{model-exc}$ are the static, polarization and model exchange potentials respectively [66]. $V^{model-exc}$ also depends on the kinetic energy of the ejected electron. The Schrödinger equation is solved by expanding the three-dimensional potentials and wavefunctions by employing the single-centre expansion (SCE) techniques [66]. FDCSs obtained for each orientation are averaged to get the TDCSs which can be compared with that of the experimental TDCS.

In order to include the electron-electron interaction in the final state (PCI) Botero et al [67] proposed to multiply the 3DCS by the so-called Gamow factor, N_{ee},

$$\frac{d^3\sigma}{d\Omega_1 d\Omega_2 dE_2} = N_{ee} \frac{d^3\sigma}{d\Omega_1 d\Omega_2 dE_2}\Big|_{\text{DWBA}} \tag{2.26}$$

Such a modification is used to include the PCI effects since the DWBA model. In models like M3DW [24] post-collision interactions are included exactly, by considering the final state with Coulomb distortion factors between the two outgoing electrons, whereas for models like MCDW, MCTDW etc where PCI is not included, Gamow's factor has to be applied. It is expressed as,

$$N_{ee} = \frac{\pi/k_{12}}{\exp(\pi/k_{12}) - 1} \tag{2.27}$$

where $k_{12} = \mu v_{12}$ is a simplification to the original Gamow factor which is the product of the reduced mass μ and the relative velocity between two outgoing electrons v_{12} introduced by Ward and Macek [68].

2.3 Cluster formation

Clusters are aggregates of individual atoms or molecules which are intermediate in size compared to atoms/molecules and bulk matter. They can be classified broadly as small, medium and large clusters based on their properties. Small clusters generally have no more than a few hundred particles. Although their properties vary with their size and shape, a simple and smooth dependence of properties on the number of particles does not exist. For medium-sized clusters properties starts to vary smoothly as the size increases, but still reflect the small size of the cluster. If the properties approach that of the bulk material one can call it a large cluster. They have typically dimensions in the order of a few nanometers. A small/medium-sized cluster differs from bulk matter mainly in the energy level structure, wherein the bulk matter the quantum states occur in bands of a large number of states very close to each other, whereas for a molecule or a small cluster the spacing between the individual levels is larger.

Clusters are held together by different forces, from weak van der Waals forces to strong ionic bonds. Clusters such as $(NaCl)_n$ are kept together by strong forces of attraction between the two opposite charges. Some others have covalent bonds playing between them, such as clusters of silicon or the famous fullerene or C_{60}. Metal clusters like clusters of sodium or Iron are held together by metallic bonds similar to their bulk counterparts. However, very small metal clusters have covalent bonds between the constituents. Clusters of rare gases which have closed shell structures belong to weakly-bound systems bound by van der Waals interaction, therefore, they are also called van der Waals molecules/clusters. Another important cluster types are hydrogen-bonded clusters held by the hydrogen bond. Clusters of water molecules are an example. They are much more tightly bonded than van der Waals clusters but more weakly bound compared to all other categories discussed.

Earlier studies of clusters were more focused on the geometrical structures and their properties in the electronic ground state [69]. Clusters can be generated in several ways. The most popular of them is cluster formation in a supersonic gas jet (see section 3.3.1), where a gas or a vapor is expanded from a high-pressure region to a low-pressure region through a nozzle of typical diameter in the range 10 μm to 1 mm. The first report on such a cluster source was given by Becker et al in 1956 [70]. The mean gas velocity in the expanding direction increases dramatically at the expense of the thermal motion in the transversal direction of expansion. Typical temperatures of gas in an expanding supersonic jet are within the Kelvin range making it ideal for aggregate formation. Varieties of clusters can be prepared using supersonic gas jets. The source could be made continuous or pulsed. Pure gas or a mixture of gas can be used. Aggregates can also be prepared

using laser ablation or by using electrical discharges.

Cluster formation in the supersonic gas jet occurs if the local temperature in the beam becomes less than the binding energy of the dimer. Condensation starts with the formation of the dimer and later larger aggregates are formed. Considering energy and momentum conservation laws, it is a three-body collision process in which three atoms collide to form one molecule and another free atom which carries away the binding energy of the dimer. Once a dimer is formed it acts as a condensation nucleus for bigger clusters. In the presence of inert carrier gas, such as helium, the nucleation process is much more efficient as it takes away the heat of condensation. The use of an inert carrier gas has been long known to promote cluster growth [70, 71]. If a heavier gas, like argon, is used the flow is slow and the clusters have more time to grow. For efficient clustering of polyatomic organic molecules, the use of a mono-atomic carrier gas ('seeded gas') reduces the temperature much faster [72]. The efficiency of cluster growth depends on the number of three-body collisions during the expansions, which is proportional to $p_0^2 D$ where p_0 is the stagnation pressure and D is the diameter of the nozzle. However, the mass throughput is proportional to $p_0 D^2$. Therefore, the cluster production can be maximized by increasing the reservoir pressure and decreasing the nozzle diameter while maintaining the mass throughput [73]. The mean cluster size is determined by the properties of the supersonic expansion, such as stagnation pressure, temperature, nozzle diameter and shape of the nozzle. A semi-empirical formula for the dependence of the mean cluster size to the properties of the supersonic gas jet was first introduced by Hagena [71, 74]. In addition to that, the works from Buck et al. also help in assessing cluster size distributions [75]. The mean cluster size can be related to the reduced Hagena parameter Γ^* as [76],

$$\begin{aligned} \langle n \rangle &= D\Big(\frac{\Gamma^*}{1000}\Big)^a \\ &= D\Big(\frac{\Gamma}{1000.\Gamma_{ch}}\Big)^a \end{aligned} \tag{2.28}$$

where Γ is the original Hagena parameter introduced in [74] which relates the mean cluster size to the experimental parameters of the supersonic gas jet using,

$$\Gamma = n_0 d_{eq}^q T^{0.25q-1.5} \tag{2.29}$$

where n_0, T, d_{eq} is the number density, temperature of the gas and equivalent diameter of the nozzle. The reduced Hagena parameter Γ^* is introduced to extend the above relation to metal cluster beams and is given by,

$$\Gamma^* = \frac{\Gamma}{\Gamma_{ch}} = \frac{n_0 d_{eq}^q T^{0.25q-1.5}}{r_{ch}^{q-3} T_{ch}^{0.25q-1.5}} \tag{2.30}$$

Therefore, from equation (2.30), Γ_{ch} is the characteristic scaling number defined as, $\Gamma_{ch} = r_{ch}^{q-3} T_{ch}^{0.25q-1.5}$, where r_{ch} represents radius of the gas and T_{ch} sublimation temperature. The effect of different geometry of the nozzle is taken into consideration using the quantity equivalent diameter as $d_{eq}/d = 0.74/\tan\theta$ (d is the throat diameter and 2θ, is the opening angle for the conical nozzle) for conical nozzles, which is estimated to enhance cluster production [77]. The quantities D and a are usually determined experimentally [76].

2.3.1 Non-covalent interactions in clusters of organic molecules

This section gives a brief summary of the interactions that are involved in the intermolecular binding of the studied clusters. For a more detailed description refer reviews [78, 79].

Non-covalent interactions are interactions which do not involve sharing of electrons. They hold molecules together in complexes such as molecular dimers and trimers. In nature, these complexes (clusters) play crucial roles in a variety of settings, including in the structure of large bio-molecules such as DNA [80]. Non-covalent interactions were first introduced by J D van der Waals [81], in the work where he reformulated the equations of state for real gases. Cluster formation is detected from the changes made to the properties of the subsystems due to the non-covalent interactions between them. An example is the change in the stretch frequencies upon complex formation in H-bonded systems. The stronger the non-covalent interaction, the larger the change in the properties of the subsystem. Covalent and non-covalent interactions differ in their origins and strength. Covalent interactions originate when partially occupied orbitals overlap and share the electrons, which makes them short range, typically less than 2 Å, whereas non-covalent interactions act at distances as large as a few tens of angstroms, therefore overlap between the orbitals is non-existent. As a consequence, non-covalent interactions are known to be considerably weaker than covalent interactions. The strength of such interactions is quantified using *stabilization energy* which is defined as the difference between the energy of the molecular cluster and the energies of the isolated subsystems. The total stabilization energy of a molecular cluster typically lies in the range of 1 - 20 kCal/mol (0.043-0.867 eV) whereas that of a covalent bond is around 100 kCal/mol (4.336 eV). Non-covalent interactions originate from the interaction between permanent multipoles (electrostatic), between a permanent multipole and an induced multipole (induction) or between an instantaneous time-varying multipole and an induced multipole (dispersion). Therefore, the interaction potential can be written as,

$$V_{non-cov} = V_{elec} + V_{ind} + V_{dis} + V_{rep} \tag{2.31}$$

The final repulsion term, called exchange repulsion prevents the orbitals of the subsystems from overlapping.

The vast majority of molecular clusters are non-rigid (floppy) systems dominated by large amplitude motions, rendering the concept of equilibrium structure meaningless. Therefore, a key characteristic of these systems, which are significantly more complex than covalent systems, is the potential energy surface. By using several *ab initio* molecular dynamics (MD) or Monte Carlo (MC) simulations to optimize the stabilization energy, the structure associated with the global and local minima of the potential energy surfaces (PES) is deduced [79]. While it is relatively simple to obtain the global minima experimentally, the local minima can only be attributed with certainty if the PES is known. The number of minima increases as the cluster number and the number of subsystems increase. For example, water dimer has only one global minima [82, 83] whereas uracil dimer has 11 minima [84].

From perturbation theory, the stabilization energy for the non-covalent interactions can be separated into the contributions from electrostatic, induction (charge-transfer) and dispersion terms which contribute to the attractive interaction between the subsystems. Clusters can be classified into different types according to the relative dominance of these terms. In some types of clusters a particular energy term will dominate, for instance, van

der Waals clusters where the stabilization energy constitute solely from dispersion forces. While several terms contribute to the overall stabilization in H-bonded (Hydrogen-bond) systems.

H-bonded systems

H-bonded systems are interactions with the participation of hydrogen. They are stabilized by all the energy terms. (ie. electrostatic, induction (charge-transfer) and dispersion terms). Most H-bonded systems are of the type X−H$\cdots$Y, where X is an electronegative atom and Y is either an electronegative atom, an atom having one or two lone pair of electrons or a group having excess electron density (eg. π electrons of aromatic systems). Most known and strong H-bonds systems are the ones having F, O or N [85]. Therefore, such dipole-charge/ dipole-dipole interactions caused by the electrostatic term give the H-bonds their directionality. H-bond formation is generally accompanied by an elongation of the X−H bond which causes a red-shift in its stretching frequency. Such an elongation and red-shift is a manifestation of the charge-transfer (CT) term of the stabilization energy [86]. Charge-transfer occurs from the lone pair (electronegative atom) or the π molecular orbital of the electron donor (proton acceptor) to the anti-bonding molecular orbitals of the X−H bond of the electron acceptor (proton donor). This causes an increase in the electron density in these anti-bonding orbitals which in turn causes an elongation of the X−H bond and a red shift in the stretching frequency. However, the amount of CT in these systems is not greater than $0.01e^{-}$, much smaller compared to the ionic clusters.

H-bonds in the organic molecules are of the type C−H$\cdots$Y, where Y is an electronegative [87] or π system [88]. C−H$\cdots$Y type H-bonds are found to be much weaker than that of O−H$\cdots$Y or N−H$\cdots$Y type H-bonds unless the CH group is acidic. However, due to their abundance, CH-type H-bonds are much more prominent in biomolecular structures. In such structures, bonds of the type C−H$\cdots$Y are observed which are not accompanied by the C−H bond elongation. Such bonds are not considered H-bond, but instead just C−H$\cdots$Y contact [89].

Another two types of intermolecular bonds similar to H-bonds, which have the participation of hydrogen, namely, improper (blue-shifted) H-bonds and dihydrogen bonding. The former is similar to a normal H-bond but has the opposite behaviour. It causes a contraction in the bond length of the X−H bond and a blue shift in the stretching frequency. This originates in the geometrical restructuring of the electron acceptor after the charge transfer from the electron donor [90]. Contrary to the H-bonds where CT is directed to the closest X−H bonds, for improper H-bonding CT is directed to the remote part of the electron acceptor. Such kinds of bonds with C−H$\cdots\pi$ interaction are observed experimentally in chloroform$\cdots$fluorobenzene complexes [91]. A dihydrogen bond is of the type M−H$\cdots$ H−Y where M is a metal. It was observed initially in metal complexes [92] and later also in H_3BNH_3 dimer [93]. Here, the interaction between two hydrogens occurs if one hydrogen is attached to an electropositive element and the other hydrogen to an electronegative element, thereby inducing a positive charge on one hydrogen and a negative charge on the other causing a multipole attraction. This is an example where dispersive forces play a role.

Electrostatic interactions

Electrostatic interactions are prevalent in most of the systems which contain permanent multipoles. One of the classic examples is benzene clusters which interact via quadrupoles. When visualized from a side, the quadrupole moment is formed by ‘sand-

wiching' the σ-electrons in between the aromatic π-electrons (Figure 2.7). Initially, it was believed that the parallel-stacked (S) structure is the global minimum due to the maximum possible overlap [94]. But later this was identified that the simple quadrupole-quadrupole interactions are repulsive causing the T-shaped structure to be the global minima [95]. This is also true in the case of proteins for example phenylalanine, where the T-shaped (T) and parallel-displaced (PD) structure is found to be of high occurrence [96].

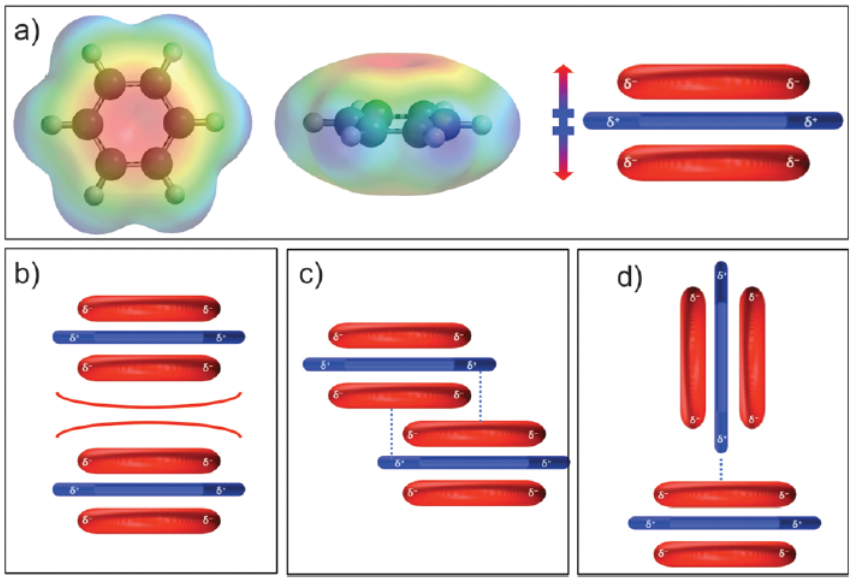

Figure 2.7: (a) Electrostatic potential map of benzene showing the quadrupole moment. (b) Parallel stacked (S), (c) Parallel-displaced (PD) and (d) T-shaped (T) conformers of benzene. Image is slightly adapted from [78]. The red-coloured region indicates the negative charge of the quadrupole and the blue-coloured region indicates the positive charge.

Dispersion interactions

Dispersion interactions play a vital role in the interactions between the biomacromolecules, such as the stacking interactions in a DNA base pair. The stability of some clusters is usually governed by the dispersion energies, whereas their structure is determined by the dipole-dipole electrostatic interaction between them. Dispersion interactions are not limited to a particular direction or path, as they are caused by the induced dipole moments of molecules, which can interact with each other regardless of their orientation. This makes them less directionally specific than electrostatic interactions. Most of the van der Waals molecules belong to this category.

Charge-transfer interactions

A charge transfer (CT) complex is formed when one system with a good electron donor (ie. having low ionization potential) interacts with another having a good electron acceptor (ie. a high electron affinity). Therefore, upon the formation of a CT complex electron flow from the donor to the acceptor. Donors and acceptors can be classified according to the type of orbitals involved in the interactions. From donors, non-bonding orbitals (n), σ or π bond interacts with the valence orbital (v), σ^* or π^* bonds of acceptors. The strength of the interaction varies from $n - v$ (strongest) to $\pi - \pi^*$ (weakest).

2.4 Inner-valence ionization and relaxation processes in small clusters

Electronic relaxation processes after inner valence or core ionization can proceed radiatively or by electron emission. Whether the excited atom/molecule decays radiatively or non-radiatively depends on the ionized energy level and its lifetime. Outer shell ionization typically decays through photon emission while inner-valence vacancies decay through electron emission via auto-ionization. Photon emission has lifetimes in the range of nanoseconds, whereas auto-ionization takes place in sub-picoseconds or in femtosecond timescales. Therefore, auto-ionization will be the preferred channel if it is energetically open. However, very deep inner-shell vacancies in high-Z atoms show X-ray emission as their prominent decay channel. If inner-valence/core ionization occurs in a cluster, relaxation processes can occur locally within the ionized monomer or non-locally by involving adjacent neighbours. A summary of different electronic decay mechanisms is given in figure 2.8. Decay proceeds via the non-local channel predominantly when the local channel is energetically non-feasible. Some of the relevant decay mechanisms will

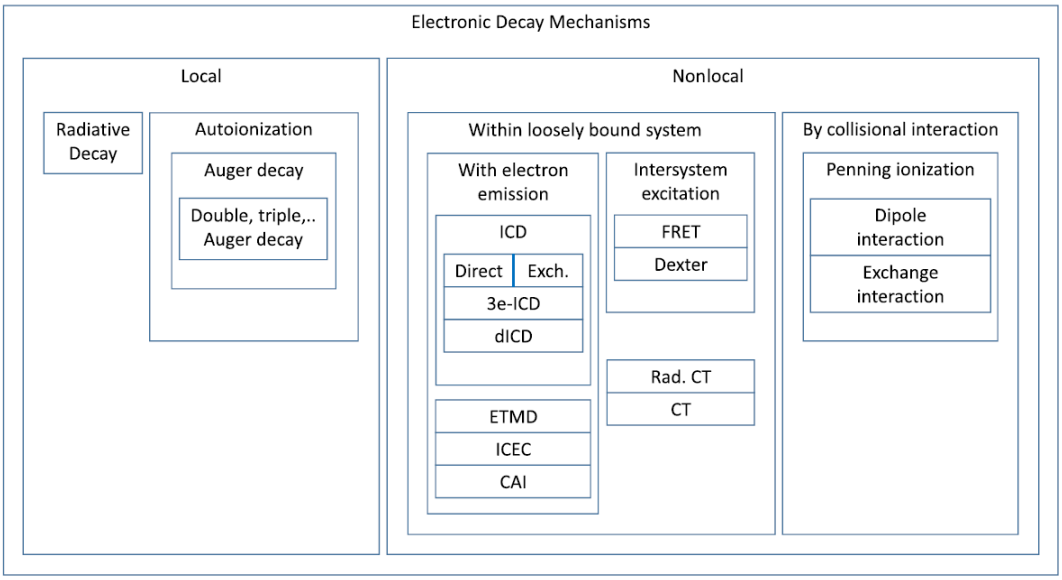

Figure 2.8: Schematic showing an overview of various relaxation mechanisms. Image is adapted from [97].

be discussed in the following section. Schematics of inner valence relaxation processes briefly discussed here are depicted in figure 2.9.

Auger decay or Auger-Meitner decay: One of the important local decay channels is Auger decay, which is an auto-ionization process upon an inner valence/core ionization/excitation. It is independently discovered by Meitner in 1922 [98] and by Auger in 1925 [99], therefore it is also called the Auger-Meitner effect. An electron undergoes a discrete transition from a less bound shell to the vacant inner valence/core vacancy transferring energy via electrostatic interaction to another bound electron that is emitted. The outgoing electron is named an Auger electron and labelled by letters corresponding to the involved energy levels (for example $KL_1L_{2,3}$, K-Core hole level, L_1 relaxing electron's energy level and $L_{2,3}$ Auger electron's energy level). Energy of the emitted Auger electron is given by $E = E_K - E_{L_1,L_{2,3}}$, where E_K is the energy of the initially ionized state

and $E_{L_1,L_{2,3}}$ is the energy of the final two hole state .

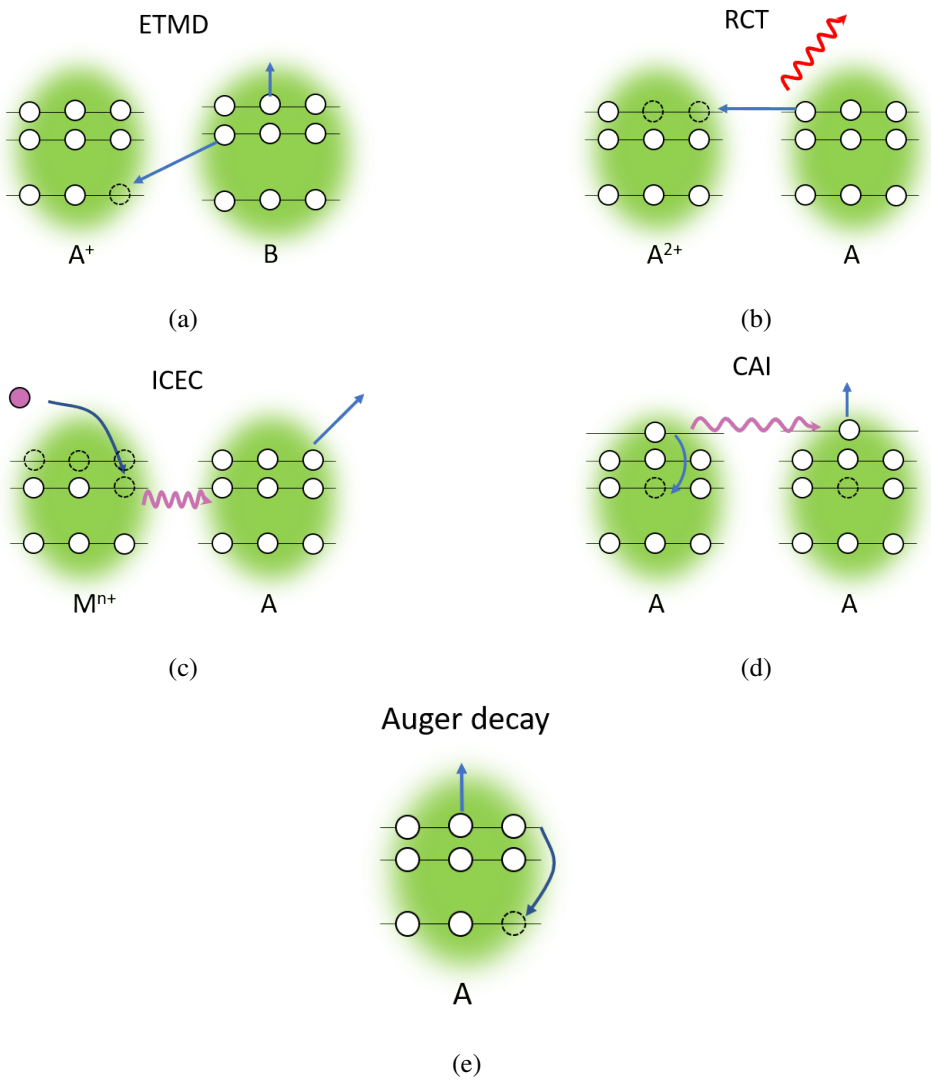

Figure 2.9: Schematics of certain inner-valence relaxation processes (a) Electron Transfer Mediated Decay (ETMD) (b) Radiative Charge Transfer (c) Interatomic and Intermolecular Coulombic Electron Capture (ICEC) (d) Collective Autoionization (CAI). Other pathways of collective autoionization also exist [101]. Only one is depicted here (e) Auger Decay.

Electron Transfer Mediated Decay: Electron Transfer Mediated Decay (ETMD) is similar to auger decay but occurs non-locally. ETMD is also triggered by an inner valence /core ionization, but contrary to Auger decay the vacancy is filled by an electron from the neighbouring molecule/atom (donor) [102]. The released energy is however transferred to the donor itself or transferred to another neighbouring atom/molecule and used to ionize it. The released energy upon the relaxation from an atom B to A must be such that enough energy is available for the ionization of atom B (2.9a), which makes it predominantly occur in heteronuclear systems. ETMD was first experimentally observed in ArKr heteroclusters [103]. However, experiments with Ar_2 also showed evidence of ETMD [104], which is enabled by the shift of energy levels due to the asymmetric charge distribution after the initial ionization. ETMD is termed as ETMD(2) or ETMD(3) [105] indicating the number of entities involved in the process.

Interatomic and Intermolecular Coulombic Electron Capture: When an atom or

an ionic species captures a low kinetic energy electron while in a cluster medium, non-radiative and non-local decay processes such as Intermolecular Coulombic Electron Capture (ICEC) can happen. Here the excess energy is transferred to the neighbouring species and ionizes it. It was theoretically predicted by Gokhberg et al in 2009 [106]. ICEC was experimentally demonstrated in 2017 in experiments with highly charged ion impinging on graphene foil [107]. It was shown that the neutralization of highly charged xenon ions during passage through the foil is a manifestation of ICEC. ICEC plays a major role in ion-induced radiation damage in cells and genes [108]. It can occur whenever there are more than two microscopic particles that can accommodate electrons. It is an important electron capture process which is prevalent in weakly bound systems and clusters whose efficiency increase with the number of neighbours.

Radiative Charge Transfer: In situations where the energy released after the relaxation of a system from the excited state does not favour further local or non-local ionization processes, excess energy can be emitted in the form of photons. Such a process termed Radiative Charge Transfer (RCT) is observed in homogenous cluster systems where processes such as ETMD (2,3) are not energetically possible. It was observed in Ne and Ar dimers with dications with $2p$ and $3p$ outer shell vacancies respectively in photoionization as well as electron impact ionization measurements [109, 110, 38]. Radiative charge transfer occurs when an electron is transferred from the neighbouring neutral atom to the dicationic state and the surplus relaxation energy is released radiatively. The process is identified indirectly in the ion-electron coincidence measurement as missing energy as well as directly by photon measurement in photon-induced fluorescence spectrometry [111]. Recently, RCT is observed in heterogeneous clusters like NeKr and NeXe after single ionization of $2p$ orbitals of Ne [112].

Collective Autoionization: Ionization with intense laser sources like free electron lasers on bigger clusters enables excitations of multiple units within a cluster, causing them to relax via different pathways 'collectively' similar to the above-mentioned mechanisms. Unlike ICD or any other related mechanisms, this process can involve multiple excited atoms at the same time. Relaxation can occur through multiple possibilities like the transfer of virtual photons or scattering of the ICD electrons. Theoretically predicted by Kuleff et al. [113], such a collective autoionization mechanism was experimentally found in He nanodroplets irradiated with FEL pulses [101].

2.4.1 Intermolecular Coulombic Decay (ICD)

Interatomic or Intermolecular Coulombic Decay (ICD) is the phenomenon which is being investigated in the second part of the thesis. It is a prominent relaxation mechanism for inner valence ionized atoms or molecules embedded in weakly interacting environments like van der Waals or H-bonded clusters. ICD was first introduced theoretically by Lorenz Cederbaum and co-workers in 1997 in small HF and H_2O clusters [33]. It was first experimentally demonstrated in Ne clusters [34, 35]. The inner shell vacancy is filled by an outer shell electron either from the same monomer or a close neighbour and the released energy is used to kick out an electron from the neighbour. ICD occurs when the second ionization from the same monomer is energetically not feasible due to the strong Coulomb repulsion of charges within the initially excited monomer, but an ionization of the neighbour is energetically feasible. The energy is transferred to the neighbour via dipole-dipole Coulombic electron-electron interaction.

According to Fermi's golden rule the electronic decay rate Γ_{iv} of the excited system

is directly proportional to the square of the electron-electron Coulomb matrix element,

$$\begin{aligned}\Gamma_{iv} &\propto \left|V_{ov_1,ov_2[iv_1,k]}\right|^2 \\ &\propto \left|V_{ov_1,ov_2,iv_1,k} - V_{ov_1,ov_2,k,iv_1}\right|^2\end{aligned} \tag{2.32}$$

The two terms in equation (2.32) $V_{ov_1,ov_2,iv_1,k}$ and V_{ov_1,ov_2,k,iv_1} shows contributions from the 'direct' and 'exchange' terms of the electron-electron correlation[1] (ov_1- outer valence orbital of atom/molecule 1, ov_2- outer valence orbital of atom/molecule 2, iv_1- initial inner valence vacancy of atom/molecule 1 and k- continuum state). The 'Direct' term represents the energy exchange between the initially excited monomer and the neighbour via virtual photon exchange after the relaxation within the excited monomer. The 'Exchange' term indicates an exchange of electrons between the monomers during relaxation, ie. the inner valence vacancy is filled by the outer valence electron of the neighbour and the energy released is used to kick-out the outer valence electron of the initially excited monomer. A pictorial representation of 'direct' and 'exchange' terms in ICD is shown in figure 2.10.

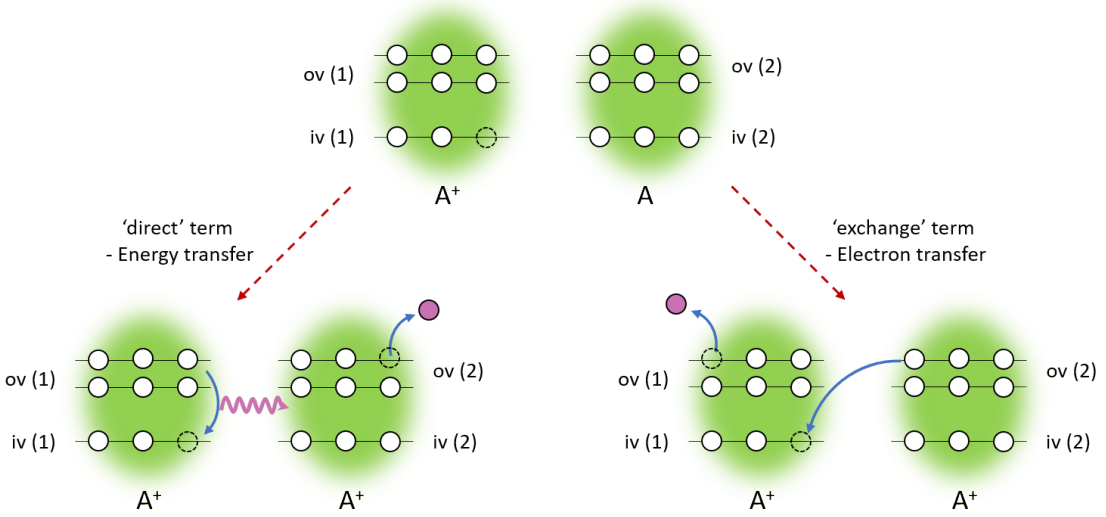

Figure 2.10: Pictorial representation of 'direct' and 'exchange' ICD processes.

The 'direct' and 'exchange' terms $V_{ov_1,ov_2,iv_1,k}$ and V_{ov_1,ov_2,k,iv_1} can be expanded in molecular orbital representations as [115],

$$\begin{aligned}V_{ov_1,ov_2,iv_1,k} &= \iint \phi^*_{ov_1}(x_1)\phi_{iv_1}(x_1)\frac{1}{|x_1-x_2|}\phi^*_{ov_2}(x_2)\phi_k(x_2)d^3x_1d^3x_2 \quad \text{- 'direct'} \\ V_{ov_1,ov_2,k,iv_1} &= \iint \phi^*_{ov_1}(x_1)\phi_k(x_1)\frac{1}{|x_1-x_2|}\phi^*_{ov_2}(x_2)\phi_{iv_1}(x_2)d^3x_1d^3x_2 \quad \text{- 'exchange'}\end{aligned} \tag{2.33}$$

Therefore, in the direct term, the electron from the outer valence orbital of the first monomer ϕ_{ov_1} fills in the inner valence vacancy of the same monomer ϕ_{iv_1} and exchanges a virtual photon, releasing an electron from the outer valence orbital of the neighbour ϕ_{ov_2} to the continuum orbital ϕ_k. In the exchange term, the inner valence vacancy ϕ_{iv_1} is filled by an electron from the outer valence orbital of the neighbour ϕ_{ov_2} and the electron from the outer valence orbital of the first monomer ϕ_{ov_1} is emitted to the continuum ϕ_k. Here x_1

[1]For a derivation of electron-electron Coulomb matrix element in direct and exchange terms refer Hartree-Fock formalism in Bransden et al. [114].

and x_2 refers to the position vectors of the correlated electrons with respect to the centre of mass of the system. Detailed theoretical description of ICD rates and the dependence with the internuclear distance R can be found elsewhere [115].

Although, the initial and final states of the direct and exchange terms are the same they differ in efficiency. This is due to the fact that the direct contribution has a leading term coming from the dipole-dipole interaction similar to the van der Waals interactions and therefore, the ICD decay rate scales with the internuclear distance as R^{-6}, whereas the exchange term depends on the overlap between the orbitals ϕ_{iv_1} and ϕ_{ov_2} and the ICD decay rate dies off exponentially with R. In addition, different selection rules apply to these contributions. For the direct term dipole-dipole interactions dominate whereas, the exchange term can arise from dipole-forbidden transitions as well [116, 117].

ICD efficiencies

In rare gas clusters, fluorescence decay is a competing process to ICD. The typical lifetime of fluorescence decay is in the nanosecond range, whereas ICD occurs in the femtosecond range. It was found in systems like helium dimers that 50% of the excited atoms relax via photon emission because of the exceptionally long ICD lifetime of thousands of femtoseconds [118, 119]. Bigger rare gas clusters like Ne [120, 121] show almost 100% ICD efficiency owing to the short ICD lifetime ∼150 fs [37]. ICD efficiencies are experimentally measured in electron-electron coincidence measurements as a ratio of the number of photoelectron-ICD electrons pairs ($n_{(e_{ph},e_{\mathrm{ICD}})}$) detected in coincidence to the number of photoelectrons ($n_{e_{ph}}$) detected [121]. If all the excited states relax through ICD the ratio should be unity. In a real spectrometer one has to apply corrections to this ratio taking care of the degree of condensation in the jet (c) and the detection efficiency for the second electron (γ). ICD efficiency can be formulated as,

$$\alpha_{\mathrm{ICD}} = \frac{1}{c.\gamma}\frac{n_{(e_{ph},e_{\mathrm{ICD}})}}{n_{e_{ph}}} \tag{2.34}$$

It has been observed in systems like Mg-CO that the ICD is quenched by pre-dissociation of the state and vice versa, due to the nuclear dynamics [122]. Whether ICD is quenched or not depends on the vibrational level and the corresponding pre-dissociation rate. For states with pre-dissociation rates higher than ICD, the molecule dissociates before the electronic decay. A similar effect is observed in water clusters where the ICD efficiencies are found to be around 10% to 45% for small clusters [123]. Here nuclear motions during the decay cause proton migration which leads the system to different configurations in which the ICD is energetically not feasible.

The differences in ICD efficiency in rare-gas clusters and water clusters are mainly due to the molecular nature of the constituents and the differences due to van der Waals interaction and the Hydrogen bonding. The directionality of hydrogen bonding gives rise to proton dynamics making proton migration a competing channel to ICD. ICD efficiency in D_2O cluster is shown to be 0.07 times larger than in H_2O clusters with cluster sizes ranging from 60-90 [123, 97]. Such an isotope effect also points to the role of nuclear dynamics in both clusters. As a result, it was observed that ICD is open for a longer time duration in D_2O than H_2O, leading to a slower deuteron transfer process in D_2O than the proton transfer in H_2O. Calculated potential energy curves for single and double ionized water clusters show that the single inner valence ionized water ($2a_1^{-1}$), which has a negative slope at the equilibrium distance may decay via ICD before an internuclear distance of around 1.3 Å to the doubly ionized state (figure 2.11). Beyond that distance,

the ICD channel is closed and the molecule undergoes proton transfer and dissociates to H_3O^+ and $OH^\bullet$.

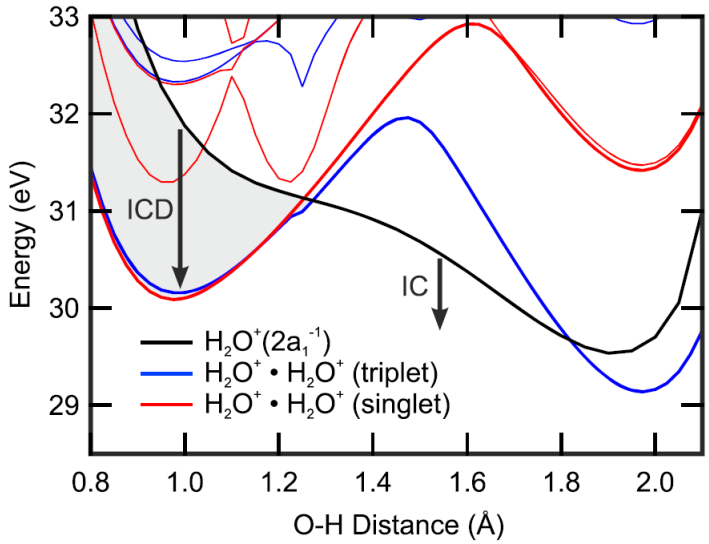

Figure 2.11: Calculated potential energy curves of singly ionized water ($2a_1^{-1}$), singlet and triplet doubly ionized states of water dimer with delocalized charges as a function of O−H distance. PECs for singly ionized water and doubly ionized water cross after 1.3 Å. Proton transfer and ICD are competing below this distance and beyond that ICD channel closes. Image slightly adapted from [123].

ICD efficiency also depends on the cluster size due to several factors. Firstly, in larger clusters the energy of the states may decrease due to polarization shielding and the decrease in energy for the doubly ionized states is larger than for the singly ionized states, causing the ICD energy to shift with the cluster size. Secondly, the increase in the number of nearest neighbours increases the chance of ICD. This is a considerably large effect in rare gas clusters, whereas the effect is less in water clusters [124]. Finally, the hydrogen bond length is smaller in liquid water than in small water clusters. Therefore, an increase in the ICD lifetime and rate can be expected with decreasing bond length, which is indeed an effect of the increase in the cluster size [97, 123].

The studies on clusters of organic molecules with water are found to be of interest since they can give insight into the radiation damage of biomolecules, notably DNA. Complexes of many organic molecules and water have been theoretically studied [125]. It has been found, for example, that in formaldehyde-water complexes the oxygen inner valance vacancy in both formaldehyde and water can initiate ICD. Additionally, O inner valence vacancy in formaldehyde can undergo Auger decay as well. Experimental studies have been done on water-THF (tetrahydrofuran) dimers in electron-ion coincidence measurements [41]. THF is of particular interest to the research on radiation damage to biomolecules since it can be considered a molecular analogue to the deoxyribose sugar ring in the DNA backbone. It has been found that the O $2s^{-1}$ vacancy in water can initiate ICD, whereas the O $2s^{-1}$ in THF is assumed to undergo Auger decay since it is an open channel in this binding energy range. An important result is that the THF^+ in the ICD final state undergo hydrogen loss by α cleavage, which is of particular interest since it sheds light on the DNA damage mechanism in hydrated environments.

Chapter 3

Experimental setup

This chapter describes the experimental setup used for the measurements described in this thesis. In short, an advanced Reaction microscope (ReMi) designed for the electron-atom/molecule collision experiments is used for particle detection. The projectile beam is generated from an electron gun based on a Tantalum photocathode. The targets used for the measurements are prepared using three different setups. This chapter explains in detail the working of the ReMi, the electron gun, the target setups, and the data acquisition system. Modifications done as part of this PhD work include two additional sources for targets which are solid at room temperature and installation of funnel MCPs on the electron detector for better detection efficiency.

3.1 Reaction microscope

A schematic of the Reaction microscope used for the measurements is shown in figure 3.1. It consists of a spectrometer inside of which is the interaction region, where the reaction takes place, two detectors and a pair of Helmholtz coils for generating a constant magnetic field. A section view of the spectrometer is shown in the image to show the trajectory of the particles and the electron gun. It is a special feature of this ReMi that the electron gun is inside the spectrometer which allows the electron beam to be aligned parallel to the electric and magnetic field. The electron beam is crossed with an atomic or molecular beam target at the interaction region. The particles generated are guided to the detectors on both sides of the spectrometer using constant electric and magnetic fields. The positively charged particles (here ions) fly to the ion detector on the right-hand side and the negatively charged particles fly to the electron detector on the left-hand side in figure 3.1. The trajectories of the unscattered projectile electron beam, the scattered projectile electron and the ion are also shown in the figure 3.1.

3.1.1 Spectrometer

The spectrometer of the ReMi provides a constant electric field for projecting the particles onto the detectors. It consists of a set of circular gold-coated aluminium electrodes with an inner diameter of 12 cm, outer diameter of 14.4 cm and thickness of 0.8 cm and field-free drift tubes. The individual electrodes are isolated from each other using alumina balls of 3 mm diameter and connected via resistors to each other as shown in figure 3.2. These electrodes form the region where the particles are accelerated which is called the acceleration region. The interaction region is at the centre of the 12th electrode from the electron side. Appropriate voltage is applied to the last electrode on the electron side

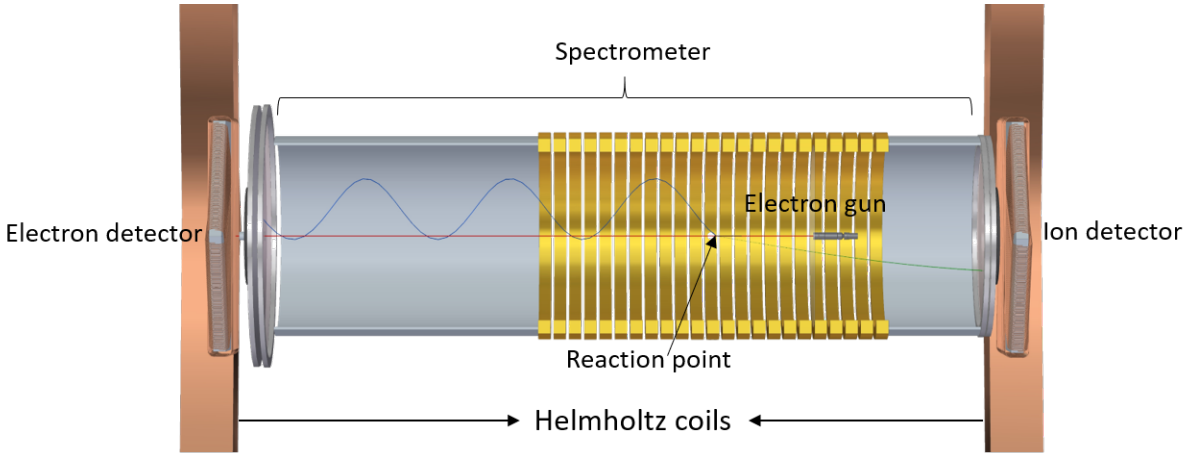

Figure 3.1: Schematic of the Reaction Microscope.

and the sixth electrode towards the right side of the interaction region to create a constant electric field within this region. The last electrodes on the ion side are connected to the drift tube on the ion side and form the ion drift region. On the electron side, a drift tube attached to the last electrode creates the field-free drift region for electrons. The length of the drift regions on both the electron and ion side of the spectrometer is chosen to be twice that of the acceleration regions such that *time-focusing* condition is satisfied. The spectrometer in this configuration called the Wiley-McLaren configuration allows compensating for the finite spatial extension of the target beam along the spectrometer axis [126]. The length of the acceleration regions of the electron and ion sides are 11 cm and 6 cm respectively. Depending on the mass and kinetic energy of the ionic fragments that are being investigated, the spectrometer is operated in constant field mode or pulsed field mode.

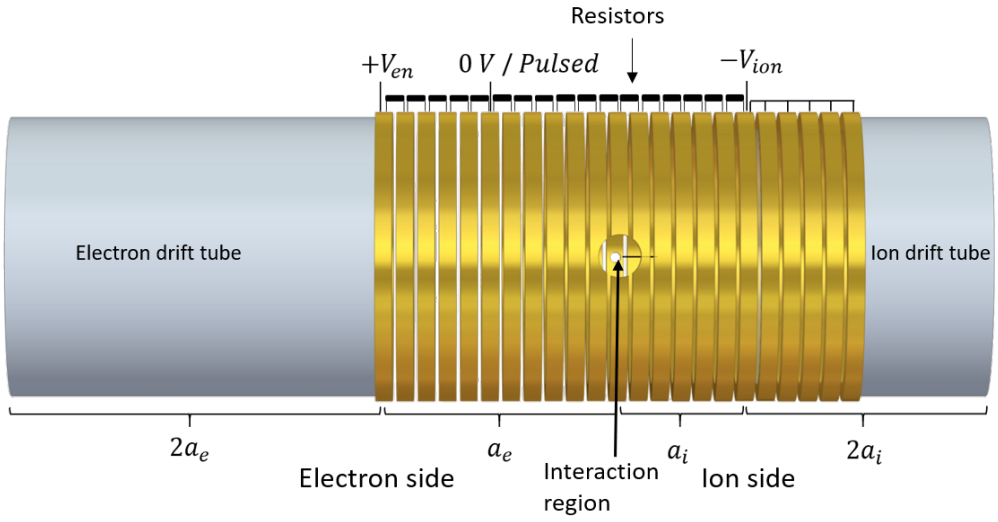

Figure 3.2: Spectrometer in Wiley McLaren configuration.

Pulsed operation

Due to the high repetition rate of the electron beam of 40kHz, the time window in which the ions have to be detected is $\sim$25 μs. Therefore, the highest m/q of the ion

fragment that can be detected using a constant extraction field is limited. On the other hand, an extraction field higher than 4 V/cm can severely worsen the electron momentum resolution. In order to detect ions of higher m/q ratio, the spectrometer is operated in pulsed field mode. Here the extraction field is increased from a low field to a high field $\sim$ 600 ns from the laser trigger within which the electrons are detected and the field is reduced to the low extraction field a few microseconds before the next projectile pulse. A high voltage positive pulse is applied to the sixth electrode from the interaction region towards the electron side as shown in the figure 3.2. Therefore, electrons are detected at a small extraction field ($<$ 4 V/cm) and the ions are detected at a high extraction field ($<$ 23 V/cm).

For the generation of the pulsed field, a square pulse is generated which is synchronized with the laser trigger and it is amplified using a pulse amplifier which can produce a maximum of 358 V. During the ramp-up and ramp-down background noise counts are produced at the detector. To reduce the noise counts, a low pass filter is used after the pulse amplifier which slows down the ramp-up and ramp-down and dampens the high frequency components of the ramp. Even with using the filtering circuit, the noise counts cannot be completely removed. Therefore, a hardware gate is applied such that data acquisition for ion signals is inhibited during the ramp-up and ramp-down. For electron signals, a similar hardware gate inhibits the data acquisition from 340 ns after the laser trigger. To make sure that the extraction field is decayed completely to the low field, the ramp down is initiated a few microseconds before the arrival of the next pulse.

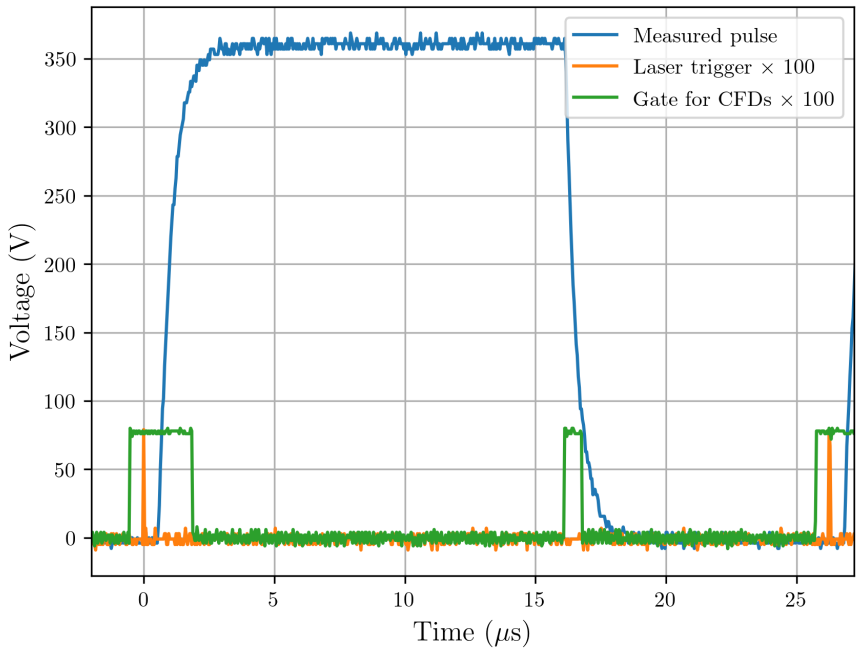

Figure 3.3: Timing diagram showing the extraction pulse voltage applied at the 6th electrode towards the electron detector side, Laser trigger signal and the gate for inhibition of data acquisition for ion signals during the ramp-up and ramp-down of the pulse. The voltage of the laser trigger and the gate is multiplied by 100 for the visual comparison with the extraction pulse voltage.

Figure 3.3 shows the laser trigger, hardware gate for the inhibition of data acquisition for ion signals and pulsed field measured at the output of the filtering circuit.

3.1.2 Time and position sensitive detector assembly

The detector system gives information about the time-of-flight of the reaction fragments from the interaction region and the position on the detector where it is hit. The important parts of the detectors which are common for both ion and electron detectors are microchannel plates (MCPs), delay-line anodes, grids and the ring anode. The schematics of the detector assembly for both electron and ion detectors are shown in figures 3.10 and 3.9a. The signals from the MCPs provide the time-of-flight information and the signals from the delay-line anodes give the position information. These time and position signals are used to reconstruct the longitudinal and transversal momentum components of the particles. There are two grids placed in front of each detector to ensure field continuity and background noise reduction. Since the MCPs are normally operated at rather high voltages ($\sim$ 2.5-3.5 keV), there is a chance that the high field at the MCP can penetrate the drift tube which has to be field free and can worsen the longitudinal momentum resolution. The two grids placed in front of the detectors can maintain a homogeneous electric field between the drift tube and the MCP. The first grid is normally connected to the same voltage as that of the drift tube. The second grid, which is closer to the MCPs can be kept at a slightly different voltage than that of the drift tube. On the electron detector, which is at a positive voltage to extract the negatively charged electrons, the second grid is often kept at a voltage more negative than that of the drift tube. This is to reduce the secondary electrons, produced by the primary electron beam by hitting some parts of the spectrometer and the electron gun. Some inhomogeneity can also be present between the MCP and delay-line anodes which can hamper the 1:1 imaging property of the detector. One of the reasons for such an inhomogeneity is the presence of the mounting screws for the MCPs which are connected to the ground. To prevent that, a ring anode is placed between the MCD stack and the delay-line anode. It is a conducting plate made of stainless steel with an outer diameter the same as that of the MCPs and has holes at the positions of the mounting screws (see figure 3.4). A voltage that is between the voltage at the back side of the MCP and the delay line anode is applied to the ring anode to ensure field continuity.

Microchannel plates (MCPs)

A microchannel plate is a lead glass plate perforated with millions of precise microchannel holes which can act as arrays of miniature electron multipliers [127]. The diameter of the miniature holes is 12 μm, the centre-to-centre distance is 15 μm and the thickness of the plate ranges from 0.75 μm to 1.5 mm. A voltage gradient of typically 1 kV is applied across the MCP and they have a resistance in the range of a few tens of megaohms. The electrical contact at the front and back side of the MCP is provided by a metallic coating on both ends of the MCP at its edge. The axis of the micro-channels is biased to 8^{o} with respect to the plane of the MCP to optimise the secondary electron emission. When a particle like an electron or ion enters from one side of the channel and hits on the walls of the channel, it emits secondary electrons. The high voltage gradient applied across the channel accelerate the electrons vertically to the back plane of MCP which leads to the parabolic trajectory within the channel. Therefore, the bias of 8^{o} forces the electrons to collide several times with the wall within the channel. Amplification of the MCPs ranges from 10^4 to 10^8 depending on whether it is used singly or in cascade. Two or three MCPs can be stacked to get higher amplification in *Chevron* or Z-stack arrangement as shown in the figure 3.5b. The charges thus lost from the semiconducting walls are replenished using the voltage source which provides the potential

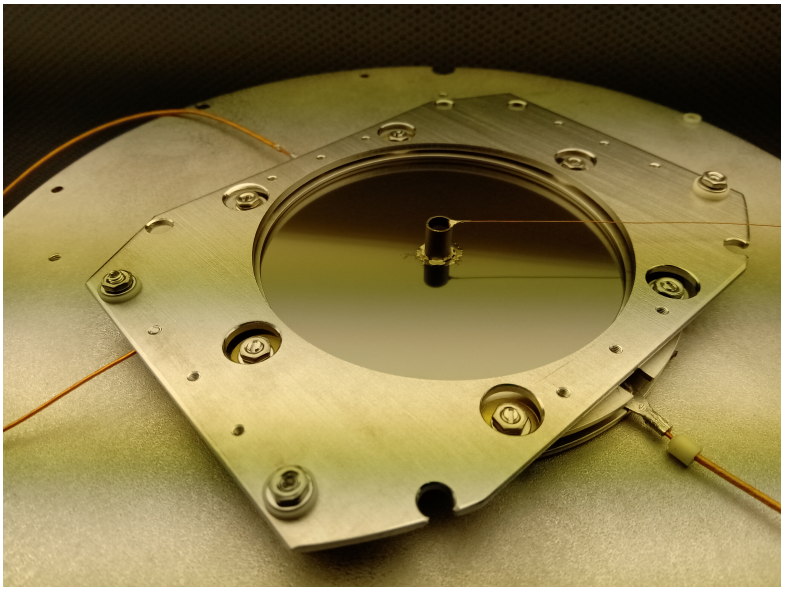

Figure 3.4: An image of part of the electron detector with MCPs together with the ring anode. The detector assembly is placed upside down such that the grids are on the bottom end of the image. One can see the inner diameter of the ring matches that of the MCP diameter and there are holes at the position of the mounting screws, thereby shielding the high field between the screws and the ring from the constant field regions between the MCP and the delay line anode.

difference across the MCP, therefore, producing a drop in the voltage applied across the MCP. This can be coupled out using a capacitor and therefore, providing the time signal of the particle hit.

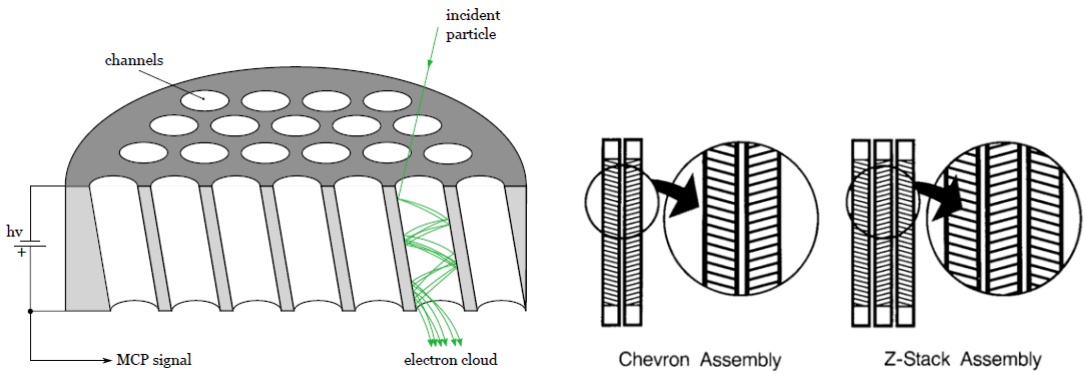

(a) (b)

Figure 3.5: (a) Schematic of an MCP and the amplification of signals. Image adapted from [128] (b) MCPs in chevron and z-stack configurations. Image adapted from [129]

The efficiency of an MCP depends on the kinetic energy and mass of the detected particle. Efficiency rises as the impact energy or the velocity of the particle increases and it saturates at a value that is limited by the open area ratio (OAR), which refers to the channel open area to the entire effective area of the MCP. The standard MCPs have a detection efficiency of roughly 58% [130] which is slightly higher than the OAR. An increase in OAR can further increase the efficiency, but it leads to reduced timing resolution and increased ion feedback [131]. Novel approaches to expand the OAR have been developed by increasing the opening angle of the channels at the surface, like a funnel

(see figure 3.6), therefore, they are called 'funnel MCPs'. These can give efficiencies up

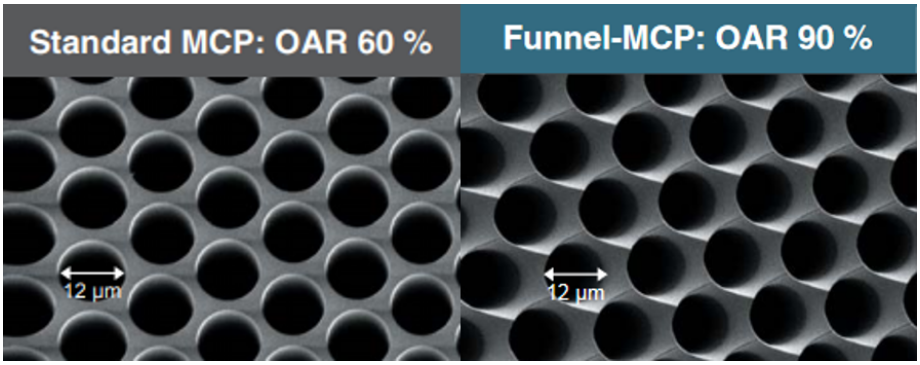

Figure 3.6: Zoomed image of the surface of standard MCP and 'funnel' MCP [132]

to 86% for an OAR of 90% [133]. For the experiments described in this thesis, we have used standard MCPs for the ion detector and funnel MCPs for the electron detector.

Hexagonal delay-line anode or Hexanode

The position information of the signal from the MCP stack is obtained using a delay-line anode. It is a wire wound around a base plate connected to a voltage, typically, 200 V more positive than the voltage on the backside of the MCP. The electron cloud from the MCP induces a charge distribution on the wire and it propagates to both ends of the wire at the same speed. This signal is then capacitively coupled out and gives the time taken for the signal to propagate to both ends of the wire, t_{x_1} and t_{x_2}. The difference between these two time signals is proportional to the spatial coordinate of the electron cloud on the wire.

$$\begin{aligned} x &= v_\perp((t_{x_1} - t_{mcp}) - (t_{x_2} - t_{mcp})) = v_\perp(t_{x_1} - t_{x_2}) \\ y &= v_\perp((t_{y_1} - t_{mcp}) - (t_{y_2} - t_{mcp})) = v_\perp(t_{y_1} - t_{y_2}) \end{aligned} \tag{3.1}$$

where t_{mcp} is the MCP signal and $v_\perp = c_z \frac{\Delta x}{l_w}$ is the average velocity with which the electron cloud moves perpendicular to the direction of the winding (see figure 3.7a), where Δx is the spacing between each winding, l_w is the length of each winding and c_z, the propagation velocity of the signal along the wire.

To reduce common-mode noise, another wire called reference wire is wound parallel to the signal wire which is applied with a voltage typically 50 V lower than that of the signal wire. The common-mode noises will be the same on both the wires, whereas, the signal due to the electron cloud will have different amplitude due to the different bias voltages applied. These time signals from both signal and reference wires are then passed through a differential amplifier as shown in the circuit diagram 3.7b and the common-mode noise is then subtracted out.

To get the (x, y) position of the particle hit, we need to have another layer of wire winding perpendicular to the first winding and insulated from each other. Resolution can further be increased by adding a third layer as shown in the figure 3.8. Due to the hexagonal shape, it is called a hexagonal delay line anode or hexanode. The additional layer improves also the multi-hit capability, since now we have three different wire combinations to calculate the position from, namely $(x, y)_{uv}$, $(x, y)_{uw}$ and $(x, y)_{vw}$ [135]. A detailed description of the processing of the signals is given in chapter 4.

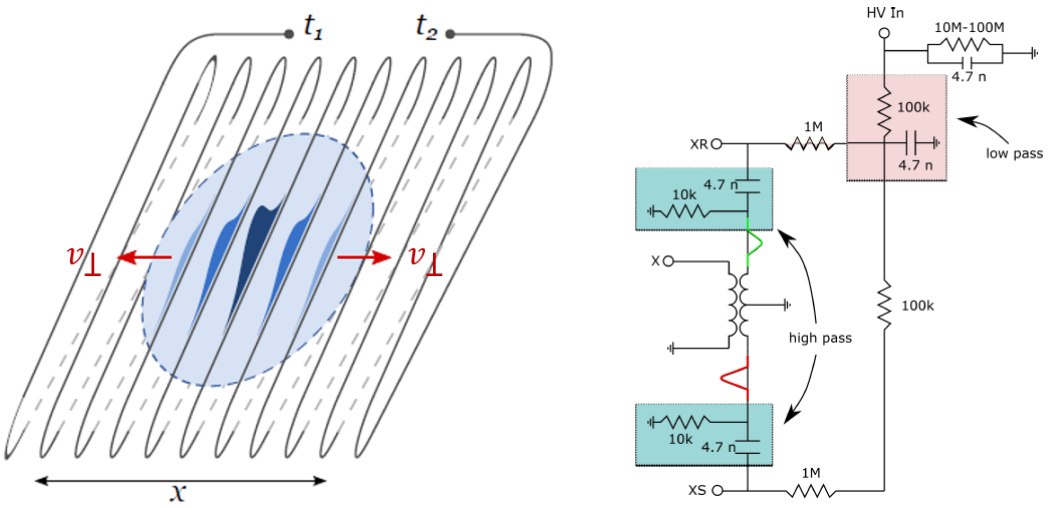

(a) (b)

Figure 3.7: (a) Schematic showing the charge propagation on a delay-line wire. Image adapted from [128]. (b) Circuit diagram of the differential amplifier circuit used to reduce the common-mode noise from the delay line anode. The time signals from reference and signal wires are represented by XR and XS. HV In represents the high voltage applied to the circuit. The output of the differential amplifier is indicated by X. Image adapted from [134].

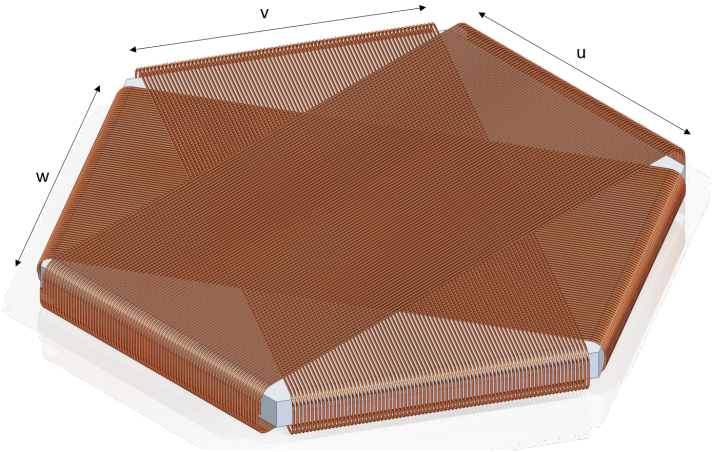

Figure 3.8: Hexanode

Ion detector

Figure 3.9a shows a schematic of the ion drift region and the ion detector arrangement together with the electron gun assembly. The first grid is placed in front of the electron gun and touching the electron gun assembly as shown in the figure 3.9a to separate the acceleration/extraction field from the drift region.

A hole is made at the centre of the grid to facilitate the passage of the projectile beam. The body of the electron gun is connected to the same voltage as that of the drift region to maintain field homogeneity of the drift region. Two grids are placed right in front of the MCP stack. The second grid (grid 2 3.9a) terminates the field-free drift region. The third grid could be biased to a slightly higher or lower voltage compared to the drift region depending on the purpose. For the measurements described in this work, a slightly more positive voltage is applied to grid 3 to facilitate background reduction. Two MCPs are

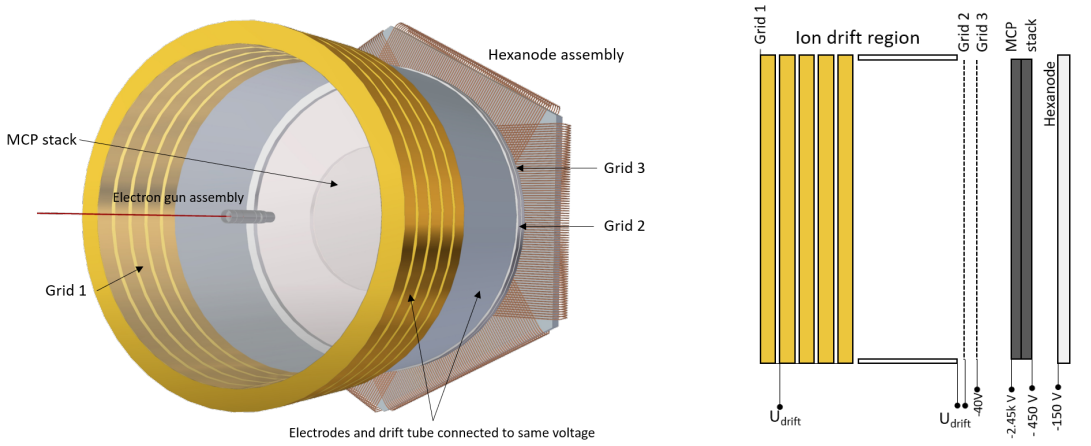

(a) (b)

Figure 3.9: (a) Ion detector assembly together with the drift region and the electron gun assembly. The first grid is attached to one of the electrodes as shown in the figure. All the electrodes from the first grid are connected to the drift tube voltage. The second grid is placed after the drift region and is also connected to the drift tube voltage to maintain the uniform potential. Yet another grid, grid 3, is placed in front of the MCP and can be kept at the same voltage as the drift tube or at a slightly higher or lower voltage. (b) Schematic showing the voltages applied to individual parts within the ion drift region and detector assembly.

stacked in a *Chevron* configuration for the ion detector and a voltage difference of $\sim$2 kV is applied across the MCP stack. To enhance multi-hit capability, we use a hexanode for the position signals. A circuit diagram showing the voltages applied to different parts of the ion detector is shown in figure 3.9b.

Electron detector

The arrangement of the electron detector is different from that of the ion detector because we have to take care of the projectile beam aligned along the spectrometer axis. The incoming unscattered projectile beam is dumped onto a hole in the electron detector. The main challenge to get a good coincidence rate is to separate the electron hits from the target ionization from that of the undesired electrons, such as secondary electrons produced by either the primary beam hitting on parts of the spectrometer or the electron gun assembly, the electrons produced by the scattered laser pulse hitting inside the electron gun assembly, elastically scattered projectile beam, etc. Proper dumping of the projectile beam can reduce a lot of such undesired electrons. The electrostatic lensing effect due to the field lines within the hole penetrating outside is utilized for proper focusing of the projectile beam into the dump as can be seen in figure 3.10. In order to assure a homogenous electric field in between grid 2 and the MCP surface, a ceramic tube of outer diameter 8 mm with a resistive coating of Germanium on the outer walls is fixed between the grid 2 and the front end of the first MCP (see figure 3.10).

This coating acts like a continuous resistive divider and ensures a constant potential gradient in front of the MCP in the vicinity of the tube between the second grid and the front side of the MCP. At the same time, the field lines can penetrate the inside of the tube and focus the projectile beam. Industrially available MCP with a central hole, have a hole diameter of 6.3 mm and a dead area of 2 mm from the edge of the central hole. The

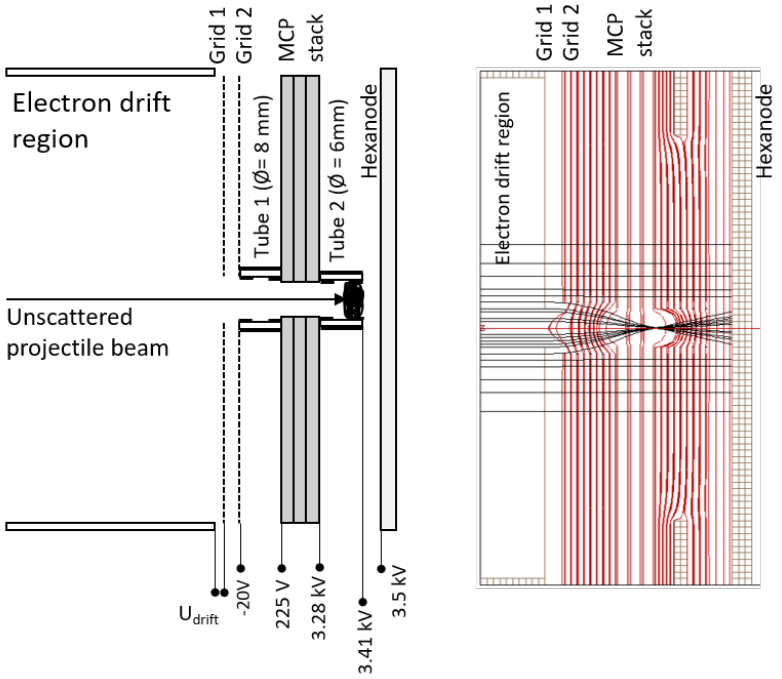

Figure 3.10: Schematic showing the electron detector comprising of grids, MCP stack, hexanode and germanium-coated ceramic tubes in the front and back side of the MCP. On the right side, the SIMION simulation of the electron detector assembly is shown.

effective dead area for such MCP is a central circle with a diameter of ∼12 mm. A tube with 8 mm can be fixed into this dead area without affecting the good electrons.

Similarly another tube of outer diameter 6 mm with the resistive outer coating is fixed at the back side of the MCP stack. A voltage ∼100 V higher than that of the back side of the MCP is applied to the farther end of this tube. The purpose of this second tube is also to ensure a constant field for the electron cloud exiting the MCP stack. The voltage to this tube is optimised by looking at the detector image and comparing the size of the hole to its physical size. Too high voltage at the tube will attract the electron cloud towards the tube making the hole look larger and too low voltage will make the hole look smaller than its physical size. The projectile beam is dumped at the end of this tube onto a tiny ball made of a string of beryllium-copper alloy and dipped in graphite. This ball is electrically connected to the end of the tube and the graphite layer absorbs the projectile electrons. Therefore, the ball serves the purpose of a Faraday cup. In the absence of this ball, the projectile beam with an energy ∼ 4kV, after passing through the MCP stack and the tube falls on the base plate of the hexanode, creating a bunch of ions. Part of them fly back to the ion detector and create huge signals at the lower ion time-of-flight region, somewhere close to the position where protons are supposed to arrive. Therefore, the presence of the ball acts as an effective electron dump and prevents the creation of such ions.

The MCP stack of the electron detector placed in between the tubes, is arranged in a Z stack configuration 3.5b. This allows us to have an amplification of upto 10^8. Besides that, to a greater extent, it suppresses the number of positive feedback ions created within the channels from the background ionization or desorption from the channel walls. This is particularly a problem for the electron detector since the ions created would fly directly

towards the ion detector and creates background signals.

3.2 Electron gun

The projectile beam which is a pulsed beam of electrons is generated using an electron gun. The electrons are emitted from a tantalum photocathode, which is of a diameter 0.84 mm with a work function of 4.22 eV when a pulsed UV laser of wavelength 266 nm (photon energy = 4.66 eV) is focused on it. The pulse duration and repetition rate of the electron gun correspond to that of the UV laser which amounts to 0.5 ns and 40 kHz, respectively. Figure 3.11 shows the schematic of the electron gun assembly.

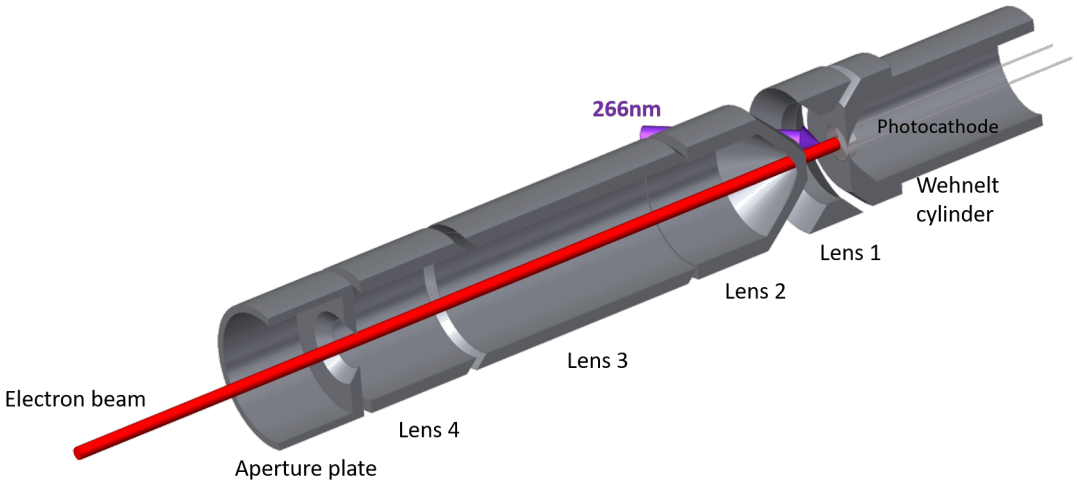

Figure 3.11: Schematic of the electron gun.

The photocathode is enclosed within a Wehnelt cylinder which is applied with a slightly negative voltage than the photocathode. Wehnelt cylinder together with lens 1 enables the beam to be collimated along the spectrometer axis. It is further focused on the target interaction region using the electrostatic lens arrangement lens 2, lens 3 and lens 4 which forms an 'Einzel lens'. Additionally, an aperture plate can be used to adjust the beam size and focus. The axial magnetic field confines and guides the projectile electron beam along the spectrometer axis. The projectile electron beam is further dumped into the hole on the electron MCP. The electron detector assembly can be moved slightly along the xy-plane in order to ensure proper dumping of the projectile beam into to MCP hole.

The electron gun has a diameter of 8 mm and length of 60 mm and it is mounted within the ion drift region. Since the distance between the electron gun and the interaction region is only approximately 6 cm, the temporal width enhancement of the electron bunches due to the space charge effects is negligible. The number of electrons per bunch can be adjusted by adjusting the laser beam intensity using a motorised rotating polarizer. The optical setup for the laser beam is mounted outside of the chamber.

The energy of the projectile beam is given by the voltage difference between the photocathode and the interaction region.

$$E_{kin}[eV] = (V_{int} - V_{bias}) \tag{3.2}$$

In our experiment, the projectile energy can be adjusted in the range from ∼0 eV to 3 keV which is the maximum voltage the power supply can provide.

3.3 Target preparation

The targets used for the measurements are prepared using three different setups. The volatile biomolecules are prepared using the supersonic gas jet. 1-Methyl-5-Nitroimidazole (1Me5NIZ) target is prepared using a setup using a syringe which is introduced horizontally towards the interaction region. This setup can be replaced by an oven setup to produce the lithium atomic beam.

3.3.1 Supersonic gas jet

The momentum gain of the ions after an ionizing collision is typically in the range of 1 au. To resolve such low momenta, the initial state momentum spread of the target must be smaller than that. The average momentum spread of gases at room temperature 300 K is much larger than the required resolution. For example, He at room temperature (300 K) has an average momentum of 4.7 a.u. It has to be cooled down to $\sim$ 10 K such that the transferred momentum is resolvable. An ideal gas can be cooled down efficiently by adiabatic expansion. In our experiment, we use supersonic gas jets which work on the principle of adiabatic expansion to obtain target temperatures in the kelvin range.

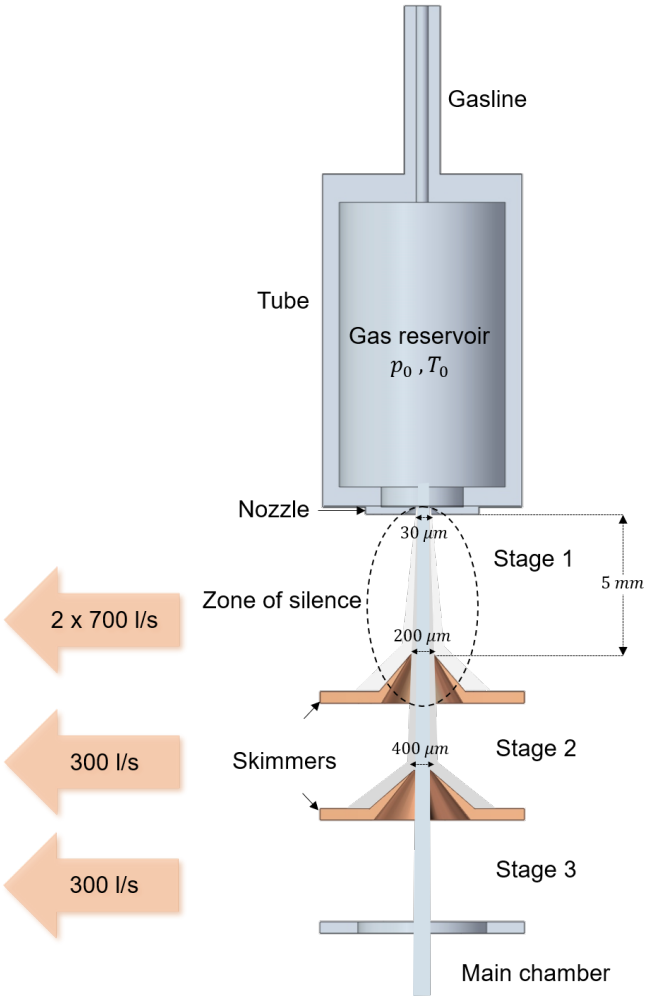

Figure 3.12: Schematic of supersonic gas jet system.

The target gas in a gas reservoir at room temperature with a stagnation pressure p_0 is

adiabatically expanded through a nozzle of diameter 30 μm into a differentially pumped vacuum chamber with two turbo-molecular pumps of pumping speed 700 l/s up to a pressure of $p_1 \sim 10^{-3}$ mbar. This chamber has the highest gas load and is separated from the other parts of the entire vacuum chamber by connecting to a separate pre-vacuum scroll pump/ oil pump. Due to the pressure gradient, the particles accelerate along the jet direction after the nozzle and reach a velocity greater than the local speed of sound, therefore, the name 'supersonic' jet. The volume after the nozzle where such a supersonic gas flow happens is called *zone of silence*. If a skimmer is placed within this *zone of silence*, a beam of gas at supersonic velocities can be prepared along the jet direction. Therefore, such a supersonic expansion into a low-pressure vacuum chamber allows for the effective conversion of the undirected thermal energy of the gas in a reservoir to a directed kinetic energy. In our experiment, we use a skimmer of diameter 200 μm placed approximately 5 mm away from the nozzle, which effectively removes the particles with high transverse momentum and forms a beam into a second differential pumping stage with a background pressure, p_2 of about $\sim 10^{-6}$ mbar. Another skimmer of diameter 400 μm is placed after the first skimmer to further remove the particles with high transverse momentum and prepare a highly collimated beam. An additional third differential pumping stage with background pressure, $p_3 \sim 10^{-8}$ mbar separates the main chamber from the jet system. Both the second and third differential pumping stages are pumped out using turbo-molecular pumps with pumping speeds of 300 l/s each. An illustration of the jet system is shown in figure 3.12. The cold gas jet thus formed is directed vertically and passes through the main chamber where it crosses with the projectile beam. The jet is estimated to have a diameter of $\sim$2 mm at the interaction region. Only a very small fraction of the beam interacts with the projectile beam and the rest of the gas within the jet is dumped to another two differential pumping stages which act as the beam dump. Hence, the main chamber vacuum is unaffected by the flow of the jet.

The advantage of using the supersonic gas jets to obtain cold atomic/molecular gas targets instead of other methods like the magneto-optical trap is its flexibility to use any type of gas species. Even liquid targets with sufficient vapour pressure can be used along with a carrier gas, usually helium. Detailed descriptions of the supersonic gas jets can be found elsewhere [128, 136, 137].

Clustering

Due to the low temperatures attainable using the supersonic gas jets, often condensation of the target happens at the nozzle which facilitates the formation of clusters of different sizes. A simple explanation of the clustering process can be given using condensation theory as shown in the phase diagram (figure 3.13). The gas stored in the reservoir with a stagnation pressure, p_0, at room temperature is represented by point A. The supersonic expansion of the gas in ReMi at the nozzle follows the isentrope AB. Beyond point B, if the equilibrium temperature is maintained, it follows the path $p_v(T)$. However, for an adiabatic expansion like in the ReMi, the gas continues to expand following the 'dry' isentrope BC into a supersaturated state. Beyond point C, the supersaturated state breaks down allowing cluster formation and returns to the equilibrium line, $p_v(T)$ via the condensation path, $p(T)$. The increase in the temperature beyond point C is due to the heat of the formation of the clusters [71].

To study liquid targets in the ReMi using supersonic gas jets, it has to be vaporized and mixed with a carrier gas, usually helium. They are stored in a reservoir connected to the gas line, which can be separated by using valves between the reservoir and the

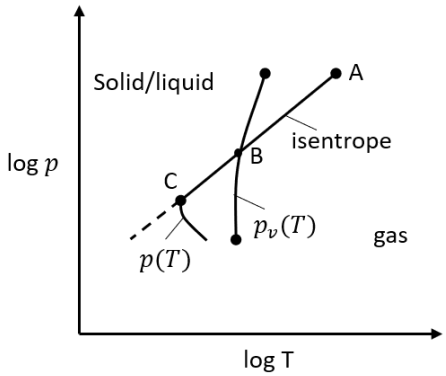

Figure 3.13: $p - T$ phase diagram explaining the condensation theory [71].

gas line. Volatile targets with at least 100 mbar pressure can be directly mixed with the carrier gas, whereas non-volatile liquid targets have to be heated to produce enough vapour pressure for cluster formation. Care should be taken to prevent over-condensation and crystallization at the nozzle, which can lead to blockage. Therefore, the entire gas line, gas reservoir and nozzle have to be kept at a higher temperature than the liquid reservoir. For the measurement of thiophene, which has a vapour pressure of 106 mbar at room temperature, heating was not required. However, for the experiment with pyridine and water, both reservoirs had to be heated. Pyridine was heated up to 62°C to produce a vapour pressure of $\sim$ 170 mbar and water was heated to 52°C to produce a vapour pressure of $\sim$ 140 mbar. During this experiment, the nozzle was kept at 87°C and the tube (gas reservoir, see fig: 3.12) was kept at 79°C.

3.3.2 Syringe needle setup

Due to particularly low vapor pressure $\sim$ 0.003 mbar at 20°C, it was not possible to produce 1-Methyl-5-Nitroimidazole (1Me5NIZ) target using the supersonic gas jet. We employed a syringe setup for the ionization. The 1Me5NIZ target vapour is introduced to the interaction region using a syringe which is fixed on an xyz manipulator. Industrial 1Me5NIZ sample in powdered form is filled inside the syringe and the whole syringe setup is moved towards the centre of the spectrometer along the x direction in the lab frame, such that the tip of the needle of the syringe is close to the interaction region but not hitting the electron beam. To obtain sufficient target density, the sample was slightly heated using two small resistors of 50 Ω, which were connected in series and fixed on the body of the syringe. For the current experiment, the target is heated up to 56°C. Figure 3.14 shows the schematic of the syringe setup and how it is assembled to the ReMi. A stainless steel rod connected to the xyz manipulator is pushed into the hollow cylinder of the syringe within which the sample can be filled. Slowly evaporating vapours come out of the needle and are crossed with the electron beam. Similar to the measurement of other heavy molecules, we employ pulsed electric fields (22.6 V/cm) for the extraction of the ions. Since the sample is at room temperature or even heated, the ion momentum resolution is inadequate to deduce the initial momenta of the ionic fragments. Unlike the supersonic gas jet which has a large velocity along the y direction, the 1Me5NIZ vapours have average velocity corresponding to the room temperature or slightly above. The large velocity of the jet causes the low momentum ions to pass the electron gun and to hit on the detector below to shift slightly downwards from the centre.

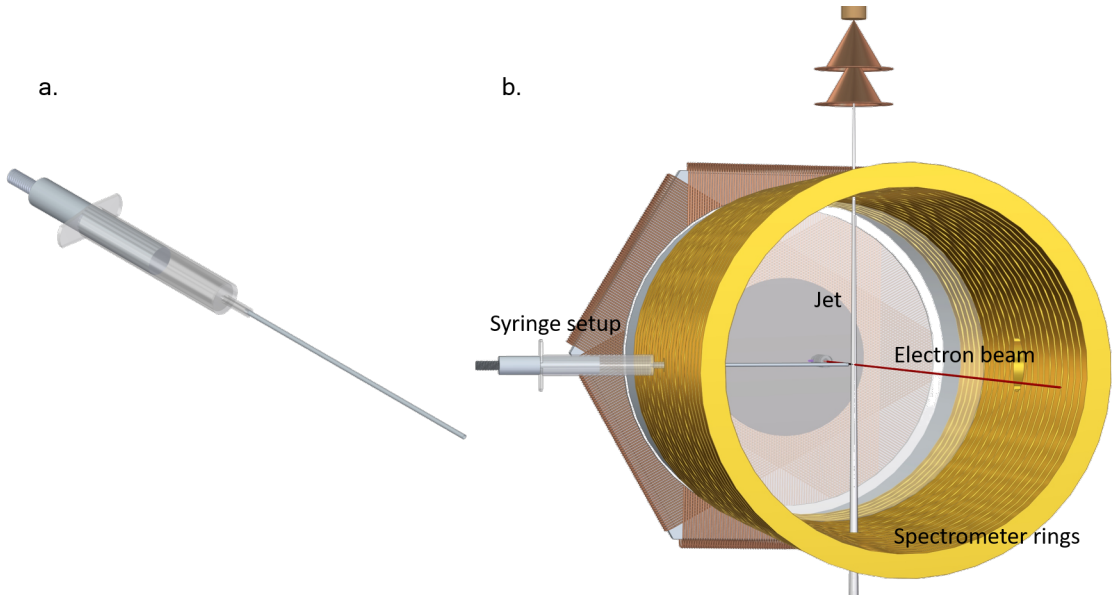

Figure 3.14: Schematic of the syringe setup. (a) Syringe with needle and stainless steel rod. The sample is filled inside the syringe cylinder and the syringe setup is connected to the xyz manipulator via the M4 thread on the stainless steel rod. Thus, the position of the tip of the needle can be adjusted, such that it is close to the focus of the electron beam but not hitting the beam. (b) Schematic showing the syringe setup assembled with the spectrometer.

However, similar low momentum ions from 1Me5NIZ (e.g, parent ion, $1Me5NIZ^{+}$) hit the electron gun which is installed along the spectrometer axis within the drift region. To prevent this, a pulsed voltage higher than the voltage of the spectrometer ring at the interaction region was applied to the syringe needle. This enables some fraction of the parent ion and other fragments of low initial momenta to be pushed out of the interaction region and detected at a position along the positive x-axis of the ion detector. Therefore, the initial momentum information of the ionic fragments is completely lost due to the inhomogeneous electric field and the time-of-flight information of the ions is used only to select the events corresponding to the reaction channel of interest. For the current experiment, a helium supersonic gas jet was also used for the calibration of the data. It crosses both the electron beam and the vapours from the syringe setup.

3.3.3 Lithium atomic beam target

The lithium atomic beam is prepared by an effusive atomic oven which emits hot lithium vapour to the interaction region in a crossed beam configuration with both the projectile and the supersonic gas jet. The oven used in this experiment is made of stainless steel and is heated using heating wires made of Inconel, wound around it which can be heated up to a temperature of 1000°C. Figure 3.15 shows a simple schematic of the oven and a cryogenic cold head assembly. The red hot oven is mounted inside a water-cooled copper housing which is connected to the chamber walls. This prevents the entire vacuum chamber from heating up due to the extremely high temperature of the oven. To keep the heat conduction from the oven as low as possible, the oven is mounted to the housing using screws as shown in figure 3.15, thereby reducing the contact surface area. Additionally, heat shields are inserted between the oven and the water-cooled copper housing to reflect the heat transferred by radiation back to the oven. Lithium vapours come out through a nozzle of diameter 1.5 mm. They are emitted outside of the oven in a cone. A copper

aperture, A1 at a distance of 2.5 cm facilitates the initial collimation of the beam. It is collimated further by a second copper aperture A2. This is connected to a copper assembly as shown in the figure to a cryogenic cold head that can be cooled down to a temperature of 105 K. The passage of the lithium beam into the spectrometer and to the interaction region is made possible using a hole of 1 cm on the spectrometer ring (figure 3.15). Hot lithium vapours exiting out of the spectrometer through a bigger hole of 2.5 cm are trapped on the cold copper rod fixed to a cryogenic cold head. This prevents the ReMi and the chamber walls from getting contaminated by the lithium vapours. The entire cold head and the copper rod assembly are mounted on a manipulator which enables slight adjustments.

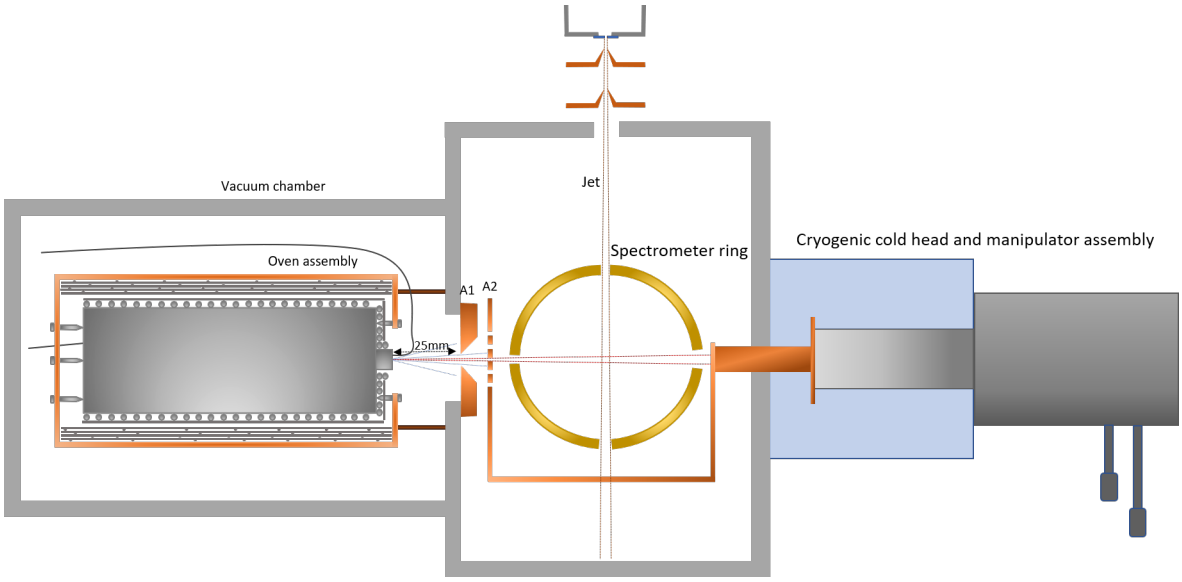

Figure 3.15: Schematic of the oven assembly.

Estimation of the target density

The target density at the interaction region can be estimated by knowing the geometry of the oven assembly. The vapour pressure of alkali metals is given by the formula,

$$log(p_v) = A + BT^{-1} + Clog(T) + DT \times 10^{-3} \tag{3.3}$$

where p_v is atm and T in K.

For lithium A $= 8.409$, B $= -8320$, C $= -1.0255$ and D $= 0$ [138]. At 973K, (700°C) vapour pressure of lithium is 0.630279 mbar.
Using the ideal gas law for a Maxwell-Boltzmann distributed atomic vapour, the number density of atoms (n_0) follows as

$$n_0 = \frac{p_v}{k_B T} = 4.69177 \times 10^{21} \text{ atoms/m}^3 \tag{3.4}$$

The total flux of atoms per second per unit area evaporated from a sample of lithium inside the oven is given by,

$$\Phi = \frac{1}{4} n_0 \overline{v} \tag{3.5}$$

where the average thermal velocity $\overline{v} = \sqrt{\frac{8k_BT}{(\pi m)}}$ is 1710.23 m/s at $T = 973$ K. The number of atoms per second leaving the oven through an opening with an aperture of

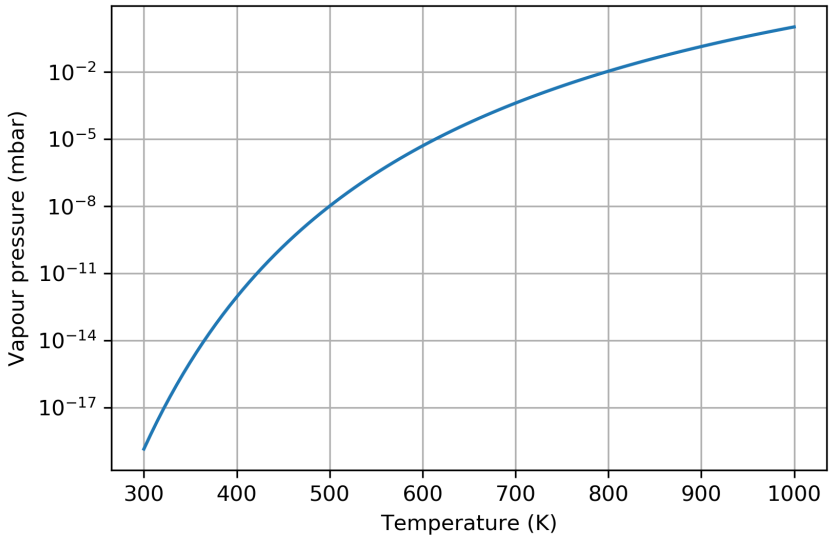

Figure 3.16: Vapour pressure of lithium calculated with equation (3.3)

radius $r = 0.75$ mm and area of $A_s = \pi r^2$ =1.767 mm^2 is,

$$\dot{N} = \Phi A_s = \frac{1}{4} n_0 \overline{v} A_s \tag{3.6}$$

The type of flow depends on the mean free path of the atoms given by,

$$\lambda_A = \frac{1}{\sqrt{2}\sigma_c n_0} \tag{3.7}$$

For a temperature of 973 K and collisional cross-section σ_c for lithium given by, $\sigma_c = 7.6 \times 10^{-16}$ cm^2 [139], λ_A can be estimated to be 1.98 mm. For $2r \sim \lambda_A$ free molecular is flow satisfied [140]. Therefore, equation (3.6) can be modified as,

$$\dot{N} = \Phi A_s = \frac{1}{4} n_0 \overline{v} A_s W \tag{3.8}$$

where $W = 1/K$, K is called the Knudsen parameter [140]. For a cylindrical channel of length L and inner radius r, W is given as [140],

$$W = \frac{8r}{3L}(1 + \frac{8r}{3L})^{-1} \tag{3.9}$$

For $L \gg r$,

$$W = \frac{8r}{3L} = \frac{4}{3}\beta \tag{3.10}$$

where $\beta = \frac{2r}{L}$. In our oven with $r = 0.75$ mm and $L = 1.95$ cm (length of the nozzle), $\dot{N} = 3.643 \times 10^{17}$atoms/sec.
The number of atoms per second going out of the oven within a solid angle of $d\Omega$ and opening angle of ϑ is given by [140],

$$d\dot{N}_0 = W \left(\frac{d\Omega}{4\pi}\right) n_0 \overline{v} A_s cos\vartheta \tag{3.11}$$

To estimate the total number of atoms emitted in the direction of the interaction region, the above equation has to be integrated to an angle θ subtended by the collimation apertures

$$\dot{N}_0 = \int_0^{\vartheta=\theta} A_s d\Phi_0 = \frac{1}{4} n_0 \overline{v} A_s W sin^2\theta \tag{3.12}$$

From the known dimensions of the oven assembly, θ can be estimated as $3.47°$. Therefore, the total number of atoms emitted into the angle $\theta = 3.47^0$ is 1.33×10^{15} atoms/sec.

The diameter of the beam at the interaction region can be calculated as [140],

$$2d = w_c + (w_c + w_s)\left(\frac{l_{sd}}{l_{sc}} - 1\right) \tag{3.13}$$

where 2d is the diameter of the beam at the interaction region, w_c is the width of the collimator, w_s is the width of the source slit, l_{sd} is the distance from the source to the interaction region, l_{sc} is the distance from the source to the collimator. The width of the beam at the interaction region is estimated to be 8.36 mm. Therefore, the target density at the interaction region can be estimated to $\sim 1.417 \times 10^{10}$ atoms/cm^3.

3.4 Data acquisition

In the present work, two or more particles emerging from the reaction are detected in coincidence. Each event is referenced with respect to the time of emission of the UV laser pulse which creates the electron bunch for the ionization. An electronic pulse is derived from the laser at the time of emission of the laser pulse. This laser trigger pulse and the signals from the detectors constitute the data set for an event. The data acquisition system consists of electronics for time-to-digital conversion of the signals and the VME bus system which controls the data flow. Additionally, logic gates are implemented to facilitate the selection of events corresponding to the coincidence hits.

Altogether we need to process 15 time signals: a laser pulse time signal and 14 time signals from both detectors, (one ion MCP signal, 6 ion delay line signals, one electron MCP signal, and 6 electron delay line signals). These signals are converted to NIM signals using the ORTEC MODEL 935 constant fraction discriminator (CFD) and sent to the time-to-digital converters (TDC). A CFD converts the analog time signals from the detector which are typically Gaussian signals to NIM signals when the input pulse has risen to 20% of its pulse amplitude if properly adjusted. The details about the working principle of the CFDs can be found in the literature [141]. We use a 16-channel Caen V1290 N multihit-TDC which has a time resolution of 100 ps and can record multiple hits with a dead time of 5 ns [142]. The TDCs are controlled by the VME bus system. Although the maximum measurement range for the TDCs is 52 μs, the present range is limited by the repetition rate of the laser which allows a range of 25 μs. The stored data represent absolute time measurements (where time 0 refers to the latest reset of the TDCs). All the 'true' times with respect to the laser pulse are obtained by subtracting the time of the TDC signals with the TDC signal corresponding to the laser pulse. The TDCs work in *trigger matching mode*, which means that the times of the signals stored in the TDC buffer are read out to a common read-out FIFO when a trigger signal is detected (figure 3.17). A trigger signal could be any signal, for example, a NIM pulse corresponding to an ion MCP hit.

For the measurements that are discussed in the thesis, mainly two types of coincidence triggers are used, namely electron-ion coincidence trigger and electron-2ion coincidence

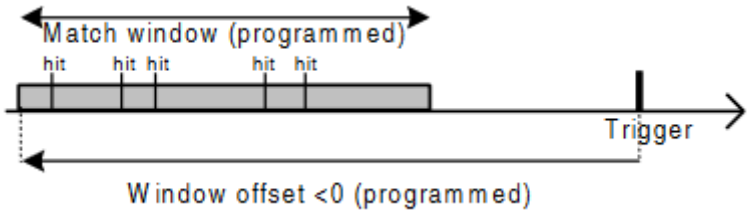

Figure 3.17: Timing diagram describing the trigger matching mode. Image adapted from [142]

trigger. That means we do not record every event registered by the detectors. We record only events where the particles of interest for the study are detected in coincidence. This is done by implementing hardware electronic gates which inhibit CFDs from producing the outputs in the time window where we do not expect real hits. The following sections describe the implementation of these coincidence trigger signals using logic gates and delay generators.

Electron - Ion coincidence trigger

This trigger signal is used to start the data acquisition when an electron is detected in coincidence with an ion. Initially, a time window (340 ns) is generated using the laser pulse signal (A) as the input to a gate-and-delay generator, within which the electrons that are from the collisions are expected to arrive (Electron gate B). An AND gate is applied between this gate window and the electron MCP signal such that if an electron is detected within this gate B, another time window is generated where ions are supposed to be detected (Ion gate D). This is again applied to another AND gate along with the ion MCP signal (E). If an ion is detected within this second time window (gate D) a NIM pulse is generated which indicates an electron-ion coincidence. The output of this AND gate (Ion hit E AND Ion gate D) is applied to the VME trigger input and the data acquisition is triggered to be read out. Therefore, an event is read out when an electron is detected in coincidence with the ion. Figure 3.18 shows the timing diagram which illustrates the electron-ion trigger.

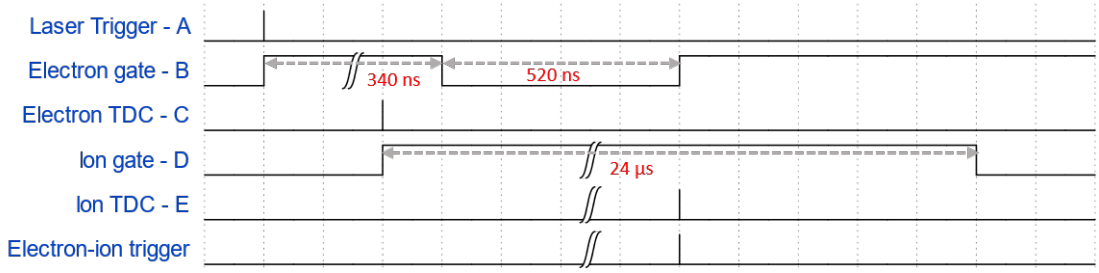

Figure 3.18: Timing diagram for the electron-ion coincidence trigger signal. The final trigger for the data acquisition is the ion signal in coincidence with an electron signal.

The first time window for the electrons includes the region where both the scattered and ejected electrons are supposed to be detected. Therefore some events that are read out contain more than one electron, but only one ion. This trigger is used for (e,2e+ion) measurements.

Electron - Ion - Ion coincidence trigger

This trigger is used for measurements in which two ions need to be detected in coincidence with the electrons. Here in addition to the above-mentioned electron-ion coincidence trigger output another AND gate is also used (figure 3.19). One of the input signals to the additional AND gate is a delayed laser pulse (delayed laser trigger G). The laser pulse is delayed by the maximum time window within which the second ion is supposed to be detected. Here we delay it by 25 μs which the almost the maximum possible measurement time.

The second input of the AND gate is derived from the output of the electron-ion coincidence trigger, which is the ion MCP signal in coincidence with an electron MCP signal (electron-ion coincidence gate). A time window is generated from this signal which is slightly smaller than the delayed laser pulse and used as the second input of the AND gate (Ion-Ion gate H). Therefore, a trigger output is generated at $\sim$ 25 μs, ie. the time of the delayed laser pulse when a first ion signal is detected. The subsequent ion signals if any (ion hit 2, ion hit 3, etc), will be stored in the buffer until the trigger signal is sent at $\sim$ 25 μs. At the time of the delayed laser pulse, all the successive ion hits from the first ion hit stored during the ion time window (H) are read out from TDC buffer. This allows

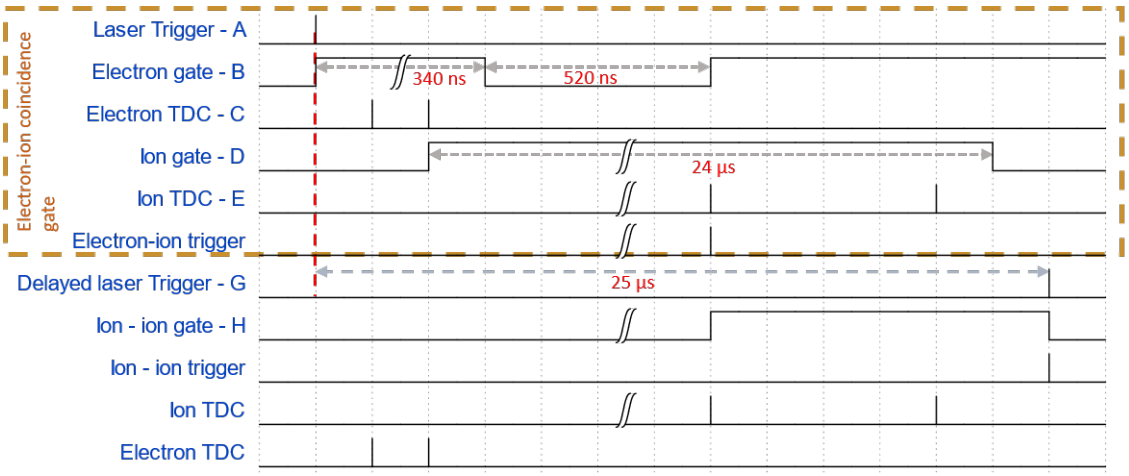

(a)

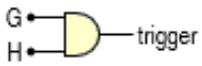

(b)

Figure 3.19: (a) Same as 3.18 but for electron-ion-ion coincidence measurement. The trigger signal is the delayed laser pulse when an ion and electron are detected in coincidence. Since the data acquisition operates in trigger matching mode 3.17 all the ion and electron hits after the first electron-ion coincidence hit are read out. (b) Block diagram for the electron-ion-ion coincidence trigger.

us to perform electron-ion-ion coincidence measurements.

In our experiment, the VME (front-end pc) forms a private network with the experimental PC. When the VME bus system is triggered by any of the triggers mentioned above, the data from the TDC buffer is sent to a experimental PC equipped with a raid system via an MBS stream server. The MBS stream server is a software that controls the data acquisition and writes the data into a *list mode file*. The online monitoring of the data

is enabled using the *go4* user interface. The MBS stream server directly streams the data to the *go4* analysis software.

Chapter 4

Data analysis

The raw data stored in the experimental computer consists of a total fourteen time signals from both detectors and the laser pulse time signal. In order to extract the physics from this data, we need to convert these time signals into the momentum of each reaction fragment. This chapter describes in detail, how these data are reconstructed into the momenta and how the cross-sections are extracted. By reconstructing the momenta of all the reaction fragments, the complete kinematics of the collision can be obtained. Furthermore, the calibration procedure for the experimental data and the resolution and acceptance of both detectors are discussed in detail.

4.1 Data readout and analysis

Conventional electron spectroscopy methods involve scanning the position of an electrostatic electron spectrometer to various angles and particle energies to measure count rates, and then calculating the triple differential cross-sections (TDCS) proportional to the count rates. In contrast, the ReMi does not directly measure the particle energies and scattering angles. Instead, ReMi involves projecting particles onto detectors to reconstruct the momentum of the fragments. The processing of the data is done by an analysis program. The requirements of the analysis program are many. First of all, it should facilitate easy integration of the data acquisition system such that, online monitoring of the time and position of the hit is possible. The calculation of the momenta of the particles and the selection of coincidences must be automatically done.

Our analysis code is mainly based on the two frameworks. The ROOT framework, developed by CERN, and the *go4* Analysis framework developed by GSI. ROOT framework is a set of C++ libraries that can be used for big data visualization, manipulation, and analysis. *Go4* inherits the classes of the ROOT and provides a graphical user interface (GUI) for online monitoring and offline analysis. It allows multi-step processing of the experimental data. For the analysis of the experimental data obtained from the reaction microscopes, a complete analysis code, 'GENERiC', is developed which can be used to analyse the data from a multitude of experiments [136].

A basic outline of the analysis is shown in figure 4.1. The complete analysis is divided into three steps, namely Unpack, Calc, and FDCS. The processing of the raw data to the time and position signals is done in the Unpack step. Additionally, filtering of signals which corresponds to real hits, reconstruction of missing MCP and delay-line signals, and selection of events with valid coincidences are also done in this step. The input of the step can be the data directly from the MBS stream server or the saved list mode files. The output of the step is the time and position signals corresponding to the valid

coincidences. They can be either directly send to the next step or can be saved as root files. The latter is particularly useful if a huge number of data files has to be processed. In the Calc step that comes next, we do the calculation of the momenta and energies of the particles. The input to this step is the output events directly from the Unpack step, which satisfy the required coincidence condition, or the root files saved after the Unpack step. The processing of data up to this point is identical for all the measurements with the reaction microscope. Therefore, the GENERiC code can be used as a starting step for most of these measurements. Experiment-specific calculations like energies of the particles, double differential cross-sections, etc. are also calculated in this step. The output of the Calc step goes to the third step: FDCS as input or can be saved as root files similar to the Unpack output. Here, as the name suggests, fully differential cross-sections are calculated for different ejected electron energies and scattering angles. Additionally, molecular alignments can also be determined in this step. The FDCS step takes output events from the Calc step or the save root files after the Calc step as input and the output of this step is the final result of the analysis. The analysis could also be expanded further into more steps according to the necessity.

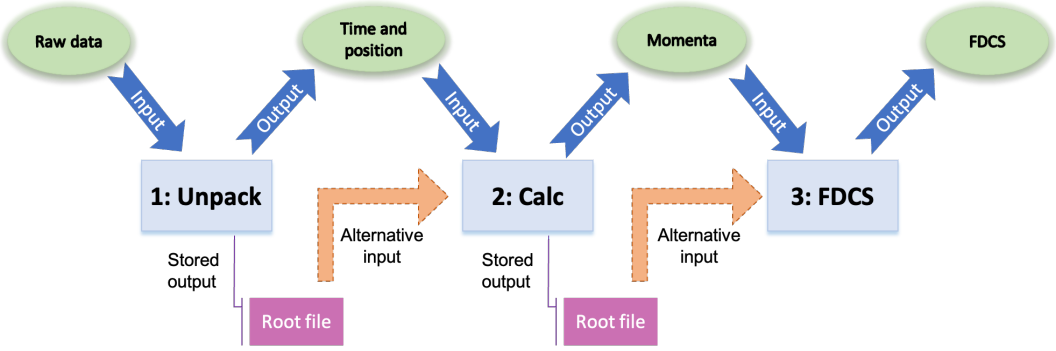

Figure 4.1: Diagram showing the analysis steps, input, and outputs of each step.

Another advantage of using *Go4* is the parameter classes. One can define parameter classes in each step, whose objects can be used as variables that can be used for calibration of the experimental data. Another important feature is the possibility of defining conditions in the histograms. For example, a condition in the time-of-flight window allows the selection of time-of-flight regions interactively within the GUI, such that only events which satisfy the set time-of-flight window is considered are valid events. A detailed explanation for each step is given in the following sections. Additionally, there is a possibility to save either all the TDC events or the outputs of each step to an ASCII file.

4.2 Unpack step: Time and position information

The first part of the analysis code is processing the time signals from the TDCs. This includes identifying the 'good' or 'bad' signal, reconstructing the missing signals, and calculating the real time and position of the particle hit. All the signals from the TDCs represent the absolute time signals referred to the latest reset of the TDC buffer. The first step of the analysis is to subtract each TDC signal corresponding to the detector time signals from the TDC signal corresponding to the laser pulse time signal. Therefore, we get signals that are referred to the laser pulse time. The time-of-flight of the particles are obtained by subtracting the TDC time signals corresponding to the MCPs from the TDC signal corresponding to the laser pulse. The time-of-flight thus obtained does not corre-

spond to the true time-of-flight of the particle it also includes the time that the laser pulse takes to hit the photocathode and the time that the projectile electrons take to travel from the photocathode to the interaction region. This extra time which is in the nanosecond range is not important for the ions whose time-of-flight are typically in the microsecond range, but for electrons, it is crucial to precisely calculate this value. This time, which specifies the time of birth of particles relative to the laser trigger, is identified in the second part of the analysis.

4.2.1 Identification and reconstruction of signals

Each real MCP hit on a detector should have corresponding signals from the hexanode of the same detector. A 'good' or 'bad' signal can be identified by looking at the so-called 'time-sum' of a hit which is given by,

$$t_{sum} = t_1 + t_2 - 2t_{mcp} \tag{4.1}$$

where t_1, and t_2 are time signals from the two ends of a delay line and t_{mcp} is the MCP signal. $(t_1 - t_{mcp}) + (t_2 - t_{mcp})$ gives the time taken for a signal to travel across a delay line and it will be constant for all signals irrespective of the hit position on the detector. Therefore, selecting events having the same t_{sum} can serve as a way to filter out 'good' signals from the 'bad' signals. Besides that, one can calculate any missing signals, if the other two in the equation 4.1 are available. A detailed description of the origin of the loss of signals and the reconstruction routines are described in the previous theses ([136],[44]).

4.2.2 Position calculation

In order to reconstruct the position coordinate on the detector, an event should have signals from at least two delay lines. For delay line anode, the position can be reconstructed using the equations 3.1. With a hexanode, one can calculate the position from any three pairs of wires (u, v),(u, w), and (v, w).

$$\begin{aligned} x_{uv} &= u \\ y_{uv} &= \frac{1}{\sqrt{3}}(u - 2v) \\ x_{uw} &= u \\ y_{uw} &= -\frac{1}{\sqrt{3}}(u + 2w) \\ x_{vw} &= (v - w) \\ y_{vw} &= -\frac{1}{\sqrt{3}}(v + w) \end{aligned} \tag{4.2}$$

u, v, and w are coordinates of the hit on three different layers. They are calculated from the equation 3.1.

Position calculation from the equations 4.2 assumes that the centre of the three layers is the same and the time sum for the three layers is the same. In reality, these vary due to the imperfect alignment of the three layers or the different resistance of the wires. In order to compensate for these differences, four parameters are introduced in the position calculation $ScaleU$, $ScaleV$, $ScaleW$, and $ShiftW$. The first three take care of the difference in the time sum and the last one takes care of the shift from the origin according

to the following equation.

$$\begin{aligned} u &= ScaleU(t_{u1} - t_{u2}) \\ v &= ScaleV(t_{v1} - t_{v2}) \\ w &= ScaleW(t_{w1} - t_{w2}) - ShiftW \end{aligned} \tag{4.3}$$

The optimum values for the scale factors and shift parameter are obtained using an iterative routine implemented within *Go4* and is documented in [143]. For each event, the routine iteratively goes through a set of scale factors for v and w keeping $ScaleU$ as 1, thereby scaling the layers v and w to u. It generates an optimum value for the scale factors such that the best overlap between the layers is obtained. $ScaleV$ and $ScaleW$ are plotted on a 2D histogram as shown in the figure 4.2 and the mean value of the histogram gives the optimum scale factors. The parameter $ShiftW$ has to be obtained by manual

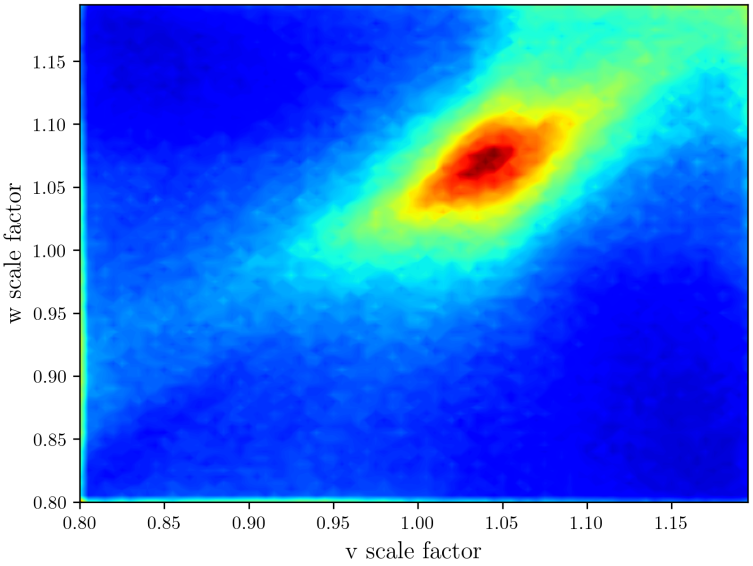

Figure 4.2: Histogram showing the optimized scale factors for v and w delay line calculated using the Resort routine[143]. The maximum of the histogram gives the optimum value for the scale factors $ScaleV$ and $ScaleW$.

iteration. Thus, the iteration process is simplified reducing a lot of manual work and time. The final reconstructed position images for ions and electrons are shown in figure 4.3. The central region on the position image shows the presence of the hole on the MCP stack of the electron detector (figure 4.3a). The elongated region on the ion position image is due to the presence of the electron gun and the corresponding mounting rods (figure 4.3b). The ions emitted towards the electron gun assembly are scattered on it and lost, casting a shadow on the ion detector image.

The shape of the trajectory of the particle depends on its mass. Since the particle is moving in a magnetic field, it undergoes cyclotron motion with a cyclotron period T_c given by,

$$T_c = \frac{2\pi m}{Bq} \tag{4.4}$$

For ions, whose mass is higher compared to electrons, the cyclotron period is in the range of hundreds of microseconds, while their times-of-flight are typically less than 25 mi-

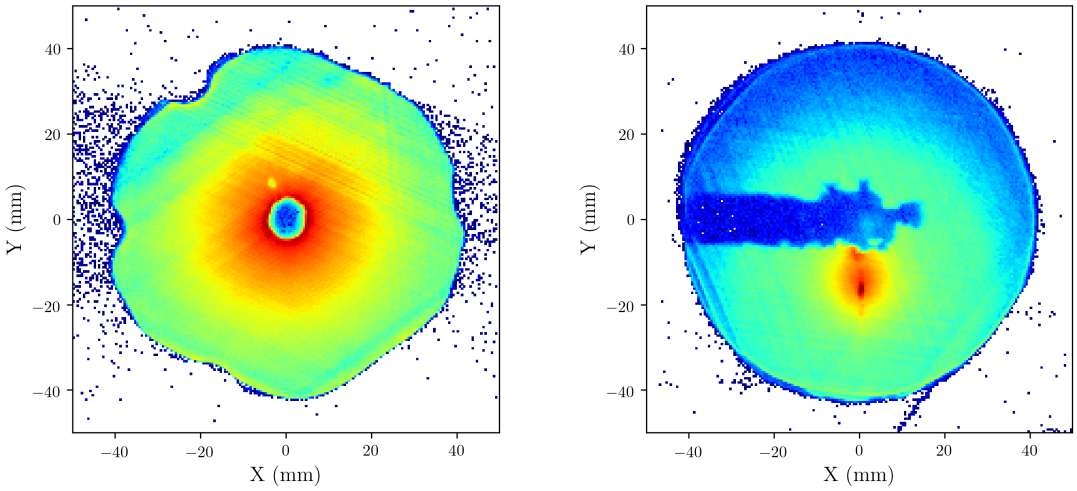

(a) Electron detector image

(b) Ion detector image

Figure 4.3: Position distribution of ions and electrons

croseconds for the electric field used in this work. Therefore, their trajectory follows a half parabola as shown in the figure 3.1. However, for electrons that take part in the collision, whose cyclotron frequency is around a few tens of nanoseconds, follow a helical trajectory (figure 3.1), due to their non-zero transversal momentum. They come back to the spectrometer axis after each cyclotron revolution. Such a helical motion produces a so-called 'wiggle' structure in the radius vs time-of-flight plot as shown in the figure 4.4.

If the time-of-flight corresponding to the momentum of the particle is equal to the integer multiple of the cyclotron period, they fall into the hole, and therefore, we get a node at this time-of-flight. Identification of the node position helps to calibrate the magnetic field and time-of-birth of electrons. Such a calibration procedure will be explained in detail in the next section. It should be noted that the unscattered projectiles and ejected electrons with zero energy ideally do not deviate transversely and falls to the hole.

Ions with near zero momentum, who follow a parabolic trajectory make a blob on the position image. The position of the blob depends on the velocity of the molecule in the jet and also on the mass of the ion. Fragments with heavier mass hit farther away from the centre of the detector. The velocity of the molecule in the jet can be calculated if the y position and the time-of-flight of the fragments from the same molecule are known,

$$v_{jet} = -\frac{y_{frag1} - y_{frag2}}{t_{frag1} - t_{frag2}} \tag{4.5}$$

Derivation of the above-mentioned formula is available in a previous thesis [136]. The figure 4.5 below shows the y position versus time-of-flight of different fragments of thiophene.

If the time-of-flight and position information is available for a particle, it is identified as a valid hit. Each event that contains hits that satisfy the coincidence condition is considered a valid event and sent to the next step of the analysis. Coincidence conditions can be defined depending on the type of reaction channel that we are interested in. For example, for single ionization of helium, two electrons that are coincidentally detected with a helium ion constitute a valid event. Thus we detect all the particles corresponding to a collision channel and therefore, the complete kinematic information is obtained. For double ionization and the Coulomb explosion of the dimer, we detect two ions and

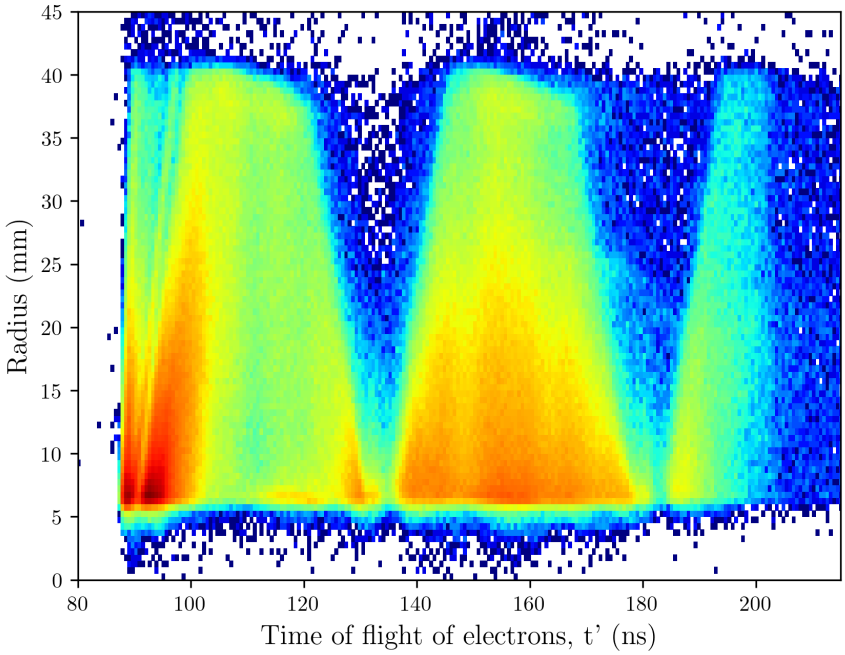

Figure 4.4: Radial distribution of the electrons as a function of its time-of-flight.

one electron. Events that contain two ions in the expected time-of-flight of the Coulomb explosion fragments and an electron hit are considered valid and sent to the next step.

4.3 Calc step: Momentum calculation

In this step, the momentum of the particles corresponding to each valid event from the Unpack step is calculated. Since the magnetic field and the electric field is aligned along the spectrometer axis, the total momentum can be separated into longitudinal and transversal components and can be calculated independently.

$$|p| = \sqrt{p_z + p_\perp} \tag{4.6}$$

Longitudinal momentum, which is a function of the time-of-flight of the particle, is dependent on the electric field, the dimensions of the spectrometer, and the charge and mass of the particle. Whereas the transversal momentum, which is a function of (x, y) coordinates of the hit position on the detector is dependent on the magnetic field and not on the electric field. It is convenient to represent the momenta in the cylindrical coordinates due to the cylindrical symmetry of the spectrometer. The figure 4.6 shows the momentum of the particle in cylindrical coordinates and the momentum components along the longitudinal (z axis) and the transversal direction. A routine for the momentum reconstruction of all the particles is implemented in the previous work [136].

4.3.1 Longitudinal momentum

The motion of the charged particle along the spectrometer axis (z-axis) is determined by the electric field applied. The time-of-flight of the particle with mass m, charge q and

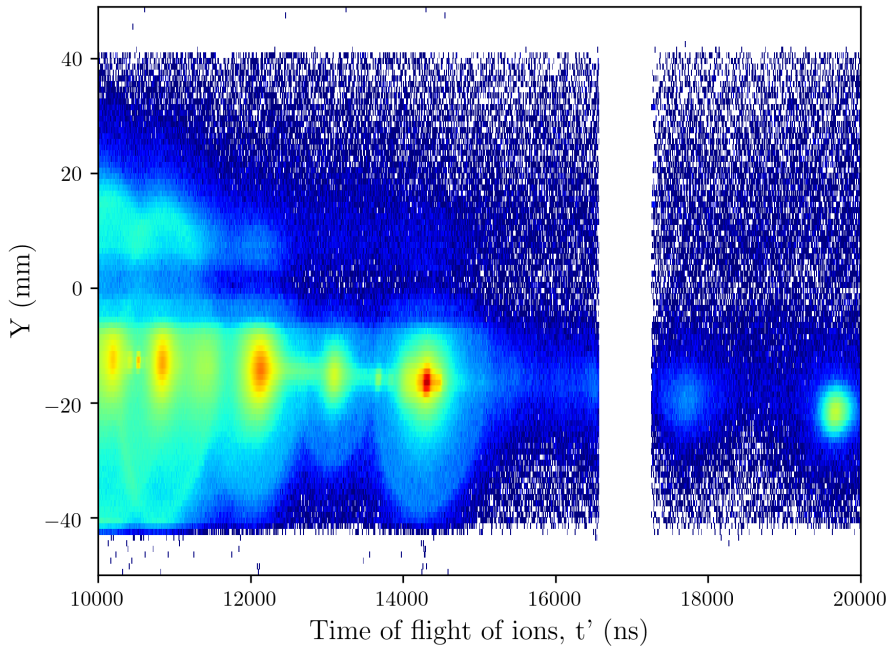

Figure 4.5: Y position of different fragment ions from thiophene as a function of the time-of-flight. Fragments with higher mass hit farther away from the centre of the detector.

initial momentum p_z along the z-axis accelerated by a uniform field $\frac{U}{l_a}$ is given by,

$$t(p_z) = m.\left(\frac{2l_a}{\sqrt{p_z^2 + 2mqU} \pm p_z} + \frac{l_d}{\sqrt{p_z^2 + 2mqU}}\right) \tag{4.7}$$

where l_a is th acceleration length and l_d is the drift length. Equation (4.7) can be determined by Newton's equations of motion for charged particles in a uniform electric field ([144]). The equation can be split into two parts, the first part describes the motion of a particle with initial momentum p_z in an electric field $\frac{U}{l_a}$. The second part describes the drift motion of the particle through a region of length l_d. The longitudinal momentum p_z can be calculated from the equation 4.7 numerically since no analytical expression exists for p_z. p_z for each particle corresponding to an event is calculated using the Newton-Raphson method by finding the root of the equation $f(p_z) = t(p_z) - t$, where $t(p_z)$ is the right-hand side of the equation 4.7 and t is the measured time-of-flight of the particle of concern. The implementation of the method on the analysis program is given in the thesis [136]. p_z is varied from a given value until $f(p_z)$ is less than a minimum allowed error for p_z. The sign $\pm$ refers to the acceleration direction, ie. along the '$+z$' or '$-z$' direction along the spectrometer axis. In our experimental setup, we refer to the direction towards the electron detector as the '$+z$' direction. This method is applicable for the calculation of the momenta of both the electrons and ions.

4.3.2 Transversal momentum

The motion of the particle perpendicular to the direction of the spectrometer axis is governed by the magnetic field, B which makes the particle undergo cyclotron motion.

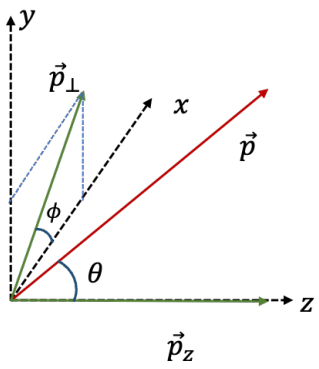

Figure 4.6: Momentum vector $\vec{p}$ and its components in the cylindrical coordinates

The cyclotron frequency, ω_c can be determined from the equation (4.4).

$$\omega_c = \frac{|q|\,B}{m} \tag{4.8}$$

T_c, the cyclotron period, and therefore, ω_c can be determined from the 'wiggle' structure in the radius vs time-of-flight plot as the distance between the two adjacent nodes corresponds to T_c. The transversal momentum $p_\perp = \sqrt{p_x^2 + p_y^2}$: can be is related to the cyclotron radius as,

$$p_\perp = \frac{2\pi m R_c}{T_c} \tag{4.9}$$

R_c is determined from the geometrical considerations from the figure 4.7 as,

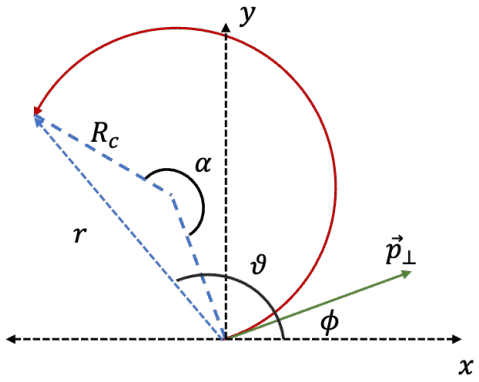

Figure 4.7: Electron's cyclotron motion projected on the detector plane.

$$R_c = \frac{r}{2\,|\sin(\alpha/2)|} \quad = \frac{r}{2\,|\sin(\omega_c t/2)|} \tag{4.10}$$

where $\alpha = \omega_c t$ which is the total angle that the particle passed and can be related to the measured time-of-flight. Therefore, using equation (4.9), the transversal momentum is described as,

$$p_\perp = \frac{\pi m r}{T_c\,|\sin(\omega_c t/2)|} \quad = \frac{\omega_c m r}{2\,|\sin(\omega_c t/2)|} \tag{4.11}$$

Individual components p_x and p_y are further calculated from the azimuthal angle, ϕ. It is also determined from the geometrical consideration from the figure 4.7.

$$\phi = \vartheta \pm \frac{\omega_c t \bmod 2\pi}{2} \tag{4.12}$$

Here $\omega_c t \bmod 2\pi$ gives the number of rotations the electron takes until it reaches the detector. The second term is positive for the electrons which move clockwise since the magnetic field is parallel to the electric field direction and negative for ions which move anti-clockwise direction in the fields. For heavier ions, transversal momentum can be determined by applying l'Hôpital's rule,

$$\lim_{\omega_c \to 0} p_\perp = \frac{mr}{t} \tag{4.13}$$

Kinetic energy release

Ions that originate from a dissociation channel or Coulomb explosion channel gain momentum while dissociating through a repulsive potential energy curve or by Coulomb explosion between the two charge centres respectively.

$$\begin{aligned} AB + e^- &\rightarrow A^+ + B + 2e^- \qquad \text{Dissociation} \\ AB + e^- &\rightarrow A^+ + B^+ + 3e^- \qquad \text{Coulomb explosion} \end{aligned} \tag{4.14}$$

In such cases the total momenta of the ion contains two contributions, one from the recoil after the emission of ionized electrons and the second from the dissociation or Coulomb explosion.

$$\begin{aligned} \vec{p}_{ion} &= \vec{p}_{recoil} + \vec{p}_{diss} \qquad \text{Dissociation} \\ \vec{p}_{ion} &= \vec{p}_{recoil} + \vec{p}_{Coulomb} \qquad \text{Coulomb explosion} \end{aligned} \tag{4.15}$$

If $\vec{p}_{diss}, \vec{p}_{Coulomb} \gg \vec{p}_{recoil}, \vec{p}_{recoil}$ can be neglected. Usually for Coulomb explosion channels, this is the case.

For a dissociation channel, if $\vec{p}_{recoil}$ is comparable to $\vec{p}_{diss}$, momentum of ion is given by,

$$\vec{p}_{ion} = \vec{p}_{diss} + \frac{m_{A^+}}{m_{AB}}(\vec{q} - \vec{p}_{e2}) \tag{4.16}$$

where $(\vec{q} - \vec{p}_{e2})$ is the fraction of momentum transfer to the ionic system. Therefore, the kinetic energy of the ion becomes,

$$KE_{ion} = \frac{\vec{p}^2_{ion}}{2m_{ion}} \tag{4.17}$$

The total kinetic energy release (KER) from the collision can be calculated as,

$$KER = \frac{\vec{p}^2_{ion}}{2}\{\frac{m_{A^+} + m_{B^+}}{m_{A^+} \cdot m_{B^+}}\} \tag{4.18}$$

4.4 FDCS step: FDCS calculation

In the final part of the analysis, fully differential cross-sections (FDCS) are obtained. For (e,2e) analysis, FDCS is expressed as a function of three variables and is called triple differential cross-section (3DCS). In the present work, 3DCS is expressed as,

$$\frac{d^3\sigma}{d\Omega_{e1} d\Omega_{e1} dE_2} \tag{4.19}$$

which is presented as normalized counts in a small interval of solid angles $d\Omega_{e1,2} = \sin\theta_{1,2} d\theta_{1,2} d\phi_{1,2}$ and a small energy interval of dE_2: $\Omega_{e1,2}$ are the solid angles of the

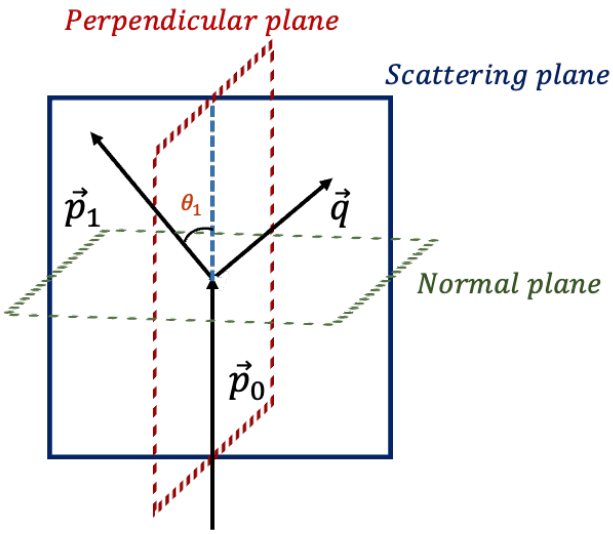

Figure 4.8: Schematic of the collision geometry for the (e,2e) experiments. Angular distributions of electrons in the scattering, perpendicular, and all perpendicular planes are studied. θ_1 indicates the scattering angle. For more details refer to the text.

outgoing electrons and E_2 is the energy of the ejected electron. To specify the solid angles $d\Omega_{e1,2}$ corresponding to each event, we have to define a scattering geometry. For each event, one can define three planes *scattering plane*, *perpendicular plane* and *normal plane or all perpendicular plane* as shown in the figure 4.8. The plane in which the incoming and scattered projectile momentum vector lies is called the scattering plane. Another vector $\vec{q}$, which is the momentum transferred from the incoming projectile to the system can be defined as $\vec{q} = \vec{p}_0 - \vec{p}_1$ and it lies in the scattering plane. The plane which is perpendicular to the scattering plane and containing the $\vec{p}_0$ is the perpendicular plane. The plane perpendicular to both the scattering plane and the perpendicular plane is the normal plane or all perpendicular plane.

Since the emission is isotropic with respect to the azimuthal angle ϕ, ie. the scattered projectile is randomly oriented around the incoming projectile direction for different events, each event has to be transformed from the laboratory frame to the a frame defined by the projectile scattering plane which is given by the projectile incoming, $\vec{p}_0$ and outgoing momenta, $\vec{p}_1$. This is done by rotating each vector corresponding to an event by the azimuthal angle of $\vec{q}$, the momentum transfer vector. After such a transformation the azimuthal angle of $\vec{p}_1$ of all the events becomes $180°$. Two-dimensional TDCS are obtained by cutting through the 3D angular distributions of ejected electrons in various plane and a quantitative comparison between the experimental data including error bars and the theoretical predictions can be done.

The acceptance of the electron detector due to the central hole on the electron detector shows gaps in the 3D cross-sections. These gaps can be filled by doing multiple runs with the same target at different extraction fields without changing any other parameters. This method shifts the nodes in the electron time-of-flight to different positions, thereby filling the gaps. A detailed description of this method is given in the previous theses [136, 44, 137, 128]. For the (e,2) studies described in this thesis, such a filling of nodes is not done. Therefore, we do not have a complete 3D distribution of ejected electrons.

4.5 Data calibration

For the precise reconstruction of the momenta of the outgoing fragments, precise knowledge of the applied fields and the geometry of the spectrometer are required. Although the physical length of the spectrometer geometry could be measured precisely, the real spacial extension and the magnitude of the fields might be unknown and impossible to measure. In such cases, calibration methods are used to determine the fields. Additionally, corrections can be introduced to the calculated momenta in case of field inhomogeneities.

Calibration methods used in this analysis make use of the energy and momentum conservation laws. The physics of a well-known reaction channel can be used for this purpose. In most cases, helium is used as a calibration target and is measured simultaneously with all the targets studied in this work. Since the mass of the proton is 1836 times higher than that of the electrons, the energy carried by the ions will be negligible compared to the energy of the electrons. Electrons can be calibrated by using the energy conservation law since the total sum of the outgoing electrons energies is a constant. For (e,2e) studies, only the calibration of electrons is required, whereas, for studies involving the ions, we need to calibrate the ions as well. Since ions gain considerable momentum after the collision, the law of momentum conservation is used to calibrate the ions. After the calibration procedure, one will be able to determine the precise information of the spectrometer fields and use those values for the target species that is being studied. This section gives an overview of how such a calibration is done.

4.5.1 Electron momentum calibration

Electron momentum is calibrated by looking at the single ionization channel of helium. According to the energy conservation law, incoming projectile energy and the outgoing electron energies are related by,

$$E_0 = E_1 + E_2 + Q \tag{4.20}$$

where Q is the internal energy or the binding energy, which is the ionization potential of helium in this case. Therefore, $E_{sum} = E_1 + E_2 = \frac{p_{e1}^2 + p_{e2}^2}{2m_e}$ is a constant. The expected E_{sum} can be easily calculated from the equation (4.20). The calibration procedure involves optimizing the field and length parameters via iteration until the expected E_{sum} is obtained. It is convenient to look at the plot, $p_{z(ei)}$ vs E_{sum}, for such an optimization of parameters. An example of such a plot for optimized parameters is shown in the figure 4.9. It should show a vertical distribution at the expected E_{sum} value. Here we look at the single ionization channel of helium ionized with a projectile of energy $E_0 = 97$ eV. The first step is to find the correct magnetic field and the time of birth of the electron. The time of birth of the electron does not coincide with the time of the laser trigger due to the finite amount of time that the projectile electron takes to travel from the photocathode to the interaction region. Therefore, the real time-of-flight of the electron is $t = t' - shiftT$, where $shiftT$ is the time-of-birth of the electron and t' is the time-of-flight determined by subtracting the time signal from electron MCP and the laser trigger. In addition to the $p_{z(ei)}$ vs E_{sum} plot, figure 4.10 is also useful to determine B and $shiftT$. The x-axis shows t/T_c, which is the number of cyclotron cycles that the electron underwent. For the correct magnetic field and $shiftT$ values, the wiggles in the plot should fall on the integer numbers of the x-axis indicating the precise determination of the time of birth and the cyclotron period. False determination of the magnetic field and $shiftT$ make the distribution in the figure 4.9 diverge and tilt close to the wiggles. Incorrect calibration of the

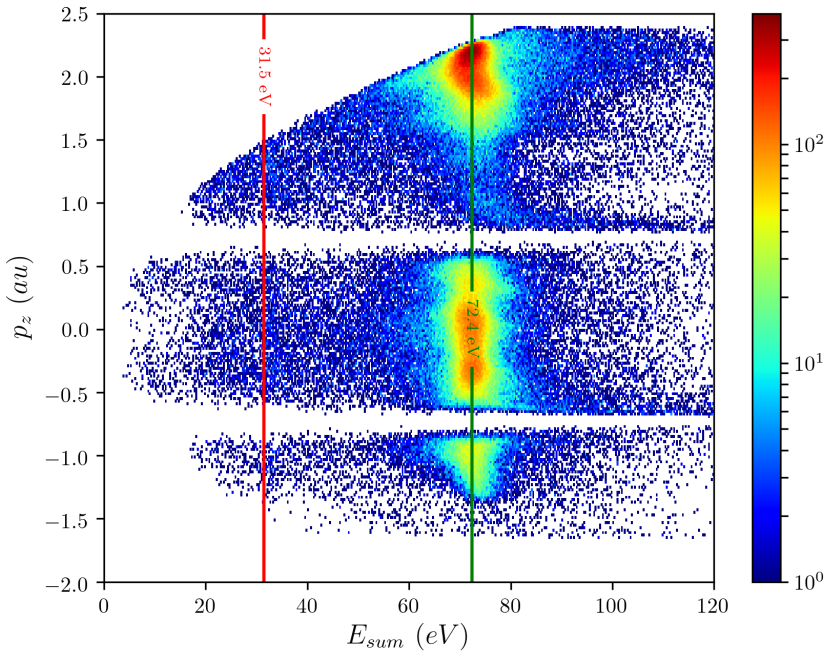

Figure 4.9: Longitudinal momentum p_z vs the sum of the energies of the outgoing electron pairs for the single ionization channel of helium. The green vertical line indicates the expected energy sum at 72.4 eV. The red line at 31.5 eV indicates events where the helium ion is excited to the n=2 state during ionization.

electric field makes the distribution tilt away from the vertical line in figure 4.9. This can be corrected by optimizing the acceleration voltage U, acceleration length a, drift length d, and the scaling parameter for the time-of-flight $scaleT$. A detailed description of the effect of these parameters in the figure 4.9 is discussed elsewhere [128, 137].

4.5.2 Ion momentum calibration

Ion information becomes important when the reaction channels such as dissociative ionization or Coulomb explosion are studied. It is also important for (e,2e) analysis if only one of the two final state electrons is detected. In such a case, information about the missing second electron can be calculated using the momentum conservation law, if the momentum information of the ion is available. For all the other cases the ion signal is used as a trigger to identify the events corresponding to the channel of concern (e.g. the charge state or the fragmentation channel). For the works described in this thesis the ion momentum information is important only for the studies on ICD.

For the ICD studies, we detect two ions and one electron in coincidence. Here, the two ions correspond to the Coulomb exploding fragments after the double ionization of the dimer and one of the outgoing electrons could be either a scattered projectile, an ejected electron, or the ICD electron. Applying the law of momentum conservation to the reaction channel,

$$\vec{p}_0 = \vec{p}_{ion1} + \vec{p}_{ion2} + \vec{p}_{e1} + \vec{p}_{e2} + \vec{p}_{e_{ICD}} \tag{4.21}$$

Since we have information about only one of the last three terms of equation (4.21), it cannot be used for the calibration in this case. However, the magnitude of momenta

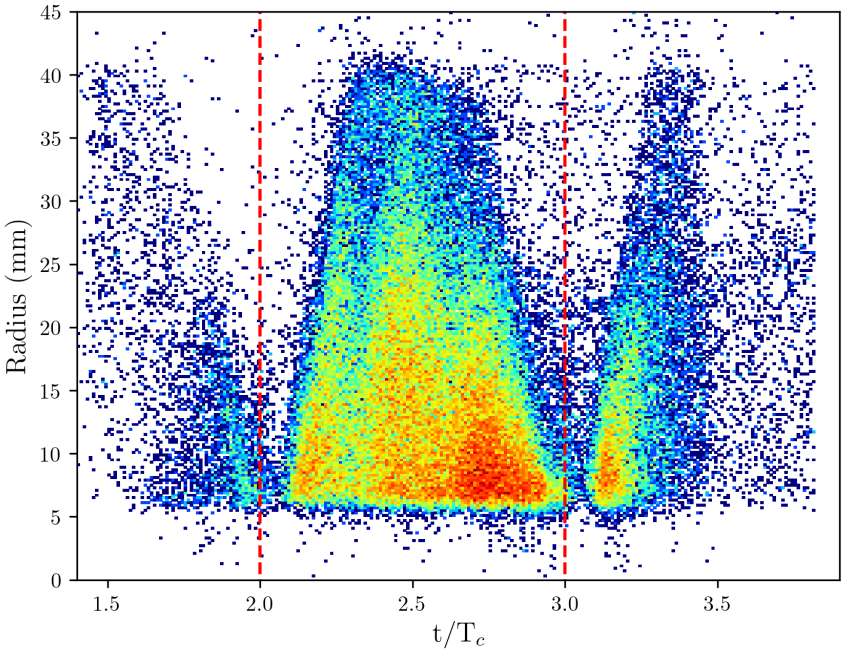

Figure 4.10: Ejected electron radial distribution versus the number of cycles the electrons underwent during the flight. The Red dashed line shows the nodal positions at the integer number of cycles indicating proper the magnetic field and the time of birth calibration.

gained by the ions 1 and 2 are very high (in the order of hundreds of au.) compared to the momenta of outgoing final state electrons and incoming projectile (typically less than 5 au.). Such a huge momentum gain is due to the Coulomb explosion of the ions. The momentum gain from the recoil is negligible in comparison to the momentum gain from the Coulomb explosion.

Therefore,

$$|\vec{p}_{ion1}| = |\vec{p}_{ion2}| = |\vec{p}_{Coulomb}| \tag{4.22}$$

Calibration of the ions for the Coulomb explosion channel becomes important due to two main reasons. One is to correct the field inhomogeneities caused due to the pulsed extraction field. The second reason is to separate Coulomb explosion events that stem from the double or multiple ionization of bigger clusters with $n > 2$.

Correction of time-of-flight

Since the electric field is ramped up with a definite time constant ($\sim$1 μs), not all the ionic fragments do experience the same field. Lighter fragments leave the acceleration region before the field gets ramped up to the maximum value. The field experienced by the fragments from the same Coulomb explosion but emitted to $+z$ and $-z$ direction will be different. Those ions that are emitted to $-z$ direction, ie. towards the ion detector, experience an average electric field that is smaller than the maximum value, whereas those that are emitted to $+z$ direction experience an average field closer or the same as that of the maximum of the pulsed extraction field. Therefore, both fragments reach the detector later than expected for constant field. The change from the expected time-of-flight Δt depends on the average field U_{mean}/a. This is manifested as a distortion in reconstructed Newton's sphere (the surface where the tip of all the momentum vectors lie). This is

clearly visible in the x/y vs tof plot 4.11 and therefore, in $p_{x/y}$ vs p_z momentum plot (not shown). This creates a 'banana-like' tilted line in the ion-ion time-of-flight coincidence

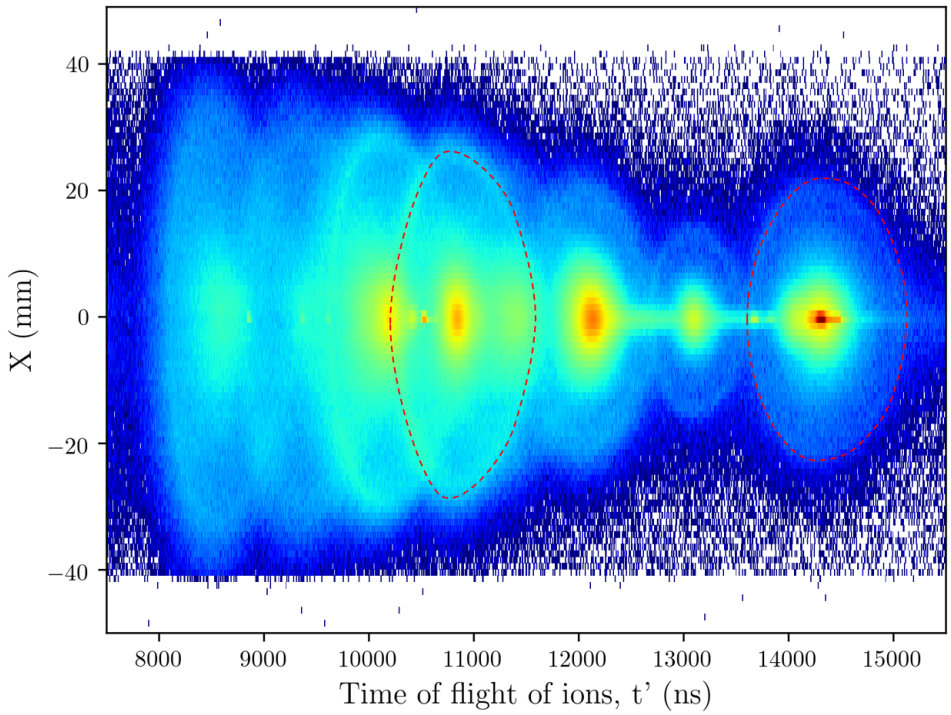

Figure 4.11: X position of ions on the detector versus the time-of-flight of fragments after ionization of thiophene. The dashed circles represent fragments from the Coulomb explosion. The deviation from a symmetric circle or an ellipse shows the distortion of Newton's sphere caused by the different average fields experienced by different fragments. The distortion is more for lighter fragments than that of the parent ions.

and the p_{z2} vs p_{z1} plot (Figure 4.12). For correcting the tilt, a correction to the time-of-flight was applied as given in the equation (4.23).

$$t_{corr} = t - C\frac{|t - t_{p_z=0}|}{|t_{p_z=0} - t_{p_z(min/max)}|} \tag{4.23}$$

where C is the correction factor and $t_{p_z(min/max)}$ is the time-of-flight corresponding to the fragments emitted to $\pm z$ direction with zero transversal momentum. The time-of-flight corresponding to the fragments with $p_z = 0$ is identified and correction is applied as a function of the difference of the time-of-flight from that of the events with $p_z = 0$. Figure 4.13 shows the corrected time-of-flight and momentum coincidence maps.

Filtering events from Coulomb explosions of dimers

Events that arrive at the detector within the region of time-of-flight where we expect the parent ions from Coulomb explosions, may stem also from other reaction channels. To obtain a clear ion-ion coincidence line as in figure 4.13, the fraction of events that stem from the Coulomb explosion (CE) of dimer should be higher than any other reaction channels. The origin of other events around the CE coincidence line could be the following. Firstly, the straight horizontal and vertical lines at the time-of-flight of the monomer

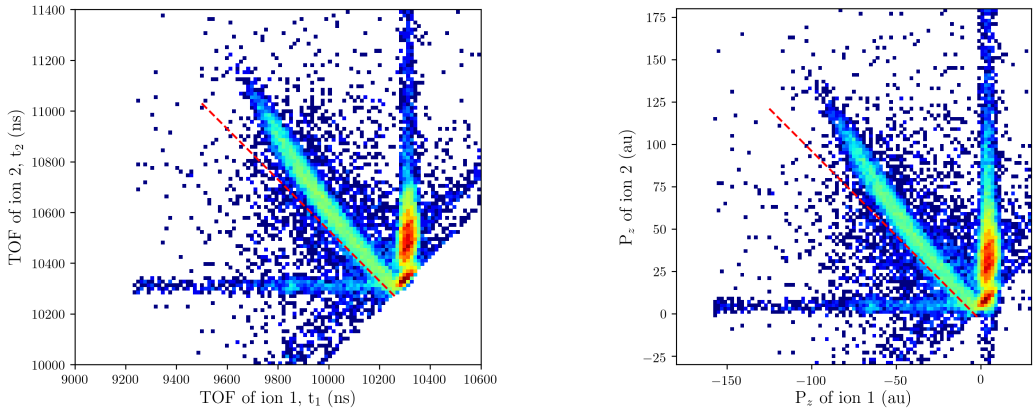

(a) (b)

Figure 4.12: The figure shows the time-of-flight and momentum coincidence maps for the Coulomb explosion of argon dimers. (a) Time-of-flight of ion 2 versus time-of-flight of ions 1. (b) Momentum of ion 2 versus momentum of ion 1. The coincidence line is expected to be along the red dashed line.

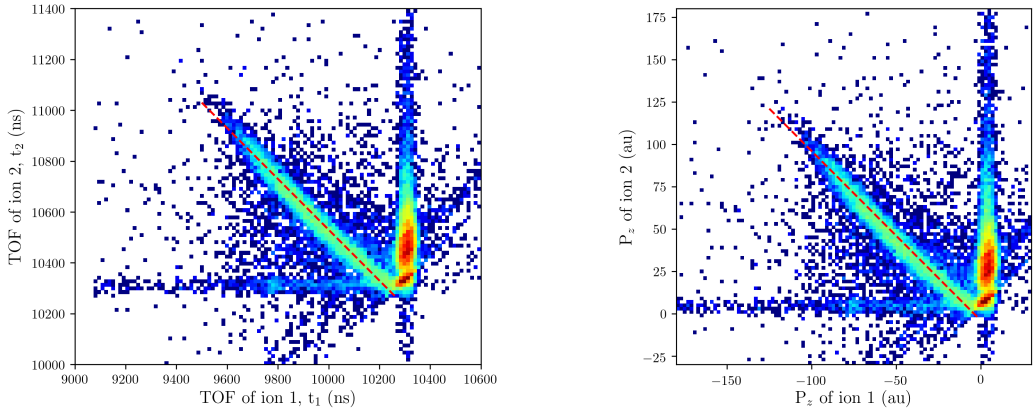

(a) (b)

Figure 4.13: Same as figure 4.12 but with corrected time-of-flight and momentum coincidences.

are due to the false coincidence between a monomer fragment and other ionic fragments. Secondly, the background around the ion-ion coincidence line could be from different reaction channels. For example, the CE of fragments from a bigger cluster into different fragments in which one is a parent ion.

$$Ar_n + e^- \rightarrow Ar^+ + Ar^+ + Ar_{n-2} + 3e^- \tag{4.24}$$

where $n > 2$. Production of clusters with $n > 2$ depends on the stagnation pressure and the diameter of the nozzle [145]. By varying the stagnation pressure one can find an optimum value at which the production of the dimer is higher than that of the bigger clusters thereby optimizing the desired coincidence signal.

However, in the case of bio-molecules in which hydrogen is an important element, reactions involving hydrogen loss or hydrogen gain also exist in addition to the CE channel of the dimers (4.24) [146]. In our experiment, these reaction channels are not resolved in the time-of-flight axis. All these reaction channels cause events around the coincidence line from the CE of the dimer, causing the background to be so strong. Thus, it is difficult to distinguish the dimer coincidence line.

In such a case, the law of conservation of momentum is used to separate the events from dimer coincidence. The sum of the momenta of ions from the Coulomb explosion of the dimer should be close to zero. Figure 4.14 renders quite useful in this case, which shows KER as a function of the sum of momenta of the ions. The events from the Coulomb explosion of dimer can thus be filtered out by selecting events with a small momentum sum.

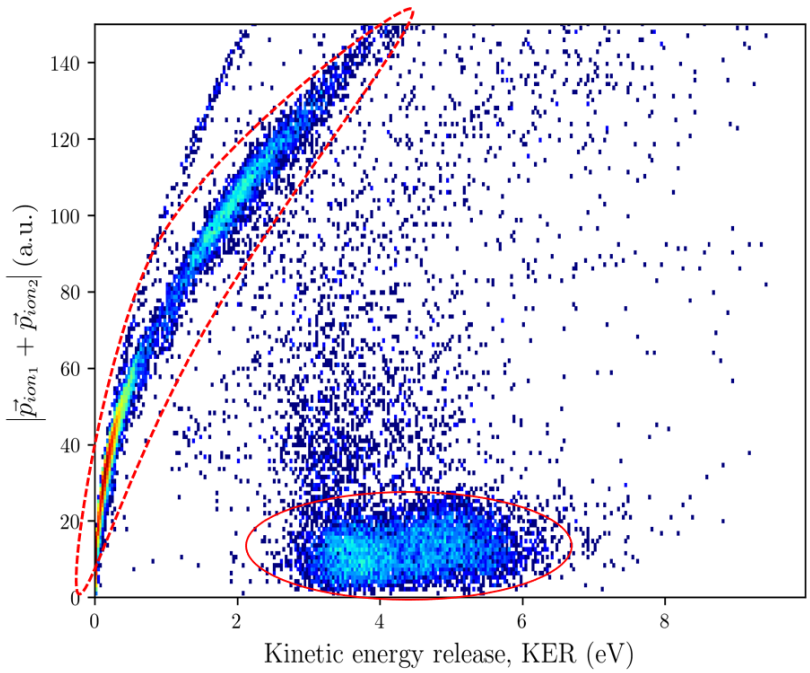

Figure 4.14: Sum momenta of ion versus Kinetic energy release, KER. Events that lie within the solid red curve stem from the Coulomb explosion of argon dimers. Those that lie within the dashed red curve come from the false coincidence of any ion having non-zero momentum with an argon monomer. The rest of the events comes from other reaction channels that are mentioned in the text.

4.6 Acceptance and resolution

This section describes in detail the energy and the momentum acceptance range of particles that can be detected by the ReMi and the energy and momentum resolution of the detected particles. Both acceptance and resolution depend on the mass and charge of the particle and the applied electric and magnetic fields.

4.6.1 Acceptance of electrons

The transversal and longitudinal acceptance of the electrons depends on the geometry of the spectrometer, the detector diameter, and the applied field. The minimum and maximum transversal momentum that can be detected can be calculated from the equation (4.11) by substituting equation (4.4) and (4.10).

$$p_{\perp}^{(max/min)} = eB \times R_{c(max/min)} \tag{4.25}$$

$R_{c(max/min)}$ is determined by the radial dimensions of the detector as 2.5 mm and 20 mm. For electrons starting on the spectrometer axis their minimum cyclotron orbit diameter to

reach the sensitive area of the MCP outside its center hole is 5 mm. The maximum orbit diameter is 40 mm corresponding to the MCP radius. Therefore, $R_{c(max/min)}$ are 2.5 mm and 20 mm. The longitudinal acceptance depends on the electric field applied. All the electrons moving towards the electron detector, i.e, $+z$ direction and with $p_{\perp e} > p_{\perp e}^{min}$ are detected, except, those with time-of-flight equal to the integer multiples of the cyclotron period. Such regions of non-acceptance can be filled by repeating the measurement at a different magnetic or electric field, thereby shifting the wiggle positions. Such a procedure is not done for the measurements described in this thesis. A detailed description of it can be obtained elsewhere [44].

The electrons that are moving towards the ion detector, beyond a longitudinal momentum of $p_{ze} = -\sqrt{2eUm_e}$ cannot be detected, since they fly into the ion drift region and are lost. U is the total uniform extraction field applied between the interaction region and the ion drift tube. The minimum energy of the electron that can be detected is given by the minimum transversal momentum, i.e $E_{1,2}^{min} = (p_{\perp e}^{min})^2/2m_e$.

The corresponding minimum and maximum transversal momentum, the maximum longitudinal momentum towards $-z$ direction, $-p_{ze}$ and the minimum energy of the electrons detected for the magnetic and electric fields used for the experiments described in this thesis are summarized in the table 4.1.

Experiment	B (G)	$p_{\perp e}^{min}$ [a.u]	$p_{\perp e}^{max}$ [a.u]	$E_{1,2}^{min}$ (eV)	E (V/cm)	p_{ze}^{max} [a.u]
Thiophene	6.9	0.138	1.108	0.26	3	-1.149
1Me5NIZ	7.415	0.149	1.19	0.301	4	-1.327
Lithium	7.115	0.143	1.143	0.278	2	-0.938

Table 4.1: Summary of electron momentum acceptance for the measured species and the fields applied.

4.6.2 Acceptance of ions

First we consider the ion mass acceptance of the ReMi since we are interested to detect rather large masses of organic molecular ions. For single ionization without fragmentation, the momentum gain is negligible, ie. $p_{zi} \approx 0$. The maximum ion mass that can be detected for such events can be calculated by setting $p_z = 0$ in equation (4.7).

$$m_{ion,max.}[amu] = 0.12048.\frac{t_{max}^2[\mu s]}{l_a}E[V/cm] \tag{4.26}$$

where t_{max} is the maximum time-of-flight of ion that can be measured and E, the electric field. In the current measurement, the maximum allowed time-of-flight window is set to be around 26 μs. Therefore, with a field of 1 V/cm the maximum detectable ion mass is $\sim$14 amu.

The situation gets more complicated when we use a pulsed electric field instead of a homogeneous field because the time-of-flight of each fragment depends on the average field that the ion experienced during its trajectory. The average extraction field $\langle U \rangle$ experienced by the ions is different from the maximum of the pulse that we use. For fragments with negligible momentum, we can use the measured time-of-flight of the ions to determine $\langle U \rangle$ using the equation (4.7) and by substituting $p_{zi} = 0$.

$$t_{p_{zi}=0} = m\frac{2l_a + l_d}{\sqrt{2mq\langle U \rangle}} \tag{4.27}$$

The corresponding values for a pulsed extraction field with amplitude of 358 V as shown in figure 3.3 are summarized in table 4.2. To formulate a general expression for the

Ionic species	Mass [amu]	Time-of-flight (μs)	Average extraction voltage, $\langle U \rangle$ [V]
He^+	4	4.28	65.37
H_2O^+	18	7.37	99.35
D_2O^+	20	7.70	101.03
$C_5H_5N^+$	79	13.91	122.52
$C_4H_4S^+$	84	14.31	122.85
$(C_5H_5N)_2^+$	158	19.14	129.35
$(C_4H_4S)_2^+$	168	19.67	130.15
$(C_4H_4S)_3^+$	252	23.79	133.44

Table 4.2: Parent ions with $p_{zi} = 0$ detected in the measurement, their corresponding measured time-of-flight and the estimated average extraction voltages for pulsed extraction as shown in figure 3.3.

average extraction voltage, we use an exponential fit given by,

$$\langle U \rangle = U_{max}(1 - e^{\left[-\frac{t}{t_c}\right]_{p_z=0}}) \tag{4.28}$$

where U_{max} is the maximum average extraction voltage, t the measured time-of-flight of a ionic fragment with $p_{zi} = 0$ and t_c time constant for the exponential fit. Figure 4.15 shows the fit for the applied pulse voltage (refer figure 3.3). From the fit parameters, one can

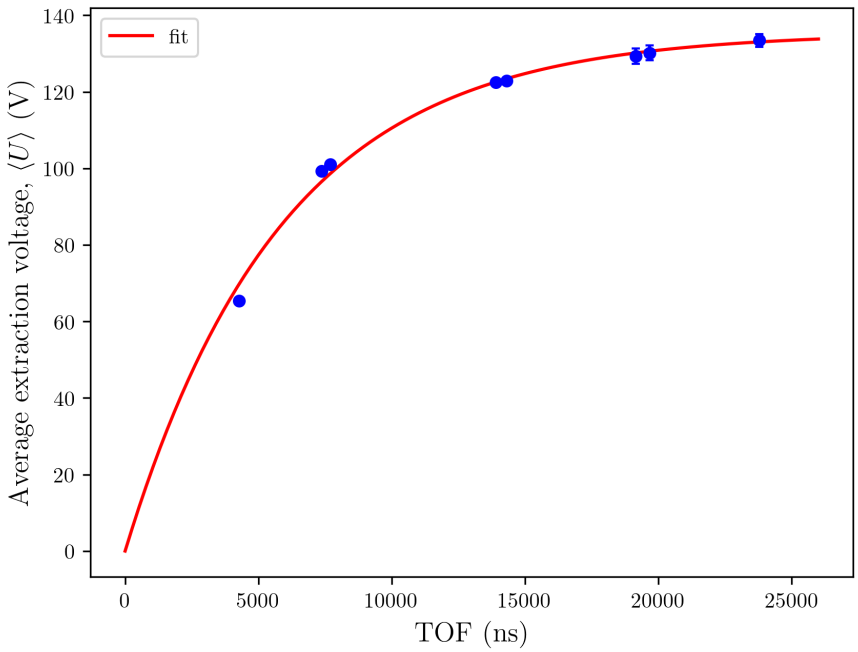

Figure 4.15: Exponential fit for the average extraction voltage $\langle U \rangle$. Fit parameters $t_c = 5.91\ \mu s$ and $U_{max} = 135.45\ V$. Error bars represent the error in determining $\langle U \rangle$ due to the FWHM of the parent ion peak in the time-of-flight distribution.

determine the maximum field ions can experience for the particular pulse that we apply,

ie. $E = U_{max}/l_a = 22.57\, V/cm$. By substituting this value to the equation (4.26), we can determine the maximum ion mass that can be detected with the current pulsed field to be ∼306 amu. Note that equation (4.28) cannot be applied to ions with $|p_{zi}| > 0$ since the ions flying to the different directions experience different average fields from that of the ones with $p_{zi} = 0$.

For channels such as dissociation or Coulomb explosion, the ions gain a considerable amount of momentum. In such cases, the maximum transversal momentum acceptance is determined by the mass of the ionic fragment and the diameter of the detector. Due to the finite jet velocity, the position of the ion hit is shifted away from the centre of the detector towards the $-y$ direction as explained in section 4.2.2. Therefore the position of the ionic fragment with a finite transversal momentum, $p_{\perp i}$ is given by,

$$\begin{aligned} r &= r_o + r' \\ &= v_{jet}t + p_{\perp i}\frac{t}{m} \end{aligned} \tag{4.29}$$

where r_o is the distance of the centre of distribution of the ions from the centre of the detector and r' is the distance of the fragment with $p_{\perp i} \neq 0$ from the centre of distribution.

Even for ions with $p_{\perp i} \neq 0$ transversal momentum acceptance is not 100% because some fraction of ions will hit the electron gun as shown in the figure 4.3b. One can define a maximum transversal momentum, $p_{\perp i}^{max}$ such that all ions lie within the detector radius. For determining the maximum transversal momentum acceptance, one can substitute $r = 40$ mm on the right-hand side of equation 4.29, which is the radius of the detector, and $r_\circ = 0$. By knowing t, ie the time-of-flight for ions with $p_{zi} = 0$ a.u and their mass, one can determine the maximum transversal momentum acceptance, $p_{\perp i}^{max}$. Beyond that value, the fraction of ions that hit the detector decreases. The maximum transversal acceptance of certain dimer species that are measured is summarized in the table 4.3. The maximum

Dimer fragment	$p_{\perp i}^{max}$ [a.u]	KE_{max} [eV]	Dimer	KER_{max} [eV]
Ar^+	129.05	3.11	Ar_2	6.22
$C_5H_5N^+$	190.13	3.41		
H_2O^+	80.54	2.69	C_5H_5N-H_2O	3.30
D_2O^+	85.77	2.74	C_5H_5N-D_2O	3.43
$C_4H_4S^+$	196.77	3.43	$(C_4H_4S)_2$	6.85

Table 4.3: Maximum ion transversal momentum acceptance, $p_{\perp i}^{max}$ for ionic fragments originating from dissociation or Coulomb explosion and the corresponding maximum kinetic energy release KER_{max} for the studied dimers.

kinetic energy of the ion (KE_{max}), that can be detected can also be calculated from $\vec{p}_{\perp i}^{max}$ using the equation (4.17). Here we discuss only the case of ions which are emitted in the X-Y plane, since the z direction has higher KER acceptance. The maximum kinetic energy release acceptance (KER_{max}) values of dimers that are studied in this work are also summarized in the table 4.3. KER_{max} of homodimers (eg. Ar_2) can be calculated as twice the KE_{max}, whereas for heterodimers like C_5H_5N-H_2O, KER_{max} is determined by the maximum transversal momentum acceptance ($p_{\perp i}^{max}$) of the lighter molecule in the dimer (in this case H_2O or D_2O) because ion-ion coincidence will be missing for a momentum larger than this value.

4.6.3 Resolution of electrons

The uncertainty in determining the momentum of the particle depends on the spectrometer geometry, fields, and also the time and position resolution, δt and δr. The fields can be determined precisely in the calibration procedure, but the resolution is mostly determined by the temporal spread of the projectile and the spatial extension of the interaction region.

The temporal spread of the projectile predominantly depends on the pulse duration of the UV laser. Additionally, it also depends on the expansion of the electron bunch during its trajectory from the photocathode to the interaction region. The secondary electrons produced within the electron gun assembly by the primary electron beam and the scattered laser beam add to the temporal width of the beam. This can be determined either from the experimental data or by looking at the width of the projectile beam itself, if it is allowed to fall on the detector with strongly reduced beam current. From the experimental data, one can look at the time-of-flight peak corresponding to the elastically scattered projectile beam, which normally appears before the inelastically scattered projectile as a separate peak. The width of the time-of-flight peak for elastic scattering events with small scattering angle (θ_{e1}) gives the temporal resolution. For the work presented in this thesis, the temporal spread δt is determined to be ~ 1.6 ns.

The spatial extension of the beam depends on the electron beam focus diameter at the interaction region. Focusing the beam precisely on the jet is a tricky process because of the compact geometry of the electron gun lenses. The ideal scenario would be to have a magnetic field node at the interaction region, where all the particles come back to the spectrometer axis. At the same time, one would prefer to have another node slightly before the electron detector hole to ensure proper dumping of the electron beam. This makes the alignment of the electron beam challenging. In addition, the jet size at the interaction region also plays a role, if the focus size is not small enough. The width of the jet along the x direction can have a maximum value of around 2.5 mm. It gives a limitation to the spatial extension in the x direction. But if the focus size is larger than this value, ions beyond the length of 2.5 mm along the y direction can be ionized. Focus size can also be extracted experimentally, by looking at the ion position distribution for a calibration gas like helium measured with a constant field. Transversal distribution of ions after single ionization will be a convolution of the Compton profile of the helium 1s orbital and the spatial size of the electron beam interaction region. Since the Compton profile of helium 1s orbital is known, the spatial spread can be determined. This method gives a spatial resolution of $\delta r \sim 1.5$ mm.

Furthermore, the momentum uncertainty can be split into longitudinal and transversal momentum uncertainty and can be calculated using the Gaussian error propagation from the equations (4.7) and (4.11). Hence the longitudinal momentum uncertainty is given by,

$$\delta p_z = \sqrt{\left(\frac{1}{\partial t/\partial p_z}\delta t\right)^2} \tag{4.30}$$

Here we do not take into account the uncertainty in the time and momentum due to the finite spatial extension, δa, of the interaction volume, since we use time-focusing geometry for the spectrometer (3.1.1). The transversal momentum uncertainty can be written as,

$$\delta p_\perp = \frac{\omega_c m}{2\left|\sin(\omega_c t/2)\right|}\sqrt{\delta r^2 + \left(\frac{\omega_c r}{2tan(\omega_c t/2)}\delta t\right)^2} \tag{4.31}$$

Similarly, the uncertainty in the azimuthal angle and the polar angle can be calculated from the equation (4.12) and $\theta = \tan^{-1}\frac{p_\perp}{p_z}$.

$$\begin{aligned}\delta\phi &= \sqrt{\left(\frac{\delta r}{r}\right)^2 + \left(\frac{\omega_c}{2}\delta t\right)^2} \\ \delta\theta &= \frac{1}{p_\perp^2 + p_z^2}\sqrt{(p_z\delta p_\perp)^2 + (p_\perp \delta p_z)^2}\end{aligned} \tag{4.32}$$

It is clear from the above equations that the transversal momentum resolution and the angular resolutions depend on the transversal and longitudinal momentum values. The estimated values of the uncertainties for the current experimental settings are depicted in the figures 4.16, 4.17 and 4.18.

Particularly important is to note that the energy resolution δE can be calculated similarly by Gaussian error propagation of the equation $E = \left(\frac{p_z^2}{2m_e} + \frac{p_\perp^2}{2m_e}\right)$.

$$\delta E = \frac{1}{m_e}\sqrt{(p_\perp \delta p_\perp)^2 + (p_z \delta p_z)^2} \tag{4.33}$$

Since δE is also dependent on p_z and $p_\perp$ it can be represented as a function of p_z and $p_\perp$ as shown in figure 4.18a. Except for the longitudinal momentum resolution, which depends only on p_z, all other quantities depend on both p_z and $p_\perp$ of electrons. Therefore, one can see that the resolutions get worse close to the nodes where the acceptance goes to zero. Another feature is that the longitudinal momentum resolution gets worse as the p_z increases and thereby the energy resolution. Therefore, the projectile with low energy will have a better resolution for the same fields. Care has to be taken to adjust the fields such that the node close to the detector hole should be far away from the hole since it could worsen the resolution for the scattered projectile.

A distribution showing the sum of energies of the detected two electrons in an (e,2e) measurement ($E_{sum} = E_1 + E_2$) is a good way to compare the estimated energy resolution and the experimental energy resolution. Using Gaussian error propagation the full-width half maximum (FWHM) of the E_{sum} distribution gives δE_{sum}, which is given by,

$$\delta E_{sum} = \sqrt{\delta E_1^2 + \delta E_2^2} \tag{4.34}$$

Figure 4.18b shows such a distribution for single ionization of helium at an electric field of 3 V/cm and magnetic field of 6.9 G. A Gaussian fit to the distribution gives an FWHM of 6.725 eV. From our experimental data, most of the scattered projectiles lie in the region $1.7\ a.u < p_z < 2.4\ a.u$, which gives an average resolution for these electrons ~ 6 eV. For the ionized electrons, which lie mostly around $-0.1\ a.u < p_z < 0.2\ a.u$, the average resolution is ~ 1 eV. Therefore, our experimental energy resolution is in close agreement with the estimated energy resolution for the determined values of δr and δt.

4.6.4 Resolution of ions

For estimating the longitudinal momentum resolution of ions, one can use equation (4.30). It depends on the mass, m, and average extraction field, $\langle U \rangle$. For measurements with the pulsed extraction field, it was observed that the width of the time-of-flight peak for fragment ions with small momentum ($\vec{p_i} \sim 0$) increases for increasing m/q ratio (figures 5.19 and 5.28). The observed time-of-flight width (δt_i) as a function of m/q ratio is shown in the figure 4.19a. The figure also shows a polynomial fit to the measured

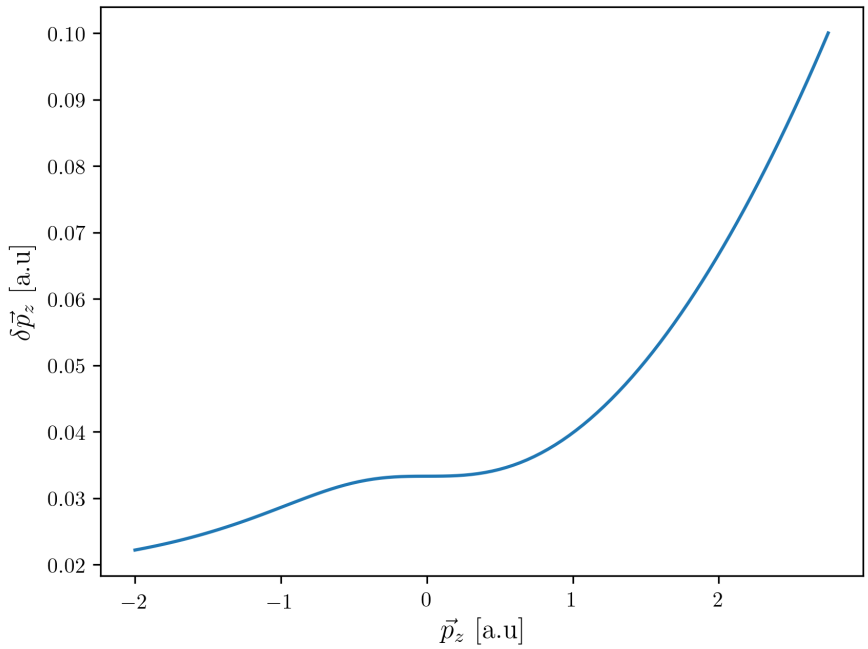

(a)

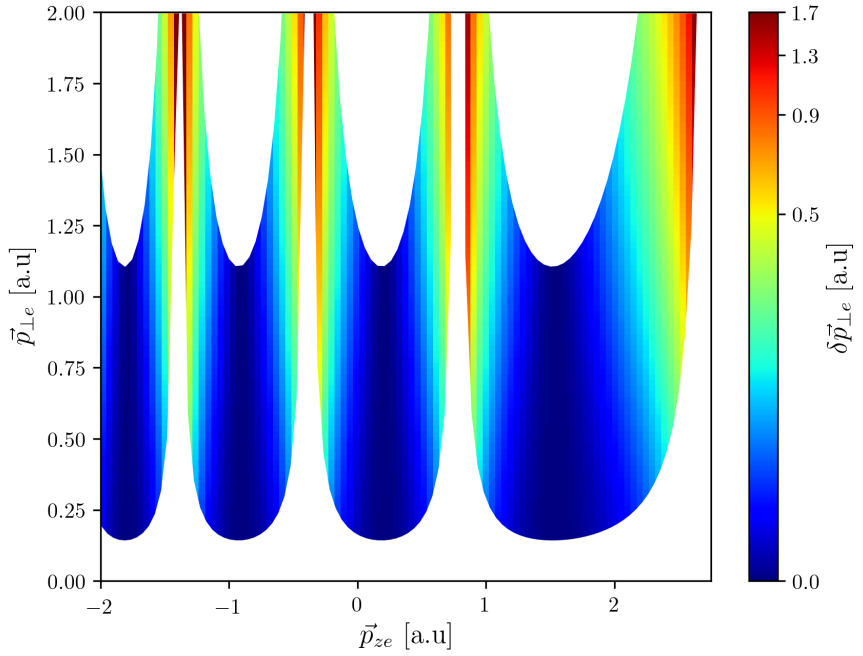

(b)

Figure 4.16: Longitudinal and transversal momentum resolution of electrons for an electric field of 3 V/cm and 6.9 G magnetic field. The white area shows the regions of non-acceptance.

width. The longitudinal resolution seems to be increasing as a result of this definite time-of-flight width (δt_i). Figure 4.19b shows the estimated longitudinal resolution using the equation (4.30) due to the time-of-flight width, δt_i.

The determination of the resolution for fragments with $|\vec{p}_i| > 0$ a.u. can be understood from figure 4.20 which shows the momentum distribution of ions from the CE of thiophene dimers. To determine the longitudinal momentum resolution (δp_{zi}), the events

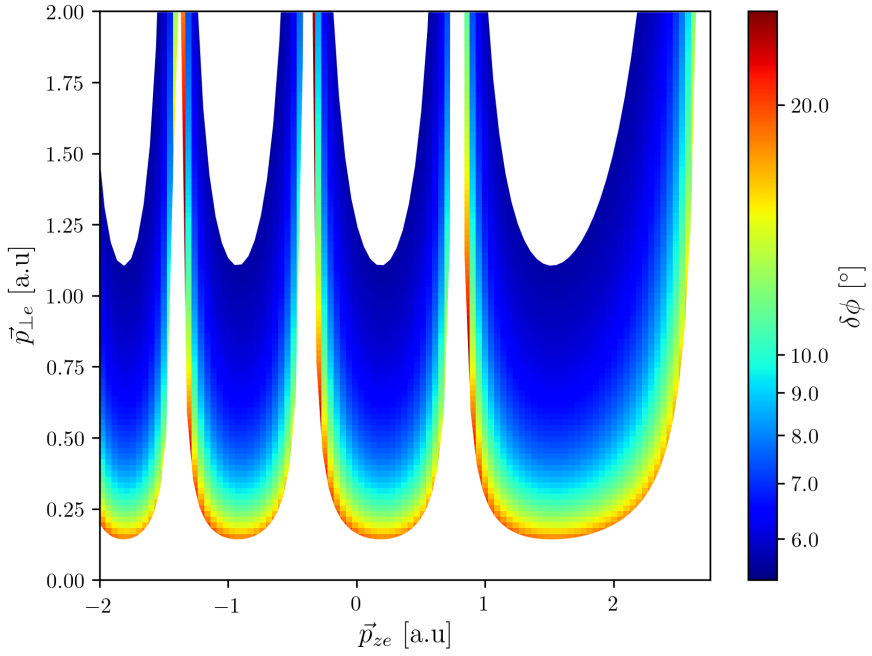

(a)

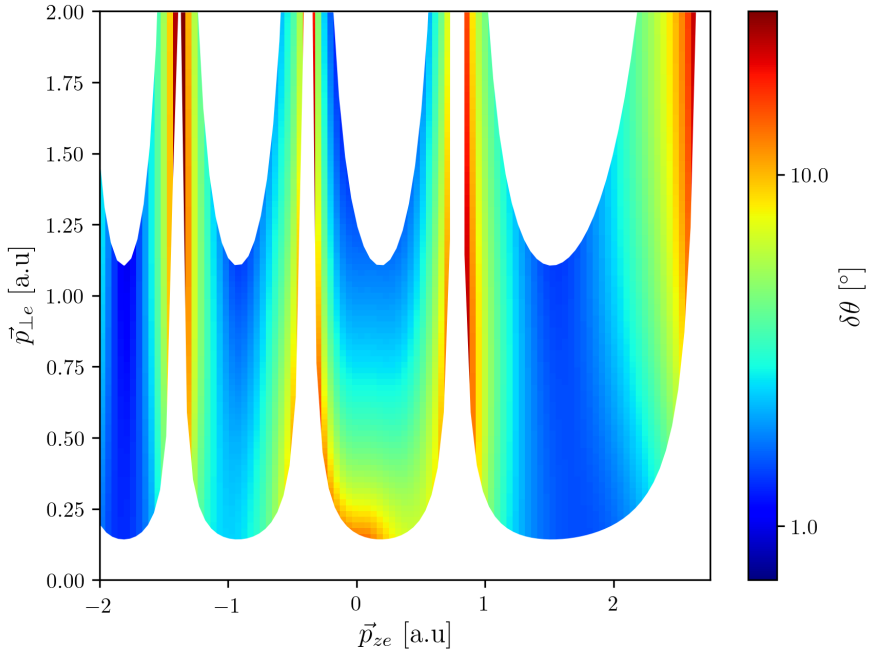

(b)

Figure 4.17: Azimuthal and polar angle resolution of electrons for an electric field of 3 V/cm and 6.9 G magnetic field. The white area shows the regions of non-acceptance.

with $|p_{\perp i}| < 40$ a.u. (blue-shaded region) are projected onto the p_{zi} axis. The FWHM of the Gaussian fit of the distribution yields the longitudinal momentum resolution δp_{zi}. Similarly, the transversal momentum resolution ($\delta p_{\perp i}$) is determined by integrating the counts within the grey-shaded region having $|p_{zi}| < 20$ a.u. The determined resolution for the fragments measured in the course of this work is summarized in table 4.4. Note that the momentum resolution is expected to get worsen for heavier fragments according

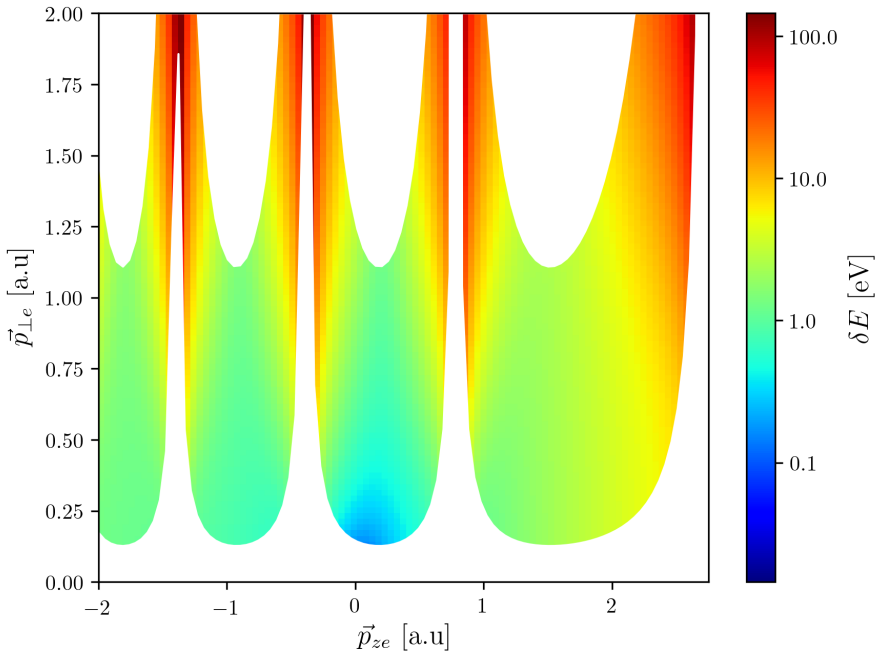

(a)

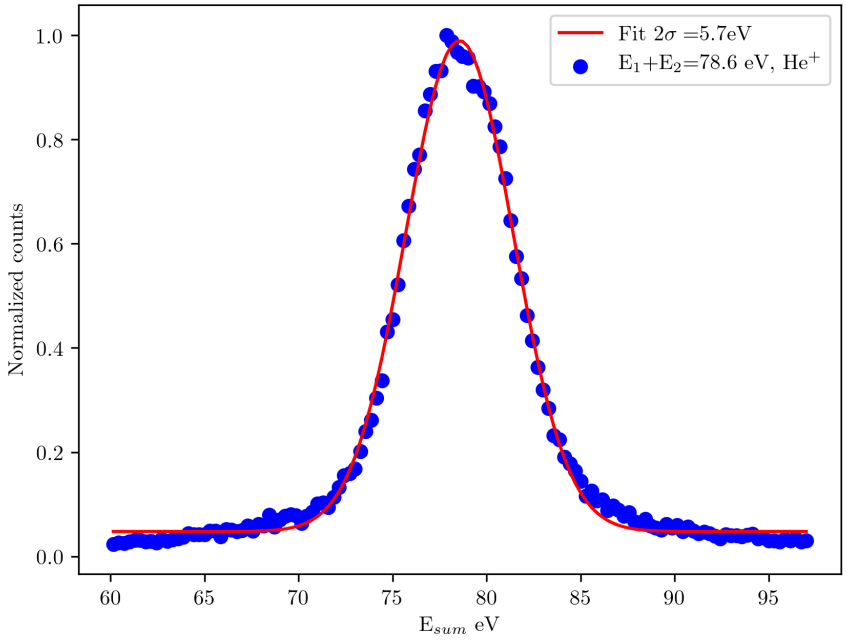

(b)

Figure 4.18: (a) Energy resolution of electrons for the same experimental conditions as in the figures 4.16 and 4.17. The electrons with large longitudinal momentum show higher uncertainty. Therefore, lower the projectile momentum better the energy resolution. (b) Experimental energy sum $E_{sum} = E_1 + E_2$ for He single ionization. FWHM, $\Gamma = 6.725$ eV of the Gaussian distribution gives the experimental energy resolution.

to equation (4.30). In addition, it is observed that δp_z is increasing with increased average extraction field, $\langle U \rangle$. Particularly, the fragments for thiophene moving in $\pm z$ direction have different longitudinal resolutions due to different average extraction fields experienced. However, the transversal momentum resolution is due to the velocity of the jet in

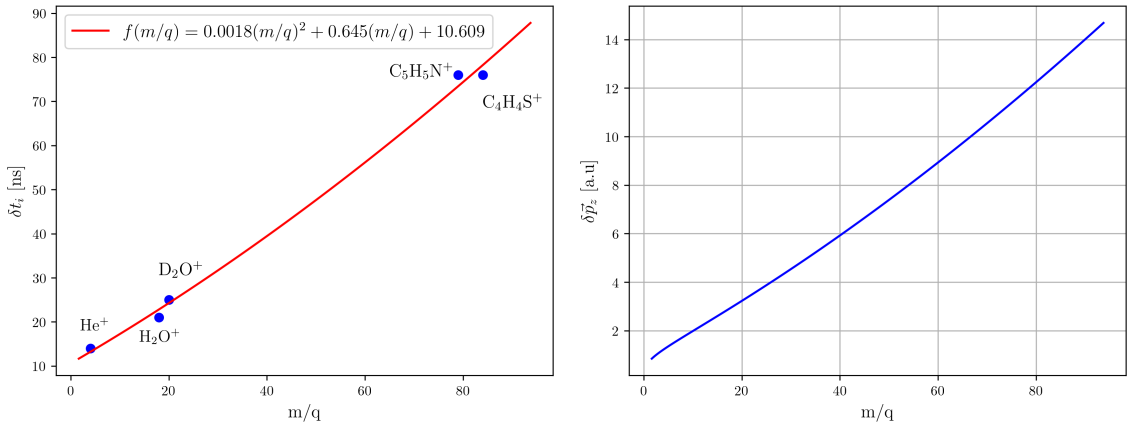

(a) (b)

Figure 4.19: (a) The width of the monomer peak for different parent ions measured as a function of m/q ratio. The red curve shows a polynomial fit of the data points with the mentioned fit function. (b) The longitudinal momentum resolution for parent ions as a function of the m/q ratio due to the time-of-flight width.

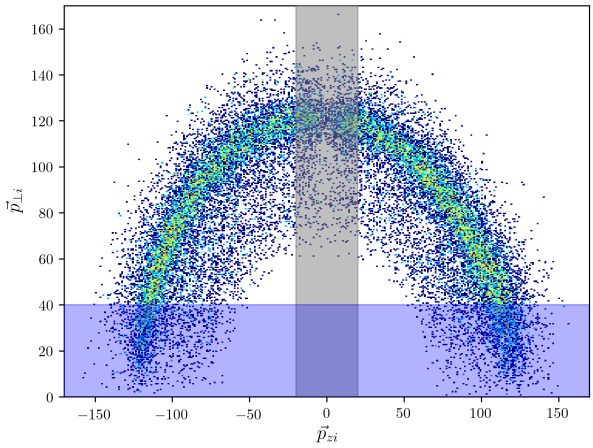

Figure 4.20: Momentum distribution of fragments from the Coulomb explosion of thiophene dimers. Counts in the blue and grey shaded region are integrated and projected to the x/y axis, and the FWHM of the Gaussian fit gives the experimental longitudinal/ transversal momentum resolution respectively.

Dimer fragment	m/q [amu]	p_z [a.u.]	δp_z [a.u.]	$\delta p_\perp$ [a.u.] ($\lvert p_z \sim 0 \rvert$)
$C_4H_4S^+$	84.14	-122	11.6	15.
	84.14	122	18.1	15.
D_2O^+	20	-70	4.6	9.7
$C_5H_5N^+$	79.101	70	16.	16.9

Table 4.4: Experimentally determined momentum resolutions for different fragments measured in the course of this work.

the y direction.

For pyridine$\cdots D_2O$ dimer, we consider only half of the CE events, since the other half of the CE coincidence line is not resolved due to the presence of events from the

CE involving $C_5H_5N^+$ ions and D_3O^+ ions from larger clusters (figure 5.29). In the considered events, the D_2O^+ ions are emitted in the $-z$ direction and the $C_5H_5N^+$ ions are emitted in the $+z$ direction. Therefore, in table 4.4 for D_2O^+, δp_z for only the events with $p_z < 0$ is mentioned. Similarly, for $C_5H_5N^+$, δp_z for only the events with $p_z > 0$ is mentioned. Considerably low momentum resolution for D_2O^+ in comparison to other fragments is due to its smaller mass. Further optimization of the pulsed extraction field and other parameters like magnetic fields, electron beam focus, etc. can improve the resolution.

Chapter 5

Experimental results and discussion

In this chapter, the evaluation of the measurements done during the course of this work will be summarized. The performed measurements can be broadly classified into two parts. One involves the (e,2e) studies on lithium and 1-Methyl,5-Nitroimidazole (1-Me,5-NIZ). Both targets are in the solid phase at room temperature. Therefore, the experiments required modifications of the existing reaction microscope to incorporate solid targets. Triple differential cross-sections (TDCS) in different planes and three-dimensional TDCS of ejected electrons will be presented. For 1-Me,5-NIZ molecule, a comparison of the measured TDCS with MCTDW theory for ionization of the valence orbitals, which leads to the formation of parent cations will be presented. The second part is the studies on ICD in heterocycle molecular dimers and heterocycle-water complexes. Fragments originating from the Coulomb explosion (CE) of the dimers are detected in coincidence with one outgoing electron. The kinetic energy release (KER) of the CE channels and the ICD electron spectra are presented.

5.1 (e,2e) of Lithium at 105 eV impact energy

Lithium is a hydrogen-like atom which has a simple valence electron structure. It contains two orbitals 1s with two electrons and 2s with one valence electron having binding energies of 59 eV and 5.49 eV respectively. 1s orbital is localized closer to the nucleus around < 1 a.u and the 2s orbital has two radial probability maxima, one close to the nucleus < 1 a.u and the second part extends to around 7 a.u [147]. Due to the large difference between the binding energies and the spatial separation, single ionization by low-energy electron impact takes place almost exclusively from the outer shell. Fully differential cross-sections (FDCSs) for the single ionization of lithium from the 2s shell are thus very important because theoretical models should be able to provide accurate results. So far only one FDCS measurement of lithium after electron impact is published [148], although several fast ion impact measurements on lithium were done before, producing double [147, 149] and triple differential cross-sections [150] of single ionization of lithium. The latter showed a considerable amount of out-of-the-scattering plane emission indicating the multiple scattering of the projectile at the ion core which gives rise to a 'wing-like' structure in the directions perpendicular to the scattering plane. Therefore, (e,2e) studies on lithium will complement the ion-impact studies with different projectile species. Another motivation for studying lithium was to measure double ionization. This could finally not be performed due to the small cross-section which is about three orders of magnitude smaller than for single ionization [151].

The following section describes the incorporation of an oven to produce an effusive

atomic lithium beam to the existing reaction microscope which measures the momenta of the ionization fragments emitted in 4π solid angle. A detailed description of the target setup (oven) and the atomic beam arrangement is given in section 3.3.3. Here we present (e,2e) triple differential cross-sections for single ionization of lithium measured over a large final state phase space with a reaction microscope. The difficulty for the (e,2e) measurements on lithium is mainly due to the target preparation since it is solid at room temperature and it has a melting point at 180.5°C. Due to its low vapour pressure, it has to be heated to rather high temperatures $\sim$ 700-800°C. Such an effusive atomic beam can cause buildup on the spectrometer electrodes. Besides that, due to the high temperature of the target, the ion momentum measured predominantly shows the thermal momentum distribution rather than the momentum distribution from the collision. However, the ion signal can be used as a trigger to acquire lithium ionization events and separate different ionization channels for obtaining (e,2e) fully differential cross-sections. Figure 5.1a shows the ion time-of-flight distribution of electron impact ionization of lithium with a projectile energy of 105 eV. A helium supersonic jet was used in a crossed-beam configuration as a calibration target. Therefore, one can see events from He^+, $^7Li^+$ and $^6Li^+$. The two collimation apertures in front of the oven nozzle reduce the ion momentum distribution along both the transversal directions y and z. Along the atomic beam (x direction) the momentum distribution is large, as seen in the position distribution for ions (figure 5.1b) which spans almost half of the detector diameter along x direction. An estimate of the ion resolution gives the values $\Delta p_z = 1.574$ au, $\Delta p_y = 1.187$ au and $\Delta p_x = 11.875$ au.

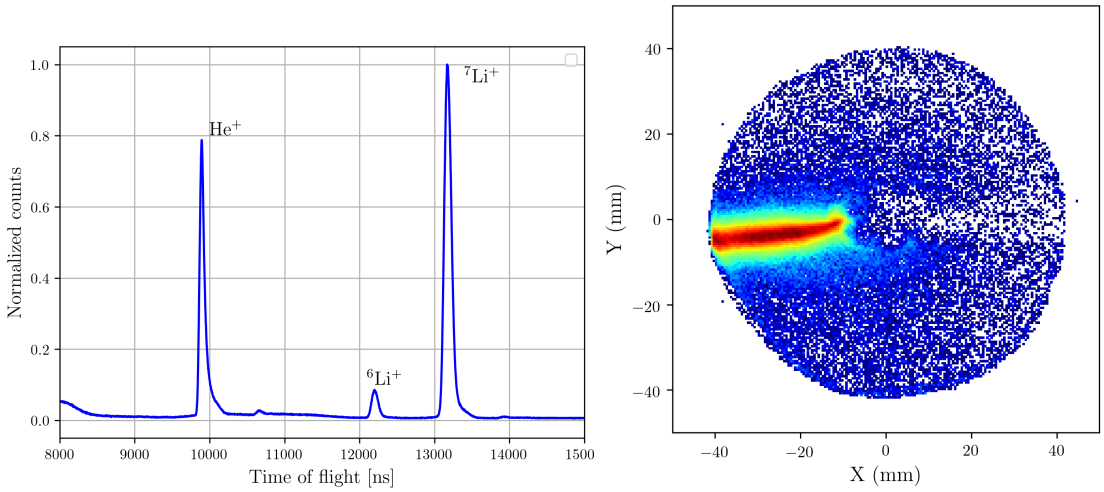

(a) (b)

Figure 5.1: (a) The time-of-flight showing He^+, $^6Li^+$,$^7Li^+$ (isotopes of lithium in the atomic beam). (b) Image of the ion detector showing events from lithium. Due to the temperature of the beam, the x distribution on the detector is broad. The transversal velocity spread in y and z directions is shortened using the apertures in front of the oven.

The two outgoing electrons were detected in coincidence with the $^7Li^+$ ions. Figure 5.2 shows the measured binding energy distribution given by the equation IP $= E_0 - E_1 + E_2$. The distribution peaks at the theoretical first ionization potential which is indicated by the black dashed line. The full-width half maximum of the distribution gives the experimental binding energy resolution for the electrons. As explained in the subsection 4.6.3 the experimental electron resolution varies for different experimental field

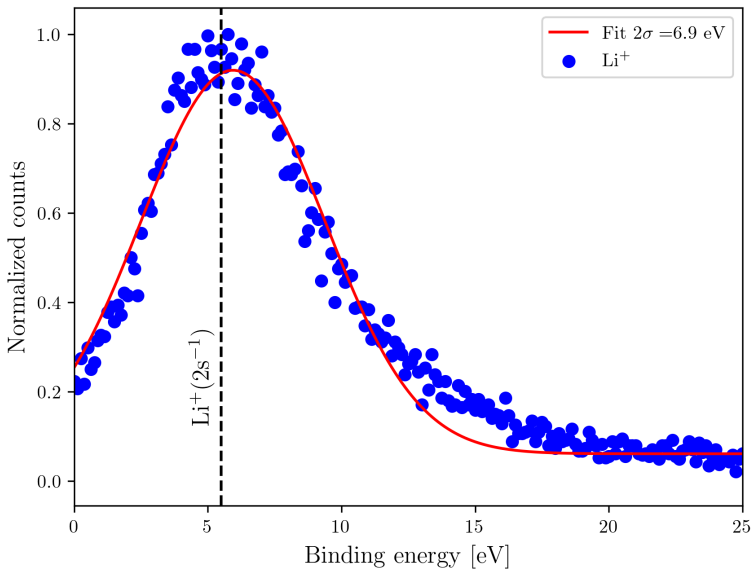

Figure 5.2: Binding energy distribution for single ionization of lithium with FWHM = 8.084 eV which indicates the experimental resolution for the channel. The Vertical dashed line indicates the theoretical first ionization potential of the lithium 2s state.

strengths used and the electron energies. A rather high value of 8.1 eV is mostly the contribution of fast outgoing electron resolution (7.9 eV) which appears close to one of the magnetic nodes. This is due to the fact that the energy loss for the projectile is rather low due to the low ionization potential of the 2s orbital of lithium, therefore the scattered projectile arrives rather close in time-of-flight to the unscattered projectile. Since the presence of a magnetic node is utilized in dumping the projectile into the detector hole, one has to take care that the node is positioned slightly behind or in front of the detector. Otherwise, all good events would also get dumped into the hole. In this case of 2s ionization of lithium, since the energy difference of the unscattered and scattered projectile is rather low, finding a node position while maintaining proper alignment of the beam to the hole and simultaneously getting a good resolution for the scattered projectile is tricky. However, the resolution of the second slow electron is around 1 eV. The resolution can be optimized further by optimizing the magnetic and electric fields.

5.1.1 Three dimensional triple differential cross-sections

Figure 5.3b shows one of the angular distributions of ejected electrons for single ionization of lithium at scattering angle $\theta_1 = -15° \pm 2.5°$ and ejected electron energy of $E_2 = 5 \pm 2.5$ eV. For each scattering angle θ_1 discussed in the following section, the counts are integrated within an interval of $\Delta\theta_1 = 2.5°$. For each ejected electron energy, the integration interval ΔE_2 used is, as mentioned in the figures. Each data point in the 3D and 2D distributions (figure 5.3c) is cross normalized to $\sin(\theta_1)\Delta\theta_1\Delta E_2$.

In order to study the collision dynamics, we examine the angular distributions in different planes, namely, the scattering plane, perpendicular plane, all perpendicular plane and azimuthal plane as indicated in figure 5.3a. Details of each plane are described in section 4.4. Additionally, the azimuthal plane is introduced, which contains the momentum transfer vector and is perpendicular to the scattering plane. Figure 5.3c shows the angular distribution in each plane. Angles are measured with respect to the projectile beam axis (z-axis) for the scattering and perpendicular planes, with respect to the x-axis for the

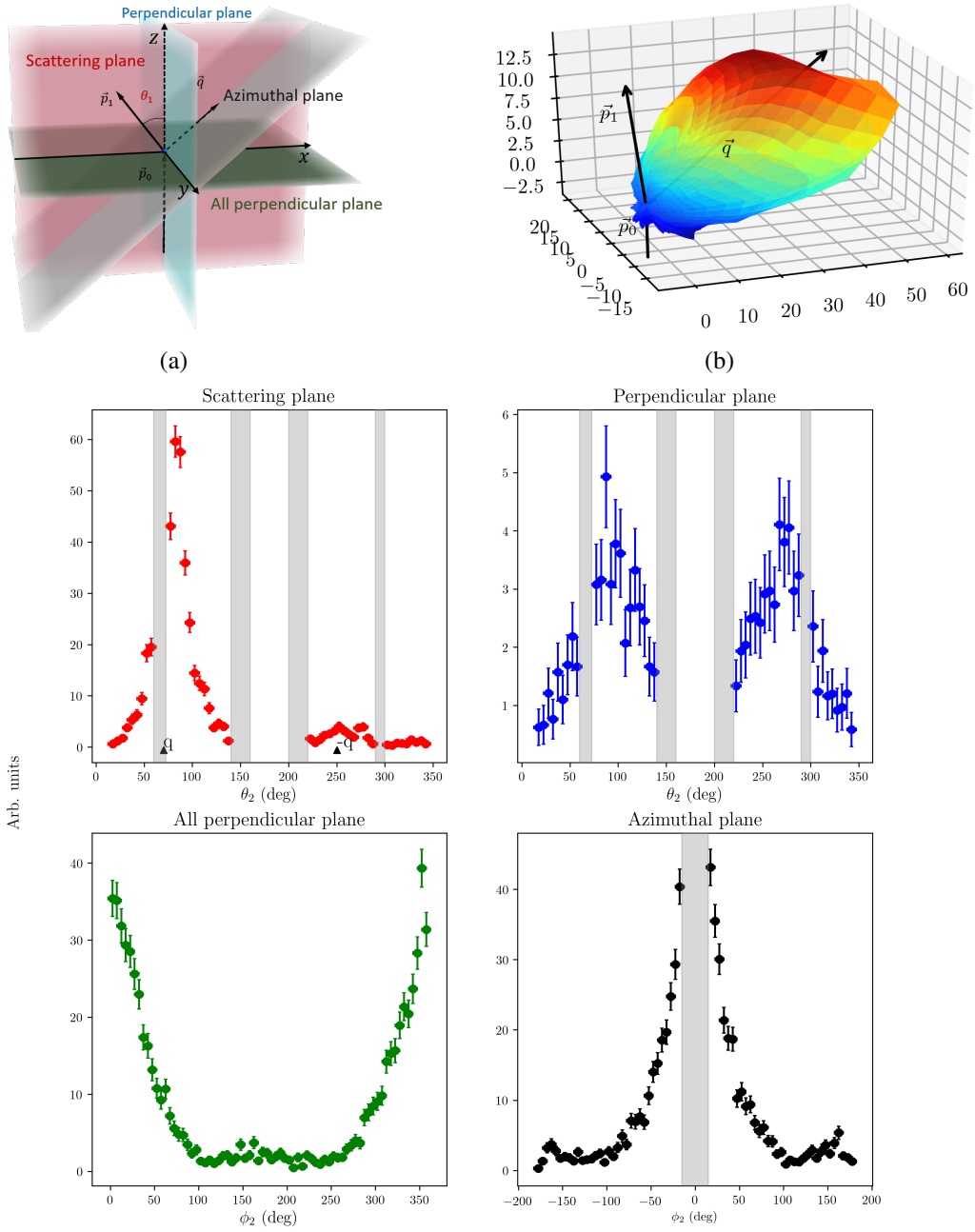

Figure 5.3: (a) Schematic of the collision geometry similar to 4.8. Additionally, the azimuthal plane is introduced which contains the momentum transfer vector and is perpendicular to the scattering plane. (b) Three dimensional triple differential cross-section (TDCS) $\frac{d^3\sigma}{d\Omega_{e1}d\Omega_{e2}dE_2}$ for scattering angle $\theta_1 = -15° \pm 2.5°$ and energy of the second electron $E_2 = 5 \pm 2.5$ eV. The ticks on the axes represent the counts. The magnitude of the arrows is scaled for visual appeal. (c) TDCS in different planes indicated in the figure 5.3a. Y-axis indicate the counts. For more details refer to text.

full perpendicular plane and relative to the momentum transfer vector $\vec{q}$ for the azimuthal plane. Counts on each plane are integrated over $\pm 20°$ out of the plane at each data point. Grey-coloured blocks indicate the angular ranges where the electron acceptance is zero

due to the presence of nodes of the electron trajectories due to the spectrometer magnetic field as explained in the subsection 4.6.1. Since the measurement procedure for filling up such wiggles is not carried out for the measurements described in this thesis, the data points corresponding to that angular range are omitted. In the 3D TCDS, these points are interpolated to the mean values of the neighbouring points, since the non-acceptance angular range is small compared to the available range. Particularly noticeable is the acceptance gap at 0° in the azimuthal plane. This is because of the presence of a magnetic field 'wiggle' in the scattering plane close to the momentum transfer vector, $\vec{q}$. Since the azimuthal plane is defined by $\vec{q}$ and is perpendicular to the scattering plane, at 0° one can expect a reduction in cross-section due to the wiggle. In addition to that, in the scattering and perpendicular plane there are missing counts close to the direction of the projectile, due to the detector hole. Therefore, those electrons that are ejected in this region are not detected.

The main features which are noticeable in the plots are the binary peak and the recoil peak which differ largely in amplitude from one another. This is in contrast to helium, where often a pronounced double lobe structure is observed [30, 152]. It gets more asymmetric with respect to its amplitude as the momentum transfer increases, owing to the increasing non-dipole transitions and strong rescattering of the ejected electron in the ionic potential. The huge difference observed between the binary and recoil lobe amplitude in lithium can be explained by the small ionization potential for the 2s orbital. Since the electron is loosely bound and farther away from the nucleus compared to the 1s electrons in Helium, rescattering of the ejected electron is less likely to occur.

Another feature present is the considerable amount of 'out of the scattering plane' emission which manifests in the binary peak being wider in the azimuthal plane compared to the scattering plane (figure 5.3). It can also be seen in the perpendicular and all perpendicular planes. Generally, for the collision that can be described by the first-born approximation which is due to a single interaction of the projectile with the target system, the ionized electron angular distribution is axially symmetric with respect to the direction of momentum transfer. If multiple interactions of the projectile are involved in the collision, the subsequent interactions could shift the total momentum transfer vector, in a direction different from that of the ionizing collision. Since the momentum transfer is determined in the experiment by the scattered projectile momentum vector, and the ejection of the electron could occur with any of these interactions transferring part/full of $|\vec{q}|$, the emission direction can differ considerably from the determined momentum transfer. This is observed in the measurement as out of the scattering plane emissions. Such out-of-the-plane emissions are visible in the perpendicular planes and the azimuthal plane. By looking at the TDCS as a function of scattering angle/momentum transfer amplitude and the second electron energy one can learn further about the higher-order effects that come to play.

Figure 5.4 shows the variation of the angular distribution for increasing scattering angle (momentum transfer) (across the columns) and with increasing second electron energy (across the rows). One can see that the recoil lobes become smaller with higher momentum transfer and the binary lobes get narrower with increasing ejected electron energy.

Broad lobes and slight dependence of the out-of-the-plane amplitude as a function of momentum transfer are observed for small energy $E_2 = 5 \pm 2.5$ eV (figure 5.5). The triple differential cross-sections in various planes for scattering angles $\theta_1 = -15^\circ \pm 2.5^\circ, -20^\circ \pm 2.5^\circ, -25^\circ \pm 2.5^\circ$ for $E_2 = 5 \pm 2.5$ eV is shown in figure 5.5. The y-axis shows the cross-normalised counts which decrease with increasing scattering angle. All

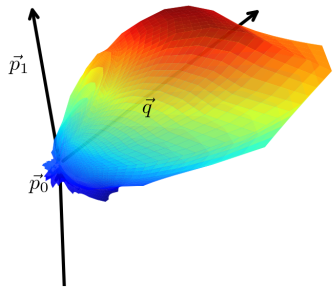

(a) $\theta_1 = -15° \pm 2.5°$, $|\vec{q}| = 0.73$ au, $E_2 = 5 \pm 2.5$ eV

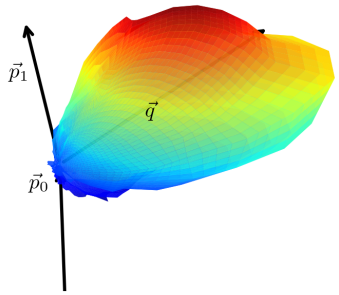

(b) $\theta_1 = -20° \pm 2.5°$, $|\vec{q}| = 0.91$ au, $E_2 = 5 \pm 2.5$ eV

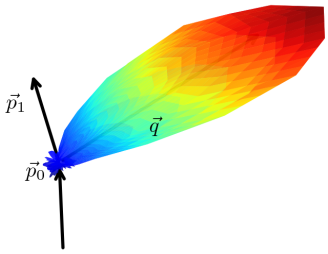

(c) $\theta_1 = -15° \pm 2.5°$, $|\vec{q}| = 0.73$ au, $E_2 = 15 \pm 2.5$ eV

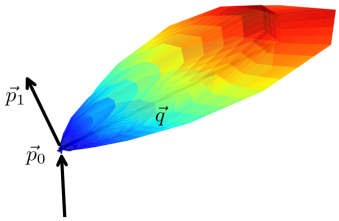

(d) $\theta_1 = -20° \pm 2.5°$, $|\vec{q}| = 0.91$ au, $E_2 = 15 \pm 2.5$ eV

Figure 5.4: Three-dimensional triple differential cross-sections for different scattering angles and second electron energies.

three cases ($\theta_1 = -15° \pm 2.5°, -20° \pm 2.5°, -25° \pm 2.5°$) have considerably high momentum transfer ($\vec{q} = 0.73a.u., 0.91a.u, 1.1a.u.$), which suggests prominent non-dipole transitions. As a consequence, the recoil peak is very small for the first case and completely disappears at $|\vec{q}| = 1.1$ au. Along with that, out-of-the-plane emissions in the perpendicular plane seem to increase in amplitude for increasing momentum transfer. This is observed as an increase in the ratio (r) of the peak of perpendicular plane emission to the binary lobe magnitude in the scattering plane ($\vec{q} = 0.73a.u. : r = 0.067, \vec{q} = 0.91a.u. : r = 0.11, \vec{q} = 1.1a.u. : r = 0.25$). This emission in the perpendicular plane appears as a bridge between the binary and recoil lobes similar to the 3D cross-sections of helium described in section 2.2.2. However, it is less clear from the 3D cross-sections of lithium due to the large difference in magnitude between the binary and recoil lobes. By comparing the momentum of the ejected electron ($\vec{p}_{e2} = 0.606$ au), we conclude that the momentum transferred to the ionic core increases for increasing $|\vec{q}|$. This is suggestive of multiple scattering at the target, with both the nucleus and the bound electron. With increasing momentum transfer number of scattering at the nucleus increases, thereby increasing the out-of-the-plane emission amplitude.

At higher E_2, the effects of the non-dipole transitions are prominent, as can be seen at the amplitude of the recoil lobe which completely disappears above $|\vec{q}| > 0.8$ au (figure 5.6). One can conclude that a large fraction of momentum transfer is carried by the outgoing ejected electron ($\vec{p}_{e2} = 1.05$ au) than to the ionic core. For smaller

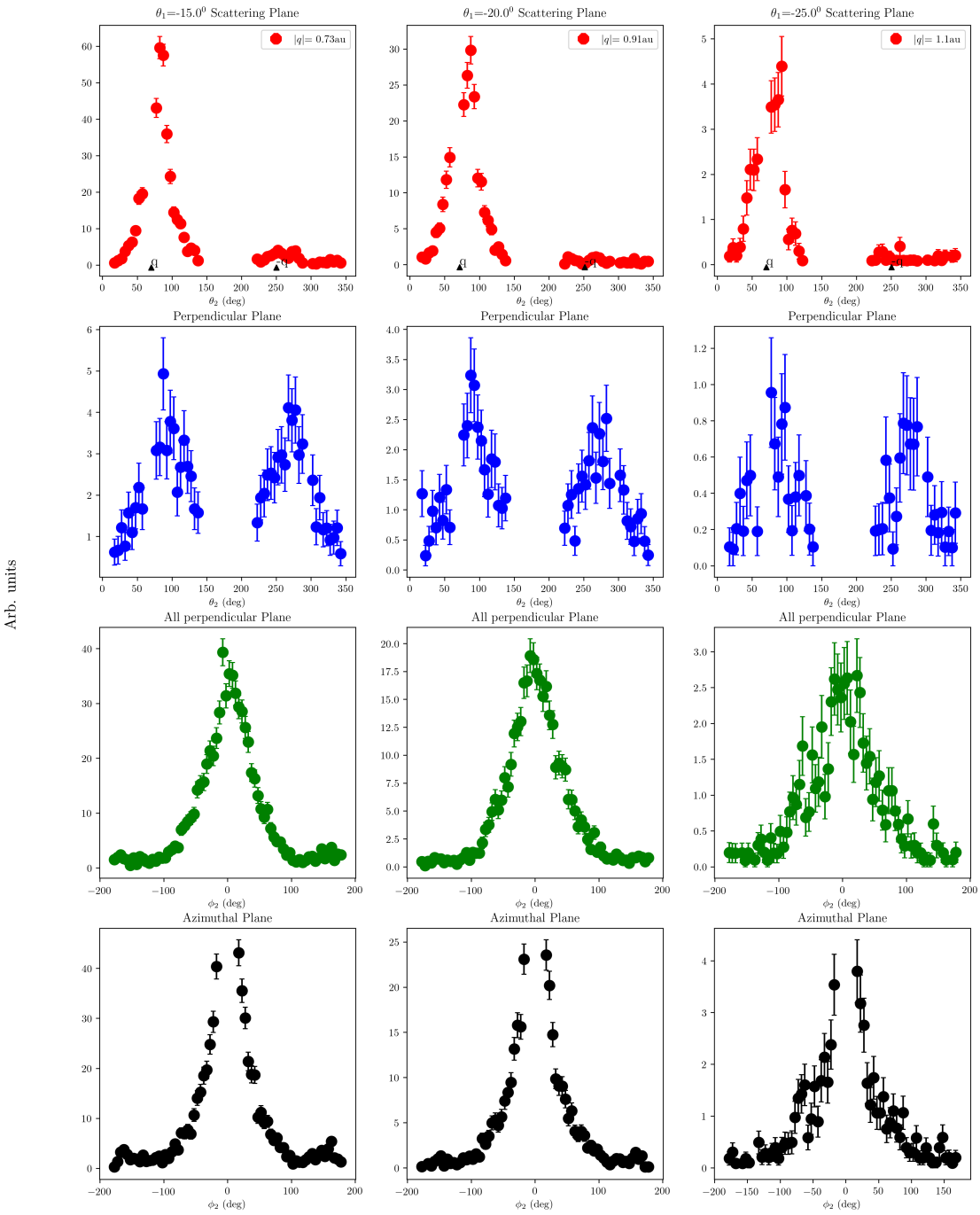

Figure 5.5: TDCS in different collision planes for scattering angles $\theta_1 = -15^\circ \pm 2.5^\circ, -20^\circ \pm 2.5^\circ, -25^\circ \pm 2.5^\circ$ and ejected electron energy $E_2 = 5 \pm 2.5$ eV.

$|\vec{q}| = 0.73, 0.91$ au, $|\vec{p}_{e2}| > |\vec{q}|$. One can assume that the extra momentum comes from the linear momentum of the bound electron in the direction of momentum transfer. In this case, scattering at the ionic core is minimal.

The decreasing higher-order effects with increasing energy of the ionized electron can be quantitatively observed from the reducing angular width of the binary peak in the scattering plane for increasing energies. Figure 5.7 shows the variation of the binary peak width for increasing energies at $\theta_1 = 20^\circ$. The width of the binary peak is not deducible for $E_2 = 1.25$ eV due to the acceptance gap of electrons in the forward direction. For the

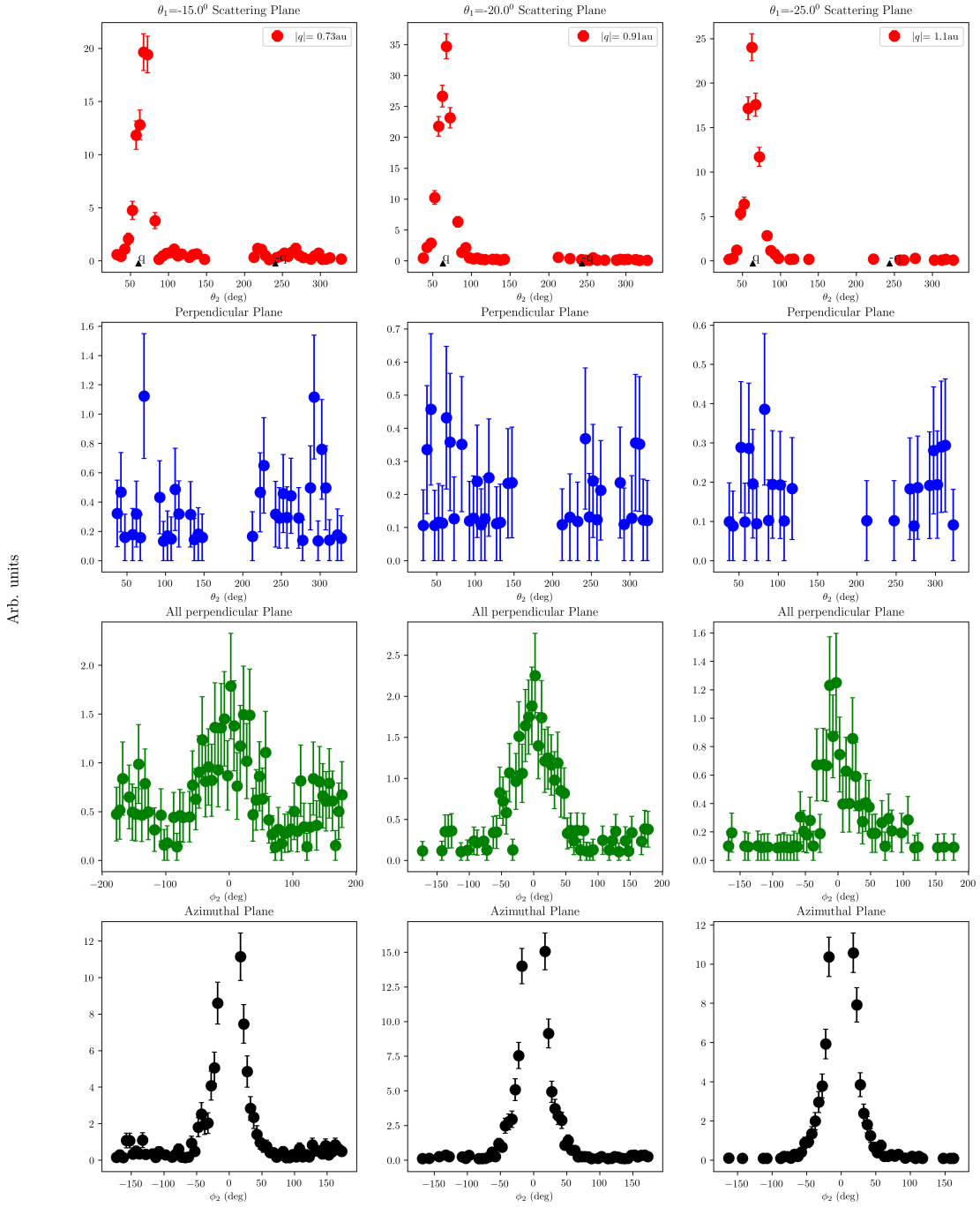

Figure 5.6: TDCS in different collision planes for scattering angles $\theta_1 = -15^\circ \pm 2.5^\circ, -20^\circ \pm 2.5^\circ, -25^\circ \pm 2.5^\circ$ and ejected electron energy $E_2 = 15 \pm 2.5$ eV.

other energies, one can identify a trend of decreasing width with increasing energies. The width ceases to decrease further beyond $E_2 = 10$ eV.

For small ejected electron energies, a slight tilt of the binary peak away from the momentum transfer direction is observed (figure 5.7). For a large scattering angle, as E_2 increases such a tilt reduces to a negligible value. This is in contradiction to that observed in single ionization of helium [30], where the tilt is persistent even at similar scattering angles and energies as discussed here. One of the reason for such a sharp contrast may be due to the orbital where the electrons originate from in both cases. Since for helium,

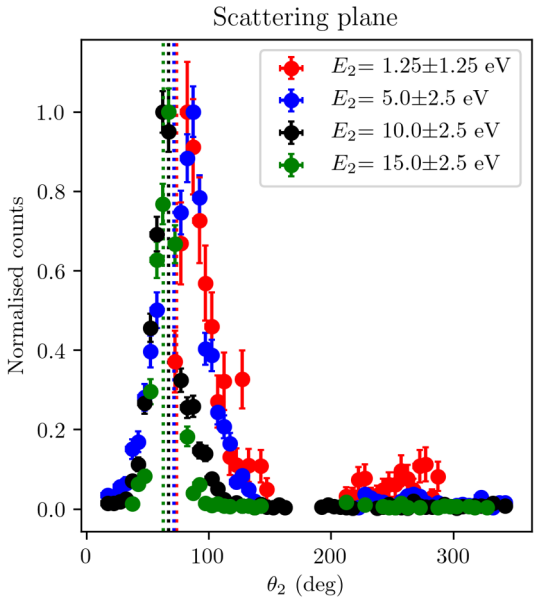

Figure 5.7: TDCS in scattering plane for ejected electron energy $E_2 = 2.5 \pm 1.25$ eV, 5 ± 2.5 eV, 10 ± 2.5 eV and 15 ± 2.5 eV for scattering angle $\theta_1 = -20° \pm 2.5°$. Counts are normalised to the peak value of the distribution. Comparison shows that the angular width of the binary peak decreases as a function of ejected electron energy. Vertical dotted lines in the scattering plane indicate the direction of momentum transfer. Same colour is used for the line and the corresponding angular distribution.

the electron comes from the 1s orbital which is closer than the 2s shell, the collision is considered to be dominated by three body interactions at all ejected electron energy ranges in the impact regime. Whereas for lithium, since the 2s orbital is far away from the nucleus, at certain ejected electron energy two body effects become comparable to the three body interactions [147]. Therefore, for higher energies and larger scattering angles binary one-to-one collisions become more prominent, and the interaction with the ion can be completely neglected. In such a case, one can consider the system as a two-body system where the interaction is just between the incoming projectile and the bound 2s electron. Whereas, in the three-body system, post collisions interactions (PCI) between all outgoing particles are more prominent leading to the increasing tilt.

Comparison to the 2S Compton profile

Collisions involving large momentum transfers at high impact energies can be described as the binary encounter between the projectile and bound electron, effectively reducing it to two-body interactions, where one can neglect the presence of residual ion within the impulse approximation [153, 154]. It was pointed out that the two-body processes can be compared as the Compton scattering of photons [155]. Therefore, the momentum distribution of the ejected electron in this regime becomes comparable to the Compton profile of the bound electron when two-body effects are prominent. It has been observed previously that the angular width of the ejected electron distribution gets closer to the angular width corresponding to the Compton profile of the 2s orbital electron in single ionization of lithium by fast 95 MeV/u Ar^{+18} ion impact collisions [147]. An interpretation was made that the angular width of the distribution of emitted electrons decreases for increasing energy as the two-body contributions increase and at 300 eV it

matches with that of the Compton profile where two-body processes dominate with almost negligible three-body contributions.

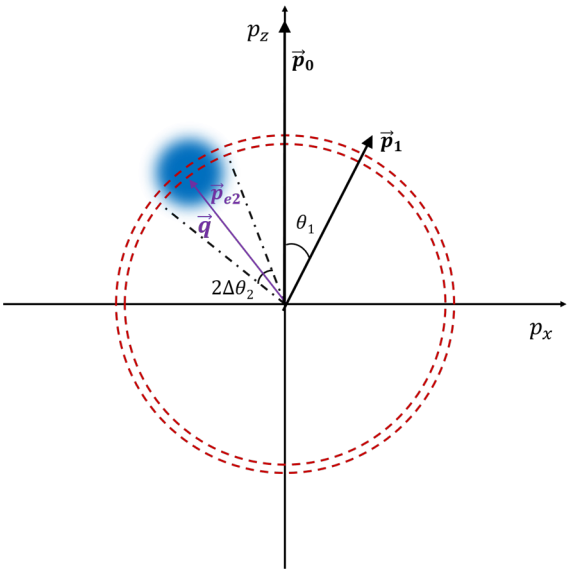

Figure 5.8: Schematic describing the projection of bound electron in the momentum space for collisions involving large momentum transfers within the first-Born approximation. The region within the red dashed lines represents the ejected electron energy interval within which the counts are integrated.

In (e,2e) experiments such an interaction can be understood as shown in the figure 5.8. Within the first-Born approximation, where the collision is described as a single interaction, the bound electron is projected to the Px-Pz plane in the momentum space, with a magnitude equal to $\vec{p}_{e2}$. For binary collisions, the entire momentum transferred in one single collision is carried by the ejected electrons. Therefore, the ejected electron momentum is the sum of the initial bound momentum (the Compton profile J($|\vec{p}_{orb}|$) and the momentum transfer, i.e., $|\vec{p}_{e2}| = |\vec{q}| +$J($|\vec{p}_{orb}|$). The differential cross-section at certain E_2, i.e., the angular distribution, basically shows the angular width of the Compton profile ($2\Delta\theta_2$) of the 2s bound electron. Figure 5.9 shows a comparison of the binary peak at ejected electron energy $E_2 = 10$ eV and 15 eV with the theoretical Compton profile for the 2s orbital of lithium [156, 157] transformed to the angular width using the formula $\Delta\theta_2 = \tan^{-1}\frac{|\vec{p}_{orb}|}{|\vec{p}_{e2}|}$, where $\vec{p}_{orb}$ is the linear momentum of the bound electron in the 2s orbital. The position of the binary peak is shifted to zero for better comparison with the Compton profile. It is evident that at $E_2 = 15 \pm 2.5$ eV the distribution matches exactly with the Compton profile. For lower energy ($E_2 = 10 \pm 2.5$ eV in figure 5.9a), there is enhanced emission outside of the Compton profile. At lower scattering angles ($\theta_2 = 15° \pm 2.5°, 20° \pm 2.5°$) an angular shift of the binary profile is present due to increasing post-collision interactions and three body contributions. Whereas at $\theta_2 = 25° \pm 2.5°$ and $E_2 = 15 \pm 2.5$ eV, the peak position matches with the momentum transfer direction and the angular width of the binary peak matches with the Compton profile. In addition to that, the magnitude of momentum transfer $|\vec{q}| = 1.1$ au is approximately equal to the magnitude of ejected electron energy $|\vec{p}_{e2}|$ at this condition, indicating that the interaction is predominantly with the bound electron. Therefore, a conclusion can be made that the two body processes dominate at this ejected electron energy and scattering angle.

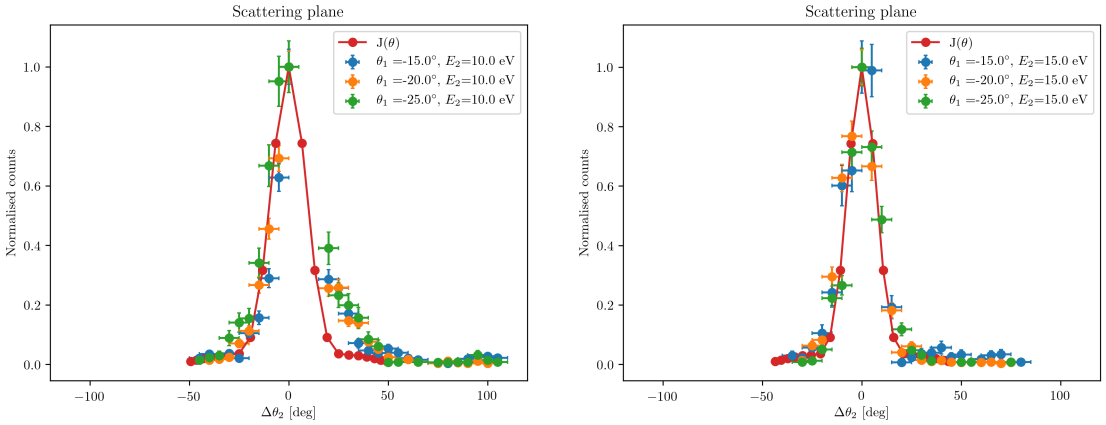

(a) (b)

Figure 5.9: Comparison of angular width of the binary peak at various scattering angles and ejected electron energy (a) $E_2 = 10 \pm 2.5$ eV and (b) 15 ± 2.5 eV to the angular width of theoretical Compton profile J($|\vec{p}_{orb}|$).

5.2 (e,2e) of 1-Methyl,5-Nitroimidazole at 97 eV impact energy

Nitroimidazoles (NIZs) have been attracting keen attention recently because of the clinical success in the radiosensitizing effects in radiation therapy [158]. Radiosensitizers are chemicals that can accelerate the damaging effect of tumour cells by ionizing radiation. Radiation damage is caused either directly by DNA strand breaks or indirectly by hydrolysis of water to create free radicals $OH^{\bullet}$, which can then react with DNA to form DNA radicals. In the presence of oxygen these damaged DNA are falsely repaired, making them unable to reproduce. Whereas, in the absence of oxygen (hypoxia) these radicals can be quenched by thiol-mediated hydrogen atom donation and DNA cross-link repair is possible, thus increasing the survival rate of damaged tumours. Nitroimidazoles are classified to be oxygen mimics due to their high electron affinity. However, the detailed mechanism of the radiosensitizing effects of NIZs is still unknown. Recent results suggest that the enhancement of radiation damage would be due to the formation of fragments such as NO/NO_2 through radiation-induced redox reactions.

Electron-ion coincidence studies of valence ionization by low energy electrons ($\sim$100 eV) provide important information in the context of radiation-induced DNA damage since the secondary electrons produced in medical X-Ray irradiation are of the same energy range and can cause DNA damage by ionizing mostly the valence orbitals. Such experiments allow us to select specific fragmentation channels and to analyse the electron spectrum corresponding to it, giving us information about the electronic structure of the molecules and the changes to it, due to the changes in the molecule itself. For example, dissociative electron attachment studies [159] and photoelectron-photoion coincidence (PEPICO) [160, 161] measurements have shown that the methylation of NIZs effectively quenches the NO production. Kinematically complete experiments like (e,2e) can provide information about the ionization dynamics involved in these processes, by measuring the fully differential cross-sections (FDCSs) from the momentum vectors of the outgoing fragments. Here we present the modifications to the existing reaction microscope to allow the FDCS measurement of Nitroimidazoles, which is solid at room temperature. A deriva-

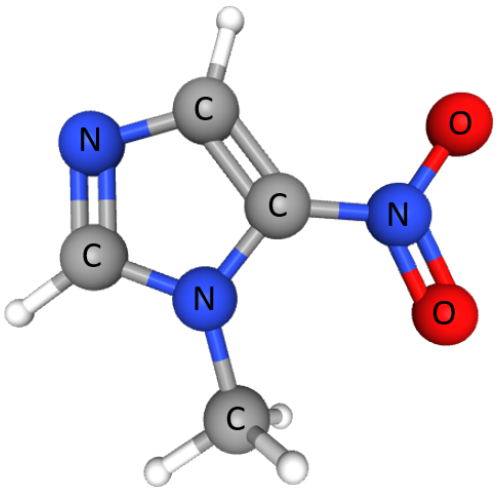

Figure 5.10: Schematic shows the structure of 1-Methyl,5-Nitroimidazole.

tive of the Nitroimidazole molecule, 1-Methyl,5-Nitroimidazole (1Me5NIZ/$C_4H_5N_3O_2$) is chosen to demonstrate the triple differential cross-section (TDCS) measurement and the experimental results are compared with theoretical calculation using multi-centre three distorted wave (MCTDW) model. The target in the solid state undergoes sublimation at a temperature, slightly higher than room temperature to produce vapours of sufficient densities for ionization with an electron beam. Subsection 3.3.2 describes in detail the setup for the target preparation.

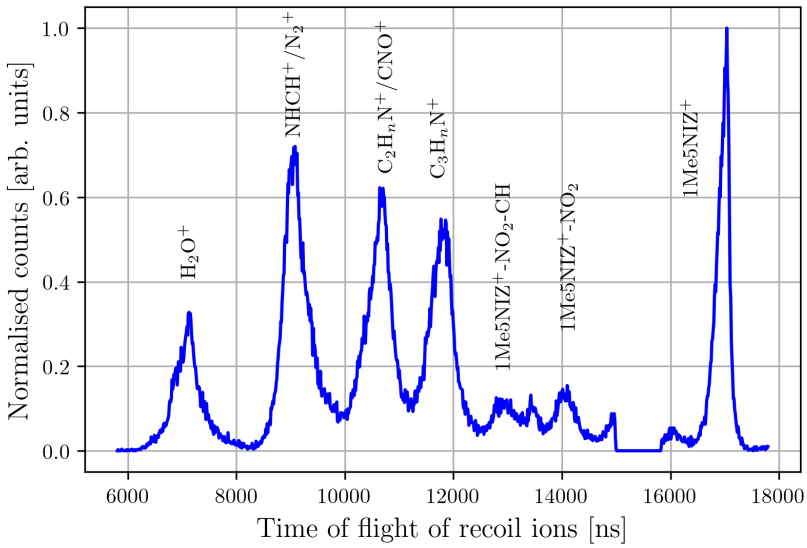

Figure 5.11: Time-of-flight distribution of fragments from 1Me5NIZ after ionization with 97 eV electrons. Ionization fragments are identified by comparing them with the photoionization mass spectra from [160]. Peaks are broadened because of the inhomogeneous electric field applied for the extraction of ions.

Figure 5.11 shows the ion time-of-flight distribution after ionization of 1Me5NIZ with 97 eV electrons. The ionic fragments detected are indicated correspondingly. The peaks are broader than usual because of the inhomogeneous electric field applied for the extraction of ions. Therefore, the momentum of ions cannot be properly reconstructed.

Nevertheless, they can be calculated from the law of momentum conservation for single ionization channels that do not undergo dissociation, if two outgoing electrons are detected in coincidence.

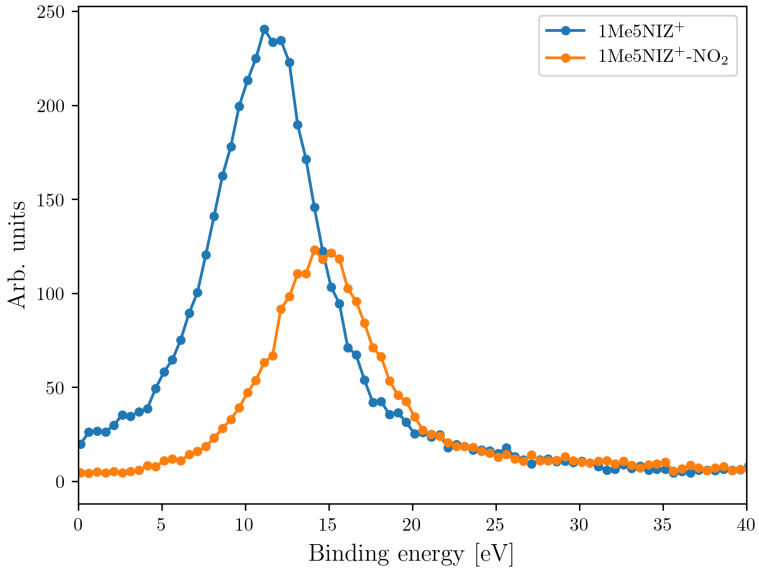

Figure 5.12: Binding energy distributions corresponding to the parent ion 1Me5NIZ$^+$ and fragment with NO_2 loss. Peak heights represent the counts of each fragment in coincidence with the corresponding two outgoing electrons.

Figure 5.12 shows binding energy distribution for electrons corresponding to the single ionization of valence orbitals to form stable parent ion (blue curve) and to the dissociation channel producing NO_2 and $C_4H_5N_2^+$ (orange curve). The peak position at higher binding energy for the dissociation fragment suggests the ionization of inner valence orbitals and subsequent dissociation.

The following discussion presents the triple differential cross-sections (TDCS) corresponding to the single ionization of valence orbitals of 1Me5NIZ that leads to the parent ion formation. Figure 5.13 shows the binding energy distribution for the channel and comparison with the calculated vertical ionization potentials of the orbitals that can lead to stable $C_4H_5N_3O_2^+$ (1Me5NIZ$^+$) parent cation [162]. Comparison of the theoretical vertical ionization potentials for the valence orbitals and the dissociation threshold [160] shows that the first five valence orbitals (6A"-9.54 eV (HOMO), 27A'-10.58 eV, 5A"-10.72 eV, 26A'-11.35 eV, 4A"-11.56 eV), including the HOMO orbital leads to the formation of $C_4H_5N_3O_2^+$ parent cation. Calculated spectroscopic pole strength for these orbitals, which is proportional to the photoionization cross-sections, suggest that all the five orbitals contribute almost equally [162]. In our experiment the contributions from these orbitals to the TDCS are not resolved individually, therefore each plot presented in the discussion shows the total TDCS from all these five orbitals.

The 3D triple differential cross-sections (TDCS), are represented as polar plots in the figure 5.14 for the scattering angles $\theta_1 = -12°, -16.5°$ and second electron energies $E_2 = 3.7$ eV, 9.5 eV. The counts are integrated within the scattering angle interval $\Delta\theta_1 = 4°$ and ejected electron energy interval $\Delta E_2 = 4.4$ eV. The ticks on each plane represent the counts in that direction. Therefore the surface of the distribution gives the counts which is proportional to the absolute TDCS. The direction and magnitude of the incoming and scattered projectile ($\vec{p}_0, \vec{p}_1$) are represented by arrows. $\vec{p}_1$ is deflected towards $-x$ and

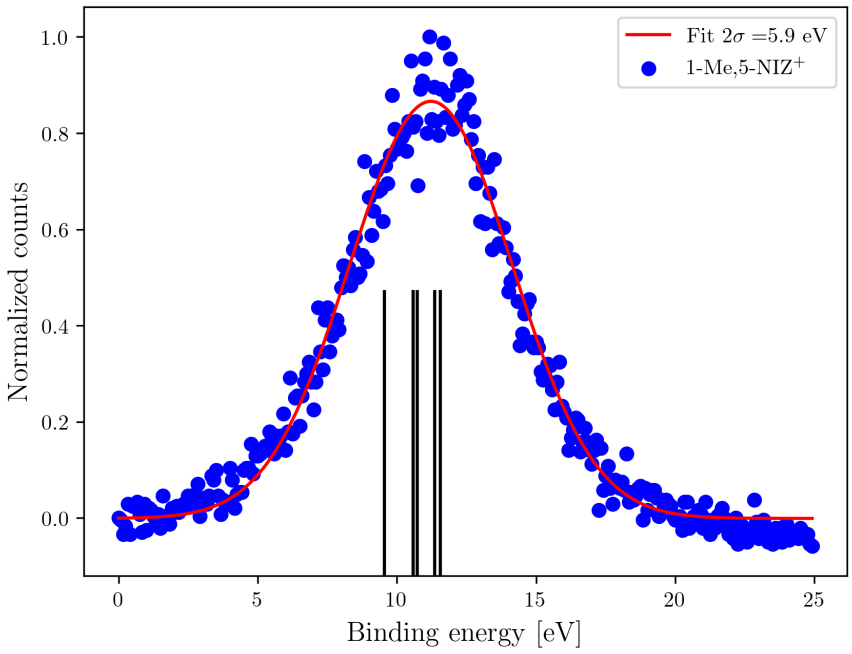

Figure 5.13: Binding energy distribution corresponding to the parent ion 1Me5NIZ$^+$. Calculated ionization energies of the five highest molecular orbitals that can lead to intact parent ion are indicated by the vertical lines [162].

$+z$ direction in the x-z plane with scattering angle θ_1. The momentum transfer vector $\vec{q}$ is calculated as $\vec{p}_0 - \vec{p}_1$ and is also represented as an arrow. In 3D plots, the length of the arrow does not represent the magnitude of $\vec{q}$. It is scaled for better visualization of the momentum transfer direction. Unlike the case of lithium shown in the previous section, one can see almost isotropic distribution. Several factors contribute to this kind of behaviour. The most prominent reason is the multi-centre nature of the target, where the ejected electron might scatter again at the different nuclei of the residual $C_4H_5N_3O_2^+$ ionic potential. This gives rise to emission in all directions filling the minima between the binary and recoil lobes. However, the presence of the binary and recoil lobes can be seen in all the 3D plots as a slight enhancement along the direction of $\vec{q}$. Higher order effects due to the multiple scattering of the projectile at the residual ion, which is significantly high in this case owing to the multi-centre nature, also contribute to the isotropic distribution. So one could expect a significantly different distribution compared to that of the atomic case.

Figures 5.15, 5.16 and 5.17 represents the TDCS in the scattering plane (x-z), perpendicular plane (y-z) and full perpendicular plane (x-y) respectively. They are compared with the TDCS values calculated using the multi-centre three distorted wave model (MCTDW) (black solid curve) [28] and the modified MCTDW-WM (green dashed curve) which takes care of the post-collision interactions (PCI) by multiplying the MCTDW cross-sections with the Ward-Macek factor [68] for the single ionization of HOMO orbital of 1Me5NIZ molecule using 97 eV electrons. The model treats the incoming, scattered projectile and the ejected electron as distorted waves in the multi-centre potential of the neutral molecule/residual ion. MCTDW cross-sections are scaled by 0.5 for better comparison with MCTDW-WM cross-sections. Since the experimental TDCS contains contributions from the first five valence orbitals, an assumption has to be made that the TDCS from all these orbitals produces similar structures. Since little is known about the

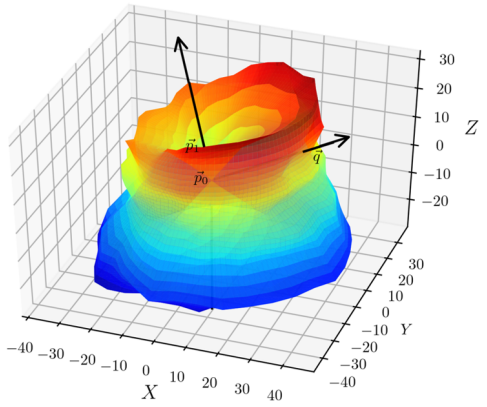

(a) $\theta_1 = -12° \pm 2°$, $|q| = 0.57$ au, $E_2 = 3.7 \pm 2.2$ eV

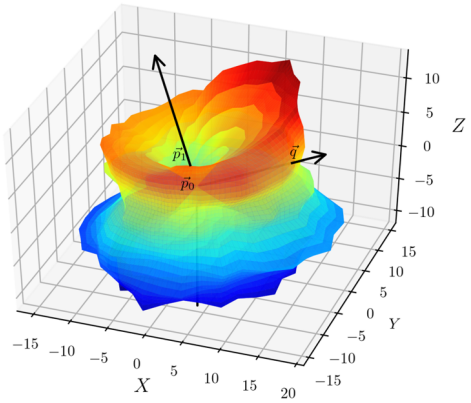

(b) $\theta_1 = -16.5° \pm 2°$, $|q| = 0.76$ au, $E_2 = 3.7 \pm 2.2$ eV

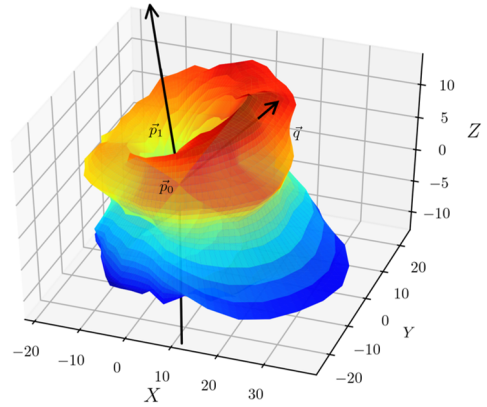

(c) $\theta_1 = -12° \pm 2°$, $|q| = 0.57$ au, $E_2 = 9.5 \pm 2.2$ eV

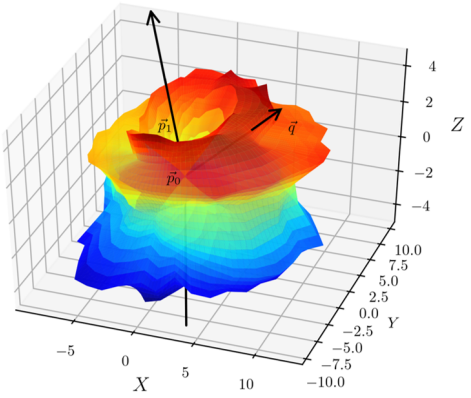

(d) $\theta_1 = -16.5° \pm 2°$, $|q| = 0.76$ au, $E_2 = 9.5 \pm 2.2$ eV

Figure 5.14: Three-dimensional triple differential cross-sections for different scattering angles and second electron energies for single ionization of the molecular orbitals which gives rise to stable 1Me5NIZ$^+$ parent ion. Ticks on the x, y and z axes represent the counts in the respective directions.

wavefunctions of these orbitals, one has to assume that the Compton profiles of these orbitals have similar shapes since they are close to each other in binding energy. In that case, the structures in the TDCS will also have similar shapes. As mentioned before, the experimental TDCS values are not absolute. They are scaled with a single scaling factor such that the cross-sections at $\theta_1 = -12°$, $E_2 = 3.7$ eV are in visual agreement with the theoretical cross-sections. All data points are cross normalised to each other by $\sin\theta_1 \Delta\theta_1 \Delta E_2$ and those in each plane are integrated within an angular interval of $\pm 20°$ out of the specified plane.

A moderate agreement between the theory and experiment can be observed from the comparison between the same. In the scattering plane, the binary and recoil region as clearly visible in the experimental TDCS as amplitude differences below and above $180°$. Both binary and recoil peaks shift away from $\vec{q}$ and $-\vec{q}$ direction due to the post-collision interaction between the outgoing electrons. A small angular shift is present in the MCTDW-WM cross-section which takes care of the PCI effects. Experimental acceptance in this region is zero, therefore one cannot conclude about such a shift. On the other hand, PCI causes a reduction in cross-section in the forward direction close to that of the scattered projectile, which can be seen in the MCTDW-WM curve. In comparison with

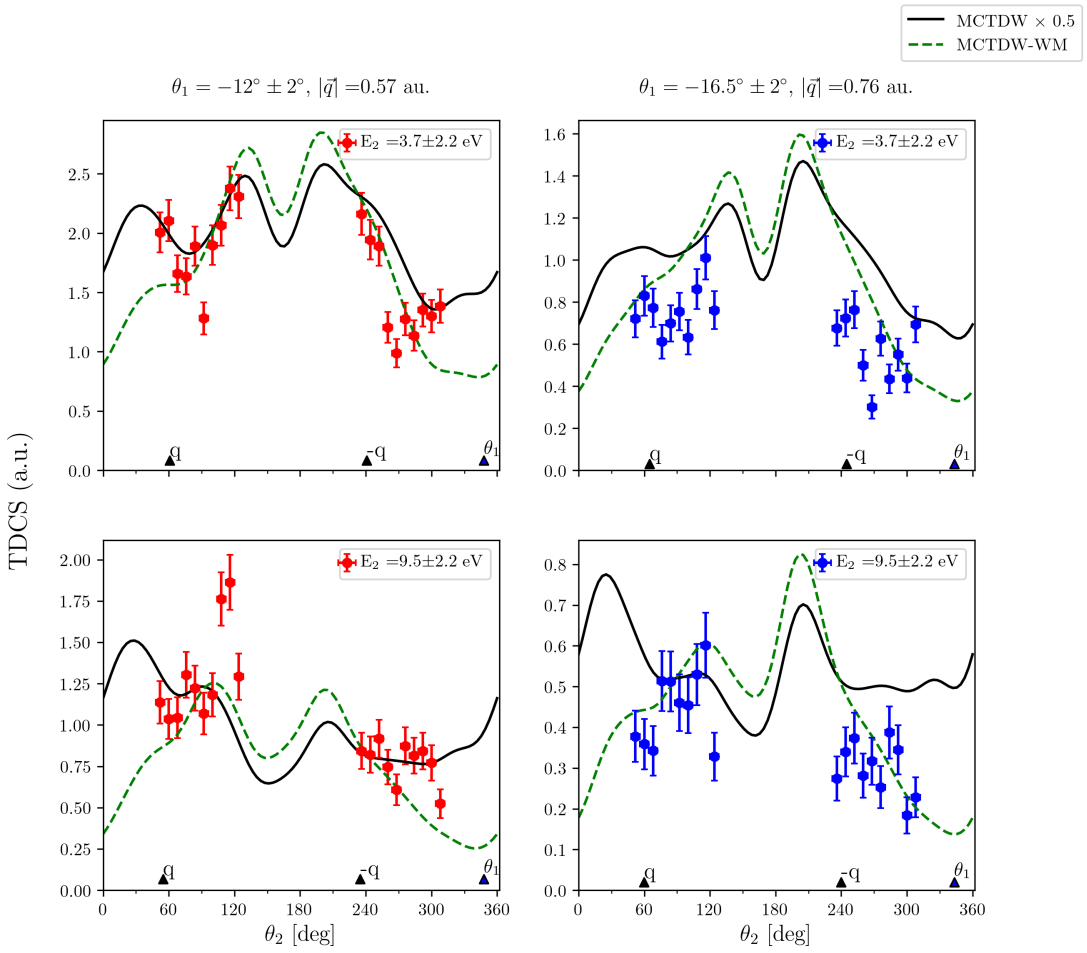

Figure 5.15: TDCS in the scattering plane for scattering angles $\theta_1 = -12° \pm 2°$, $-16.5° \pm 2°$ and ejected electron energies $E_2 = 3.7 \pm 2.2$ eV, 9.5 ± 2.2 eV as a function of the ejected electron angle θ_2. The black curve shows theoretical TDCS using the MCTDW model scaled by 0.5 and the green dashed line corresponds to MCTDW-WM.

the experimental TDCS one can observe the effects of PCI for $E_2 = 9.5$ eV, as it follows the green dashed curve close to and below $60°$, whereas for $E_2 = 3.7$ eV the experimental TDCS follows the MCTDW cross-sections, therefore the MCTDW-WM TDCS seems to over-estimate the PCI effects. However, the shape of the recoil region TDCS around $-\vec{q}$ direction seems to follow the MCTDW theory in all the cases, although the magnitudes are different. The dip in the binary peak close to the momentum transfer direction is reproduced by the theory in all the curves. This dip shows the p character of the ionized orbital [26].

Due to the symmetry of the collision process, the TDCS in the y-z plane (perpendicular plane) is supposed to be symmetric across the z-axis. This is observed in figure 5.16. Here the shape and structure of the TDCS differ significantly from that of the calculated TDCS. One can see that the binary and recoil lobe merges with each other in this plane. A dip structure is observed in all four cases roughly around $90°$ and $270°$, whereas it is around $120°$ and $240°$ in the calculated TDCSs. Similar to the scattering plane, MCTDW-WM shows smaller cross-sections in the forward direction compared to that of the MCTDW owing to the PCI effects. The experimental TDCS for $E_2 = 9.5$ eV shows a similar reduction in the forward direction, however, the magnitude of such a

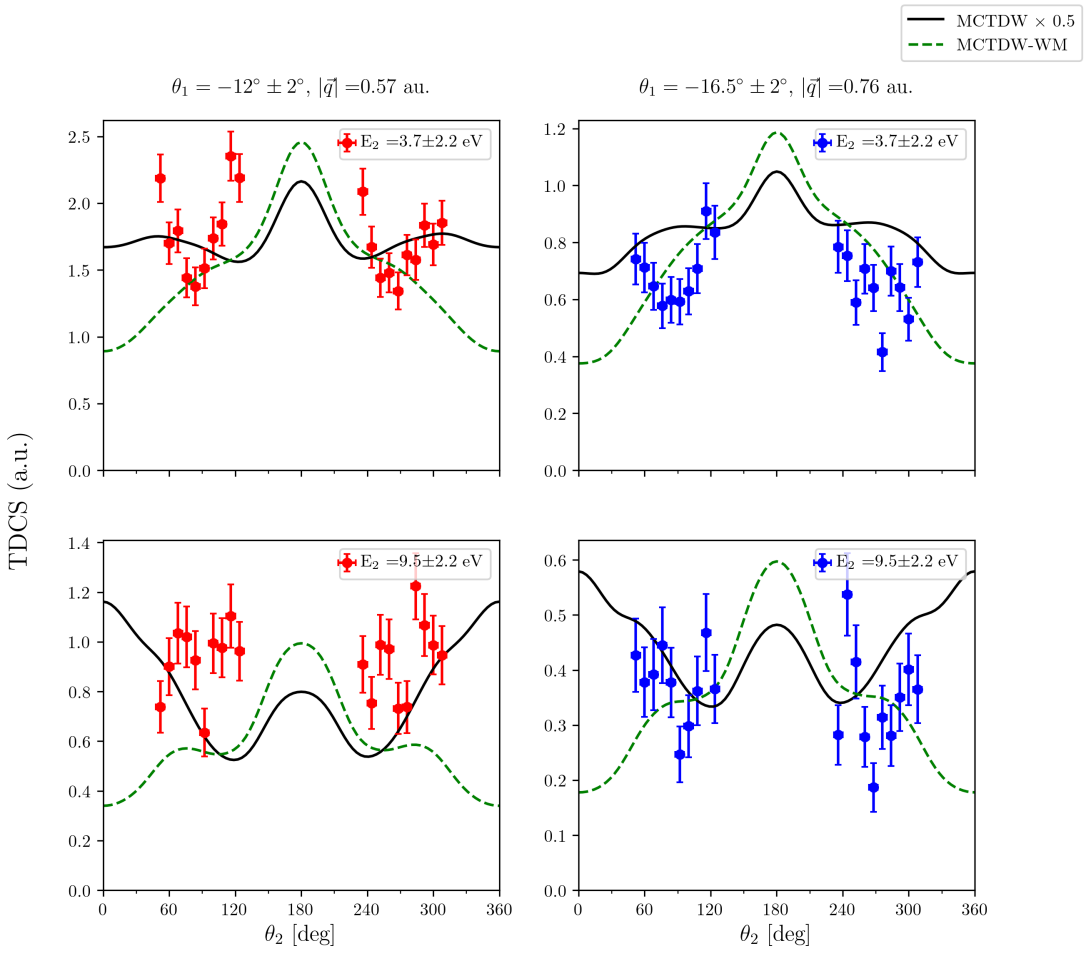

Figure 5.16: Same as that of 5.15 but for perpendicular plane.

reduction is not totally in agreement with the theory. However, for $E_2 = 3.7$ eV TDCS in the forward direction is heavily underestimated by both theories.

TDCS in the x-y plane is presented in figure 5.17 as polar plots as a function of the azimuthal angle (ϕ_2) of the ejected electrons. This plane is defined by the polar angle, $\theta_2 = 90°$ of the ejected electrons. Since it is perpendicular to the incoming projectile and the region where we define the plane does not contain any magnetic field wiggle, we have full acceptance in the entire angular range. The enhancement towards the $0°$ suggests that the plane cut through the binary region around $0°$ and the recoil, around $180°$. Similar to the perpendicular plane, due to symmetry consideration, we expect symmetric angular distribution around the x-axis which is defined by $0°, 180°$. Both theories predict two separate maxima for the binary lobe and a broader distribution around $0°$ for all the cases, except for the case of $\theta_1 = -16.5°$ and $E_2 = 3.7$ eV, where the theory predicts an additional peak around $0°$. These double maxima seem to shift closer to $0°$ for increasing ejected electron energy and merges with each other. For increasing momentum transfer, they tend to shift towards the y-axis. They indicate higher-order out-of-the-plane emissions due to the multiple scattering at the ionic core, which tends to decrease for higher ejected electron energies.

The shapes of the experimental TDCS in the binary region are in moderate agreement with the theories which reproduce the double maxima at $\sim 60°$ and $300°$ for $\theta_1 = -12.°$ and $E_2 = 3.7$ eV. Their shift close to the x-axis with increasing energy is also reproduced.

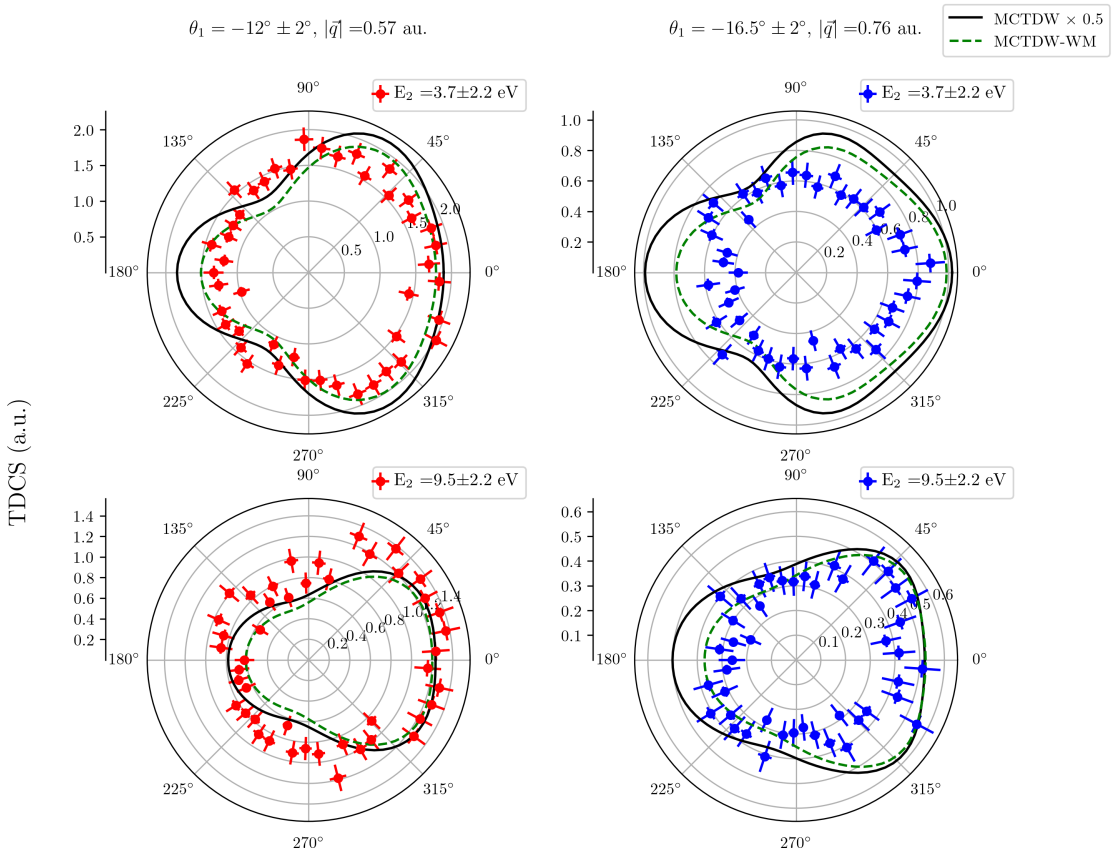

Figure 5.17: Same as that of 5.15 but for full perpendicular/normal plane.

In the case of $\theta_1 = -16.5°$ and $E_2 = 3.7$ eV, the relative magnitude of the side maxima to the one at $0°$ is smaller compared to that of the theory. Also, the side maxima appear to be slightly shifted to $90°$ and $270°$ in the experimental TDCS. However, for higher energy and the same scattering angle ($\theta_1 = -16.5°$ and $E_2 = 9.5$ eV) the side maximum appears to be in the predicted position. Both theories predict a single maximum for the recoil lobe around $180°$, whereas the experimental shape of the recoil lobe is different from that of the predicted values. A redistribution of the recoil lobe amplitude out of the scattering plane is observed in all the cases. Such a redistribution manifests as a formation of the dip in the case of scattering angle $\theta_1 = -16.5°$. In all cases, the redistributed recoil lobe tends to superimpose with the double maxima of the binary peak, indicating a merging of both lobes. Therefore, the minima separating the binary and recoil peak in the theoretical TDCS plots is absent in the experimental TCDS, instead a broad distribution is seen around $180°$ for $\theta_1 = -12°$ and a dip for $\theta_1 = -16.5°$.

5.3 ICD in Hetreocycle dimer: Thiophene dimer

Understanding the relaxation processes like ICD after inner valence ionization of biologically relevant molecular clusters has been gaining interest in the past few years. ICD has been observed in benzene dimers which is the simplest prototype of a non-covalently bonded aromatic system bound by $\pi - \pi$ interactions [42]. It has been found that ICD is initiated by the ionization of carbon 2s inner valence vacancy. The kinetic energy release (KER) from the Coulomb explosion (CE) of the dimer strongly depends on the mutual orientation of the molecule. Therefore, information about the conformational geometry of

the dimer undergoing the Coulomb explosion can be deduced from the KER distribution. A comparison of molecular dynamics simulation with the experimentally measured KER spectrum has shown a predominant contribution of T-shaped and tilted T-shaped conformers of Benzene to the ICD events in comparison to the sandwich (S) and parallel-displaced (PD) conformers.

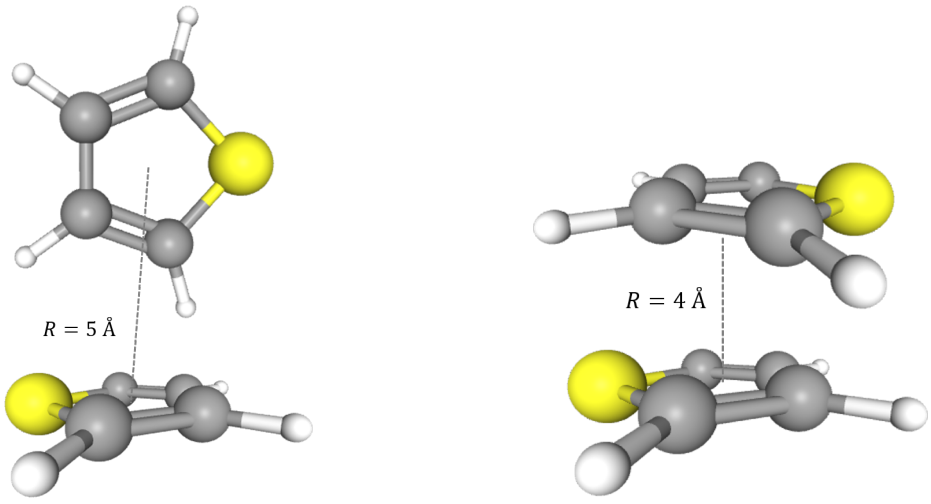

(a) (b)

Figure 5.18: Perpendicular (T-shaped) and parallel (sandwich) conformer of thiophene with interaction energies -3.12 and -1.71 kcal/mol.

This research, which was on homocycle has now been extended to heterocycles containing one electro-negative heteroatom. The following discussion describes the experimental results of ICD studies from thiophene dimers. Thiophene is a five-membered aromatic ring with one hetero atom, sulphur containing a lone pair of electrons. Theoretical calculations on the dimer geometries of thiophene consider 17 different conformers with three parallel (sandwich), seven perpendicular (T-shaped) and seven coplanar configurations [163]. Out of these, parallel (sandwich) and perpendicular geometries are found to be stable structures with interaction energies of -1.71 and -3.12 kcal/mol. In comparison with PD and T conformers of benzene conformers, which are isoenergetic, the perpendicular geometry of thiophene is considered to be more stable with similar inter-molecular separation. The larger electrostatic and dispersion interaction of the perpendicular conformer of thiophene is due to the large atomic polarizability of the sulphur atom. Figure 5.18 shows the optimised parallel (sandwich) and perpendicular shape geometries of the thiophene dimer.

Electron impact ionization has been performed on thiophene vapours from the supersonic gas jet with an electron beam of energy 103 eV. Thiophene vapours stored in a reservoir are carried by helium gas towards the supersonic gas jet assembly where it undergoes condensation to form clusters at the nozzle during the adiabatic expansion. Ionization fragments are directed to the electron and ion detectors using electric and magnetic fields. Electrons are extracted using homogeneous electric and magnetic fields of 3 V/cm and 6.9 G respectively. For the ionic fragments, a pulsed electric field of 22.57 V/cm is used which ramps up after approximately 1μs of electron detection. For studying the double ionization channels two outgoing ionic fragments are detected in coincidence with one of the outgoing electrons. The time-of-flight spectrum for the ions is shown

in figure 5.19. A comparison with the mass spectra of thiophene after ionization with synchrotron radiation upto energies 35 eV helps to identify the fragments detected [164]. The thiophene monomer has a valence shell ground state electronic configuration with C_{2v} symmetry given by,

$$(6a_1)^2(4b_2)^2(7a_1)^2 \qquad \text{inner valence}$$
$$(8a_1)^2(5b_2)^2(9a_1)^2(6b_2)^2(10a_1)^2(7b_2)^2(2b_1)^2(11a_1)^2(3b_1)^2(1a_2)^2 \qquad \text{outer valence}$$

A comparison of binding energies of the valence orbitals [165] with the appearance energies of different fragments shows that most of the heavy fragments are produced by outer valence ionization and subsequent dissociation. The time-of-flight spectra also show the stable dication of the thiophene monomer which does not undergo further dissociation at a binding energy of 25.1 eV [164].

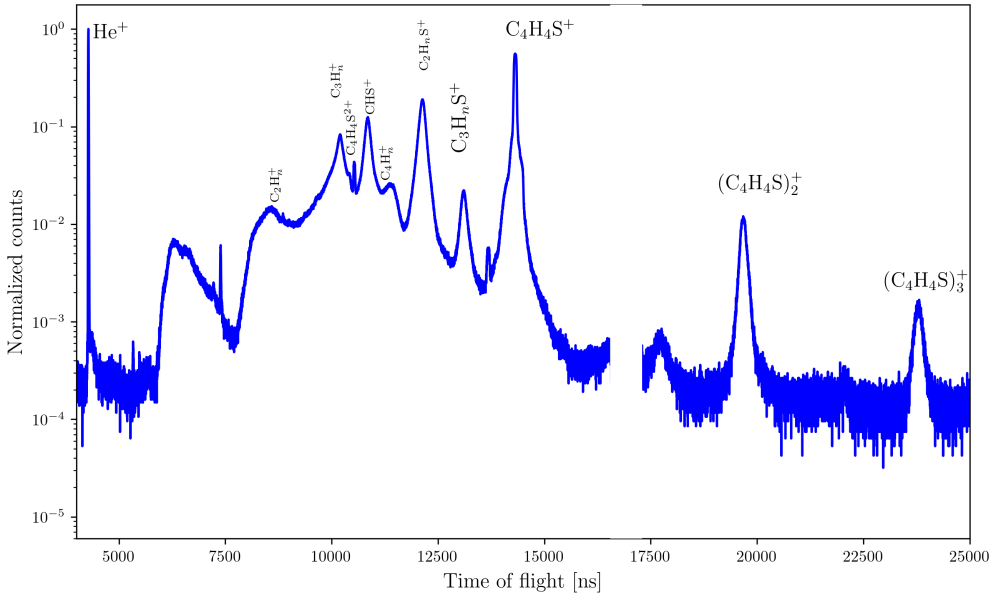

Figure 5.19: Time-of-flight distribution of fragments from Thiophene after ionization with 103 eV electrons. Ionization fragments are identified by comparing with the photoionization mass spectra from [164].

The fraction of dimers and trimers in the jet is seen from the time-of-flight spectrum around 20000 ns and 24000 ns respectively. A rough estimation shows that 5.4% of dimers and 0.86% of trimers are present in the gas jet. Fragments from the Coulomb explosion (CE) of thiophene dimers are detected around the monomer peak at 14300 ns. Shoulders towards the left of the monomer peak indicate hydrogen loss channels where the thiophene monomer loses one or more hydrogens after ionization. Towards the right of the monomer peak, there is a shoulder from the ionization of thiophene with the ^{34}S isotope. Additionally, events from ionization of bigger clusters which fragment and form $C_4H_nS^+$ also arrive in this region. To identify the CE channel, two ions detected in coincidence are plotted as shown in figure 5.20a. Calibration of the electric and magnetic fields is done using the single ionization channel of helium since it is present in the jet as the carrier gas.

Upon electron impact, one of the molecules of the dimer undergoes inner valence ionization. The excited dimer can relax by removing an electron from the same molecule

(Auger decay) or by transferring the relaxation energy to the neighbouring molecule and subsequently removing an outer valence electron from the neighbour (ICD). If the binding energy of the ionized inner valence orbital is less than the double ionization threshold of the monomer, the only channel open for relaxation is ICD. The resulting final state with charges on both centres undergoes the Coulomb explosion. Fragments gain kinetic energy from the Coulomb repulsion and are emitted back-to-back. Following the momentum conservation, they appear on a diagonal line in the time-of-flight coincidence map. The diagonal in figure 5.20a within the red marked region corresponds to the CE fragments of the dimer. The vertical and horizontal line at the time-of-flight position corresponding to the zero momentum thiophene monomers ($C_4H_4S^+$) (within the back dashed boxes) belongs to false coincidences of different mass fragments with singly charged thiophene monomers. Besides those, there are events from the above-mentioned hydrogen loss channels and ionization of bigger clusters, which appear within the same region constituting a broad background around the dimer coincidence line. All these channels involving dissociation do not fall on a line, since the abstracted neutral fragment which is not detected, carries part of the momentum gained from the Coulomb explosion. In order to separate events from CE of thiophene dimers from these background coincidences, we select events which have a vector sum of the ion momenta close to zero. In the momentum sum versus KER plot (figure 5.20b), these events appear as a separate island with the sum of ion momenta less than 20 a.u., while the kinetic energy release is rather large.

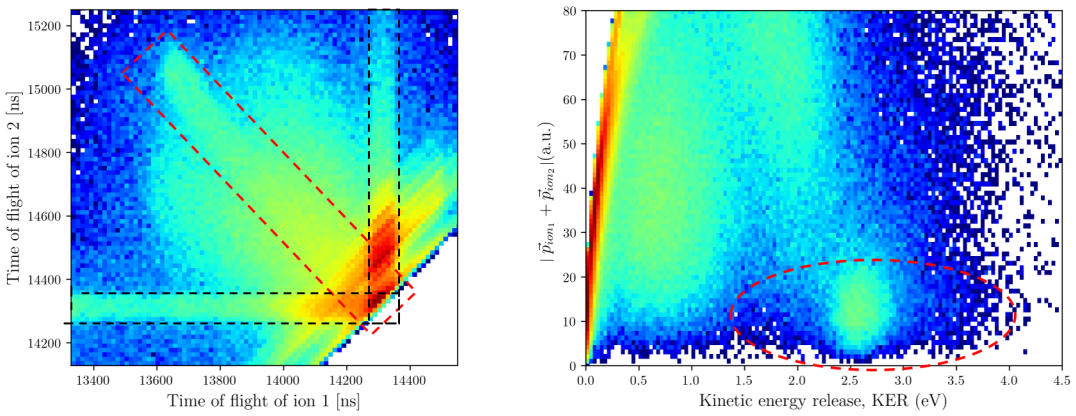

(a) (b)

Figure 5.20: (a) Time-of-flight coincidence of two ions. The marked region shows the coincidence between ions from the Coulomb explosion of the thiophene dimers. (b) Sum momenta of the ions in figure 5.20a versus the kinetic energy release. Marked region shows the events from the Coulomb explosion of thiophene dimers. Thus good events can be separated from the background in figure 5.20a.

Figure 5.21 shows the momentum coincidence map in x, y and z directions. Detected ions have a momentum of around 140 a.u. Resolution in the z and y appears considerably different from that of x direction as seen from the width of the diagonal in the momentum coincidence maps. The width in z direction is due to the inhomogeneous pulsed electric field used for the extraction of ions, whereas in y direction, it is due to the velocity of gas jet. In both directions, the ion resolution is worse than the x direction. Some events beyond 90 a.u are lost in the y momentum coincidence due to the presence of electron gun. This can be seen from the position distribution of ions with large transversal momentum (figures 4.5and 4.3b). Therefore, ion pairs where one ion is lost from hitting the electron

gun are not visible in y momentum coincidence plot (figure 5.21b). Hence, the maximum momentum detected along the y direction is 90 a.u. As a consequence of these missing momenta in y direction, a decrease in intensity is observed in the low momentum region (< 50 a.u.) of the x and z momentum coincidence maps, where these events are supposed to be present.

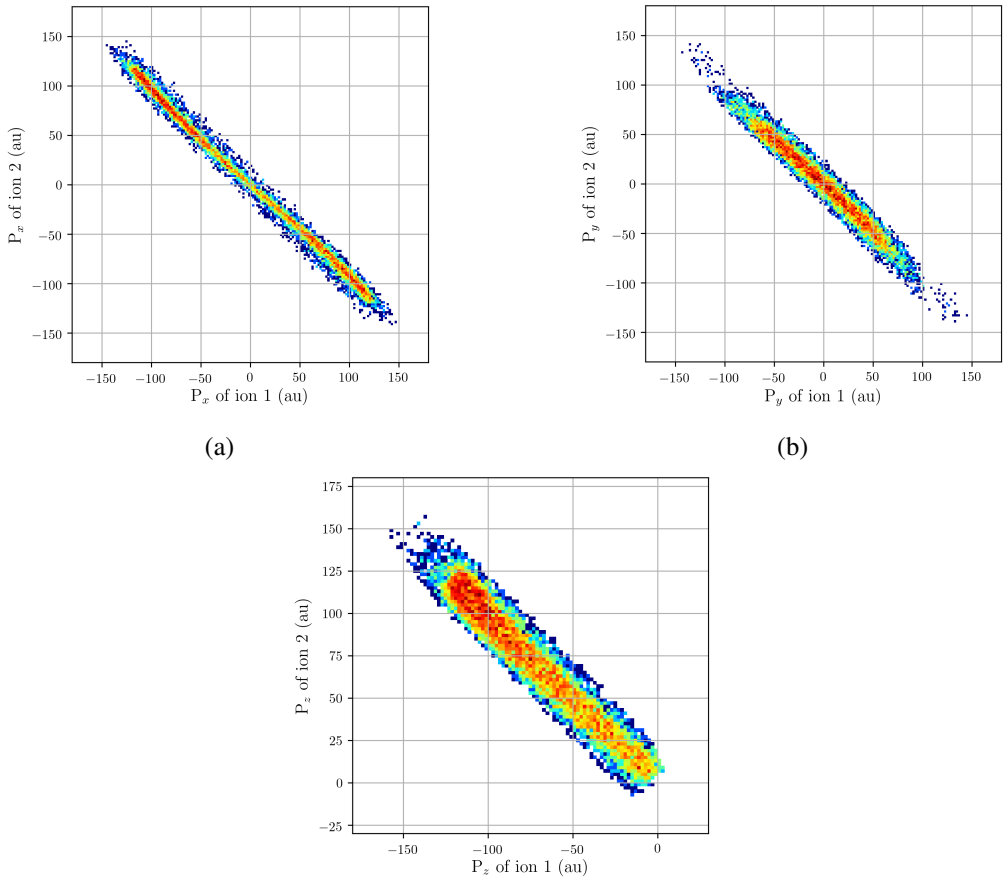

Figure 5.21: Momentum coincidence maps of ions from thiophene dimers in (a) x (b) y and (c) z directions separated from the background.

The kinetic energy release (KER) from the Coulomb explosion of thiophene dimers is shown in figure 5.22. The distribution peaks at 2.6 eV and extends from $\sim$ 1.5 eV to 3.7 eV. This is compared with the *ab initio* molecular dynamics (AIMD) simulations for the minimum energy conformer of thiophene (T-shaped I conformer [163]) preformed using the Gaussian 16 package [166] (Details of the simulation are similar to previous works [42, 146]). The equilibrium inter-molecular separation of the T-shaped conformer with minimum energy (I conformer) is around 5 Å and the expected Coulomb energy from this separation is approximately 2.9 eV, which is higher than the measured peak value of the KER distribution. It was observed in other molecular dimers that part of the kinetic energy released is transferred to rotational and vibrational degrees of freedom [42, 167]. Therefore, one can expect KER values lower than the Coulomb energy between the ionized fragments. Similarly, the minimum energy geometry of the sandwich conformers (conformer B) is expected to have KER at 3.6 eV and that of the coplanar conformers (conformer K) at 2.2 eV. The experimental KER distribution is in excellent agreement

with the AIMD simulations for the T-shaped conformer (I) and shows that a larger fraction of dimers in the jet has T-shaped geometry. However, the contributions from other T-shaped conformers cannot be excluded, since they have similar intermolecular separations. The lower tail of KER spectra indicates the presence of coplanar conformers and that at larger KER indicates contributions from sandwich conformers.

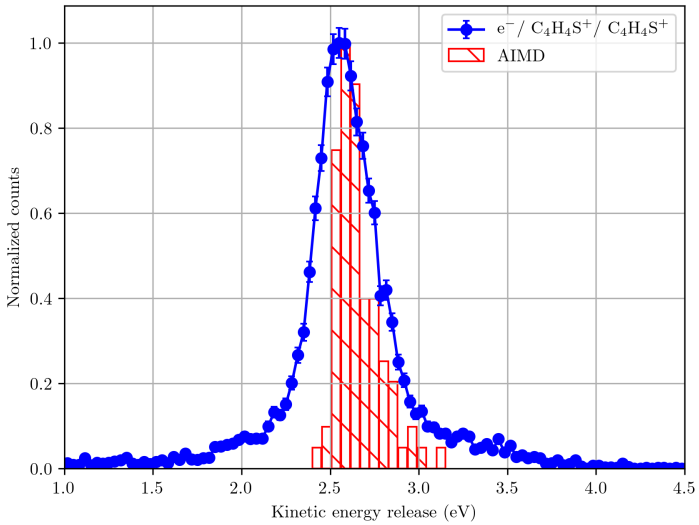

Figure 5.22: Measured KER spectra for Coulomb explosion of thiophene dimers. Red bar distribution shows the AIMD simulation for the T-shaped conformer with minimum energy structure (I) [163]. The simulated KER distribution is communicated privately by Dr. Xueguang Ren.

5.3.1 Comparison of CE channel with monomer inner valence ionization channel

The projectile energy loss spectrum, calculated as $E_0 - E_1$, for the CE channel of the thiophene dimers is shown in figure 5.24. The spectrum shows an onset at ∼20.0 eV, which indicates the binding energy of the ionized inner valence orbital. In order to identify the initial inner valence vacancy from which the ICD is initiated, we compare the projectile energy loss spectra of the ICD channel with the dissociation channels of the monomer after inner valence ionization of the same state. Excited monomers after inner valence ionization relaxes by dissipating energy to the vibrational and rotational states. If the dissipated energy is higher than the binding energy of different bonds within the molecule, it breaks apart into ionic and neutral fragments. Valence shell photoionization measurements give comprehensive information about such fragmentation channels [164]. The appearance energies, ie. the minimum photon energy at which different ionic fragments are produced indicate the binding energy of the ionized orbital.

In thiophene, most of the heavier fragments are produced from the ionization of the outer valence orbitals. Principle fragmentation processes following the valence shell photoionization, their appearance energies and the possible orbital from which the ionization takes place are summarized in table 5.1.

The fragments C_3H^+ and $C_2H_2^{+\bullet}$ have similar appearance energies 21.4 ± 0.2 eV and 19 ± 0.8 eV, respectively, and it indicates that they come from the same inner valence

Reaction	Appearance energy [eV] [164]	Possible orbital [165]
$C_4H_4S^{+\bullet} \rightarrow C_2H_2S^{+\bullet} + C_2H_2$	12.2	$2b_1(\pi)$
$C_4H_4S^{+\bullet} \rightarrow C_3H_3^+ + CHS^\bullet$	12.82	$2b_1(\pi)$
$C_4H_4S^{+\bullet} \rightarrow CHS^+ + C_3H_3^\bullet$	12.81	$2b_1(\pi)$
$C_4H_4S^{+\bullet} \rightarrow C_3HS^+ + CH_3^\bullet$	12.9	$2b_1(\pi)$
$C_4H_4S^{+\bullet} \rightarrow C_4H_3S^+ + H^\bullet$	13.05	$2b_1(\pi)$

Table 5.1: Fragments of thiophene after outer valence ionization, their appearance energies and possible orbital from which the ionization took place.

orbital [164]. Possible fragmentation channels for these ions are as follows,

$$C_4H_4S^{+\bullet} \rightarrow C_3H^+ + CS + 3H^\bullet \tag{5.1}$$

$$C_4H_4S^{+\bullet} \rightarrow C_2H_2^+ + CH + CHS \tag{5.2}$$

These fragment ions arrive within the shaded regions in the time-of-flight plot 5.23a. In addition to them, fragments of m/q ratio close to C_3H^+ and $C_2H_2^+$ but with higher kinetic energy may also arrive within this time-of-flight interval. In order to minimise the fraction of such ions with large momenta, events corresponding to $C_3H^+/C_2H_2^+$ ions with low kinetic energy are chosen by selecting the events that arrive at the centre-of-mass of the ion position distribution as shown in figure 5.23b.

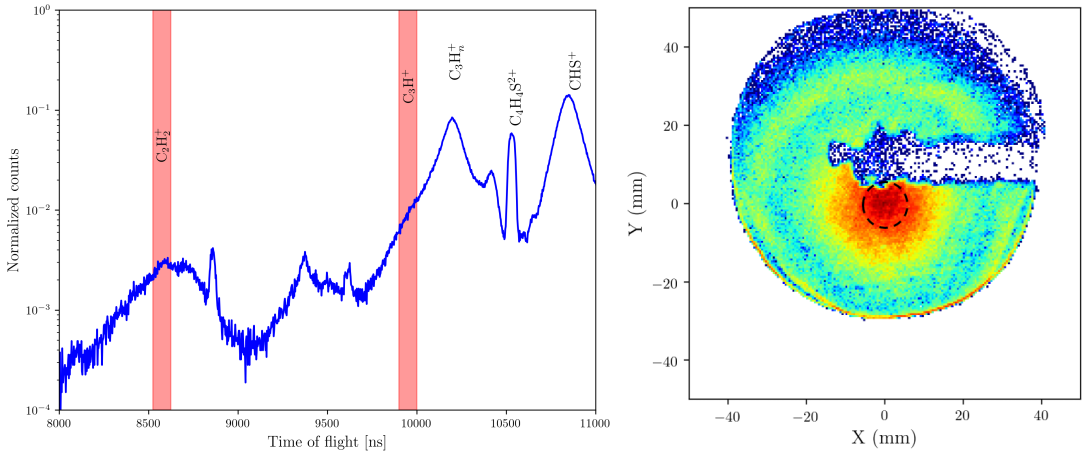

(a) (b)

Figure 5.23: (a) Red shaded region in the time-of-flight distribution shows the arrival time of the fragments $C_2H_2^+$ and C_3H^+ after inner valence ionization of thiophene monomer and within the black dashed circle in figure 5.23b. (b) Position distribution of ions corresponding to the time-of-flight window given by the red-shaded region. The outer circle indicates fragments from the double ionization of the monomer. The inner region shows events that emerge from the dissociation. Ions which have low kinetic energy within the black dashed circle correspond to those having the same initial excited state as the ICD events before double ionization leading to CE.

Projectile energy loss spectra corresponding to the monomer ionization channels (C_3H^+ and $C_2H_2^+$) are compared with that of the ICD channel as shown in the figure 5.24. The similarity of the three spectra suggests that all three channels correspond to ionization of the same inner valence orbital. The onset of energy loss spectra gives the binding

energy of the ionized orbital. Additionally, the blue dashed curve shows the energy loss spectrum for single ionization of helium with binding energy (BE) of 24.6 eV at the onset of the spectrum. The tail close to the onset is due to the experimental resolution which is estimated using FWHM of the energy sum distribution ($E_{sum} = E_1 + E_2$)(refer section 4.6.3). Since the BE of ICD and monomer ionization channels are close to that of helium, we can expect the same experimental resolution for both. An onset of $\sim$ 20 eV is observed for the monomer ionization channels and the ICD channels. Another possible pathway is radiative charge transfer (RCT) [38] after double ionization of one of the constituent molecules, leading to the formation of charges on both centres and subsequent CE. The observed Coulomb explosion channel can be undoubtedly attributed to ICD since the double ionization threshold for the monomer channel is at 25.1 eV [164] and the observed onset is at $\sim$ 20 eV.

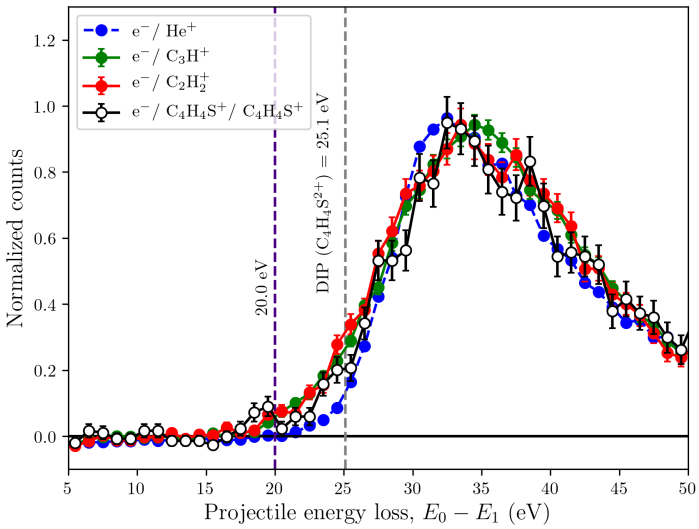

Figure 5.24: Energy loss spectra for CE channel of thiophene dimers (black open circles), monomer inner valence ionization leading to C_3H^+ (green solid circle), $C_2H_2^+$(red solid circle) and helium single ionization (blue dashed line). The dashed line at 20 eV indicates the binding energy of the CE channel and the monomer ionization channels. Grey dashed vertical lines indicate the double ionization threshold of the thiophene monomer.

An estimate of the minimum energy required to undergo ICD can be calculated as the sum of the HOMO orbital binding energies of both neighbouring molecules and the Coulomb energy,

$$BE_{ICD}^{min} = 2 \times BE_{HOMO}^{thio} + E_{Coulomb} \tag{5.3}$$

The binding energy of the HOMO orbital of thiophene is given by 9$\pm$0.15 eV [168] and the estimated the Coulomb energy for the T-shaped conformer (I) with minimum interaction energy is 2.9 eV. The estimated minimum energy for ICD corresponds to 20.9$\pm$0.3 eV which is in agreement with the onset of measured projectile energy loss. A comparison with the measured binding energies of the inner valence orbitals of thiophene using photoelectron spectroscopy suggests that ICD is initiated by the ionization of $7a_1$ orbital (BE = 20.8 $\pm$ 0.15 [168]).

5.3.2 ICD electron spectrum

A comparison of ejected electron energy spectra of the monomer ionization channel and ICD channel is shown in figure 5.25a. ICD electrons are expected to be distributed

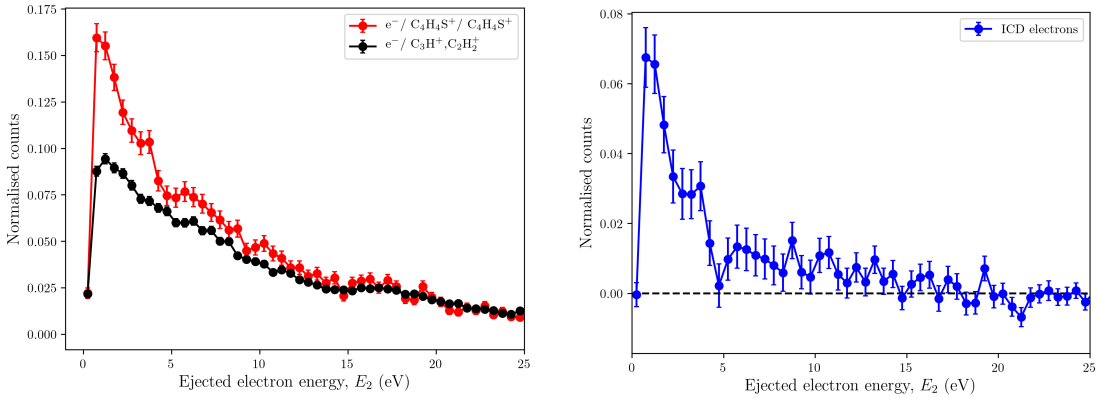

(a) (b)

Figure 5.25: (a) Ejected electron energy spectra for CE channel and monomer inner valence ionization channel. Curves are normalized from 15 eV to higher energies, since below 15 eV we expect enhancement due to ICD electrons. The difference between both curves gives the ICD electron spectrum (b).

up to ∼15 eV. Therefore, compared to the ejected electron energy spectrum of monomer ionization, we expect an enhancement in this region. The two spectra are normalised to the counts beyond 15 eV. Expected enhancement due to the ICD electrons is observed up to around 12 eV. The first data point at 0.25 eV is not reliable, due to the reduced acceptance for electrons at 0.26 eV. A difference between both curves gives the ICD spectrum (figure 5.25b).

Sequential double ionization of thiophene dimers

Another possible pathway that can lead to the formation of charges on two molecules of the thiophene dimer as in the ICD final state is- sequential double ionization (SI), where the incoming projectile removes the outer valence electron from both the molecules of the dimer successively (figure 5.26). In this case, the minimum energy required for sequential ionization and ICD is the same ($2\times BE_{HOMO}$ + Coulomb energy) 20.9 eV. Therefore, from the projectile energy loss spectra it is not clear whether ICD or SI takes place. An estimate of the fraction of sequential ionization within the Coulomb explosion events can be done by estimating the partial ionization cross-section for ICD and SI channels.

Reference to the fragmentation channels [164] and photo electron spectra [168] indicates that the ionization of $7a_1$ leads to the production of C_3H^+ and $C_2H_2^+$ ions. Assuming that ionization of the inner valence orbital leads to ICD in a dimer and to the production of C_3H^+ and $C_2H_2^+$ ions in a monomer, the sum of partial ionization cross-sections for the production of C_3H^+ and $C_2H_2^+$ ions gives the partial ionization cross-section for ICD channel. This can be calculated from the total electron impact ionization cross-section and the relative abundance of these ions in the time-of-flight/mass spectra.

$$\sigma_{\mathrm{ICD}} = \sigma_{C_3H^+}(\mathrm{E}_0 = 103\ \mathrm{eV}) + \sigma_{C_2H_2^+}(\mathrm{E}_0 = 103\ \mathrm{eV}) \tag{5.4}$$

$$= \frac{Y_{C_3H^+} + Y_{C_2H_2^+}}{Y_{\mathrm{total}}} \times \sigma_{thio}^{total}(\mathrm{E}_0 = 103\ \mathrm{eV}) \tag{5.5}$$

The relative abundance of the monomer fragments (C_3H^+ and $C_2H_2^+$) is obtained from the

NIST database [169] and is given by 1.49% and 0.68% respectively, and the total electron impact ionization cross-section for thiophene at 103 eV is given by $\sigma_{thio}^{total}(\mathrm{E_0} = 103\ \mathrm{eV}) = 11.6 \times 10^{-16}$ cm^2 [170], yielding partial cross-sections for the monomer ionization channels $\sigma_{C_3H^+}(\mathrm{E_0} = 103\ \mathrm{eV}) = 17.27 \times 10^{-18}$ cm^2 and $\sigma_{C_2H_2^+}(\mathrm{E_0} = 103\ \mathrm{eV}) = 7.95 \times 10^{-18}$ cm^2. For the ICD channel $\sigma_{\mathrm{ICD}} = 25.22 \times 10^{-18}$ cm^2 is obtained assuming that in the dimer these vacancies decay completely via ICD.

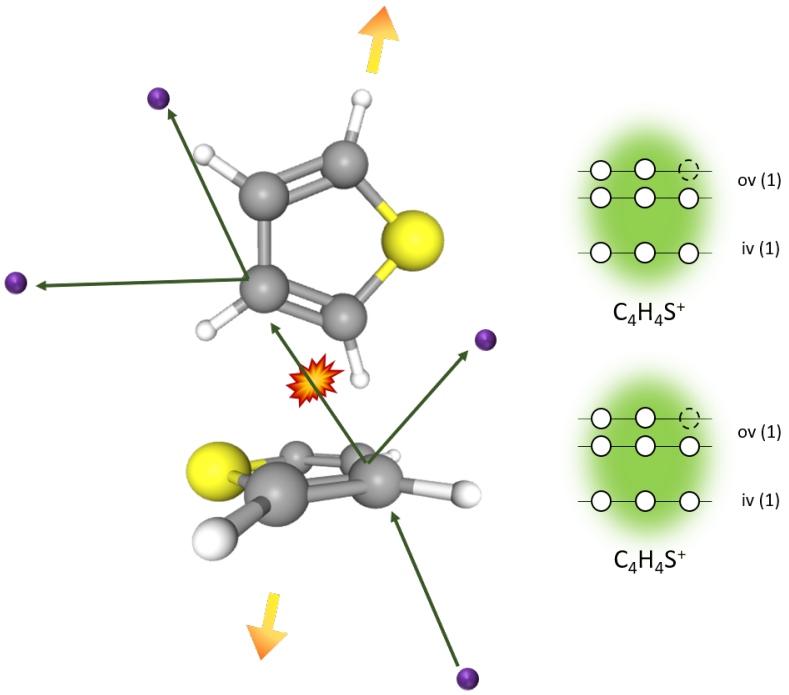

Figure 5.26: Schematic showing the sequential double ionization of thiophene by electron impact leaving the charges at two centres in the final state.

The absolute partial cross-section for SI can be calculated as a product of the partial cross-section for ionization of outer valence orbital in the first collision and the probability of the subsequent outer valence ionization of the other molecule. The second part is calculated as the ratio of partial cross-section $\sigma_{C_4H_4S^+}$ to the surface area of the sphere defined by the equilibrium intermolecular distance between the two molecules.

$$\sigma_{\mathrm{SI}} = \sigma_{C_4H_4S^+}(\mathrm{E_0} = 103\ \mathrm{eV}) \frac{\sigma_{C_4H_4S^+}(\mathrm{E_0} = 94\ \mathrm{eV})}{4\pi R^2} \tag{5.6}$$

The partial cross-section of the parent ion is calculated from the total cross-section and the relative abundance as described before $\sigma_{C_4H_4S^+}(\mathrm{E_0} = 103\ \mathrm{eV}) = 3.45 \times 10^{-16}$ cm^2 and $\sigma_{C_4H_4S^+}(\mathrm{E_0} = 94\ \mathrm{eV}) = 3.54 \times 10^{-16}$ cm^2. For the equilibrium inter-molecular separation of R = 5 Å for T-shaped conformer (I) with minimum energy structure, $\sigma_{\mathrm{SI}} = 3.896 \times 10^{-18}$ cm^2. Therefore the relative contribution of SI from the dimer is estimated as 13.4% of the CE signal. Hence it can be concluded that SI is only a minor channel in comparison to ICD.

5.4 ICD in hydrated Hetreocycles: Pyridine-D_2O

Hydrogen-bonded systems are ubiquitous in nature as water molecules surround biomatter and are weakly bound to it. In such systems several non-local decay mechanisms like ICD and ETMD open, after the inner valence ionization of either of the

neighbours. Auger decay, which is a prominent local decay mechanism, is unaffected by the presence of the neighbour. When the internal energy is not sufficient for the Auger process, ICD may occur. ETMD becomes operative in these systems as a competing channel to Auger decay, when the internal energy of the initially ionized molecule is sufficient to doubly ionize the neighbour. ICD has been studied theoretically and experimentally in systems involving biologically relevant molecules and water bound by hydrogen bonding [125, 41]. However, ETMD in such systems is not yet experimentally observed, because it forms the same final states as the Auger channel if the initially ionized molecule is water, therefore bringing in the difficulty of separating the two channels. Recent theoretical studies show that the state energy spectra of the singly ionized and the final doubly charged states are influenced strongly by the nature of hydrogen bonding, whether the water acts as electron density donor or acceptor [43]. For the experimental investigation of such systems, a nitrogen-containing heterocycle, the pyridine-water complex is chosen as an initial target.

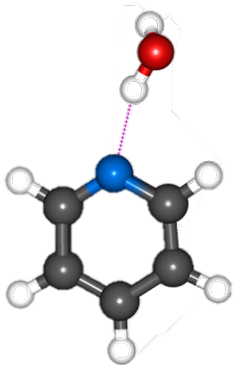

Figure 5.27: Structure of stable complex of pyridine attached to water. N$\cdots$H bond between the two molecules creates the hydrogen bond where water acts as an electron density acceptor. Image slightly adapted from [43].

Pyridine is a six-membered aromatic π system with five carbons and one nitrogen. The lone pair on the nitrogen and the two double bonds between the carbons form the conjugated π system. Upon interaction with water, the most stable structure has a hydrogen bond between the lone pair of nitrogen and one of the hydrogens of water 5.27 [43]. Here, the water acts as an electron density acceptor.

For the experimental measurements, for better separation of the coincidence lines in the time-coincidence map, D_2O is used instead of water (H_2O). Both the pyridine and D_2O, stored in separate reservoirs, are heated to produce sufficient vapour pressure and are picked up and transported to the nozzle by helium gas. Complexes of pyridine and D_2O are formed at the nozzle where the molecules cool down due to adiabatic gas expansion. Thus mixed clusters of D_2O and pyridine of different sizes are present in the gas jet. The molecules in the jet are ionized by an electron beam of 103 eV. The resulting ionization fragments, the electrons and ions, are extracted by electric and magnetic fields. For extraction of electrons, a homogenous electric field of 3V/cm is used and for ions, a pulsed field that ramps up around 1 μs after the laser trigger to a maximum of 22.57 V/cm is used. Particles undergo cyclotron motion in helical trajectory with a homogenous magnetic field of 6.9 G. Helium, used as a carrier gas, facilitates the calibration of the fields.

Figure 5.28 shows the time-of-flight spectrum of ionic fragments from the gas jet con-

taining clusters of pyridine and D_2O. Pure as well as mixed clusters of water and pyridine are detected in the spectrum. Fragments from D_2O appear around 7500 ns. Fragments OD^+ and D_2O^+ are produced from the dissociation of D_2O monomers. Therefore, their corresponding peaks in the time-of-flight appear sharp. Whereas the fragment D_3O^+- originates from larger clusters containing more than one water. This process involves the dissociation of neutral species which transfers momentum to the ionic fragment. Therefore, this peak appears broad compared to the other fragments from water. Not all the ions detected, experience the same electric field. Those ions with small masses are extracted earlier. Hence, they may leave the extraction field before the electric field has reached its maximum. Heavier ones on the other hand experience a constant field for a considerable amount of time.

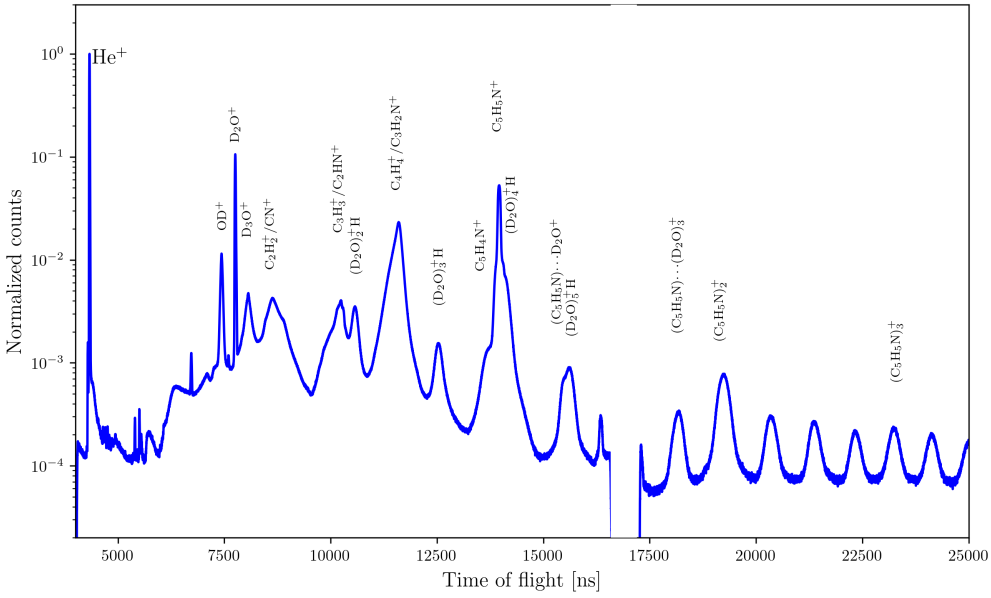

Figure 5.28: Time-of-flight distribution of fragments from pyridine and D_2O mixture after ionization with 103 eV electrons. Ionization fragments from pyridine are identified by comparing with the photoionization mass spectra from [171].

Fragments from pyridine monomers appear below 14000 ns, with the parent ion $C_5H_5N^+$ at 13894 ns. Some of them are identified by comparison with photoionization mass spectra using synchrotron radiation [171]. Previous photoelectron-photoion coincidence measurements (PEPICO) have shown that the most abundant fragment after single ionization of pyridine other than the parent ion is $C_4H_4^+$ with mass 52, which appears at 11558 ns [172]. Most of the smaller fragments are products of double ionization after Auger decay. The stable dication of pyridine monomer is not observed in the spectrum as it may undergo fragmentation after double ionization. The singly charged pyridine$\cdots D_2O$ complex appears at 15458 ns which overlaps with the singly ionized $(D_2O)_5$ cluster. Therefore, an estimation of the ratio of pyridine$\cdots D_2O$ complex to pyridine monomer is unreliable. However, with an assumption that half of this peak contains singly ionized $(D_2O)_5$, a rough estimate of dimer to monomer fraction can be obtained to be around 3.5 %.

The Coulomb explosion (CE) channel of the pyridine$\cdots D_2O$ complex is observed in the time coincidence map shown in figure 5.29a (black dashed region). Similar to the CE channel of thiophene dimers, the vertical and horizontal lines at the time-of-flight of

D_2O and pyridine monomers (Py^+) correspond to the false coincidences of ionic fragments with these monomer ions, respectively. The CE channel is observed as a sharp line which intersects with the false coincidence lines of D_2O and pyridine monomers. A broad distribution beside the CE channel is due to the Coulomb explosion of D_3O^+ and Py^+ originating from bigger clusters. The width of the distribution suggests the removal of an additional ionic or neutral fragment, indicating the origin from bigger clusters. Additionally, a faint sharp line is observed parallel to the CE channel. This is speculated to be arising from a proton transfer process from pyridine to D_2O forming D_2HO^+ and Py-H^+ which later undergo Coulomb explosion. The following discussion will be focussing only on the CE channel of D_2O^+ and Py^+.

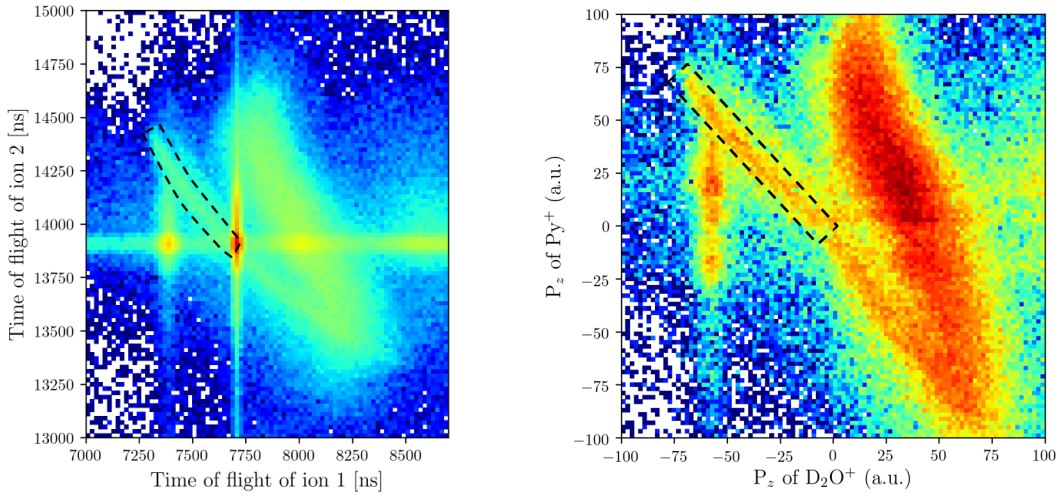

(a) (b)

Figure 5.29: (a) Time coincidence map showing the Coulomb explosion channel of Pyridine$\cdots D_2O$ dimer. (b) Momentum coincidence map corresponding to the time coincidence map in figure 5.29a. In order to separate the CE channel of D_2O^+ and Py^+ from neighbouring CE channels, events within the black dashed rectangle are selected.

Events on the CE channel in the time coincidence map appear to have a curved structure, instead of a straight line which is expected from the law of momentum conservation. This is due to different electric fields experienced by fragments moving in the $\pm z$ direction. Elongation or contraction of time-of-flight for particles moving in $\mp z$ direction is corrected using the method described in subsection 4.5.2. The reconstructed momentum coincidence map is shown in the figure 5.29b. For events with $p_z(D_2O^+) > 0$ and $p_z(Py^+) < 0$, the CE channel for D_2O^+ and Py^+ overlaps with other channels described above, therefore making it difficult to separate them. Besides, it is difficult to judge if the time-of-flight correction applied is right in this region. However, the events with $p_z(D_2O^+) > 0$ and $p_z(Py^+) < 0$ lie on a straight diagonal line after the time-of-flight correction and are clearly separated from the other possible channels within this region. For further analysis of the desired CE channel, this region is chosen (within a black dashed rectangle). Since the entire events from the CE channel of D_2O^+ and Py^+ lie on a sphere in the momentum space, selection of this particular event means selecting almost half of this sphere which will give the same distribution of KER and electron spectra.

A distribution showing the sum of momenta of ions versus kinetic energy release (KER) for the above-mentioned event selection is shown in the figure 5.30. Events are mostly distributed at low momentum sum indicating that they originate from the Coulomb

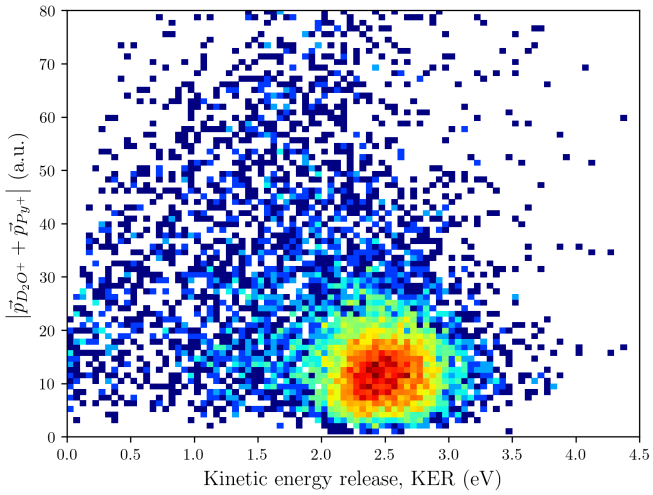

Figure 5.30: Sum of ion momenta versus kinetic energy release for the CE channel of D_2O^+ and Py^+ for events within the specified region in figure 5.29b.

explosion of the pyridine$\cdots D_2O$ complex. Further background can be reduced by selecting events with a momentum sum of less than 15 a.u.

The momentum coincidence in the x direction after the background reduction is shown in the figure 5.31a. Events with maximum momenta of 75 a.u. are observed. The corresponding KER spectrum is shown in figure 5.31b. The expected KER from the equilibrium intermolecular separation of R$=4.12$ Å is approximately 3.5 eV. The value of R is estimated from the geometry of the dimer from the theoretical calculations [43] and is privately communicated by Dr Anna D. Skitnevskaya. The measured KER spectrum shows a peak at 2.5 eV with a shoulder at 1.2 eV. Similar to the case of the thiophene dimer one can expect a slightly lower KER value than the Coulomb energy, due to the transfer of part of the Coulomb energy to the vibrational and rotational degrees of freedom. Since we lack the AIMD simulations for the CE channel, a comparison to the different structures of the complex is not possible yet.

Previous studies of CE from hydrated THF have shown a broad distribution of KER spanning from 2 eV to 5 eV [41]. An argument could be made that the charge on two centres may arise from the radiative charge transfer (RCT) process, in which one molecule initially in an excited doubly charged state could transfer a charge to the neighbour, forming the same final states as ICD. Such a transfer process occurs preferably at a lower intermolecular distance compared to the equilibrium distance. This will give rise to a larger KER value compared to that of the ICD channel. Such a process was observed in the case of argon dimers [38] as an additional channel to the ICD which produces two separate peaks in the KER spectra. Whereas, in the case of CE of the THF$\cdots$water dimer, the origin of the broad spectra was unexplained due to the lack of experimental evidence. For the pyridine$\cdots D_2O$ complex, such a broad spectrum is not observed. Therefore, one can omit the possibility of RCT. However, the shoulder peak around 1.2 eV needs attention. Previous theoretical works suggest that all other possible structures for the complex are at least 3 kcal/mol higher in energy [43, 173]. Thus, the formation of an alternative structure with a large intermolecular distance can be neglected. Previous experiments on benzene dimers suggested a possibility of an additional excitation of stretching vibration of the CH bond accompanying ICD [42]. A similar argument could be made in the case of hydrated pyridine if CH and OD stretching vibrational modes are excited which amounts

to 0.4 eV [174] and 0.34 eV [175, 176] respectively. This will produce a shift in the KER value towards the low energy from the prominent peak by the energy of vibrational excitation.

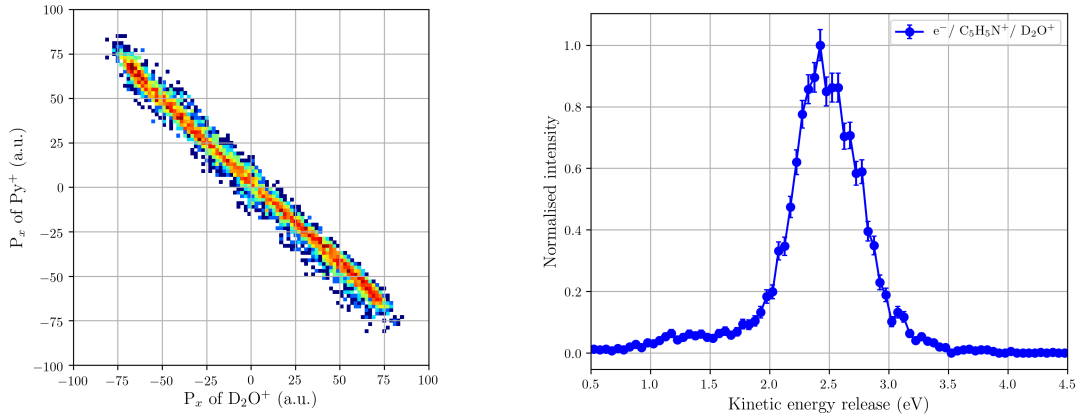

(a) (b)

Figure 5.31: (a) Momentum coincidence map in the x direction for CE channel of D_2O^+ and Py^+ after background reduction. (b) KER distribution for CE channel of D_2O^+ and Py^+ after background reduction.

5.4.1 ICD initiated from D_2O inner valence vacancy

In the following, it is attempted to identify the molecular centre and the ionized orbital initiating ICD. Therefore, we analyse theoretical calculations of the single and double ionization energies and the measured projectile energy loss spectrum. Figure 5.32 shows the calculated single ionization potentials of the pyridine$\cdots$water dimer (lower plot) and the double ionization potential leaving two charges on both molecules (upper plot, blue sticks) and on pyridine (upper plot, orange sticks). These electronic state energies should be identical for deuterated water. According to these calculations, the ICD channel opens at 22.6 eV from carbon $2s^{-1}$ vacancy producing charges on both molecules. Auger channel opens at 24.1 eV initiated by the C $2s^{-1}$ vacancy forming a final state with both the charges on pyridine [43]. To identify experimentally the electronic states from which the ICD takes place, we compare the projectile energy loss spectra of the electrons, which are detected in coincidence with the two ions from the CE channel with the theoretical single ionization spectra.

The projectile energy loss spectrum for the CE channel is shown in figure 5.34 (blue circles). The curve shows an onset at around 25 - 27 eV. The experimental resolution of this measurement is the same as for the CE channel of thiophene dimers since both measurements were done consecutively with the same experimental parameters (refer section 4.6.3). ICD can be initiated either from the inner valence orbital of D_2O or pyridine. The theoretical single ionization potentials in this energy range show carbon and nitrogen $2s^{-1}$ inner valence holes from pyridine and oxygen $2s^{-1}$ vacancy from D_2O. Since for the inner-valence vacancies in pyridine above 24.1 eV the Auger decay channel is open, which is normally faster than ICD, we first investigate water ionization as the ICD-initiating process. Singly ionized states of water are shown with green sticks in figure 5.32 and show a weak line from the oxygen $2s^{-1}$ vacancy at 29 eV which belongs to the $2a_1$

band of water. Since it is at or above the onset of the projectile energy loss spectrum one can assume that ICD may be initiated from this energy level. We can obtain the projectile energy loss spectrum for ionization of this level in water monomers which show characteristic dissociation and compare it with the CE energy loss spectrum. Ionization of this orbital in water monomers produces O^+, OD^+ and D^+ with branching ratios 24%, 16% and 60% respectively [177]. Previous photoionization measurements show that the produced O^+ has a kinetic energy of 0.3 eV [177]. It is detected in our time-of-flight distribution between 6890-7160 ns.

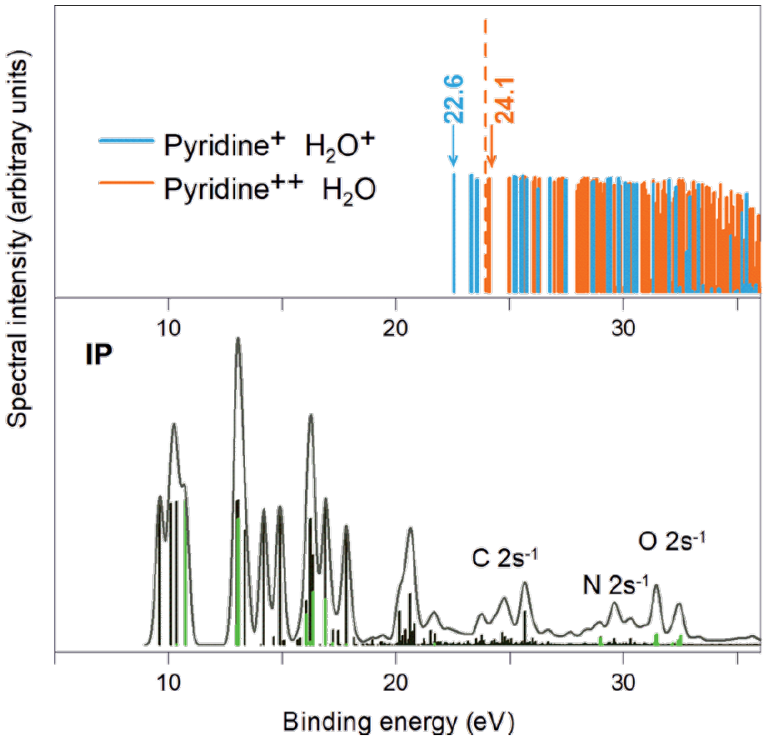

Figure 5.32: Theoretical single and double ionization spectra for pyridine$\cdots H_2O$ complex [43]. The lower panel shows the single ionization potentials of orbitals from both pyridine and water. Green sticks are orbitals water. The upper panels show the doubly-charged states with charges on pyridine molecule formed due to Auger or ETMD processes (orange sticks) and with charges on both molecules from ICD (blue sticks). The dashed orange vertical line indicates the lowest double-ionized state in pyridine.

Figure 5.33a shows the time-of-flight distribution for ionization of pure pyridine (red) and a mixture of D_2O and pyridine (blue). Both the curves are normalised to the total counts under the peak where the $C_4H_4^+$ fragment arrives (figure 5.28, 11558 ns). An enhancement of the counts after 6750 ns shows fragments from D_2O. The background counts within this time-of-flight interval where we detect O^+ fragments also consist of events from the fragmentation of pyridine after single and double ionization which is seen as an extension of the tail from 6700 ns of the red curve. O^+ fraction of 67% is estimated within this time-of-flight interval. Isolation of the O^+ fragment ions originating from the O 2s ionization of water can be done by selecting O^+ ions with small momentum corresponding to the kinetic energy ~0.3 eV [177]. This can be done with the help of the electron energy versus ion momentum plot corresponding to the time-of-flight interval of O^+ fragment (red shaded region in figure 5.33a) as shown in figure 5.33b. Y-axis shows the energy spectrum of the electrons detected in coincidence with the ionic frag-

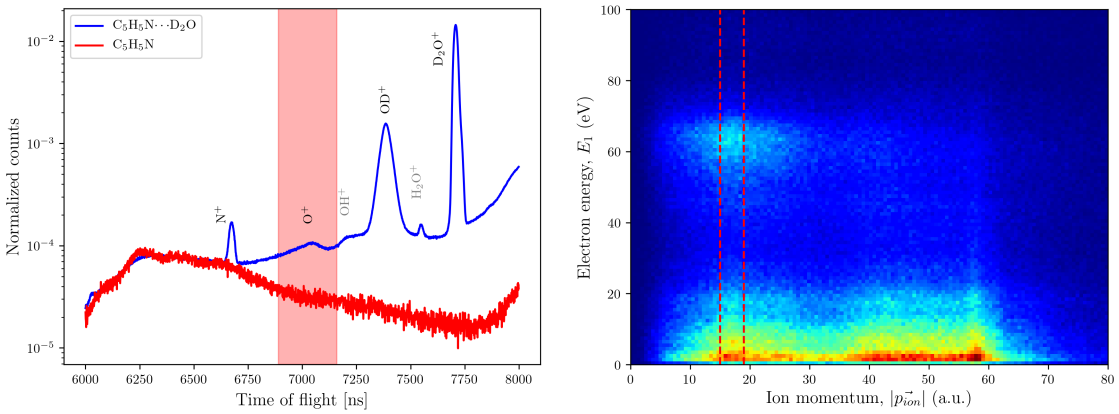

(a) (b)

Figure 5.33: (a) Red shaded region in the time-of-flight distribution shows the arrival time of O^+ fragment after inner valence ionization of D_2O. Other fragments in the spectra are indicated. (b) Electron energy versus ion momentum plot for events within the selected time-of-flight interval. Ions which have a low kinetic energy of 0.2 eV are indicated by the red dashed rectangle and correspond to those having the same initial excited state as the ICD events.

ment. The scattered projectiles are supposed to have an energy of around 70 eV and the ejected electrons up to 20 eV. This plot may contain events originating from the single and double ionization of water or pyridine (due to the above-mentioned background from pure pyridine ionization). The O^+ originating from the single ionization of O 2s orbital with 0.2 eV energy is expected around 15-20 a.u (red dashed box). The projectile energy loss spectrum for events in this region is plotted in the figure 5.34 (green solid circle) and it matches with the CE channel. Thus one can conclude that the ICD is initiated from oxygen $2s^{-1}$ vacancy.

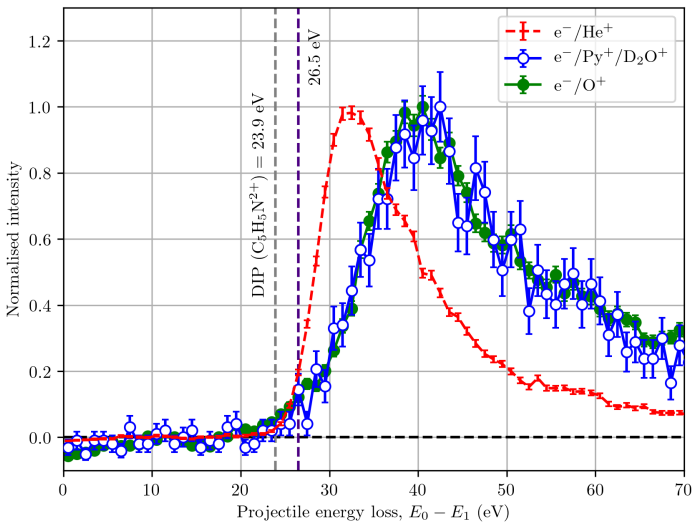

Figure 5.34: Energy loss spectra for CE channel of pyridine$\cdots D_2O$ complex (blue open circles), D_2O inner valence ionization leading O^+ (green solid circle) and helium single ionization (red dashed line). The Violet dashed line at 26.5 eV indicates the binding energy of the CE channel and the monomer ionization channels. The grey dashed vertical line indicates the double ionization threshold of the isolated pyridine monomer.

ICD electron energy spectra can be obtained in the same way as demonstrated in the previous section for the CE of thiophene dimers. The ejected electron spectrum for the CE channel of the pyridine$\cdots D_2O$ complex is shown in figure 5.35a (black open circles). For comparison, the monomer ionization spectrum of D_2O inner valence orbital ($2a_1$) leading to O^+ is shown in red open circles. Both curves are normalised above 15 eV, where no ICD electrons are expected. The spectrum beyond 15 eV is supposed to be identical for both curves, since beyond this energy we expect only scattered projectiles and the ejected electrons from the inner valence orbital which should be essentially the same for both target species. An enhancement of counts below $\sim$ 17 eV is observed due to additional ICD electrons. The difference of both spectra shown in figure 5.35b gives the ICD electron distribution. For both figures, the first data point at 0.2 eV is not reliable as the minimum energy with good acceptance is 0.26 eV for electrons. Therefore, the reduction of counts is due to bad acceptance.

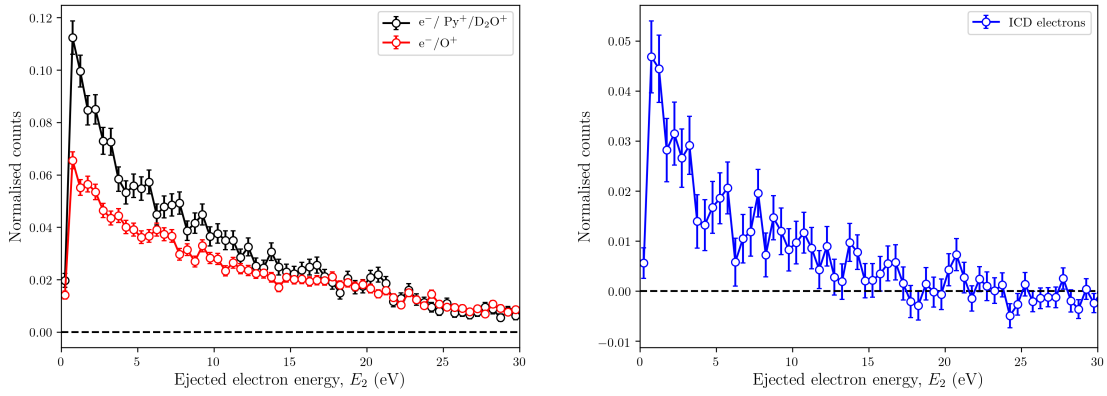

(a) (b)

Figure 5.35: (a) Ejected electron energy spectra for CE channel and monomer inner valence ionization channel. Curves are normalized from 15 eV to higher energies, since below 15 eV we expect enhancement due to ICD electrons. The difference between both curves gives the ICD electron spectrum (b).

5.4.2 ICD initiated from pyridine inner valence vacancy

The theoretical single ionization spectrum of the pyridine$\cdots$water dimer shows additional orbitals from carbon and nitrogen in the energy region of the onset of the projectile energy loss spectrum. Therefore, a question may be asked as to what happens if those inner valence orbitals of pyridine are ionized, if it may lead to ICD. Therefore, we try to identify pyridine monomer fragmentation channels which originate from inner-valence vacancies in the 25-30 eV energy range in order to obtain energy loss spectra and ejected electron spectra for comparison with the dimer CE spectra. Since these state energies are above the Auger threshold double ionization and fragmentation into two charged fragments are likely. Ion-ion coincidence measurements on pyridine monomers are not yet available in the literature within this energy range. Dissociation of pyridine below the double ionization threshold mostly gives rise to the fragment $C_4H_4^+$ [172]. Dissociative photoionization studies in the entire inner valence energy range show the production of the fragments C_4H^+ , C_3H^+ and C_2H^+ with appearance energies 29.5 eV, 27.7 eV and 29.7 eV respectively [171]. A comparison of these energies with photoelectron spectra showing the valence orbital energies suggests that these ions may be originating from the

ionization of $1a_1$ band of the inner valence orbital of pyridine [178] which is in the range from 26-30 eV.

In our time-of-flight spectrum, these fragments should be detected at 11219 ns, 9914 ns and 8446 ns respectively. However, none of the above-mentioned methods used to separate the fragments of dissociative ionization of the desired inner valence orbital produces the identical projectile energy loss spectrum corresponding to the CE channel of pyridine$\cdots D_2O$ complex. It could be due to the fact that several fragmentation channels are detected in these time-of-flight regions, hence making it difficult to separate the desired dissociation channel. Another possibility is that the ionization of $1a_1$ predominantly leads to Auger decay and subsequent fragmentation. As mentioned above the theoretical double ionization spectra in figure 5.32, show that the Auger channel is open in the binding energy region under discussion.

5.4.3 Comparison with Auger decay initiated from N $2s^{-1}$ vacancy

Several Auger and ETMD channels leading to dicationic pyridine are predicted in the theoretical double ionization spectra (figure 5.32) which may lead to fragmentation of the molecule [43]. Several such fragmentation channels are observed in the time-of-flight coincidence spectra. A comparison of such channels with the energy loss spectra of the ICD channel can render useful to understand the relaxation mechanisms of inner valence orbitals of pyridine.

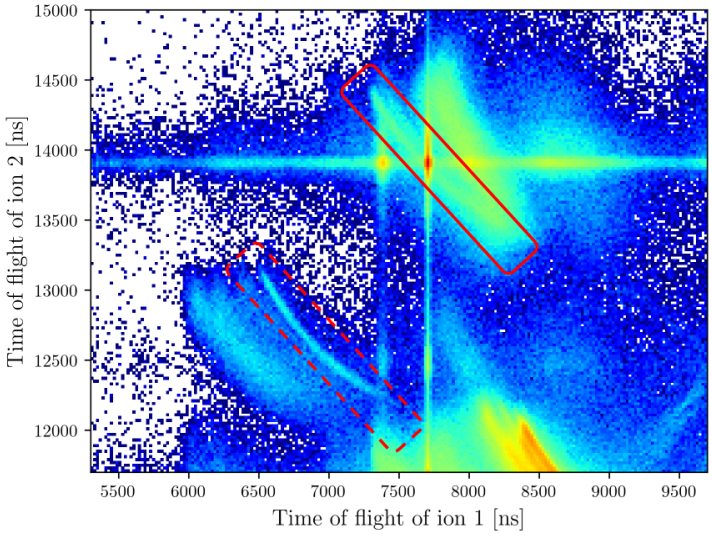

Figure 5.36: Time coincidence plot indicating the CE channel of pyridine$\cdots D_2O$ dimer (solid red box) and one of the Auger channels of pyridine leading to the fragment CH_3^+ and $C_4H_2N^+$ (red dashed box).

Figure 5.36 shows the time coincidence map of pyridine and D_2O mixtures. The solid red box shows the region of the CE channel of the pyridine$\cdots D_2O$ dimer. Another CE channel at the time coincidence position of (6750 ns, 12750 ns) is indicated by the dashed red box. The fragments involved in this Coulomb explosion should be CH_3^+ and $C_4H_2N^+$ with mass 15 amu and 64 amu respectively, giving rise to a sharp coincidence line. Additional three channels involving further hydrogen loss from CH_3^+ are observed beside the sharp line. The blurred distributions of the hydrogen loss channels are because the neutral hydrogen involved takes away a fraction of the momentum released from the

fragmentation process. The sharpness of the coincidence spectra shows that the origin of the channel should be from the isolated pyridine because the removal of water attached to it also cause blurring of the line.

A comparison of the projectile energy loss spectra for both channels is shown in figure 5.37. Both spectra are normalised to the peak around 40 eV where we expect the scattered projectile. The similarity in the onset of both spectra shows that the initially ionized state should be from the inner valence orbitals of pyridine, either from the C $2s^{-1}$ or N $2s^{-1}$, which has energy close to the oxygen inner valence orbital from which ICD is initiated. However, the spectra start to differ from each other beyond 45 eV where electron counts for the Auger channel start to increase. At energies below ∼50 eV of projectile energy loss spectra, one expects a considerable amount of scattered projectile and above ∼80 eV low energy ejected electron dominates. In the valley between both peaks, one could expect a mixture of scattered projectiles and ejected electrons. Since both channels involve the same number of electrons (scattered projectile and two ejected electrons), if the initial states were the same for both channels, one should expect the same distribution for the entire energy range. Increased counts beyond 45 eV for the Auger channel indicate, the ionization of the core orbitals which decay via the Auger process. Here the energy loss is larger and Auger electrons from these core ionized orbital have energies higher than that of the ICD electrons which have energies predominantly below 15 eV. Therefore, one can conclude that the ICD is initiated predominantly from oxygen inner valence orbital whereas the same from pyridine inner valence orbitals cannot be completely excluded. However, Auger is initiated from the inner valence orbital within the same energy range as well as from the core orbitals of pyridine. For a complete understanding of the ICD initiated from pyridine, the CE channel from the pyridine dimer should be studied.

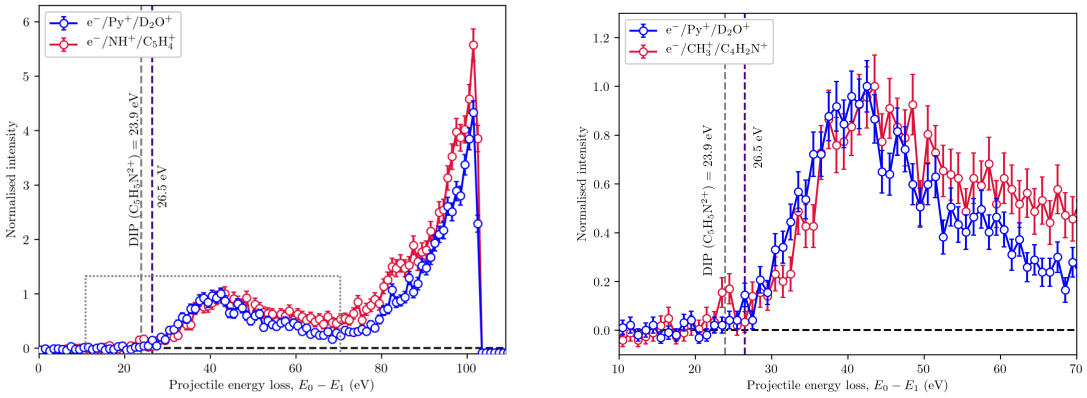

(a) (b)

Figure 5.37: (a) Energy loss spectra for the CE channel of pyridine$\cdots D_2O$ dimer (blue open circles) and the Auger channel of pyridine leading to the fragment CH_3^+ and $C_4H_2N^+$. (b) The region within the grey dotted rectangle in figure 5.37a is shown as the zoomed spectra in the range from 10 eV to 70 eV showing the similarity of both spectra up to ∼ 45 eV.

Sequential double ionization channel

Similar to the CE channel of thiophene dimers, we can expect a fraction of the Coulomb explosion channel initiated from the sequential double ionization of two molecules within the pyridine$\cdots D_2O$ complex. Here the projectile has to ionize the

HOMO orbitals of D_2O and pyridine successively. This requires a minimum energy corresponding to the sum of binding energies of HOMO orbitals of D_2O and pyridine, and the Coulomb energy between the ionized molecules (BE_{HOMO}(Py) + BE_{HOMO}(D_2O) + Coulomb energy). The binding energy of the HOMO orbital ($1a_2$) of pyridine is 9.6 eV [178] and that of D_2O ($1b_1$) is 12.6 eV [179]. The Coulomb energy corresponding to the equilibrium intermolecular distance is 3.5 eV. The estimated minimum energy for sequential ionization (SI) which amounts to 25.7 eV is slightly lower than the observed onset of the projectile energy loss spectrum of the CE channel. However, the possibility of SI cannot be completely neglected.

An estimation of the partial cross-section of SI can be done as a product of the partial cross-section for ionizing the first molecule and the probability to ionize the other molecule subsequently which can be calculated as the ratio of the partial ionization cross-section to the surface area of the sphere defined by the equilibrium intermolecular separation, R= 4.12 Å.

$$\sigma_{\mathrm{SI}} = \sigma_{Py^+}(\mathrm{E}_0 = 103)\frac{\sigma_{\mathrm{D_2O^+}}(\mathrm{E}_1 = 93.4)}{4\pi \mathrm{R}^2} + \sigma_{\mathrm{D_2O^+}}(\mathrm{E}_0 = 103)\frac{\sigma_{Py^+}(\mathrm{E}_1 = 90.4)}{4\pi \mathrm{R}^2} \quad (5.7)$$

The relevant partial ionization cross-sections are given by $\sigma_{Py^+}(\mathrm{E}_0 = 103) = 4.47 \times 10^{-16}$ cm^2, $\sigma_{\mathrm{D_2O^+}}(\mathrm{E}_1 = 93.4) = 1.38 \times 10^{-16}$ cm^2, $\sigma_{\mathrm{D_2O^+}}(\mathrm{E}_0 = 103) = 1.374 \times 10^{-16}$ cm^2 and $\sigma_{Py^+}(\mathrm{E}_1 = 90.4) = 4.6 \times 10^{-16}$ cm^2 [180, 181]. The partial ionization cross-section for SI is thus estimated to be $\sigma_{\mathrm{SI}} = 5.855 \times 10^{-18}$ cm^2.

Assuming that the ionization of O 2s orbital leads to CE in pyridine$\cdots D_2O$ complex, the partial ionization cross-section of the ICD channel is given by the partial ionization cross-section of the inner valence orbital ($2a_1$) of D_2O, which can be estimated from that of O^+ fragment produced with a branching ratio of 24% after the ionization of $2a_1$ orbital [177]. $\sigma_{\mathrm{O^+}}(\mathrm{E}_0 = 103) = 7.452 \times 10^{-18}$ cm^2 [181] yields $\sigma_{\mathrm{O2}s^{-1}} = 2.98 \times 10^{-17}$ cm^2. The fraction of SI in the CE signal is thus estimated to be 16.6%. Hence it is only a minor channel in comparison to ICD.

Chapter 6

Summary and outlook

The present study comprises measurements of electron impact ionization conducted on a variety of molecules, spanning from basic three-electron systems such as lithium to complex molecules and clusters. The objectives of this Ph.D. work can be classified broadly into two. The first part focuses on the studies of (e,2e) cross-sections on targets which are solid at room temperature and the second part is the study of relaxation mechanisms after inner valence ionization of biologically relevant molecular complexes, particularly focusing on Intermolecular Coulombic Decay (ICD). All the measurements were performed using the reaction microscope (ReMi) combined with an electron gun at the Max Planck Institute of Nuclear Physics, Heidelberg, Germany. This enables the coincidence detection of charged particles produced from an ionization event upon collision with an electron beam of well-defined energy.

The first part describes experimental modifications of the existing reaction microscope, which previously employed only a supersonic gas jet, to incorporate atomic and molecular vapours of solid targets as well. Two different experimental approaches are described in the thesis. For the measurement of (e,2e) cross-sections of lithium, an oven that produces a collimated effusive atomic/molecular beam is used. To produce a lithium beam of sufficient target density at the interaction region, the oven was heated to 800°C. (e,2e) cross-sections of a complex molecule 1-Methyl,5-Nitroimidazol which is in solid state at room temperature, is measured as a second solid molecular target. Vapours of the molecules are introduced to the interaction region using a syringe needle setup. For optimization of target density, the syringe reservoir can be heated to around 100°C.

Measured 3D cross-sections, covering a large part of the full solid angle, on lithium are the first for the single ionization of 2s orbital with intermediate projectile energy of 105 eV and could serve as a stringent test for theories. The angular distribution of the ejected electrons with energies $E_2 = 5, 15 \pm 2.5$ eV and at scattering angles $\theta_1 = -15°, -20° \pm 2.5°$ are presented. TDCS at various scattering angles and with different ejected electron energies are presented in scattering, perpendicular, all perpendicular, and azimuthal planes. In contrast to the previously measured helium TDCS [17], a large difference in magnitude is observed between the binary and recoil peaks. This is as expected since the ionization takes place from the 2s orbital which is farther away and loosely bound to the nucleus, thereby reducing the probability of backscattering in the ionic potential. A considerable amount of 'out of the scattering plane' emission is observed for small ejected electron energy as a result of higher-order effects which can be a manifestation of multiple scattering of the projectile at the target nucleus or at the other electrons in the atom. Further comparison with theoretical models is required to get better insight into the collision dynamics.

At large ejected electron energy $E_2 = 15 \pm 2.5$ eV, the recoil peak completely disappears, and the measured width of the binary peak matches with that of the theoretical Compton profile of 2s orbital for lithium. This is an important result as it shows that the three-body effects become considerably low and the collision is governed by the two-body interactions between the projectile and the bound electron. This allows us to resolve the initial state of the bound electron. A long-term goal of this project is to measure the electron-electron angular correlation of outgoing electrons after double ionization of lithium close to the ionization threshold. This was motivated by a theoretical prediction that the outgoing electrons will proceed through in a 'T'- shaped break-up pattern for lithium [31] in contrast to the Wannier break-up dynamics which predicts the outgoing electrons with mutual angle 120° with each other [15]. A low ionization cross-section of the channel at threshold energy makes the experiment technically challenging. Improved detection efficiency of the detectors and better optimization of the target can realize the experiment, even though it requires a longer beam time.

Similarly, the triple differential cross-sections (TDCS) for the single ionization channel of 1-Methyl,5-Nitroimidazole (1-Me,5-NIZ) with an electron beam of energy 97 eV, forming parent ions, are presented for ejected electron energies $E_2 = 3.7, 9.5 \pm 2.2$ eV and at scattering angles $\theta_1 = -12°, -16.5° \pm 2°$. Both the 3D distributions of ejected electrons and two-dimensional TDCS, i.e. cuts through the 3D TDCS, are presented. Comparison with the theoretical vertical ionization potentials suggests the parent ion is formed from the ionization of five valence orbitals [162] which are energetically not resolved experimentally. The experimental TDCSs are compared with that of the multi-centre three distorted wave (MCTDW) [28] model calculations for single ionization of the HOMO orbital. Since the experimental TDCS contains contributions from five orbitals, an assumption has to be made that the structure of TDCS is similar for all these orbitals, since they are very close to each other in binding energy therefore, the Compton profile corresponding to them is similar. Although the distribution is rather isotropic in all directions, enhancement of cross-section in the binary region in comparison to the recoil region can be identified. A dip in the distribution in the scattering plane at the momentum transfer direction suggests a strong p character of the ionized orbital. This is reasonable because the molecule contains three π bonds and all the ionized orbitals are probably of π nature. As expected, considerable out-of-the-plane emissions due to the multiple scattering of the projectile in the multi-centre target potential are observed. In general, the MCTDW theory is in moderate agreement with the measured TDCS. This demonstrates that the new additions to the present reaction microscope bring in the possibility to measure (e,2e) cross-sections of a wide range of targets in solid-state at room temperature which cannot be provided with the supersonic gas jet.

The second part of the thesis describes the study of ICD in biologically relevant molecules such as thiophene dimers and pyridine$\cdots D_2O$ dimers. Both targets were formed in the supersonic gas jet during adiabatic expansion. Thiophene in liquid form, which has a vapour pressure of 106 mbar at room temperature is stored in a reservoir connected to the gas line to the supersonic jet chamber. Vapours are carried to the nozzle by the carrier gas helium. To prepare pyridine$\cdots D_2O$ dimers, both the liquids stored in separate reservoirs are heated to have sufficient vapour pressure to produce cluster formation at the nozzle.

The ICD studies on thiophene were conducted as an extension of the previous studies in benzene [42], which is a pure carbon-based aromatic ring. The experiment enables us to study the effect of heteroatoms like sulphur on the ICD spectra and the ionized

orbital since it brings in changes to the inner valence orbitals. Doubly ionized dimers with charges on both molecules undergo a Coulomb explosion (CE) and are detected in coincidence with one of the outgoing electrons. Kinetic energy release (KER) from the CE of dimers is measured and, has a peak at 2.6 eV and tails extending to lower and higher KER values. A comparison with *ab initio* molecular dynamics simulations suggests that the peak distribution of the KER corresponds to the minimum energy conformer - 'T' shaped (I) among the 17 different conformers mentioned in the literature [163]. The appearance of the onset of projectile energy loss spectra, way below the double ionization threshold unambiguously suggests that the measured CE signal is from ICD. Therefore, the radiative charge transfer (RCT) process which could lead to the same final state as ICD cannot take place, since the Auger channel is closed in this energy range. Comparison of projectile energy loss spectra with that of the monomer ionization channel leading to the formation of C_3H^+ and $C_2H_2^+$ fragments and with the valence orbital energy spectra of thiophene monomers from the literature [168] suggest that ICD is initiated from the $7a_1$ band of the C $2s^{-1}$ orbital. In addition to that, an estimation of sequential double ionization of thiophene dimers leading to the same final states as ICD is done and found to constitute not more than 13.4% of the CE signal. The ion-ion time coincidence map of thiophene also shows several fragmentation channels after the double ionization of the monomer. So far, these channels remain unanalysed. The study of these channels can give more insight into the Auger processes initiated from the inner valence orbitals in the molecules which can be a competing decay channel within this energy range.

Experiments on hydrated pyridine were conducted as part of the studies on the effect of the hydrogen bond position on the ICD process. Theoretical calculations show that the presence of a hydrogen-bonded neighbour can open additional non-local relaxation mechanisms like ICD and ETMD. It was shown by theory that water in the electron-accepting position can cause additional opening of ICD channels from the C $2s^{-1}$ orbital and water in electron-donating position can open Auger channels from the C $2s^{-1}$ vacancies [43]. First experiments towards these studies where conducted on pyridine$\cdots D_2O$ dimers, where water acts as an electron density acceptor with hydrogen attached to the nitrogen atom via H-bonding. Ionic fragments from the CE of the dimer are detected in coincidence with one of the outgoing electrons. The KER distribution shows a prominent peak structure at 2.45 eV with a shoulder at around 1.2 eV. Observed projectile energy loss spectra for the CE channel having an onset around 26.5 eV are compared with the monomer inner valence ionization channel of D_2O leading to the formation of O^+ fragments, thereby suggesting that the observed ICD is initiated from the O $2s^{-1}$ inner valence vacancy. The measured onset indicates that the binding energy of the ionized orbital is above the double ionization threshold of pyridine, meaning the Auger process is open in this energy range. ICD initialized from the pyridine inner valence vacancies of either C $2s^{-1}$ and N $2s^{-1}$ are not identified. Therefore, an assumption was made that Auger decay is faster than ICD for vacancies initiated from pyridine. A comparison of one of the Auger channels with ICD is also shown, which is initiated within the same binding energy range. Another possibility of an excited doubly ionized state with two charges on pyridine producing the same final state as the CE channel via RCT can be omitted as the KER spectrum should be broad distribution or higher values for events formed in this process. For further understanding of the Auger process, a comparison with pure pyridine dimer is necessary.

Appendix A

Atomic units

'Hartree' type atomic units (au or a.u.) form a system of natural units based on the properties of hydrogen atom and electron, which is especially convenient for atomic physics calculations. Four fundamental physical constants forms the basis of atomic units, where the numerical values are all unity by definition. Units of other quantities can be derived

Fundamental constant	Formula	Value in SI units	Value in a.u.
Mass (Electron mass)	m_e	9.10938×10^{-31}	1
Charge (Elementary charge)	e	1.60218×10^{-19} C	1
Planck constant	$\hbar$	1.05457×10^{-34}kg m^2 s^{-1}	1
Coulomb force constant	$k_e = 1/4\pi\epsilon_0$	8.98755×10^9 kg m^3 s^{-2} C^{-2}	1

Table A.1: Fundamental atomic units

from the fundamental atomic units.

Quantity	Unit	Value in SI units
length	a_0	0.529177×10^{-10} m
time	$\hbar/E_h$	2.41888×10^{-30} kg
velocity	$v_B = \alpha c$	2.18769×10^6 m/s
energy	E_h	4.3597×10^{-18} J
momentum	$\hbar/a_0$	1.99285×10^{-24}kg m/s

Table A.2: Physical quantities in atomic units with $\hbar = e = m_e = 4\pi\epsilon_0 = 1$ and $\alpha^{-1} = 137.0359$

Bibliography

[1] Professor E. Rutherford F.R.S. Lxxix. the scattering of α and β particles by matter and the structure of the atom. *The London, Edinburgh, and Dublin Philosophical Magazine and Journal of Science*, 21(125):669–688, 1911.

[2] Ueber die lichtelektrische wirkung. *Annalen der Physik*, 313(5):149–198, 1902.

[3] Carl Ramsauer. Über den wirkungsquerschnitt der gasmoleküle gegenüber langsamen elektronen. *Annalen der Physik*, 369(6):513–540, 1921.

[4] J.S. Townsend M.A. F.R.S. and V.A. Bailey M.A. Lxx. the motion of electrons in argon. *The London, Edinburgh, and Dublin Philosophical Magazine and Journal of Science*, 43(255):593–600, 1922.

[5] James Franck and Gustav Hertz. Über zusammenstöße zwischen elektronen und den molekülen des quecksilberdampfes und die ionisierungsspannung desselben. *Physikalische Blätter*, 23(7):294–301, 1967.

[6] U. Amaldi, A. Egidi, R. Marconero, and G. Pizzella. Use of a two channeltron coincidence in a new line of research in atomic physics. *Review of Scientific Instruments*, 40(8):1001–1004, 1969.

[7] H. Ehrhardt, M. Schulz, T. Tekaat, and K. Willmann. Ionization of helium: Angular correlation of the scattered and ejected electrons. *Phys. Rev. Lett.*, 22:89–92, Jan 1969.

[8] Joachim Ullrich, Robert Moshammer, Alexander Dorn, Reinhard Dörner, L Ph H Schmidt, and H Schmidt-Böcking. Recoil-ion and electron momentum spectroscopy: reaction-microscopes. *Reports on progress in physics*, 66(9):1463, 2003.

[9] R. Dörner, J. Ullrich, H. Schmidt-Böcking, and R. E. Olson. Three-body interactions in proton-helium angular scattering. *Phys. Rev. Lett.*, 63:147–150, Jul 1989.

[10] X. Flechard, H. Nguyen, E. Wells, I. Ben-Itzhak, and B. D. DePaola. Kinematically complete charge exchange experiment in the $\mathrm{cs}^{+} + rb$ collision system using a mot target. *Phys. Rev. Lett.*, 87:123203, Aug 2001.

[11] N. Kurz, D. Fischer, T. Pfeifer, and A. Dorn. Reaction microscope for investigating ionization dynamics of weakly bound alkali dimers. *Review of Scientific Instruments*, 92(12):123202, 2021.

[12] F. Schotsch, I. Zebergs, S. Augustin, H. Lindenblatt, L. Hoibl, D. Djendjur, C. D. Schroeter, T. Pfeifer, and R. Moshammer. Trapremi: A reaction microscope inside

an electrostatic ion beam trap. *Review of Scientific Instruments*, 92(12):123201, 2021.

[13] M. Dürr, C. Dimopoulou, B. Najjari, A. Dorn, and J. Ullrich. Three-dimensional images for electron-impact single ionization of he: Complete and comprehensive $(e, 2e)$ benchmark data. *Phys. Rev. Lett.*, 96:243202, Jun 2006.

[14] A. Dorn, A. Kheifets, C. D. Schröter, B. Najjari, C. Höhr, R. Moshammer, and J. Ullrich. Double ionization of helium by electron-impact: Complete pictures of the four-body breakup dynamics. *Phys. Rev. Lett.*, 86:3755–3758, Apr 2001.

[15] Xueguang Ren, Alexander Dorn, and Joachim Ullrich. Coulomb four-body problem: Electron-impact double ionization of helium in the threshold regime. *Physical Review Letters*, 101(9):1–4, 2008.

[16] TN Rescigno, M Baertschy, WA Isaacs, and CW McCurdy. Collisional breakup in a quantum system of three charged particles. *Science*, 286(5449):2474–2479, 1999.

[17] X. Ren, I. Bray, D.V. Fursa, J. Colgan, M.S. Pindzola, T. Pflüger, A. Senftleben, S. Xu, A. Dorn, and J. Ullrich. Electron-impact ionization of helium: A comprehensive experiment benchmarks theory. *Phys. Rev. A*, 83:052711, May 2011.

[18] T. N. Rescigno, M. Baertschy, W. A. Isaacs, and C. W. McCurdy. Collisional breakup in a quantum system of three charged particles. *Science*, 286(5449):2474–2479, 1999.

[19] Igor Bray and Andris T. Stelbovics. Convergent close-coupling calculations of electron-hydrogen scattering. *Phys. Rev. A*, 46:6995–7011, Dec 1992.

[20] M S Pindzola, F Robicheaux, S D Loch, J C Berengut, T Topcu, J Colgan, M Foster, D C Griffin, C P Ballance, D R Schultz, T Minami, N R Badnell, M C Witthoeft, D R Plante, D M Mitnik, J A Ludlow, and U Kleiman. The time-dependent close-coupling method for atomic and molecular collision processes. *Journal of Physics B: Atomic, Molecular and Optical Physics*, 40(7):R39, mar 2007.

[21] D. H. Madison, R. V. Calhoun, and W. N. Shelton. Triple-differential cross sections for electron-impact ionization of helium. *Phys. Rev. A*, 16:552–562, Aug 1977.

[22] K Bartschat and PG Burke. The r-matrix method for electron impact ionisation. *Journal of Physics B: Atomic and Molecular Physics*, 20(13):3191, 1987.

[23] Junfang Gao, J. L. Peacher, and D. H. Madison. An elementary method for calculating orientation-averaged fully differential electron-impact ionization cross sections for molecules. *The Journal of Chemical Physics*, 123(20):204302, 2005.

[24] Junfang Gao, D. H. Madison, and J. L. Peacher. Distorted wave born and three-body distorted wave born approximation calculations of the fully differential cross section for electron-impact ionization of nitrogen molecules. *The Journal of Chemical Physics*, 123(20):204314, 2005.

[25] Song bin Zhang, Xing Yu Li, Jian Guo Wang, Yi Zhi Qu, and Xiangjun Chen. Multicenter distorted-wave method for fast-electron-impact single ionization of molecules. *Phys. Rev. A*, 89:052711, May 2014.

[26] Maomao Gong, Zhenpeng Wang, Xingyu Li, Song Bin Zhang, and Xiangjun Chen. Theoretical study of electron impact single ionization of neon by multicenter three distorted-wave method at low projectile energy: an overall agreement with experiment. *Journal of Physics B: Atomic, Molecular and Optical Physics*, 54(1):015206, dec 2020.

[27] Xueguang Ren, Sadek Amami, Oleg Zatsarinny, Thomas Pflüger, Marvin Weyland, Alexander Dorn, Don Madison, and Klaus Bartschat. Kinematically complete study of low-energy electron-impact ionization of argon: Internormalized cross sections in three-dimensional kinematics. *Phys. Rev. A*, 93:062704, Jun 2016.

[28] Maomao Gong, Xingyu Li, Song Bin Zhang, Shanshan Niu, Xueguang Ren, Enliang Wang, Alexander Dorn, and Xiangjun Chen. Multicenter three-distorted-wave approach to three-dimensional images for electron-impact-ionization dynamics of molecules: Overall agreement with experiment. *Phys. Rev. A*, 98:042710, Oct 2018.

[29] Xiaorui Xue, Deepthy Maria Mootheril, Esam Ali, Maomao Gong, Shaokui Jia, Jiaqi Zhou, Enliang Wang, Jian-Xing Li, Xiangjun Chen, Don Madison, Alexander Dorn, and Xueguang Ren. Triple-differential cross sections in three-dimensional kinematics for electron-impact-ionization dynamics of tetrahydrofuran at 250-ev projectile energy. *Phys. Rev. A*, 106:042803, Oct 2022.

[30] M. Dürr, C. Dimopoulou, A. Dorn, B. Najjari, I. Bray, D. V. Fursa, Zhangjin Chen, D. H. Madison, K. Bartschat, and J. Ullrich. Single ionization of helium by 102 eV electron impact: Three-dimensional images for electron emission. *Journal of Physics B: Atomic, Molecular and Optical Physics*, 39(20):4097–4111, 2006.

[31] J. Colgan, A. Emmanouilidou, and M. S. Pindzola. Evidence for a T-Shape Break-Up Pattern in the Triple Photoionization of Li. *Physical Review Letters*, 110(6):1–5, 2013.

[32] Jiaqi Zhou, Esam Ali, Maomao Gong, Shaokui Jia, Yutian Li, Yingying Wang, Zhen Zhang, Xiaorui Xue, Dmitry V. Fursa, Igor Bray, Xiangjun Chen, Don Madison, Alexander Dorn, and Xueguang Ren. Absolute triple differential cross sections for low-energy electron impact ionization of biochemically relevant systems: Water, tetrahydrofuran, and hydrated tetrahydrofuran. *Phys. Rev. A*, 104:012817, Jul 2021.

[33] L. S. Cederbaum, J. Zobeley, and F. Tarantelli. Giant intermolecular decay and fragmentation of clusters. *Physical Review Letters*, 79(24):4778–4781, 1997.

[34] S. Marburger, O. Kugeler, U. Hergenhahn, and T. Möller. Experimental evidence for interatomic coulombic decay in Ne clusters. *Phys. Rev. Lett.*, 90:203401, May 2003.

[35] T. Jahnke, A. Czasch, M. S. Schöffler, S. Schössler, A. Knapp, M. Käsz, J. Titze, C. Wimmer, K. Kreidi, R. E. Grisenti, A. Staudte, O. Jagutzki, U. Hergenhahn, H. Schmidt-Böcking, and R. Dörner. Experimental observation of interatomic coulombic decay in neon dimers. *Phys. Rev. Lett.*, 93:163401, Oct 2004.

[36] T. Havermeier, T. Jahnke, K. Kreidi, R. Wallauer, S. Voss, M. Schöffler, S. Schössler, L. Foucar, N. Neumann, J. Titze, H. Sann, M. Kühnel, J. Voigtsberger, J. H. Morilla, W. Schöllkopf, H. Schmidt-Böcking, R. E. Grisenti, and R. Dörner. Interatomic coulombic decay following photoionization of the helium dimer: Observation of vibrational structure. *Phys. Rev. Lett.*, 104:133401, Mar 2010.

[37] K. Schnorr, A. Senftleben, M. Kurka, A. Rudenko, L. Foucar, G. Schmid, A. Broska, T. Pfeifer, K. Meyer, D. Anielski, R. Boll, D. Rolles, M. Kübel, M. F. Kling, Y. H. Jiang, S. Mondal, T. Tachibana, K. Ueda, T. Marchenko, M. Simon, G. Brenner, R. Treusch, S. Scheit, V. Averbukh, J. Ullrich, C. D. Schröter, and R. Moshammer. Time-resolved measurement of interatomic coulombic decay in ne_2. *Phys. Rev. Lett.*, 111:093402, Aug 2013.

[38] Xueguang Ren, Elias Jabbour Al Maalouf, Alexander Dorn, and Stephan Denifl. Direct evidence of two interatomic relaxation mechanisms in argon dimers ionized by electron impact. *Nature Communications*, 7, 2016.

[39] G. Hanel, B. Gstir, S. Denifl, P. Scheier, M. Probst, B. Farizon, M. Farizon, E. Illenberger, and T. D. Märk. Electron attachment to uracil: Effective destruction at subexcitation energies. *Phys. Rev. Lett.*, 90:188104, May 2003.

[40] Enliang Wang, Xueguang Ren, Woon Yong Baek, Hans Rabus, Thomas Pfeifer, and Alexander Dorn. Water acting as a catalyst for electron-driven molecular break-up of tetrahydrofuran. *Nature Communications*, 11(1):1–7, 2020.

[41] Xueguang Ren, Enliang Wang, Anna D Skitnevskaya, Alexander B Trofimov, Kirill Gokhberg, and Alexander Dorn. Experimental evidence for ultrafast intermolecular relaxation processes in hydrated biomolecules. *Nature Physics*, 14(10):1062–1066, 2018.

[42] Xueguang Ren, Jiaqi Zhou, Enliang Wang, Tao Yang, Zhongfeng Xu, Nicolas Sisourat, Thomas Pfeifer, and Alexander Dorn. Ultrafast energy transfer between π-stacked aromatic rings upon inner-valence ionization. *Nature Chemistry*, 14(2):232–238, 2022.

[43] Anna D. Skitnevskaya, Kirill Gokhberg, Alexander B. Trofimov, Emma K. Grigoricheva, Alexander I. Kuleff, and Lorenz S. Cederbaum. Two-Sided Impact of Water on the Relaxation of Inner-Valence Vacancies of Biologically Relevant Molecules. *Journal of Physical Chemistry Letters*, 14(6):1418–1426, 2023.

[44] Martin Dürr. *Electron Induced Break-up of Helium: Benchmark Experiments on a Dynamical Four-Body Coulomb System*. PhD thesis, Ruperto-Carola University of Heidelberg, 2006.

[45] J P D Cook, I E McCarthy, A T Stelbovics, and E Weigold. Non-coplanar symmetric (e, 2e) momentum profile measurements for helium: an accurate test of helium

wavefunctions. *Journal of Physics B: Atomic and Molecular Physics*, 17(11):2339, jun 1984.

[46] C.E. Brion, S.T. Hood, I.H. Suzuki, E. Weigold, and G.R.J. Williams. Momentum distributions and ionization potentials for the valence orbitals of hydrogen fluoride and hydrogen chloride. *Journal of Electron Spectroscopy and Related Phenomena*, 21(1):71–91, 1980.

[47] Gregory H. Wannier. The threshold law for single ionization of atoms or ions by electrons. *Phys. Rev.*, 90:817–825, Jun 1953.

[48] M. Yan, H. R. Sadeghpour, and A. Dalgarno. Photoionization cross sections of He and H_2. *The Astrophysical Journal*, 496(2):1044, apr 1998.

[49] Nobuo Oda. Energy and Angular Distributions of Electrons from Atoms and Molecules by Electron Impact. *Radiation Research*, 64(1):80–95, 10 1975.

[50] C.B. Opal, E.C. Beaty, and W.K. Peterson. Tables of secondary-electron-production cross sections. *Atomic Data and Nuclear Data Tables*, 4:209–253, 1972.

[51] R Muller-Fiedler, K Jung, and H Ehrhardt. Double differential cross sections for electron impact ionisation of helium. *Journal of Physics B: Atomic and Molecular Physics*, 19(8):1211, apr 1986.

[52] T. W. Shyn and W. E. Sharp. Angular distributions of electrons elastically scattered from h_2. *Phys. Rev. A*, 24:1734–1740, Oct 1981.

[53] H Ehrhardt, K Jung, G Knoth, and P Schlemmer. Differential cross sections of direct single electron impact ionization. *Zeitschrift für Physik D Atoms, Molecules and Clusters*, 1(1):3–32, 1986.

[54] Yong-Ki Kim. Angular and energy distributions of secondary electrons from helium. slow electrons ejected by electron impact. *Phys. Rev. A*, 28:656–666, Aug 1983.

[55] T. W. Shyn and W. E. Sharp. Doubly differential cross sections of secondary electrons ejected from gases by electron impact: 50-300 eV on helium. *Phys. Rev. A*, 19:557–567, Feb 1979.

[56] Oleg Zatsarinny and Klaus Bartschat. Nonperturbative treatment of ionization with excitation of helium by electron impact. *Phys. Rev. Lett.*, 107:023203, Jul 2011.

[57] Xueguang Ren, Arne Senftleben, Thomas Pflüger, Klaus Bartschat, Oleg Zatsarinny, Jamal Berakdar, James Colgan, Michael S. Pindzola, Igor Bray, Dmitry V. Fursa, and Alexander Dorn. Propensity for distinguishing two free electrons with equal energies in electron-impact ionization of helium. *Phys. Rev. A*, 92:052707, Nov 2015.

[58] Charles J. Joachain. *Quantum collision theory*. North-Holland publishing company, 1975.

[59] Ian E. McCarthy and Erich Weigold. *Electron-Atom collisions*. Cambridge university press, 1995.

[60] F W Byron Jr, C J Joachain, and B Piraux. Triple differential cross sections for the ionisation of atomic hydrogen by fast electrons: a second born treatment. *Journal of Physics B: Atomic and Molecular Physics*, 13(22):L673, nov 1980.

[61] M Brauner, J S Briggs, and H Klar. Triply-differential cross sections for ionisation of hydrogen atoms by electrons and positrons. *Journal of Physics B: Atomic, Molecular and Optical Physics*, 22(14):2265, jul 1989.

[62] S. Jones and D. H. Madison. Scaling behavior of the fully differential cross section for ionization of hydrogen atoms by the impact of fast elementary charged particles. *Phys. Rev. A*, 65:052727, May 2002.

[63] Don H. Madison and Ola Al-Hagan. The Distorted-Wave Born Approach for Calculating Electron-Impact Ionization of Molecules. *Journal of Atomic, Molecular, and Optical Physics*, 2010:1–24, 2010.

[64] Erich Weigold and Ian E. McCarthy. *Electron Momentum Spectroscopy*. Kluwer Academic/Plenum Publishers, New York, NY, USA, 1999.

[65] Junfang Gao, D. H. Madison, and J. L. Peacher. Interference effects for low-energy electron-impact ionization of nitrogen molecules. *Phys. Rev. A*, 72:032721, Sep 2005.

[66] N. Sanna, I. Baccarelli, and G. Morelli. The VOLSCAT package for electron and positron scattering of molecular targets: A new high throughput approach to cross-section and resonances computation. *Computer Physics Communications*, 180(12):2550–2562, 2009. 40 YEARS OF CPC: A celebratory issue focused on quality software for high performance, grid and novel computing architectures.

[67] J. Botero and J. H. Macek. Threshold angular distributions of (e,2e) cross sections of helium atoms. *Phys. Rev. Lett.*, 68:576–579, Feb 1992.

[68] S. J. Ward and J. H. Macek. Wave functions for continuum states of charged fragments. *Phys. Rev. A*, 49:1049–1056, Feb 1994.

[69] Hellmut Haberland. *Clusters of Atoms and Molecules Theory, Experiment, and Clusters of Atoms*. Springer-Verlag Berlin Heidelberg, 1994.

[70] E W Becker, K Bier, and W Henkes. Strahlen aus kondensierten Atomen und Molekeln im Hochvakuum. *Zeitschrift für Physik*, 146(3):333–338, 1956.

[71] Otto F. Hagena. Nucleation and growth of clusters in expanding nozzle flows. *Surface Science*, 106(1):101–116, 1981.

[72] D Bahat, O Cheshnovsky, U Even, N Lavie, and Y Magen. Generation and detection of intense cluster beams. *Journal of physical chemistry*, 91(10):2460–2462, 1987.

[73] Richard E Smalley, Lennard Wharton, and Donald H Levy. Molecular optical spectroscopy with supersonic beams and jets. *Accounts of Chemical Research*, 10(4):139–145, 1977.

[74] Otto F. Hagena. Cluster ion sources (invited). *Review of Scientific Instruments*, 63(4):2374–2379, 1992.

[75] Udo Buck and Reinhard Krohne. Cluster size determination from diffractive He atom scattering. *The Journal of Chemical Physics*, 105(13):5408–5415, 1996.

[76] C Bobbert, S Schütte, C Steinbach, and U Buck. Fragmentation and reliable size distributions of large ammonia and water clusters. *The European Physical Journal D - Atomic, Molecular, Optical and Plasma Physics*, 19(2):183–192, 2002.

[77] O. F. Hagena and W. Obert. Cluster formation in expanding supersonic jets: Effect of pressure, temperature, nozzle size, and test gas. *The Journal of Chemical Physics*, 56(5):1793–1802, 1972.

[78] B A Ikkanda and B L Iverson. Exploiting the interactions of aromatic units for folding and assembly in aqueous environments. *Chem. Commun.*, 52(50):7752–7759, 2016.

[79] Klaus Müller-Dethlefs and Pavel Hobza. Noncovalent interactions: A challenge for experiment and theory. *Chemical Reviews*, 100(1):143–168, 2000. PMID: 11749236.

[80] Maurizio Becucci and Sonia Melandri. High-resolution spectroscopic studies of complexes formed by medium-size organic molecules. *Chemical Reviews*, 116(9):5014–5037, 2016. PMID: 26986455.

[81] Johannes van der Waals. *Over de Continuïteit van den Gas- en Vloeistoftoestand (on the continuity of the gaseous and liquid state)*. PhD thesis, University of Leiden, 1873.

[82] Asger Halkier, Henrik Koch, Poul Jørgensen, Ove Christiansen, Ida M Beck Nielsen, and Trygve Helgaker. A systematic ab initio study of the water dimer in hierarchies of basis sets and correlation models. *Theoretical Chemistry Accounts*, 97:150–157, 1997.

[83] Martin W Feyereisen, David Feller, and David A Dixon. Hydrogen bond energy of the water dimer. *The Journal of Physical Chemistry*, 100(8):2993–2997, 1996.

[84] Martin Kratochvíl, Ola Engkvist, Jiří Šponer, Pavel Jungwirth, and Pavel Hobza. Uracil dimer: potential energy and free energy surfaces. ab initio beyond hartree-fock and empirical potential studies. *The Journal of Physical Chemistry A*, 102(35):6921–6926, 1998.

[85] Steve Scheiner. *Hydrogen Bonding. A Theoretical Perspective*. Oxford University Press: New York, 1997.

[86] Alan E Reed, Larry A Curtiss, and Frank Weinhold. Intermolecular interactions from a natural bond orbital, donor-acceptor viewpoint. *Chemical Reviews*, 88(6):899–926, 1988.

[87] Thomas Steiner and Gautam R Desiraju. Distinction between the weak hydrogen bond and the van der waals interaction. *Chemical Communications*, (8):891–892, 1998.

[88] S Djafari, H-D Barth, K Buchhold, and B Brutschy. Infrared-depletion spectroscopy study on hydrogen-bonded fluorobenzene–methanol clusters. *The Journal of chemical physics*, 107(24):10573–10581, 1997.

[89] Pavel Hobza, Jiří Šponer, Elena Cubero, Modesto Orozco, and F. Javier Luque. C-H$\cdots$O contacts in the adenine$\cdots$uracil watson-crick and uracil$\cdots$uracil nucleic acid base pairs: Nonempirical ab initio study with inclusion of electron correlation effects. *Journal of Physical Chemistry B*, 104(26):6286 – 6292, 2000. Cited by: 127.

[90] Pavel Hobza and Zdeněk Havlas. Blue-shifting hydrogen bonds. *Chemical reviews*, 100(11):4253–4264, 2000.

[91] Pavel Hobza, Vladimır Špirko, Zdeněk Havlas, Konstantin Buchhold, Bernd Reimann, Hans-Dieter Barth, and Bernhard Brutschy. Anti-hydrogen bond between chloroform and fluorobenzene. *Chemical physics letters*, 299(2):180–186, 1999.

[92] JC Lee. An unusual type of H$\cdots$H interaction-Ir-H$\cdots$HO and Ir-H$\cdots$HN hydrogen-bonding and its involvement in sigma-bond metathesis. *Journal of the American Chemical Society*, 116(24):11014–11019, 1994.

[93] Wim T Klooster, Thomas F Koetzle, Per EM Siegbahn, Thomas B Richardson, and Robert H Crabtree. Study of the N-H$\cdots$H-B dihydrogen bond including the crystal structure of BH_3NH_3 by neutron diffraction. *Journal of the American Chemical Society*, 121(27):6337–6343, 1999.

[94] Christopher A Hunter and Jeremy KM Sanders. The nature of π-π interactions. *Journal of the American Chemical Society*, 112(14):5525–5534, 1990.

[95] Pavel Hobza, Heinrich L Selzle, and Edward W Schlag. Potential energy surface for the benzene dimer. results of ab initio CCSD (T) calculations show two nearly isoenergetic structures: T-shaped and parallel-displaced. *The Journal of Physical Chemistry*, 100(48):18790–18794, 1996.

[96] Christopher A Hunter, Juswinder Singh, and Janet M Thornton. π-π interactions: the geometry and energetics of phenylalanine-phenylalanine interactions in proteins. *Journal of molecular biology*, 218(4):837–846, 1991.

[97] Till Jahnke, Uwe Hergenhahn, Bernd Winter, Reinhard Dörner, Ulrike Frühling, Philipp V. Demekhin, Kirill Gokhberg, Lorenz S. Cederbaum, Arno Ehresmann, André Knie, and Andreas Dreuw. Interatomic and intermolecular coulombic decay. *Chemical Reviews*, 120(20):11295–11369, 2020. PMID: 33035051.

[98] Lise Meitner. Über die β-strahl-spektra und ihren zusammenhang mit der γ-strahlung. *Zeitschrift für Physik*, 11:35–54, 1922.

[99] Pierre Auger. Sur l'effet photoélectrique composé. *J. Phys. Radium*, 6(6):205–208, 1925.

[100] Wikipedia contributors. Auger electron spectroscopy — Wikipedia, the free encyclopedia, 2023. [Online; accessed 14-April-2023].

[101] Y. Ovcharenko, V. Lyamayev, R. Katzy, M. Devetta, A. LaForge, P. O'Keeffe, O. Plekan, P. Finetti, M. Di Fraia, M. Mudrich, M. Krikunova, P. Piseri, M. Coreno, N. B. Brauer, T. Mazza, S. Stranges, C. Grazioli, R. Richter, K. C. Prince, M. Drabbels, C. Callegari, F. Stienkemeier, and T. Möller. Novel collective autoionization process observed in electron spectra of He clusters. *Phys. Rev. Lett.*, 112:073401, Feb 2014.

[102] Jürgen Zobeley, Robin Santra, and Lorenz S. Cederbaum. Electronic decay in weakly bound heteroclusters: Energy transfer versus electron transfer. *The Journal of Chemical Physics*, 115(11):5076–5088, 2001.

[103] Marko Förstel, Melanie Mucke, Tiberiu Arion, Alex M. Bradshaw, and Uwe Hergenhahn. Autoionization mediated by electron transfer. *Phys. Rev. Lett.*, 106:033402, Jan 2011.

[104] K. Sakai, S. Stoychev, T. Ouchi, I. Higuchi, M. Schöffler, T. Mazza, H. Fukuzawa, K. Nagaya, M. Yao, Y. Tamenori, A. I. Kuleff, N. Saito, and K. Ueda. Electron-transfer-mediated decay and interatomic coulombic decay from the triply ionized states in argon dimers. *Phys. Rev. Lett.*, 106:033401, Jan 2011.

[105] Christian Buth, Robin Santra, and Lorenz S. Cederbaum. Impact of interatomic electronic decay processes on Xe 4d hole decay in the xenon fluorides. *The Journal of Chemical Physics*, 119(20):10575–10584, 2003.

[106] Kirill Gokhberg and Lorenz S Cederbaum. Environment assisted electron capture. *Journal of Physics B: Atomic, Molecular and Optical Physics*, 42(23):231001, nov 2009.

[107] Richard A. Wilhelm, Elisabeth Gruber, Janine Schwestka, Roland Kozubek, Teresa I. Madeira, José P. Marques, Jacek Kobus, Arkady V. Krasheninnikov, Marika Schleberger, and Friedrich Aumayr. Interatomic coulombic decay: The mechanism for rapid deexcitation of hollow atoms. *Phys. Rev. Lett.*, 119:103401, Sep 2017.

[108] Janine Schwestka, Anna Niggas, Sascha Creutzburg, Roland Kozubek, René Heller, Marika Schleberger, Richard A. Wilhelm, and Friedrich Aumayr. Charge-exchange-driven low-energy electron splash induced by heavy ion impact on condensed matter. *The Journal of Physical Chemistry Letters*, 10(17):4805–4811, 2019. PMID: 31382749.

[109] K. Kreidi, T. Jahnke, Th. Weber, T. Havermeier, X. Liu, Y. Morisita, S. Schössler, L. Ph. H. Schmidt, M. Schöffler, M. Odenweller, N. Neumann, L. Foucar, J. Titze, B. Ulrich, F. Sturm, C. Stuck, R. Wallauer, S. Voss, I. Lauter, H. K. Kim, M. Rudloff, H. Fukuzawa, G. Prümper, N. Saito, K. Ueda, A. Czasch, O. Jagutzki, H. Schmidt-Böcking, S. Stoychev, Ph. V. Demekhin, and R. Dörner. Relaxation processes following $1s$ photoionization and auger decay in ne_2. *Phys. Rev. A*, 78:043422, Oct 2008.

[110] N. Saito, Y. Morishita, I.H. Suzuki, S.D. Stoychev, A.I. Kuleff, L.S. Cederbaum, X.-J. Liu, H. Fukuzawa, G. Prümper, and K. Ueda. Evidence of radiative charge transfer in argon dimers. *Chemical Physics Letters*, 441(1):16–19, 2007.

[111] Andreas Hans, Vasili Stumpf, Xaver Holzapfel, Florian Wiegandt, Philipp Schmidt, Christian Ozga, Philipp Reiß, Ltaief Ben Ltaief, Catmarna Küstner-Wetekam, Till Jahnke, Arno Ehresmann, Philipp V Demekhin, Kirill Gokhberg, and André Knie. Direct evidence for radiative charge transfer after inner-shell excitation and ionization of large clusters. *New Journal of Physics*, 20(1):012001, jan 2018.

[112] Xaver Holzapfel, Tsveta Miteva, Nicolas Sisourat, Alexander Schrodt, Lutz Marder, Dana Bloß, Christian Ozga, Catmarna Küstner-Wetekam, Arno Ehresmann, André Knie, and Andreas Hans. Properties of radiative charge transfer in heterogeneous noble-gas clusters. *Phys. Rev. A*, 105:022815, Feb 2022.

[113] Alexander I. Kuleff, Kirill Gokhberg, Sören Kopelke, and Lorenz S. Cederbaum. Ultrafast interatomic electronic decay in multiply excited clusters. *Phys. Rev. Lett.*, 105:043004, Jul 2010.

[114] B.H. Bransden and C. J. Joachain. *Physics of atoms and molecules*. Pearson education limited, 2nd edition, 2003.

[115] Robin Santra and Lorenz S. Cederbaum. Non-hermitian electronic theory and applications to clusters. *Physics Reports*, 368(1):1–117, 2002.

[116] T. Jahnke, A. Czasch, M. Schöffler, S. Schössler, M. Käsz, J. Titze, K. Kreidi, R. E. Grisenti, A. Staudte, O. Jagutzki, L. Ph. H. Schmidt, Th. Weber, H. Schmidt-Böcking, K. Ueda, and R. Dörner. Experimental separation of virtual photon exchange and electron transfer in interatomic coulombic decay of neon dimers. *Phys. Rev. Lett.*, 99:153401, Oct 2007.

[117] Vitali Averbukh, Imke B. Müller, and Lorenz S. Cederbaum. Mechanism of interatomic coulombic decay in clusters. *Phys. Rev. Lett.*, 93:263002, Dec 2004.

[118] T. Havermeier, T. Jahnke, K. Kreidi, R. Wallauer, S. Voss, M. Schöffler, S. Schössler, L. Foucar, N. Neumann, J. Titze, H. Sann, M. Kühnel, J. Voigtsberger, J. H. Morilla, W. Schöllkopf, H. Schmidt-Böcking, R. E. Grisenti, and R. Dörner. Interatomic coulombic decay following photoionization of the helium dimer: Observation of vibrational structure. *Phys. Rev. Lett.*, 104:133401, Mar 2010.

[119] F. Trinter, J. B. Williams, M. Weller, M. Waitz, M. Pitzer, J. Voigtsberger, C. Schober, G. Kastirke, C. Müller, C. Goihl, P. Burzynski, F. Wiegandt, T. Bauer, R. Wallauer, H. Sann, A. Kalinin, L. Ph. H. Schmidt, M. Schöffler, N. Sisourat, and T. Jahnke. Evolution of interatomic coulombic decay in the time domain. *Phys. Rev. Lett.*, 111:093401, Aug 2013.

[120] S. Barth, S. Marburger, O. Kugeler, V. Ulrich, S. Joshi, A.M. Bradshaw, and U. Hergenhahn. The efficiency of interatomic coulombic decay in Ne clusters. *Chemical Physics*, 329(1):246–250, 2006. Electron Correlation and Multimode Dynamics in Molecules.

[121] M. Förstel, T. Arion, and U. Hergenhahn. Measuring the efficiency of interatomic coulombic decay in Ne clusters. *Journal of Electron Spectroscopy and Related Phenomena*, 191:16–19, 2013.

[122] S. Kopelke, Y.-C. Chiang, K. Gokhberg, and L. S. Cederbaum. Quenching molecular photodissociation by intermolecular coulombic decay. *The Journal of Chemical Physics*, 137(3):034302, 2012.

[123] Clemens Richter, Daniel Hollas, Clara Magdalena Saak, Marko Förstel, Tsveta Miteva, Melanie Mucke, Olle Björneholm, Nicolas Sisourat, Petr Slavíček, and Uwe Hergenhahn. Competition between proton transfer and intermolecular Coulombic decay in water. *Nature Communications*, 9(1), 2018.

[124] Robin Santra, Jürgen Zobeley, and Lorenz S. Cederbaum. Electronic decay of valence holes in clusters and condensed matter. *Phys. Rev. B*, 64:245104, Nov 2001.

[125] Spas D. Stoychev, Alexander I. Kuleff, and Lorenz S. Cederbaum. Intermolecular coulombic decay in small biochemically relevant hydrogen-bonded systems. *Journal of the American Chemical Society*, 133(17):6817–6824, 2011. PMID: 21486035.

[126] W. C. Wiley and I. H. McLaren. Time-of-flight mass spectrometer with improved resolution. *Review of Scientific Instruments*, 26(12):1150–1157, 1955.

[127] Joseph Ladislas Wiza. Microchannel plate detectors. *Nuclear Instruments and Methods*, 162:587–601, 1979.

[128] Thomas Pflüger. *Electron Impact Ionization Studies of Small Rare Gas Clusters*. PhD thesis, Ruperto-Carola University of Heidelberg, 2012.

[129] Jürgen Barnstedt. Advanced practical course: Microchannel plate detectors, 2019.

[130] M. Krems, J. Zirbel, M. Thomason, and R. D. DuBois. Channel electron multiplier and channelplate efficiencies for detecting positive ions. *Review of Scientific Instruments*, 76(9):093305, 2005.

[131] Arno Vredenborg, Wim G. Roeterdink, and Maurice H. M. Janssen. A photoelectron-photoion coincidence imaging apparatus for femtosecond time-resolved molecular dynamics with electron time-of-flight resolution of $\sigma = 18$ps and energy resolution $\delta \mathrm{E}/\mathrm{E} = 3.5\%$. *Review of Scientific Instruments*, 79(6):063108, 2008.

[132] Hamamatsu Photonics. *Microchannel plates assembly catalog*.

[133] K. Fehre, D. Trojanowskaja, J. Gatzke, M. Kunitski, F. Trinter, S. Zeller, L. Ph. H. Schmidt, J. Stohner, R. Berger, A. Czasch, O. Jagutzki, T. Jahnke, R. Dörner, and M. S. Schöffler. Absolute ion detection efficiencies of microchannel plates and funnel microchannel plates for multi-coincidence detection. *Review of Scientific Instruments*, 89(4):045112, 2018.

[134] Niels Kurz. *Kinematically complete multiphoton ionization studies on optically trapped ^6Li and $^6Li_2$ created by single-color photoassociation*. PhD thesis, Ruperto-Carola University of Heidelberg, 2021.

[135] O. Jagutzki, A. Cerezo, A. Czasch, R. Dorner, M. Hattas, Min Huang, V. Mergel, U. Spillmann, K. Ullmann-Pfleger, T. Weber, H. Schmidt-Bocking, and G.D.W. Smith. Multiple hit readout of a microchannel plate detector with a three-layer delay-line anode. *IEEE Transactions on Nuclear Science*, 49(5):2477–2483, 2002.

[136] Arne Senftleben. *Kinematically complete study on electron impact ionization of aligned hydrogen molecules*. PhD thesis, University of Heidelberg, 2009.

[137] Khokon Hossen. *Kinematically complete experiments for electron induced break-up of small molecules and clusters*. PhD thesis, University of Santiago de Compostela (USC), 15782 Santiago de Compostela, Spain, 2018.

[138] C. B. Alcock, V. P. Itkin, and M. K. Horrigan. Vapour pressure equations for the metallic elements: 298–2500K. *Canadian Metallurgical Quarterly*, 23(3):309–313, 1984.

[139] L Valyi. *Atom and ion sources*. John Wiley and Sons, Ltd, United States, 1977.

[140] Norman Ramsey. *Molecular Beams*. Oxford University Press, 1956.

[141] Ortec. *Model 935 Quad Constant-Fraction 200-MHz Discriminator Operating and Service Manual*, 2003.

[142] CAEN SpA. *Technical Information Manual, MOD. V1290 A/N VX1290 A/N 32/16 Channel mutihit TDCs manual Rev. 15*.

[143] Achim Czasch. *Documentation for the Resort-Routine used for square and hexagonal Delayline detectors*. RoentDek Handels GmbH, Frankfurt, 2005.

[144] Daniel Fischer. Aufbau eines Reaktionsmikroskops zur Untersuchung von Ion-Atom-Stößen. Diplomarbeit, Albert-Ludwigs-Universität Freiburg im Breisgau, Deutschland, 2000.

[145] U. Buck, H. Meyer, and H. Pauly. Cluster formation in supersonic nozzle beams. In G. E. A. Meier and F. Obermeier, editors, *Flow of Real Fluids*, pages 170–178, Berlin, Heidelberg, 1985. Springer Berlin Heidelberg.

[146] Jiaqi Zhou, Shaokui Jia, Anna D. Skitnevskaya, Enliang Wang, Theresa Hähnel, Emma K. Grigoricheva, Xiaorui Xue, Jian-Xing Li, Alexander I. Kuleff, Alexander Dorn, and Xueguang Ren. Concerted double hydrogen-bond breaking by intermolecular coulombic decay in the formic acid dimer. *The Journal of Physical Chemistry Letters*, 13(19):4272–4279, 2022. PMID: 35522820.

[147] N. Stolterfoht, J. Y. Chesnel, M. Grether, B. Skogvall, F. Frémont, D. Lecler, D. Hennecart, X. Husson, J. P. Grandin, B. Sulik, L. Gulyás, and J. A. Tanis. Two- and three-body effects in single ionization of Li by 95 MeV/u Ar^{18+} ions: Analogies with photoionization. *Physical Review Letters*, 80(21):4649–4652, 1998.

[148] G. Baum, W. Blask, P. Freienstein, L. Frost, S. Hesse, W. Raith, P. Rappolt, and M. Streun. Spin asymmetries for triple-differential electron-impact ionization of lithium at 54.4 ev. *Phys. Rev. Lett.*, 69:3037–3040, Nov 1992.

[149] A. C. Laforge, R. Hubele, J. Goullon, X. Wang, K. Schneider, V. L.B. De Jesus, B. Najjari, A. B. Voitkiv, M. Grieser, M. Schulz, and D. Fischer. Initial-state selective study of ionization dynamics in ion-Li collisions. *Journal of Physics B: Atomic, Molecular and Optical Physics*, 46(3):31001, feb 2013.

[150] R. Hubele, A. Laforge, M. Schulz, J. Goullon, X. Wang, B. Najjari, N. Ferreira, M. Grieser, V. L.B. De Jesus, R. Moshammer, K. Schneider, A. B. Voitkiv, and D. Fischer. Polarization and interference effects in ionization of Li by ion impact. *Physical Review Letters*, 110(13):1–5, 2013.

[151] M. T. Huang, L. Zhang, S. Hasegawa, S. H. Southworth, and L. Young. Measurements of the electron-impact double-to-single ionization ratio using trapped lithium. *Physical Review A - Atomic, Molecular, and Optical Physics*, 66(1):7, 2002.

[152] X. Ren, I. Bray, D. V. Fursa, J. Colgan, M. S. Pindzola, T. Pflüger, A. Senftleben, S. Xu, A. Dorn, and J. Ullrich. Electron-impact ionization of helium: A comprehensive experiment benchmarks theory. *Physical Review A - Atomic, Molecular, and Optical Physics*, 83(5):1–6, 2011.

[153] P. Eisenberger and P. M. Platzman. Compton scattering of x rays from bound electrons. *Phys. Rev. A*, 2:415–423, Aug 1970.

[154] D. Brandt. Resonant transfer and excitation in ion-atom collisions. *Phys. Rev. A*, 27:1314–1318, Mar 1983.

[155] H. Bethe. Zur theorie des durchgangs schneller korpuskularstrahlen durch materie. *Annalen der Physik*, 397(3):325–400, 1930.

[156] Rodolfo O. Esquivel, Awadh N. Tripathi, Robin P. Sagar, and Vedene H. Smith. Accurate one-electron momentum-space properties for the lithium isoelectronic sequence. *Journal of Physics B: Atomic, Molecular and Optical Physics*, 25(13):2925–2941, 1992.

[157] Anupam Sarkar and Gopal Chandra Maity. Momentum-Space Properties for Ground and Rydberg States of Lithium Atom. *Brazilian Journal of Physics*, 52(3), 2022.

[158] Liuyun Gong, Yujie Zhang, Chengcheng Liu, Mingzhen Zhang, and Suxia Han. Application of radiosensitizers in cancer radiotherapy. *International Journal of Nanomedicine*, 16:1083–1102, 2021.

[159] Katrin Tanzer, Linda Feketeová, Benjamin Puschnigg, Paul Scheier, Eugen Illenberger, and Stephan Denifl. Reactions in nitroimidazole triggered by low-energy (0-2 eV) electrons: Methylation at N1-H completely blocks reactivity. *Angewandte Chemie International Edition*, 53(45):12240–12243, 2014.

[160] Eero Itälä, Hanna Myllynen, Johannes Niskanen, Jesús González-Vázquez, Yang Wang, Dang Trinh Ha, Stephan Denifl, and Edwin Kukk. Controlling NO production upon valence ionization of nitroimidazoles. *The Journal of Physical Chemistry A*, 123(14):3074–3079, 2019.

[161] Eero Itälä, Katrin Tanzer, Sari Granroth, Kuno Kooser, Stephan Denifl, and Edwin Kukk. Fragmentation patterns of 4(5)-nitroimidazole and 1-methyl-5-nitroimidazole — The effect of the methylation. *Journal of Mass Spectrometry*, 52(11):770–776, 2017.

[162] Linda Feketeová, Oksana Plekan, Mayanthi Goonewardane, Marawan Ahmed, Abigail L. Albright, Jonathan White, Richard A.J. OHair, Michael R. Horsman, Feng Wang, and Kevin C. Prince. Photoelectron Spectra and Electronic Structures of the Radiosensitizer Nimorazole and Related Compounds. *Journal of Physical Chemistry A*, 119(39):9986–9995, 2015.

[163] Seiji Tsuzuki, Kazumasa Honda, and Reiko Azumi. Model chemistry calculations of thiophene dimer interactions: Origin of π-stacking. *Journal of the American Chemical Society*, 124(41):12200–12209, 2002.

[164] E. E. Rennie, D. M.P. Holland, D. A. Shaw, C. A.F. Johnson, and J. E. Parker. A study of the valence shell spectroscopic and thermodynamic properties of thiophene by photoabsorption and photoion spectroscopy. *Chemical Physics*, 306(1-3):295–308, 2004.

[165] S. F. Zhang, X. G. Ren, G. L. Su, C. G. Ning, H. Zhou, B. Li, G. Q. Li, and J. K. Deng. Electron momentum spectroscopy study of thiophene: Binding energy spectrum and valence orbital electron density distributions. *Chemical Physics*, 327(2-3):269–277, 2006.

[166] M. J. Frisch, G. W. Trucks, H. B. Schlegel, G. E. Scuseria, M. A. Robb, J. R. Cheeseman, G. Scalmani, V. Barone, G. A. Petersson, H. Nakatsuji, X. Li, M. Caricato, A. V. Marenich, J. Bloino, B. G. Janesko, R. Gomperts, B. Mennucci, H. P. Hratchian, J. V. Ortiz, A. F. Izmaylov, J. L. Sonnenberg, D. Williams-Young, F. Ding, F. Lipparini, F. Egidi, J. Goings, B. Peng, A. Petrone, T. Henderson, D. Ranasinghe, V. G. Zakrzewski, J. Gao, N. Rega, G. Zheng, W. Liang, M. Hada, M. Ehara, K. Toyota, R. Fukuda, J. Hasegawa, M. Ishida, T. Nakajima, Y. Honda, O. Kitao, H. Nakai, T. Vreven, K. Throssell, J. A. Montgomery, Jr., J. E. Peralta, F. Ogliaro, M. J. Bearpark, J. J. Heyd, E. N. Brothers, K. N. Kudin, V. N. Staroverov, T. A. Keith, R. Kobayashi, J. Normand, K. Raghavachari, A. P. Rendell, J. C. Burant, S. S. Iyengar, J. Tomasi, M. Cossi, J. M. Millam, M. Klene, C. Adamo, R. Cammi, J. W. Ochterski, R. L. Martin, K. Morokuma, O. Farkas, J. B. Foresman, and D. J. Fox. Gaussian~16 Revision A.03, 2016. Gaussian Inc. Wallingford CT.

[167] Oriol Vendrell, Spas D. Stoychev, and Lorenz S. Cederbaum. Generation of highly damaging H_2O^+ radicals by inner valence shell ionization of water. *ChemPhysChem*, 11(5):1006–1009, 2010.

[168] A. D.O. Bawagan, B. J. Olsson, K. H. Tan, J. M. Chen, and B. X. Yang. The correlation states of furan and thiophene by high resolution synchrotron photoelectron spectroscopy. *Chemical Physics*, 164(2):283–304, 1992.

[169] Nist chemistry webbook, nist standard reference database 69, 1997.

[170] P. Mozejko, E. Ptasińska-Denga, and Cz Szmytkowski. Cross sections for electron collision with five-membered ring heterocycles. *European Physical Journal D*, 66(2), 2012.

[171] Sebastian Tixier, Glyn Cooper, Renfei Feng, and C. E. Brion. Measurement of absolute dipole oscillator strengths for pyridine: Photoabsorption and the molecular and dissociative photoionization in the valence shell (4-200 eV). *Journal of Electron Spectroscopy and Related Phenomena*, 123(2-3):185–197, 2002.

[172] Henry M. Rosenstock, Roger Stockbauer, and Albert C. Parr. Unimolecular kinetics of pyridine ion fragmentation. *International Journal of Mass Spectrometry and Ion Physics*, 38(2):323–331, 1981.

[173] Jun Ying Feng, Yuan Pern Lee, Henryk A. Witek, Po Jen Hsu, Jer Lai Kuo, and Takayuki Ebata. Structures of Pyridine-Water Clusters Studied with Infrared-Vacuum Ultraviolet Spectroscopy. *Journal of Physical Chemistry A*, 125(34):7489–7501, 2021.

[174] Muhamad A. Martoprawiro and George B. Bacskay. Quantum chemical studies of the pyrrole-water and pyridine-water complexes. *Molecular Physics*, 85(3):573–585, 1995.

[175] Pablo Nieto, Melanie Letzner, Torsten Endres, Gerhard Schwaab, and Martina Havenith. IR spectroscopy of pyridine-water structures in helium nanodroplets. *Physical Chemistry Chemical Physics*, 16(18):8384–8391, 2014.

[176] Luigi De Marco, William Carpenter, Hanchao Liu, Rajib Biswas, Joel M. Bowman, and Andrei Tokmakoff. Differences in the Vibrational Dynamics of H_2O and D_2O: Observation of Symmetric and Antisymmetric Stretching Vibrations in Heavy Water. *Journal of Physical Chemistry Letters*, 7(10):1769–1774, 2016.

[177] A. Hult Roos, J. H.D. Eland, J. Andersson, R. J. Squibb, and R. Feifel. Dissociations of water ions after valence and inner-valence ionization. *Journal of Chemical Physics*, 149(20), 2018.

[178] Maria Sabaye Moghaddam, A. D.O. Bawagan, K. H. Tan, and W. Von Niessen. Study of the electronic structure of pyridine by synchrotron photoelectron spectroscopy. *Chemical Physics*, 207(1):19–29, 1996.

[179] S. Y. Truong, A. J. Yencha, A. M. Juarez, S. J. Cavanagh, P. Bolognesi, and G. C. King. Threshold photoelectron spectroscopy of H_2O and D_2O over the photon energy range 12-40 eV. *Chemical Physics*, 355(2-3):183–193, 2009.

[180] C. Q. Jiao, C. A. DeJoseph, R. Lee, and A. Garscadden. Kinetics of electron impact ionization and ion-molecule reactions of pyridine. *International Journal of Mass Spectrometry*, 257(1-3):34–40, 2006.

[181] H. C. Straub, B. G. Lindsay, K. A. Smith, and R. F. Stebbings. Absolute partial cross sections for electron-impact ionization of H_2O and D_2O from threshold to 1000 eV. *The Journal of Chemical Physics*, 108(1):109–116, 1998.

Acknowledgment

Last but not the least, I would like to express my heartfelt gratitude to all those who helped me throughout this fascinating journey.

First and foremost, I would like to thank, Max Planck Institute for Nuclear Physics for giving me the opportunity to be part of the scientific community here. Especially, International Max Planck Research School - Quantum Dynamics (IMPRS-QD) for funding my PhD program in the initial years.

Words are not enough to express my thanks to Alexander Dorn, my PhD supervisor. I am deeply grateful to you for being my mentor all these years and for the incredible amount of knowledge and opportunities that you gave me.

I would like to express my appreciation to Thomas Pfeifer for the opportunity to be part of the division, for the excellent working atmosphere, for the support and helpful discussions especially during difficult times.

I thank all my colleagues and guest scientists- Xueguang Ren, Jiaqi Zhou, Wania Wolff, Krishnendu Gope, Niels Kurz and Silva Mezinska for all their fruitful discussions and practical support in the lab. Special thanks to Ranko Grimm and Alexander von der Dallen for their technical help.

I would like to express my thanks to our external colleagues, Gustavo Gracia and Carlos Guerra Castillo for the experimental collaboration and support, and to Maomao Gong and Anna Skitnevskaya for providing the theoretical support.

I am immensely grateful to all other members of the Pfeifer division especially Ana Denhi Martinez, Hemkumar Srinivas, Weiyu Zhang, Divya Bharti, David Chicharro, Felix Hermann, Keshav Shishodia, Christian Medina, etc for the fun and cheerful daily life at MPIK. I would like to thank you for all the lunchtime and coffee-time fun and for numerous outings and gatherings.

I would like to remember and thank all my friends who have been persistently keeping my days happier and inspiring me, especially Arsha, Bichu, Deepak, Nandan, Lakshmi, Parveena, Aleena, Sibeesh, Arunkumar, Abhijith, Arya, Susmitha, Induja, Keerthana, Anjusree, Vishnu and Gopika. Special appreciation to Jael, Anto Melvin and Merin for the beautiful weekends full of music.

My heartfelt gratitude to my better-half Brijesh Babu for always being my pillar of support. Thanks for all the encouragement and patience through all my ups and downs all these years.

Finally, I wish to express my gratitude to my parents who have been there in all phases of my life, for all the encouragement, love and support. Thanks for giving wings to my dreams.